Transferts aux petites échelles : application au rayonnement thermique, aux forces de Casimir et à la conduction thermique

Document annexe : recueil de publications

par Karl JOULAIN

Maître de Conférences

Université de Poitiers

Ecole Nationale Supérieure de Mécanique et d'Aérotechnique

Spécialité : Sciences pour l'ingénieur. Secteur : Energétique, Thermique Combustion

Jury composé de :

Pierre CHAVEL, CNRS, Laboratoire Charles Fabry de l'Institut d'Optique, Orsay.

Jean-Jacques GREFFET, ECP, Laboratoire EM2C, Châtenay-Malabry.

Astrid LAMBRECHT, CNRS, Laboratoire Kastler-Brossel, Paris.

Bernard PERRIN, CNRS, Institut des NanoSciences de Paris, Paris.

Jean-Bernard SAULNIER, ENSMA, Laboratoire d'Etudes Thermiques, Poitiers.

Table des matières

Near-Field Spectral Effects due to Electromagnetic Surface Excitations

A. Shchegrov, K. Joulain, R. Carminati et J.-J. Greffet

Physical Review Letters, vol 85, pp1548–1551 (2000)

Near-Field Spectral Effects due to Electromagnetic Surface Excitations

Andrei V. Shchegrov*
Rochester Theory Center for Optical Science and Engineering
and Department of Physics and Astronomy, University of Rochester, Rochester, New York 14627-0171

Karl Joulain, Rémi Carminati, and Jean-Jacques Greffet
Laboratoire d'Energétique Moléculaire et Macroscopique, Combustion, Ecole Centrale Paris, Centre National de la Recherche Scientifique, 92295, Châtenay-Malabry Cedex, France

(Received 14 March 2000)

We demonstrate theoretically that the spectra of electromagnetic emission of surface systems can display remarkable differences in the near and the far zones. The spectral changes occur due to the loss of evanescent modes and are especially pronounced for systems which support surface waves.

PACS numbers: 78.20.–e, 05.40.–a, 44.40.+a, 87.64.Xx

Spectroscopy of electromagnetic radiation is perhaps the most powerful exploration tool employed in natural sciences: astronomy, atomic and molecular physics and chemistry, materials science, biology, etc. The central question considered in this paper—whether the spectral content of the radiation emitted by an object can change on propagation to the observer—usually does not arise, since it seems natural that nothing can happen to waves traveling through empty space. Surprisingly similar failure of common sense was put forward by the recent progress of near-field optical microscopy [1,2], which achieves subwavelength resolution exactly because evanescent modes carrying subwavelength spatial information do not propagate far away from the object. However, a great deal of work devoted to such an irreversible *change of spatial information* on propagation has been accompanied with significantly lesser interest in the possibility of the *change of spectral information*.

The subject of spectral changes on propagation has, however, been addressed. In the 1980's, Wolf [3] predicted that the spectrum of light can be changed on propagation from the source to the observer, even through empty space. This effect, whose origin lies in the fluctuating nature of the source, has been intensively studied in a variety of systems [4,5]. Typically, the Wolf effect is manifested in small spectral shifts and can be viewed as a redistribution of the weights of different spectral components.

In this Letter, we demonstrate spectral changes, whose physical origin is very different from that of Wolf spectral shifts and lies in the presence of the evanescent component in the emitted field. We show that the near-field and far-field spectra of emitted electric fields can display drastic differences. For a broadband emission, such as thermal emission which is considered in detail in this paper, the near-field spectrum dominated by evanescent modes can be entirely different from the far-field spectrum of propagating modes. These spectral changes occur not due to the statistical nature of the source (as in the Wolf effect) but due to the loss of evanescent components on propagation. We analyze how such spectral changes can be enhanced by electromagnetic surface waves (SW) near the interface. These SW are known to play an important role in the enhancement of interaction between nanoparticles near the surface [6], in localization effects on random surfaces [7], in surface-enhanced Raman scattering [8], in extraordinary transmission of light through subwavelength holes [9], etc. In this Letter, we show that SW provide the leading contribution to the density of energy in the near-field zone of electromagnetic emission.

We now proceed with analyzing near-field effects in the spectra of thermal emission, which provides an easy way to excite both propagating and evanescent electromagnetic modes in a wide range of frequencies (at least, in the infrared [10–12]). Thermal emission is frequently associated with the textbook example of equilibrium blackbody radiation. The Planck spectrum $I_{BB}(\omega)$ of such radiation is obtained by multiplying the thermal energy $\theta(\omega,T) = \hbar\omega/[\exp(\hbar\omega/k_BT) - 1]$ of a quantum oscillator by the density of oscillations (modes) per unit volume $N(\omega)d\omega = \omega^2 d\omega/(\pi^2c^3)$ in the frequency interval $(\omega, \omega + d\omega)$, and dividing the result by $d\omega$ [13],

$$I_{BB}(\omega) = \theta(\omega,T)N(\omega) = \frac{\hbar}{\pi^2c^3}\frac{\omega^3}{\exp(\hbar\omega/k_BT) - 1}. \tag{1}$$

Here T is the body temperature, k_B is Boltzmann's constants, $\hbar$ is Planck's constant divided by 2π, and c is the speed of light in vacuum. A well-known representation of blackbody radiation is the equilibrium radiation in a closed cavity with lossy walls when only *propagating* modes of the field are taken into account.

To demonstrate the importance of near-field effects, we consider a somewhat more sophisticated example of thermal emission from a semi-infinite ($z < 0$) slab of homogeneous, nonmagnetic material held in local thermodynamic equilibrium at a uniform temperature T, into the empty half-space $z > 0$. We will describe the macroscopic dielectric properties of the material by a frequency-dependent, complex dielectric function $\varepsilon(\omega) = \varepsilon'(\omega) + i\varepsilon''(\omega)$. The

Fourier component $\mathbf{E}(\mathbf{r},\omega)$ of the electric field $\mathbf{E}(\mathbf{r},t)$ at a point $\mathbf{r}=(x,y,z)$ in the empty half space $z>0$ is generated by thermal currents with density $\mathbf{j}(\mathbf{r}',\omega)$, which is nonzero only for $z'<0$. It can be computed following the procedure outlined in Refs. [12,14],

$$E_\alpha(\mathbf{r},\omega) = i\mu_0\omega \sum_{\beta=x,y,z}\int_V d^3r'\, G_{\alpha\beta}(\mathbf{r},\mathbf{r}',\omega)\, j_\beta(\mathbf{r}',\omega)\,, \tag{2}$$

where V is the volume of the hot body which occupies the half-space $z'<0$, and $G_{\alpha\beta}(\mathbf{r},\mathbf{r}',\omega)$ is the electromagnetic Green tensor for the system of two homogeneous materials separated by a planar interface $z=0$. According to the fluctuation-dissipation theorem [14], the fluctuations of thermal currents are described by the correlation function

$$\langle j_\alpha(\mathbf{r},\omega) j_\beta(\mathbf{r}',\omega')\rangle = \frac{\omega\theta(\omega,T)}{\pi}\,\varepsilon_0\varepsilon''(\omega)\delta_{\alpha\beta}\delta(\mathbf{r}-\mathbf{r}') \times \delta(\omega-\omega')\,, \tag{3}$$

where the angle brackets denote the statistical ensemble average. The Kronecker symbol $\delta_{\alpha\beta}$ and the spatial δ function in this formula follow from the assumption that the dielectric function is isotropic, homogeneous, and local [14].

The energy density $I(\mathbf{r},\omega)$ of the emitted electric field at the point $\mathbf{r}$ is defined by the formula

$$\sum_{\alpha=x,y,z}\frac{\varepsilon_0}{2}\langle E_\alpha^*(\mathbf{r},\omega)E_\alpha(\mathbf{r},\omega')\rangle \equiv I(\mathbf{r},\omega)\delta(\omega-\omega')\,. \tag{4}$$

Using Eqs. (2) and (3) into (4), we obtain, for $I(\mathbf{r},\omega)$,

$$I(\mathbf{r},\omega) = 8\pi^3\frac{\omega^3}{c^4}\theta(\omega,T)\varepsilon''(\omega)\sum_{\alpha,\beta=x,y,z}\int_{-\infty}^{0}dz' \times \int\frac{d^2k_\parallel}{(2\pi)^2}|g_{\alpha\beta}(\mathbf{k}_\parallel,\omega\mid z,z')|^2, \tag{5}$$

where $g_{\alpha\beta}(\mathbf{k}_\parallel,\omega\mid z,z')$ is the analytically known [12] 2D spatial Fourier transform (in x and y) of the Green's tensor $G_{\alpha\beta}(\mathbf{r},\mathbf{r}',\omega)$. Note that $I(\mathbf{r},\omega)$ in Eq. (5) is independent of x and y, due to the translational invariance of the system in x and y directions.

We now assume that the interface $z=0$ between the material and a vacuum can support electromagnetic SW. The dispersion relation between the wave number $k_\parallel = |\mathbf{k}_\parallel|$ and frequency ω of SW is

$$[k_\parallel^{\mathrm{SW}}(\omega)]^2 = (\omega^2/c^2)\varepsilon(\omega)/[\varepsilon(\omega)+1]. \tag{6}$$

Such waves exist for materials having $\varepsilon'(\omega) < -1$ in one or several frequency ranges [10]. We consider SiC, which supports SW known as surface phonon polaritons and which has been used in previous experimental [11] and theoretical [12] investigations of thermal emission. The dielectric function of this material is given by the expression $\varepsilon(\omega)=\varepsilon_\infty(\omega_L^2-\omega^2-i\gamma\omega)/(\omega_T^2-\omega^2-i\gamma\omega)$ with $\varepsilon_\infty = 6.7$, $\omega_L = 182.7\times10^{12}\ \mathrm{s}^{-1}$, $\omega_T = 149.5\times10^{12}\ \mathrm{s}^{-1}$, and $\gamma = 0.9\times10^{12}\ \mathrm{s}^{-1}$ [11]. By substituting $\varepsilon(\omega)$ into Eq. (5) and performing a straightforward evaluation of integrals (only the integral over the magnitude of $\mathbf{k}_\parallel$ has to be calculated numerically, the other two integrals can be evaluated analytically), we obtain the spectra of thermal emission for SiC at different heights z above the surface. We plot the results in Fig. 1 in the frequency range $0<\omega<400\times10^{12}\ \mathrm{s}^{-1}$ for $T=300$ K at three different heights.

Although one could expect to find differences of the SiC spectra with the blackbody spectrum (1), it is striking that near-field and far-field spectra of the same SiC sample are so dramatically different, as seen in Fig. 1. An observer doing a traditional far-zone spectroscopic measurement (Fig. 1a) would detect the spectrum with a rather wide dip in the range $150\times10^{12}\ \mathrm{s}^{-1} < \omega < 180\times10^{12}\ \mathrm{s}^{-1}$ due to the low emissivity of SiC in that range [11]. Note that the sample effectively acts as a *nonradiating* source in this frequency range. However, when the probe moves within a *subwavelength* distance from the material (typical thermal emission wavelengths at $T=300$ K are of the order of 10 μm), the spectrum starts to change rapidly. In Fig. 1b, showing the emission spectrum at 2 μm above the surface, this change is seen as a peak emerging at $\omega = 178.7\times10^{12}\ \mathrm{s}^{-1}$. At very close distances (Fig. 1c), the peak becomes so strong that an observer would surprisingly see almost *monochromatic* emission with photon energies not represented in the far zone.

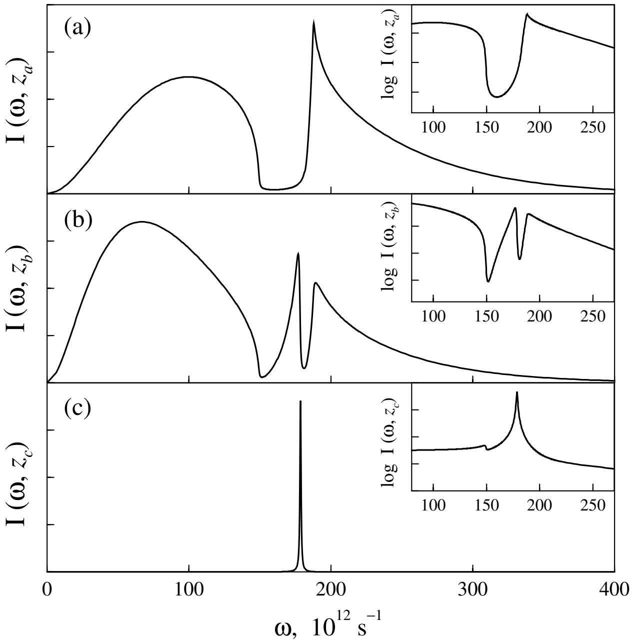

FIG. 1. Spectra of thermal emission of a semi-infinite sample of SiC at $T=300$ K and three different heights above the surface: (a) $z_a = 1000\ \mu$m, (b) $z_b = 2\ \mu$m, (c) $z_c = 0.1\ \mu$m. The insets magnify the spectra plotted on a semilog scale in the range of strong contribution from evanescent surface modes.

Thus, we find that the spectrum changes *qualitatively* on propagation. The occurrence of such striking spectral changes is related to SW existing in the region $150 \times 10^{12}\ \mathrm{s}^{-1} < \omega < 180 \times 10^{12}\ \mathrm{s}^{-1}$. We shall now clarify the mechanism of the formation of spectra $I(\mathbf{r}, \omega)$ at different distances from the surface.

We note that the spectrum of the elctric field (5) has a similar structure as that of blackbody radiation (1),

$$I(z, \omega) = \theta(\omega, T) N(z, \omega). \tag{7}$$

In Eq. (1), $N(\mathbf{r}, \omega)$ does not depend on $\mathbf{r}$, while in Eq. (5) it depends on z. *Equation* (7) *is a pivotal point of our paper since it accounts for the evolution of the spectrum on propagation by relating it to the local density of electromagnetic modes* $N(\mathbf{r}, \omega)$. Note that $N(\mathbf{r}, \omega)$ includes only relevant modes excited in the material ($z < 0$) and emitted into vacuum ($z > 0$). The correct counting of modes is done automatically in the integral in Eq. (5), which has a typical structure that relates the density of modes to the Green's tensor of the system. The function $|g_{\alpha\beta}(\mathbf{k}_\parallel, \omega \mid z, z')|^2$ in Eq. (5) represents a mode that is excited in the plane z' with a 2D wave vector $\mathbf{k}_\parallel$ and polarization β and arrives at the plane z with the same 2D wave vector (due to translational invariance in x and y) and polarization α. The sum over β and the integrals over $\mathbf{k}_\parallel$ and $z' < 0$ take into account all possible modes that are initially excited.

The origin of a sharp peak seen in the near-field emission spectrum (Fig. 1c) becomes clear when we analyze the dispersion relation (6) for SW (Fig. 2). Near the frequency $\omega_{\max}$ defined by the condition $\varepsilon'(\omega_{\max}) = -1$, there exists a large number of surface modes with different wave numbers but with frequencies that are very close to each other. Therefore, the density of surface modes will necessarily display a strong peak at $\omega = \omega_{\max}$. However, since SW decay exponentially away from the surface, this peak is not seen in the far zone (Fig. 1a).

To achieve a detailed understanding of the z dependence of the emission spectrum, we calculate an approximate expression for the density of modes $N(z, \omega)$ from Eqs. (5) and (7) for small distances z and in the limit of large $k_\parallel$ (according to Fig. 2, the modes with large $k_\parallel$ define the behavior near the peak):

$$N(z, \omega) = \frac{\varepsilon''(\omega)}{|1 + \varepsilon(\omega)|^2} \frac{1}{16\pi^2 \omega z^3}. \tag{8}$$

This $1/z^3$ contribution can be recognized as a well-known quasistatic behavior exhibited near the surfaces of all materials [12,14]. Note that if ε'' is not very large at $\omega = \omega_{\max}$ then the density of modes exhibits a resonance at that frequency. This is the origin of the peak in the near-field spectrum of SiC at $\omega = 178.7 \times 10^{12}\ \mathrm{s}^{-1}$. The presence of a resonance in the density of modes $N(z, \omega)$ is, however, not required for observing spectral changes caused by the loss of evanescent modes. Indeed, in the short distance regime, the spectrum is given by Eq. (8), whereas, in the far field, the spectrum is given by Eq. (1) multiplied by the emissivity of the surface. Thus, even in the absence of resonant SW, the near-field spectrum is different from the far-field spectrum, but the changes are less dramatic.

The result (8) is valid only in the limit of distances much smaller than the wavelength. We show in Fig. 3 the variation of the spectral density $I(\omega, z)$ with the distance z from the surface. We consider two different frequencies none of which is very close to the resonance at $\omega_{\max}$. In agreement with Eq. (8), we observe that the spectral density increases sharply for $z < 1\ \mu\mathrm{m}$, i.e., when the distance to the surface is much smaller than the wavelength. However, the decay behavior of the two curves for larger values of z exhibits an essential difference. The exponential decay seen in the solid curve for the values of z between 1 and 5 μm is a signature of the presence of a SW whose energy decays exponentially with z. This SW is a surface phonon polariton that exists at $\omega = 166 \times 10^{12}\ \mathrm{s}^{-1}$ (solid curve) but not at $\omega = 210 \times 10^{12}\ \mathrm{s}^{-1}$ (dashed curve). The different z dependence of the $I(\omega, z)$ for different values of ω causes the spectrum to change on propagation of emitted radiation from the surface to the far zone.

This analysis allows us to conclude that the spectral changes in thermal emission should be observable in a wide variety of solid-state systems supporting evanescent

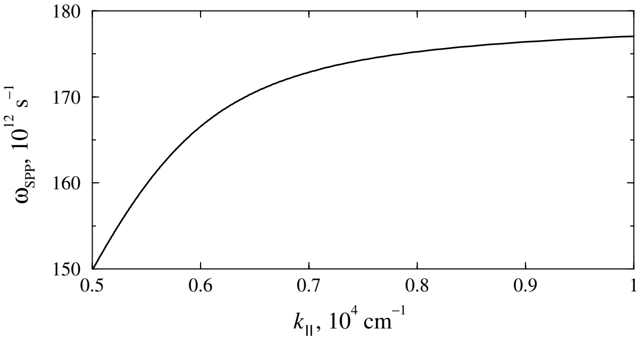

FIG. 2. Dispersion curve for SW on the vacuum-SiC planar interface. $\mathrm{Re}(\omega_{SPP})$ is calculated for a given real $k_\parallel$.

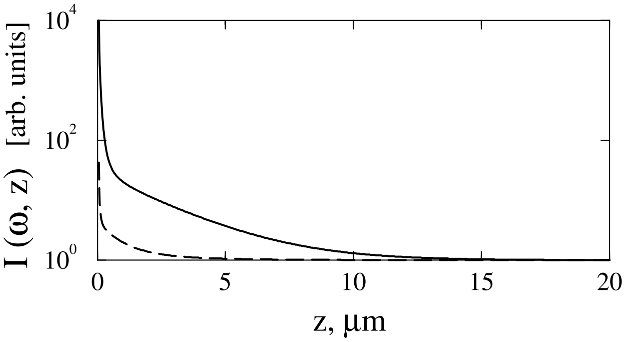

FIG. 3. The variation of the spectral density of the thermal emission for SiC at $T = 300$ K with the distance z from observer to the surface. Solid line: $\omega = 166 \times 10^{12}\ \mathrm{s}^{-1}$ ($\lambda = 11.4\ \mu\mathrm{m}$), dashed line: $\omega = 210 \times 10^{12}\ \mathrm{s}^{-1}$ ($\lambda = 9.0\ \mu\mathrm{m}$).

surface waves or guided waves (in layered structures [5]). Resonant features in the near-field spectra (such as in Fig. 1c) correspond to resonances in the local density of surface modes $N(z,\omega)$ and appear when the dispersion curve for SW has a flat portion (as in Fig. 2). In addition to our example of SiC, such resonances $N(z,\omega)$ are displayed by metals (supporting surface plasmon polaritons), semiconductors (supporting surface exciton polaritons Φ), and several other materials. Yet, a peak in the emission intensity $I(z,\omega)$ will be observable only if $\theta(\omega,T)$ is not too small. For example, the near-field spectrum of thermal emission from amorphous glass near-field spectrum has a sharp peak for $\omega = 9.24 \times 10^{13}\ \mathrm{s}^{-1}$ ($\lambda = 20.4\ \mu$m) visible at room temperature. All of the III-V and II-VI semiconductors can support surface waves in the midinfrared. However, although the number of modes (8) has a resonance in the case of silver at about $\omega = 5.57 \times 10^{15}\ \mathrm{s}^{-1}$ ($\lambda = 0.339\ \mu$m), no sharp peak is seen if the temperature silver sample is lower than 4000 K.

Equations (7) and (8) also suggest a new application for near-field spectroscopy. As a near-field spectrum at a given distance to the interface gives access to $\varepsilon''(\omega)/|1 + \varepsilon(\omega)|^2$, one can hope to retrieve the material dielectric constant, similar to the method usually used to obtain ε from reflectivity measurements [15]. With the rapid development of near-field optical microscopy, such near-field spectra can be measured. This could open the way to a new technique of local solid-state spectroscopy. Finally, we anticipate that the effects reported in this paper should significantly improve our understanding of the radiative heat transfer at nanometric scale with particular applications in the field of near-field microscopies. This might have applications for high density storage where the local control of temperature is essential in the writing process. Also, note that the effect of near-field thermal fluctuations was measured recently using the induced brownian motion on an atomic force microscope tip [16].

To summarize, we have demonstrated that the spectrum of thermal emission can undergo significant, qualitative changes on propagation due to the loss of evanescent modes. Such novel spectral changes are caused by the change in the local density of emitted electromagnetic modes, and are especially pronounced in the systems supporting surface waves.

We thank Professor Emil Wolf and Dr. Carsten Henkel for useful discussions. The work of A. V. S. was supported by the Engineering Research Program of the Office of Basic Energy Science at the Department of Energy under Grant No. DE-FG02-90ER 14119 and by the Air Force Office of Scientific Research under Grant No. F49620-00-1-0125.

---

*Present address: KLA-Tencor Corporation, 160 Rio Robles, San Jose, CA 95134.
Email address: Andrei.Shchegrov@KLA-Tencor.com

[1] *Near Field Optics,* edited by D. W. Pohl and D. Courjon (Kluwer, Dordrecht, 1993); J.-J. Greffet and R. Carminati, Prog. Surf. Sci. **56**, 133 (1997).

[2] Q. Wu, R. D. Grober, D. Gammon, and D. S. Katzer, Phys. Rev. Lett. **83**, 2652 (1999).

[3] E. Wolf, Phys. Rev. Lett. **56**, 1370 (1986); Nature (London) **326**, 363 (1987).

[4] E. Wolf and D. F. V. James, Rep. Prog. Phys. **59**, 771 (1996).

[5] T. A. Leskova, A. A. Maradudin, A. V. Shchegrov, and E. R. Méndez, Phys. Rev. Lett. **79**, 1010 (1997); A. V. Shchegrov and A. A. Maradudin, Phys. Rev. B **59**, 7732 (1999).

[6] H. R. Stuart and D. G. Hall, Phys. Rev. Lett. **80**, 5663 (1998).

[7] A. R. McGurn, A. A. Maradudin, and V. Celli, Phys. Rev. B **31**, 4866 (1985); S. I. Bozhevolnyi, I. I. Smolyaninov, and A. V. Zayats, Phys. Rev. B **51**, 17916 (1995).

[8] *Surface-Enhanced Raman Scattering,* edited by R. K. Chang and T. E. Furtak (Plenum, New York, 1982).

[9] T. W. Ebbesen, H. J. Lezec, H. F. Ghaemi, T. Thio, and P. A. Wolff, Nature (London) **391**, 667 (1998).

[10] E. A. Vinogradov, G. N. Zhizhin, and V. I. Yudson, in *Surface Polaritons,* edited by V. M. Agranovich and D. L. Mills (North-Holland, Amsterdam, 1982), p. 145.

[11] P. J. Hesketh, J. N. Zemel, and B. Gebhart, Nature (London) **324**, 549 (1986); J. Le Gall, M. Olivier, and J.-J. Greffet, Phys. Rev. B **55**, 10105 (1997).

[12] R. Carminati and J.-J. Greffet, Phys. Rev. Lett. **82**, 1660 (1999).

[13] L. D. Landau, E. M. Lifshitz, and L. P. Pitaevskii, *Statistical Physics, Part I* (Pergamon, Oxford, 1980), p. 183.

[14] S. M. Rytov, Yu. A. Kravtsov, and V. I. Tatarskii, *Principles of Statistical Radiophysics 3* (Springer-Verlag, Berlin, 1989), p. 118.

[15] E. W. Palik, *Handbook of Optical Constants of Solids* (Academic Press, San Diego, 1985).

[16] I. Dorofeyev, H. Fuchs, G. Wenning, and B. Gotsmann, Phys. Rev. Lett. **83**, 2402 (1999).

Spatial coherence of thermal near fields

C. Henkel, K. Joulain, R. Carminati et J.-J. Greffet

Optics Communications, vol 186, pp57–67 (2000)

1 December 2000

Optics Communications 186 (2000) 57–67

OPTICS COMMUNICATIONS

www.elsevier.com/locate/optcom

Spatial coherence of thermal near fields

C. Henkel [a,*], K. Joulain [b], R. Carminati [b], J.-J. Greffet [b]

[a] *Institut für Physik, Universität Potsdam, Am Neuen Palais 10, 14469 Potsdam, Germany*

[b] *Laboratoire d'Energétique Moléculaire et Macroscopique, Combustion, Ecole Centrale Paris, 92295 Châtenay-Malabry Cedex, France* [1]

Received 27 July 2000; received in revised form 2 October 2000; accepted 3 October 2000

Abstract

We analyze the spatial coherence of the electromagnetic field emitted by a half-space at temperature T close to the interface. An asymptotic analysis allows to identify three different contributions to the cross-spectral density tensor in the near-field regime: thermally excited surface waves, skin-layer currents and small-scale polarization fluctuations. It is shown that the coherence length can be either much larger or much shorter than the wavelength depending on the dominant contribution. © 2000 Elsevier Science B.V. All rights reserved.

PACS: 42.72; 71.36; 73.20.M; 42.25.K; 07.79.F

Keywords: Black body radiation; Polaritons; Surface plasmons; Coherence in wave optics; Scanning near-field optical microscopy

1. Introduction

The typical textbook example of an incoherent source is a thermal source. From the point of view of temporal coherence, its spectrum is given by Planck's function and modified by its emissivity. For usual sources, the emissivity is a smooth function of frequency. Thus, the spectral width is usually on the order of the peak frequency of Planck's function. From the point of view of spatial coherence, a thermal source is often assumed to be delta correlated. Yet, an exact form of the cross-spectral density tensor has been derived for a blackbody radiator and it has been shown that the spatial coherence length is $\lambda/2$ [1]. These exact results seem to support the statement that a thermal source is incoherent. Yet, one has to analyze more carefully the problem when dealing with a real thermal source. The radiation emitted by a semiconductor (SiC) grating in the infrared, for example, is partially coherent in space, as was shown both theoretically and experimentally by LeGall et al. (see Ref. [2] and references therein). In the present paper, we consider a source that consists of a half-space filled with a lossy material at temperature T. We are interested in the emitted field so that we assume that there are no other sources. Thus there is no incident radiation illuminating the sample. Note in particular that this is not an equilibrium situation.

Since we explicitly introduce a model for the source, the emitted field contains evanescent waves

---

[*] Corresponding author. Tel.: +49-331-977-1498; fax: +49-331-977-1767.

E-mail address: carsten.henkel@quantum.physik.uni-potsdam.de (C. Henkel).

[1] Unité propre de recherche no. 288 du Centre National de la Recherche Scientifique.

PII: S0030-4018(00)01048-8

in the vicinity of the interface. These evanescent waves are not taken into account when dealing with blackbody radiation. Yet, they modify the coherence properties of the source in the near field as was shown in Ref. [3]. The effect is particularly striking if a resonant surface wave is excited. It has been shown that the coherence length can be either much larger than the wavelength or much shorter than $\lambda/2$ close to the surface. Temporal coherence is also dramatically modified. For example, the emitted radiation is almost monochromatic when a surface wave is excited [4]. These results were obtained using a direct calculation of the field emitted by a half-space in the framework of fluctuation electrodynamics [5–8].

The aim of this paper is to analyze the spatial coherence of the emitted field by means of an asymptotic evaluation of the cross-spectral density tensor in the near-field limit (interface–detector distance small compared to the wavelength). This analysis permits to retrieve the properties reported in Ref. [3] and yields insight into the physical mechanism responsible for these effects. We are thus able to identify all the possible contributions to the cross-spectral density tensor: thermally excited surface waves, skin-layer currents and small-scale polarization fluctuations. We show that to a good approximation, the sum of these three asymptotic contributions coincides with the exact result. We obtain different characteristic behaviors that vary in accordance with the dominant term. Surface waves such as surface plasmon–polaritons or surface phonon–polaritons yield long-range spatial coherence on a scale of the surface wave propagation length which may be much larger than the wavelength when absorption is small. On the contrary, skin-layer currents and small-scale polarization fluctuations lead to a much shorter spatial coherence length that only depends on the distance to the interface. A surprising consequence of this property is that the macroscopic theory of radiometry may be extended into the mesoscopic regime insofar as emission is concerned. Note however that this conclusion is based on the assumption of a local medium. The ultimately limiting scale is thus given by the electron screening length or the electron Fermi wavelength, whatever is larger [9,10].

2. Overview

2.1. Radiation emitted by a thermal source

In this section, we review the source theory approach we use for the computation of the thermal electromagnetic field [5–8]. We focus on the radiation in the vacuum close to a source that we model as a linear dielectric with dielectric function $\varepsilon(\mathbf{r};\omega)$. The frequency dependence will not be indicated explicitly in the following since we calculate quantities at fixed frequency (or, equivalently, at fixed wavelength $\lambda = 2\pi c/\omega$. The source radiates because it contains a fluctuating polarization field $\mathbf{P}(\mathbf{r})$. The spectral density of this field is characterized by the cross-correlation tensor $S_P^{ij}(\mathbf{r}_1,\mathbf{r}_2)$ that, according to the fluctuation–dissipation theorem [5,6,11,12], is given by

$$S_P^{ij}(\mathbf{r}_1,\mathbf{r}_2) = \frac{2\hbar\varepsilon_0 \operatorname{Im}\varepsilon(\mathbf{r}_1)}{e^{\hbar\omega/k_B T} - 1}\delta^{ij}\delta(\mathbf{r}_1 - \mathbf{r}_2) \tag{1}$$

The Kronecker delta δ^{ij} and the spatial δ-function in this formula follow from the assumption that the dielectric function is isotropic and local. We have taken the normal-ordered form for the polarization field spectrum since we are ultimately interested in the electromagnetic field measured by a photodetector (given by normally ordered field operators [1,11]). The electric field $\mathbf{E}(\mathbf{r})$ radiated by the polarization $\mathbf{P}(\mathbf{r})$ is now given by the Green function for the source geometry

$$E_i(\mathbf{r}) = \int_V \mathrm{d}\mathbf{r}' \sum_j G^{ij}(\mathbf{r},\mathbf{r}')P_j(\mathbf{r}') \tag{2}$$

where V is the volume of the source, i.e., the domain where $\operatorname{Im}\varepsilon(\mathbf{r}')$ is nonzero according to Eq. (1). All quantities in Eq. (2) are understood as temporal Fourier transforms at frequency ω. The coherence function $W^{ij}(\mathbf{r}_1,\mathbf{r}_2)$ of the electromagnetic field is now obtained as a thermal average of Eq. (2), using the polarization spectrum (1). One obtains [3,4]

$$W^{ij}(\mathbf{r}_1,\mathbf{r}_2) = \frac{2\hbar\varepsilon_0}{e^{\hbar\omega/k_B T} - 1}\sum_k \int_V \mathrm{d}\mathbf{r}' \operatorname{Im}\varepsilon(\mathbf{r}') \times G^{ik*}(\mathbf{r}_1,\mathbf{r}')G^{jk}(\mathbf{r}_2,\mathbf{r}') \tag{3}$$

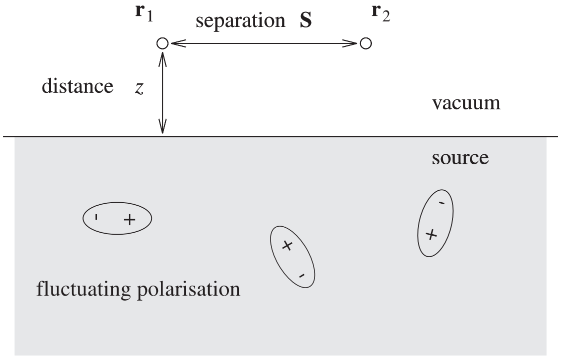

Fig. 1. Model geometry for a planar source.

The problem is now to evaluate this expression analytically and to obtain an estimate for its dependence on the separation $\mathbf{s} \equiv \mathbf{r}_2 - \mathbf{r}_1$ between the observation points.

To proceed in the calculation, we focus on the simplified geometry shown in Fig. 1: an infinite half-space with uniform dielectric constant ε, separated by the plane $z = 0$ from the empty half-space $z > 0$. For this arrangement, the Green tensor is explicitly known as a spatial Fourier transform with respect to the lateral separation $\mathbf{S} = (s_x, s_y) \equiv \mathbf{R}_2 - \mathbf{R}_1$. Details may be found in Refs. [11,13,14] and in Appendix A. As to be expected for this source geometry, the electric coherence tensor depends on the distances z_1, z_2 of the observers and their lateral separation $\mathbf{S}$. For simplicity, we put in the following $z_1 = z_2 = z$. We also normalize the coherence tensor W^{ij} to its value for $\mathbf{r}_1 = \mathbf{r}_2$ in the case of blackbody radiation

$$W_{\mathrm{bb}} = \frac{2\hbar k^3}{3\pi\varepsilon_0 (\mathrm{e}^{\hbar\omega/k_{\mathrm{B}}T} - 1)} \tag{4}$$

where as usual $k = \omega/c$. As outlined in Appendix A, we thus get the following expression for the spatial Fourier transform of the coherence tensor

$$w^{ij}(\mathbf{S}, z) = \frac{W^{ij}(\mathbf{S}, z)}{W_{\mathrm{bb}}} = \int \frac{\mathrm{d}^2\mathbf{K}}{(2\pi)^2} \mathrm{e}^{\mathrm{i}\mathbf{K}\cdot\mathbf{S} - 2z\,\mathrm{Im}\,\gamma} w^{ij}(\mathbf{K}) \tag{5}$$

where $\mathbf{K}$ denotes a wave vector parallel to the interface and $(\mathbf{K}, \gamma)$ is the vacuum wave vector of a plane wave emitted by the source. The tensor $w^{ij}(\mathbf{K})$ is given in Appendix A, Eq. (A.10). The integration over $\mathbf{K}$ in Eq. (5) also includes wave vectors $|\mathbf{K}| > k$, describing evanescent waves the source excites in the vicinity of the interface (the quantity γ is then purely imaginary with positive imaginary part).

2.2. Near-field coherence function

In this subsection, the typical behavior of the field coherence function is discussed. We identify several distance regimes showing a very different behavior of the lateral coherence function. Analytical approximations for the coherence function are deferred to the next section.

In Fig. 2 is shown the ‘energy density’ (the trace of the coherence tensor at coinciding positions) above a metal surface in double logarithmic scale. One observes a strong increase with respect to the far-field energy density when the distance z is smaller than the wavelength. For moderate distances $z \leqslant \lambda$, the energy density is dominated by an exponentially increasing contribution (cf. Fig. 2(b)). This is due to the excitation of surface plasmon resonances, whose contribution is calculated analytically in Section 3.1. The other curve in Fig. 2(b) shows the energy density for the case of tungsten with $\mathrm{Re}\,\varepsilon > -1$ where no surface mode exists and no exponential increase is found. For small distances $z \ll \lambda$, the energy density follows a $1/z^3$ power law (‘static limit’) that is discussed in Section 3.2. The prefactor of this power law involves the imaginary part of the electrostatic reflection coefficient $\mathrm{Im}[(\varepsilon - 1)/(\varepsilon + 1)]$. The second curve in Fig. 2(a) illustrates the resonantly enhanced energy density for a wavelength where $\mathrm{Re}\,\varepsilon \approx -1$. The ‘static limit’ contribution then overwhelms that of the plasmon resonance.

In Fig. 3, we show the normalized lateral coherence function at chosen distances from the interface. In the far field (Fig. 3(a)), the coherence length is $\lambda/2$, and the coherence function the same as for the blackbody field ($(\sin ks)/ks$ behavior). This is not surprising since at large distances $z \gg \lambda$, only propagating plane waves radiated into the vacuum half-space contribute to the field.

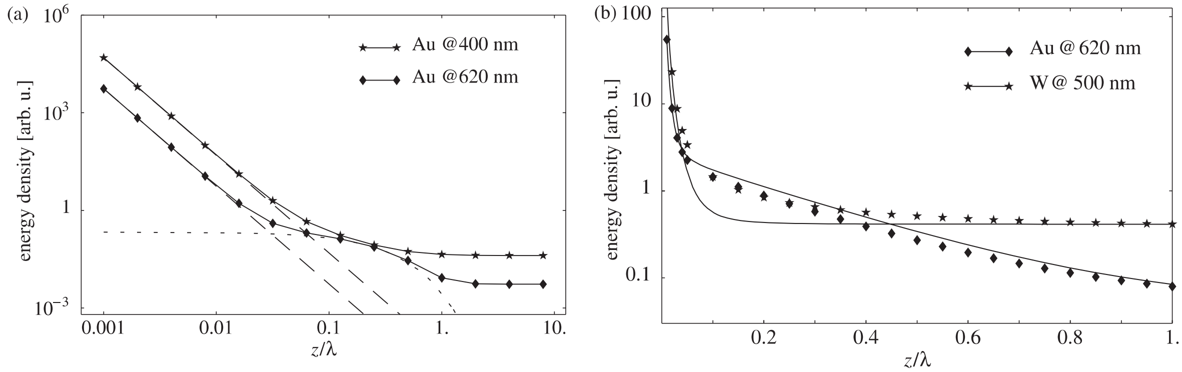

Fig. 2. Energy density $\mathrm{Tr}\, w^{ij}(\mathbf{S} = \mathbf{0}, z)$ vs. distance from a metal surface. Dots: numerical evaluation of the integral (5), solid lines: sum of the asymptotic approximations discussed in the text. In the far field, the numerically computed value is taken. (a) log–log scale for gold at $\lambda = 620$ nm ($\varepsilon = -9.3 + 1.2\mathrm{i}$) and at $\lambda = 400$ nm ($\varepsilon = -1.1 + 6.5\mathrm{i}$). The dielectric constants are extracted from Ref. [15]. Dashed line: $1/z^3$ power law dominating the extreme near-field; dotted line: exponentially decaying contribution of excited surface modes. (b) log–linear scale, showing the exponentially decaying surface plasmon contribution for gold at $\lambda = 620$ nm. For comparison, the case of tungsten at $\lambda = 500$ nm is shown where no plasmon resonance is found ($\varepsilon = 4.4 + 18\mathrm{i}$).

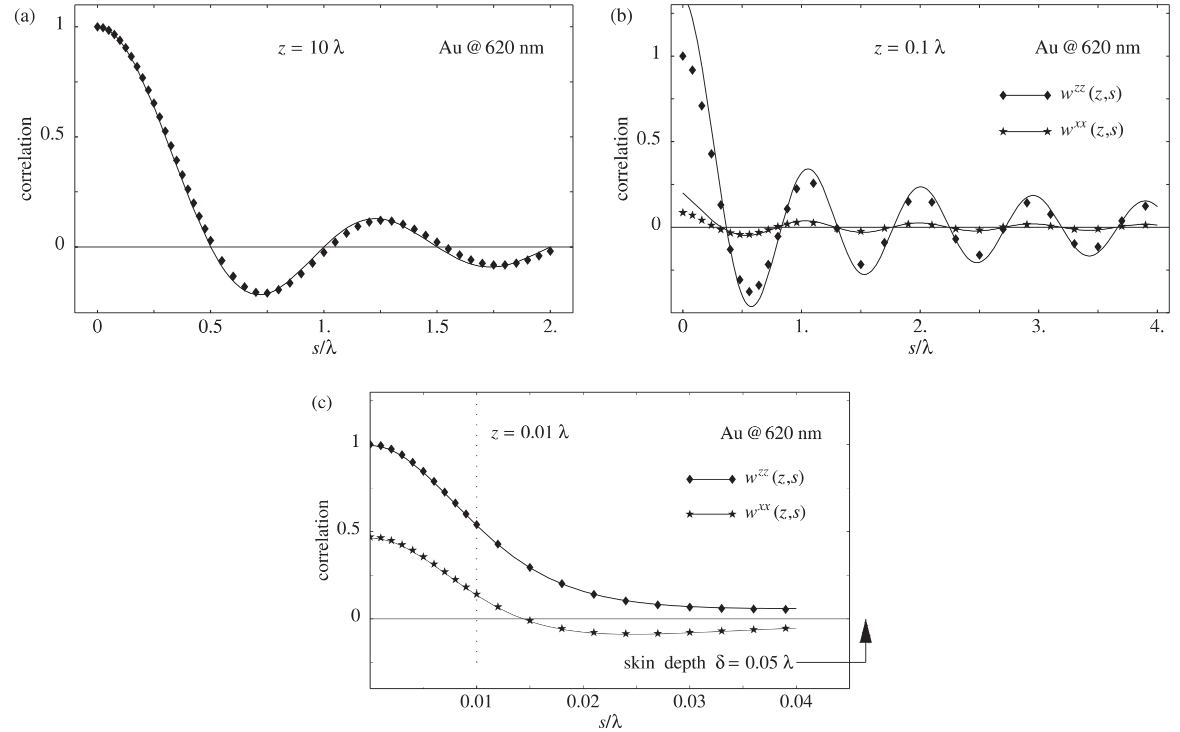

Fig. 3. Normalized lateral coherence functions for three fixed distances z, plotted vs. the lateral separation $s = |\mathbf{S}|$. All plots are for a gold surface at $\lambda = 620$ nm. Dots: numerical evaluation of Eq. (5), solid lines: analytical approximations discussed in the text. The numerically computed values were used to normalize all curves. (a) Far field regime $z = 10\lambda$. The trace of the coherence tensor is plotted, normalized to its value for $s = 0$. Solid line: free space coherence function $\sin(ks)/(ks)$. (b) Plasmon dominated regime $z = 0.1\lambda$. The components w^{xx} and w^{zz} are plotted, normalized to (the numerically computed) $w^{zz}(\mathbf{S} = \mathbf{0}, z)$. (c) Static regime $z = 0.01\lambda$. The components w^{xx} and w^{zz} are plotted and normalized as in (b). The solid curve only contains the extreme near-field contribution (17).

When the surface plasmon excitation dominates the field energy ($z \leqslant \lambda$), the field coherence extends over much longer distances (Fig. 3(b)). This is because of the weak damping of the plasmon modes in this case. We show below (Section 3.1) that the coherence length is indeed given by the plasmon propagation length. The figure also shows that the field is strongly polarized perpendicular to the interface, as is the surface plasmon mode.

At distances $z \ll \lambda$ even closer to the source, the field coherence length gets shorter again (Fig. 3(c)). We show below that in this regime, the field behaves as if it was quasi-static (Section 3.2). This leads to a lateral coherence length equal to the vertical distance z from the interface and hence much shorter than the wavelength. We thus find the surprising result that thermal near fields have no lower limit in their coherence length, as long as the dielectric function of the source may be taken as local.

One might finally ask whether the skin depth δ (defined in Eq. (23)) is relevant for the radiation emitted by a metallic source. This question is discussed in Section 3.3 where we show that in the regime $\delta \ll z \ll \lambda$, a different power law ($\propto 1/z^2$) governs the energy density (see Fig. 4(a)). The lateral coherence behaves similar to the static regime $z \ll \delta$, however, as shown in Fig. 4(b).

3. Analytical approximations

3.1. Plasmon contribution

It is well known that a dielectric–vacuum interface supports surface plasmon polariton (or phonon polariton) modes provided the dielectric constant satisfies $\operatorname{Re}\varepsilon < -1$ [16,17]. These surface modes propagate parallel to the surface with a wave vector $K_{\rm pl}$ and are exponentially localized in the direction perpendicular to the interface. In addition, if there are losses in the dielectric, the propagation parallel to the interface is damped which may be described by a nonzero imaginary part of $K_{\rm pl}$. Mathematically, we obtain the plasmon dispersion relation by identifying the poles of the transmission coefficients t_μ ($\mu = \mathrm{s, p}$) as a function of the wave vector K. Only the p-polarization (magnetic field perpendicular to the plane of incidence) gives a pole at the (complex) position

$$K_{\rm pl} = k\sqrt{\frac{-\varepsilon}{-\varepsilon - 1}}, \quad \operatorname{Re}K_{\rm pl},\ \operatorname{Im}K_{\rm pl} > 0 \tag{6}$$

The plasmon pole shows up as a sharp peak when the integrand $w^{ij}(\mathbf{K})$ in Eq. (5) is plotted as a function of the lateral wave vector magnitude K (cf. Eq. (A.10)). This suggests that we get a good approximation to the plasmon contribution by taking slowly varying terms outside the integral

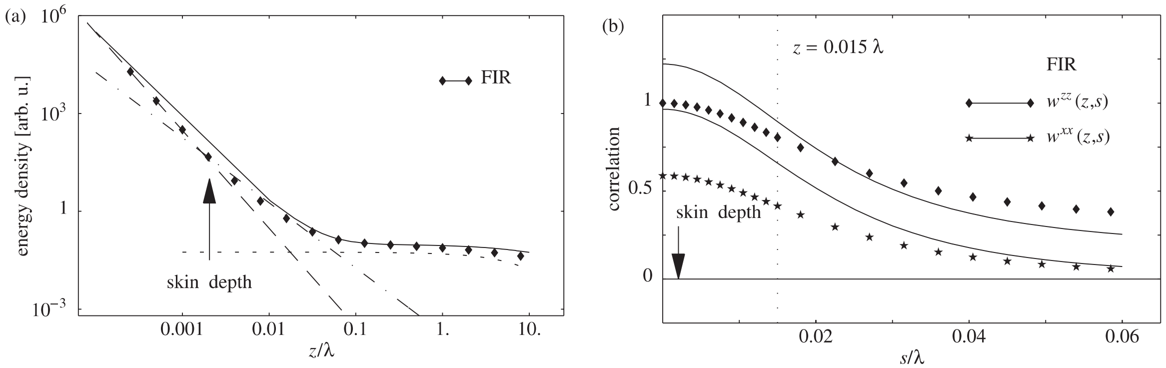

Fig. 4. Near-field coherence in the skin-effect dominated regime $\delta \ll z \ll \lambda$, typical for metals in the far infrared. Dots: numerical evaluation of the integral (5), lines: analytic asymptotics discussed in the text. (a) Energy density $\operatorname{Tr} w^{ij}(\mathbf{S} = \mathbf{0}, z)$ above a metallic surface with $\varepsilon = -8.26 + \mathrm{i}\,10^4$ (gold extrapolated to $\lambda = 3.7$ μm). The solid line is the sum of the asymptotic contributions derived in this paper. (b) Normalized lateral coherence functions $w^{ii}(\mathbf{S}, z)/w^{zz}(\mathbf{0}, z)$ ($i = x, z$) for fixed distance z, plotted vs. the lateral separation $s = |\mathbf{S}|$. The x- and z-polarizations differ because the plasmon contribution already comes into play. The numerically computed $w^{zz}(\mathbf{0}, z)$ was used to normalize all curves, this is why the analytic correlations exceed unity.

and evaluating the pole contribution by contour integration. For example, the denominator of the $|t_p|^2$ transmission coefficient may be approximated as

$$\frac{1}{|\varepsilon\gamma+\gamma_2|^2} \approx \frac{4|\varepsilon|^2}{|\varepsilon+1|\,|\varepsilon-1|^2}\,\mathrm{Im}\frac{1}{K^2-K_{\mathrm{pl}}^2} \qquad (7)$$

where $\gamma = \gamma(K)$ and γ_2 are the vertical wave vector components above and below the interface. It is essential for the contour integration to work that one expresses the absolute square on the left-hand side as the imaginary part of an analytic function of K (right-hand side).

It is easily checked from Eq. (A.10) that the trace of $w^{ij}(\mathbf{K})$ only depends on the magnitude K of the lateral wave vector $\mathbf{K}$. The integration over the angle between $\mathbf{K}$ and $\mathbf{S}$ therefore gives

$$\mathrm{Tr}\, w^{ij}(\mathbf{S},z) = \int_0^\infty \frac{K\,\mathrm{d}K}{2\pi} J_0(Ks)\,\mathrm{e}^{-2z\,\mathrm{Im}\,\gamma}\,\mathrm{Tr}\, w^{ij}(\mathbf{K}) \qquad (8)$$

where $J_0(\cdot)$ is the ordinary Bessel function and $s = |\mathbf{S}|$. The individual tensor components also involve Bessel functions $J_2(Ks)$, as discussed in Appendix B.1. The integration over K may be done using the identity (B.2) proven in Appendix B.2.1. The diagonal elements of the coherence tensor finally take the suggestive form

$$w^{ii}(\mathbf{S},z) \approx C_{\mathrm{pl}}\,\mathrm{e}^{-2\kappa_{\mathrm{pl}}z} g^i(K_{\mathrm{pl}}s) \qquad (9)$$

$$g^{\parallel}(u) = \frac{1}{2}\mathrm{Re}\left[H_0(u) - H_2(u) - \frac{4\mathrm{i}}{\pi u^2}\right] \qquad (10)$$

$$g^{\perp}(u) = \frac{1}{2}\mathrm{Re}\left[H_0(u) + H_2(u) + \frac{4\mathrm{i}}{\pi u^2}\right] \qquad (11)$$

$$g^{z}(u) = |\varepsilon|\mathrm{Re}\,H_0(u) \qquad (12)$$

$$C_{\mathrm{pl}} = \frac{3\pi}{2}\frac{|\varepsilon|^2}{|\varepsilon+1|^{7/2}} \qquad (13)$$

where $\kappa_{\mathrm{pl}} = \mathrm{Im}\,\gamma(K_{\mathrm{pl}})$ is the perpendicular plasmon decay constant and $H_{0,2}(\cdot) \equiv H_{0,2}^{(1)}(\cdot)$ are Hankel functions (or Bessel functions of the third kind) [18]. The superscripts $\parallel$, $\perp$ indicate the directions parallel and perpendicular to the separation vector $\mathbf{S}$ in the interface plane.

Eq. (9) shows that the plasmon resonance gives a contribution to the energy density that increases exponentially when approaching the source. This behavior is reproduced by the numerical evaluation of Eq. (A.10), as shown in Fig. 2(b). As a function of the lateral distance s, the correlation tensor (9) shows damped oscillations whose wavelength is fixed by the plasmon wave vector K_{pl}, as shown in Fig. 3(b). These oscillations can be made explicit using the asymptotic form of the Hankel function [18]

$$|K_{\mathrm{pl}}s| \gg 1: \quad H_n(K_{\mathrm{pl}}s) \approx \sqrt{\frac{2}{\pi K_{\mathrm{pl}}s}}\,\mathrm{e}^{\mathrm{i}(K_{\mathrm{pl}}s-\pi/4-n\pi/2)} \qquad (14)$$

We thus conclude that the propagation distance of the plasmon resonance, as contained in the imaginary part of K_{pl}, determines the coherence length of the field in this regime. For a dielectric constant with small imaginary part, the inverse propagation distance is approximately

$$\mathrm{Im}K_{\mathrm{pl}} \approx \frac{(\mathrm{Re}K_{\mathrm{pl}})^3}{k^2}\frac{\mathrm{Im}\,\varepsilon}{2(\mathrm{Re}\,\varepsilon)^2} \ll k \qquad (15)$$

Thermally excited plasmons thus lead to a spatially coherent field on a length scale well exceeding the vacuum wavelength. They also create a net field polarization, as shown by the anisotropy of the tensor elements in Eqs. (10)–(12) (see also Fig. 3(b)). This anisotropy may be understood from the fact that the coherence between points separated by $\mathbf{S}$ is created by plasmons propagating parallel to this direction, and the latter are polarized in the plane spanned by $\mathbf{S}$ and the normal vector $\mathbf{e}_z$.

3.2. Extreme near field: quasi-static regime

We now turn to the near-field limit $z \ll \lambda$. Inspecting the integrand of Eq. (A.10), one finds that in addition to the plasmon resonance, large wave vectors $K \gg k$ dominate the integral. This is because the exponential cutoff $\mathrm{e}^{-2z\,\mathrm{Im}\,\gamma(K)} \approx \mathrm{e}^{-2zK}$ gets effective only for $K \geqslant 1/z \gg k$. We thus obtain the asymptotic behavior of the integral when we expand the integrand to leading order in the limit

$1/z \geqslant K \gg k$. The transmission coefficients, e.g., become in this limit

$$|t_\mathrm{p}|^2 \approx \frac{4|\gamma_2|^2|\varepsilon|}{K^2|\varepsilon+1|^2}\left(1+\frac{k^2}{K^2}\mathrm{Re}\,\frac{\varepsilon}{\varepsilon+1}\right)$$
$$|t_\mathrm{s}|^2 \approx \frac{4|\gamma_2|^2}{K^2}\left(1+\frac{k^2}{4K^2}\mathrm{Re}\,(\varepsilon+1)\right) \tag{16}$$

We perform the integration over K using Eq. (B.8), as explained in Appendix B.2.2 and get the following asymptotic form for the diagonal elements of the cross-correlation tensor

$$w^{ii}(\mathbf{S}, z) \approx \frac{C_\mathrm{xnf}}{(kz)^3} g^i(s/z) \tag{17}$$

$$g^{\|}(u) = \frac{1-u^2/2}{(1+u^2/4)^{5/2}} \tag{18}$$

$$g^{\perp}(u) = \frac{1}{(1+u^2/4)^{3/2}} \tag{19}$$

$$g^{z}(u) = \frac{2-u^2/4}{(1+u^2/4)^{5/2}} \tag{20}$$

$$C_\mathrm{xnf} = \frac{3}{32}\mathrm{Im}\,\frac{\varepsilon-1}{\varepsilon+1} = \frac{3}{16}\,\frac{\mathrm{Im}\,\varepsilon}{|\varepsilon+1|^2} \tag{21}$$

The coherence tensor given by Eq. (17) shows a power law increase $1/z^3$ when the interface is approached, as plotted in Fig. 2(a). It therefore takes over compared to the plasmon contribution in the ‘extreme near-field limit’ $z \ll 1/\kappa_\mathrm{pl}$. In this regime, the lateral coherence of the field is characterized, as shown by the scale functions $g^i(s/z)$ in Eqs. (18)–(20), by a Lorentzian shape whose scale is set by the distance z to the source. Hence, the closer one detects the field, the more it is spatially incoherent.

This behavior may be understood from electrostatics: in the near field, the electromagnetic fields behave as if they were quasi-static because they vary on a length scale much smaller than the wavelength (retardation is negligible). A near-field detector is thus sensitive to a source area of the order of πz^2, and spatial coherence is observed when these areas overlap, hence for a separation smaller than the distance z. Similar arguments have also been put forward to interpret subwavelength resolution in optical near-field microscopy [19,20]. The electrostatic analogy may be pushed even further: it is easily checked that we get the same result as Eq. (17) using electrostatic image theory. As a consequence of the fluctuation–dissipation theorem [5,6,11,12], we have indeed

$$W^{ij}(\mathbf{r}_2, \mathbf{r}_1) \propto \mathrm{Im}\, G^{ij}(\mathbf{r}_2, \mathbf{r}_1) \propto \mathrm{Im}\, E^i_\mathrm{image}(\mathbf{r}_2; \bar{\mathbf{r}}_1, \bar{\mathbf{d}}_j) \tag{22}$$

where G^{ij} is again the electric Green function. The electric field $\mathbf{E}_\mathrm{image}$ is created by the image $\bar{\mathbf{d}}_j$ of a dipole $\mathbf{d}_j$ (polarized along the x^j-axis) at position $\mathbf{r}_1$, the image dipole being located at the mirror position $\bar{\mathbf{r}}_1 = (x_1, y_1, -z_1)$. This image dipole field dominates the Green function G^{ij} at sufficiently close distance from the source if the electrostatic reflection coefficient $(\varepsilon-1)/(\varepsilon+1)$ has a nonzero imaginary part (see Eq. (21)).

We stress that there is no lower limit to the spatial coherence length of the near field, provided one uses the framework of a local dielectric susceptibility. Model calculations for a free electron gas confined to a half-space show that this framework breaks down at wave vectors K of the order of the Fermi wave vector [9,10]. For our problem, this corresponds to typical distances of the order of 0.1 nm that are difficult to achieve for near-field probes even in the optical range.

3.3. Relevance of the skin depth

It has become clear from the two preceding subsections that the lateral coherence of near-field radiation strongly depends on the distance of observation to the source. It might have been expected that the skin depth shows up in this discussion, since it governs the penetration depth for electric fields into the metal. We conclude our analytical work by identifying the relevance of this length scale.

Recall that the skin depth is given by

$$\delta = \frac{\lambda/2\pi}{\mathrm{Im}\sqrt{\varepsilon}} \tag{23}$$

In many cases (metals at low frequencies, semiconductors in the infrared), the dielectric function is large and therefore the skin depth much smaller than the wavelength, $\delta \ll \lambda$. In this regime, the source material approaches a perfect conductor. The large K expansion of the transmission coefficients in Eq. (A.10) then has to be reconsidered: while the limit $K \gg k$ may be justified, the limit $K \gg k|\sqrt{\varepsilon}|$ may be not. We find that there exists an intermediate distance regime $\delta \ll z \ll \lambda$ (corresponding to wave vectors $k|\sqrt{\varepsilon}| \gg K \gg k$) where the coherence tensor shows a different behavior [21]. The expansion of the transmission coefficients in this regime reads

$$\begin{aligned} |t_{\mathrm{p}}|^2 &\approx \frac{4|\gamma_2|^2}{|\varepsilon|K^2}\left[1 + \mathcal{O}\left(\frac{K}{k\sqrt{\varepsilon}}\right)\right] \\ |t_{\mathrm{s}}|^2 &\approx \frac{4|\gamma_2|^2}{|\varepsilon|k^2}\left[1 + \mathcal{O}\left(\frac{K}{k\sqrt{\varepsilon}}\right)\right] \end{aligned} \tag{24}$$

We finally get an isotropic coherence tensor

$$w^{ii}(\mathbf{S}, z) \approx \frac{3}{16}\frac{\delta}{kz^2}g(s/z) \tag{25}$$

$$g(u) = \frac{1}{(1 + u^2/4)^{3/2}} \tag{26}$$

The skin layer dominated regime is thus characterized by a $1/z^2$ power law for the energy density. As shown in Fig. 4(a), the skin depth δ separates this regime from the extreme near field where a different power law $1/z^3$ prevails. We observe from Fig. 4(b) and Eq. (25) that the lateral coherence length is equal to the distance z from the source, as in the extreme near-field regime. This is not so surprising since the field propagation in the vacuum half-space above the source is governed by the length scales λ and z, whatever the smaller, while the skin depth is only relevant for the propagation inside the source.

To conclude, we recall that the different contributions to the correlation tensor originate in distinct domains on the K-axis in the integral (5). The total correlation tensor is therefore given by the sum of the surface plasmon, extreme near field, and skin-layer contributions. The accuracy of this approximation is visible in Figs. 2 and 4(a). Note that in the figures, the numerically computed far-field energy density has been added to get the correct large distance limit.

4. Conclusion

In the near field, the spatial coherence of thermal radiation differs strongly from the blackbody field. Confined field modes like surface plasmon polaritons that propagate along the source surface make the field spatially coherent over large scales if they dominate the radiation density. At close distance (smaller than the skin depth), the radiation is dominated by quasi-static fields, and the coherence length drops well below the wavelength, being limited only by the (non)locality of the dielectric response of the source material. The crossover between these regimes is determined by the skin depth and the electrostatic reflection coefficient. We conclude that in the near field, macroscopic concepts like a local emissivity are still meaningful at the subwavelength scale, provided coherent surface excitations are absent or subdominant. For rough surfaces, the validity of these macroscopic concepts has been discussed in Ref. [22].

The asymptotic forms for the cross-spectral density tensor obtained in this paper are useful to characterize thermal noise fields that may perturb particles in integrated microtraps 'mounted' with electromagnetic fields above a solid surface [23–30]. The concomitant scattering and decoherence of the guided matter waves is discussed elsewhere [31,32].

The fluctuation electrodynamics used in this paper enabled us to treat a non-equilibrium situation (thermal source in vacuum at $T = 0$) where the fluctuation–dissipation theorem for the electric field is not immediately applicable. In particular, we neglected the zero-point radiation impinging on the interface from the empty half-space. The domain of validity of this approximation, as well as the calculation of anti-normal-ordered correlation functions will be the subject of future investigations.

Acknowledgements

C.H. thanks S. Scheel for many fruitful exchanges.

Appendix A. Notations for the plane interface

The Green tensor describing the emission from the source $z' < 0$ into the vacuum half-space $z > 0$ may be written in spatial Fourier space as [11,13]

$$G^{ij}(\mathbf{r},\mathbf{r}') = \int \frac{\mathrm{d}^2\mathbf{K}}{(2\pi)^2} \mathrm{e}^{\mathrm{i}\mathbf{K}\cdot(\mathbf{R}-\mathbf{R}')} G^{ij}(\mathbf{K},z,z')$$
$$G^{ij}(\mathbf{K},z,z') = \frac{\mathrm{i}k^2}{2\varepsilon_0\gamma_2} \sum_{\mu=\mathrm{s},\,\mathrm{p}} e^{(t)}_{\mu,i} e^{(2)}_{\mu,j} t_\mu \mathrm{e}^{\mathrm{i}(\gamma z-\gamma_2 z')} \qquad (\mathrm{A}.1)$$

We use bold capitals to denote vectors parallel to the interface, e.g., $\mathbf{K} = (k_x, k_y, 0)$. The vertical components of the wave vectors in vacuum and inside the source are, respectively,

$$\gamma = +\sqrt{k^2 - \mathbf{K}^2}, \quad \mathrm{Im}\,\gamma > 0 \qquad (\mathrm{A}.2)$$

$$\gamma_2 = +\sqrt{\varepsilon k^2 - \mathbf{K}^2}, \quad \mathrm{Im}\,\gamma_2 > 0 \qquad (\mathrm{A}.3)$$

The polarization vectors for the s- (or TE-) and p- (TM-) polarized waves are taken as

$$\mathbf{e}^{(t)}_{\mathrm{s}} = \mathbf{e}^{(2)}_{\mathrm{s}} = \hat{\mathbf{K}} \times \hat{\mathbf{e}}_z \qquad (\mathrm{A}.4)$$

$$\mathbf{e}^{(t)}_{\mathrm{p}} = \frac{K\hat{\mathbf{z}} - \gamma\hat{\mathbf{K}}}{k} \qquad (\mathrm{A}.5)$$

$$\mathbf{e}^{(2)}_{\mathrm{p}} = \frac{K\hat{\mathbf{z}} - \gamma_2\hat{\mathbf{K}}}{\sqrt{\varepsilon}k} \qquad (\mathrm{A}.6)$$

where $\hat{\mathbf{K}}$ is the unit vector parallel to $\mathbf{K}$. Finally, with this choice for the polarization vectors, the Fresnel transmission coefficients are

$$t_{\mathrm{s}} = \frac{2\gamma_2}{\gamma + \gamma_2}, \qquad t_{\mathrm{p}} = \frac{2\gamma_2\sqrt{\varepsilon}}{\varepsilon\gamma + \gamma_2} \qquad (\mathrm{A}.7)$$

When the Green tensor (A.1) is inserted into the integral (3), the spatial integration over $\mathbf{R}'$ yields a δ-function for the lateral wave vectors. The integration over z' is then

$$\int_{-\infty}^{0} \mathrm{d}z'\, \mathrm{e}^{-\mathrm{i}(\gamma_2-\gamma_2^*)z'} = \frac{1}{2\,\mathrm{Im}\,\gamma_2} \qquad (\mathrm{A}.8)$$

where the convergence is ensured by the positive imaginary part of γ_2. The resulting coherence tensor is then of the form (5). We use the identity

$$k^2\mathrm{Im}\,\varepsilon = 2\,\mathrm{Im}\,\gamma_2\,\mathrm{Re}\,\gamma_2 \qquad (\mathrm{A}.9)$$

and get after some elementary algebra:

$$w^{ij}(\mathbf{K}) = \frac{3\pi}{4k}\frac{\mathrm{Re}\,\gamma_2}{|\gamma_2|^2} \sum_{\mu} e^{(t)}_{\mu,i} e^{(t)*}_{\mu,j} |\mathbf{e}^{(2)}_{\mu}|^2 |t_\mu|^2 \qquad (\mathrm{A}.10)$$

Appendix B. Components of the coherence tensor

In this appendix, we outline the calculation for the components of the coherence tensor.

B.1. Angular integrations

The only quantities in Eq. (A.10) that depend on the angle φ between the lateral wave vector $\mathbf{K}$ and the separation $\mathbf{S}$ are the polarization vectors $\mathbf{e}_\mu$. To simplify the calculation, we choose the x-axis parallel to $\mathbf{S}$. We then get the following azimuthal integrals (Eq. (9.1.18) of Ref. [18])

$$\int_{-\pi}^{\pi} \frac{\mathrm{d}\varphi}{\pi} \mathrm{e}^{\mathrm{i}Ks\cos\varphi} \begin{pmatrix} \sin^2\varphi \\ \cos^2\varphi \end{pmatrix} = J_0(Ks) \pm J_2(Ks) \qquad (\mathrm{B}.1)$$

The integrals with $\sin\varphi\cos\varphi$ vanish due to parity. We also note that one also gets nonzero off-diagonal elements W^{xz}, W^{zx} due to p-polarized modes. For simplicity, these are not discussed here.

B.2. Radial integrations

We are left with integrals over the radial wave vector K. These are worked out using the definitions (A.4)–(A.6) of the polarization vectors and the transmission coefficients (A.7).

B.2.1. Plasmon pole

To find the plasmon contribution, we extract, as mentioned in the main text, the pole of the t_{p} coefficient and approximate the other factors by their values at the pole. The remaining integral can be reduced to the following standard form

$$\int_0^{\infty} \frac{x\,\mathrm{d}x}{x^2 - q^2} J_0(xs) = \frac{\mathrm{i}\pi}{2} H_0^{(1)}(qs) \qquad (\mathrm{B}.2)$$

for $\mathrm{Im}\,q > 0$, $s > 0$. To prove this identity, we use contour integration. The Bessel function is written as [18, Eqs. (9.1.3) and (9.1.39)]

$$J_0(x) = \frac{1}{2}\left[H_0^{(1)}(x) - H_0^{(1)}(\mathrm{e}^{\mathrm{i}\pi}x)\right] \tag{B.3}$$

where $H_0^{(1)}(x)$ is the Hankel function. The integral may now be written as

$$\frac{1}{2}\int_{\mathrm{e}^{\mathrm{i}\pi}\infty}^{\infty} \frac{x\,\mathrm{d}x}{x^2 - q^2} H_0^{(1)}(xs) \tag{B.4}$$

with an integration path running just above the negative real axis. The Hankel function is analytic in the upper half-plane and vanishes exponentially for $|x| \to \infty$ there (see Eq. (14)). Therefore, closing the integration contour with a half-circle, the integral is given by the residue at the pole $x = +q$ (because $\mathrm{Im}\,q > 0$), and we get

$$\int_{\mathrm{e}^{\mathrm{i}\pi}\infty}^{\infty} \frac{x\,\mathrm{d}x}{x^2 - q^2} H_0^{(1)}(xs) = \mathrm{i}\pi H_0^{(1)}(qs) \tag{B.5}$$

This proves Eq. (B.2). Taking the imaginary part, we find both the trace and the zz-component (12) of the correlation tensor (9).

For the xx- and yy-components of the coherence tensor, we also need the integral (B.2) with the Bessel function $J_2(xs)$ instead of $J_0(xs)$ (cf. Eq. (B.1)). Using the same reasoning as above, this integral is transformed into

$$\frac{1}{2}\int_{\mathrm{e}^{\mathrm{i}\pi}\infty}^{\infty} \frac{x\,\mathrm{d}x}{x^2 - q^2} H_2^{(1)}(xs) \tag{B.6}$$

In addition to the pole at $x = q$, we now have a contribution from the $-4\mathrm{i}/(xs)^2$ singularity of the Bessel $H_2^{(1)}(xs)$ function at the origin. This singularity lies on the integration path and is therefore taken into account by half its (negative) residue at $x = 0$. Combining the latter with the residue at $x = q$, we get

$$\int_{\mathrm{e}^{\mathrm{i}\pi}\infty}^{\infty} \frac{x\,\mathrm{d}x}{x^2 - q^2} H_2^{(1)}(xs) = \mathrm{i}\pi H_2^{(1)}(qs) - \frac{4\pi}{q^2 s^2} \tag{B.7}$$

We may verify the sign of the second term by checking that the function (B.7) vanishes in the limit $s \to 0$, as is the case for the left-hand side of Eq. (B.6).

B.2.2. Near-field regime

In the near-field regimes $K \gg k|\sqrt{\varepsilon}|$ (extreme near field) and $k|\sqrt{\varepsilon}| \gg K \gg k$ (skin layer dominated regime), the expansions (16) and (24) of the transmission coefficients are straightforward to obtain. The final integration involves integer powers of K times products of Bessel functions and exponentials and is performed using the following identity

$$\int_0^{\infty} \mathrm{d}K\, J_0(Ks)\mathrm{e}^{-2Kz} = \frac{1}{\sqrt{4z^2 + s^2}} \tag{B.8}$$

This may be proven starting from the Fourier expansion of the Coulomb potential (writing $\mathbf{k} = (\mathbf{K}, k_z)$)

$$\frac{1}{r} = \frac{1}{2\pi^2}\int \mathrm{d}^2\mathbf{K}\,\mathrm{d}k_z\,\frac{\mathrm{e}^{\mathrm{i}\mathbf{k}\cdot\mathbf{r}}}{\mathbf{k}^2} \tag{B.9}$$

and evaluating the integral over the vertical wave vector component k_z with contour integration (for $z > 0$, a single pole at $k_z = \mathrm{i}|\mathbf{K}|$ contributes). The derivatives of Eq. (B.8) with respect to z and s then provide all necessary integrals.

References

[1] L. Mandel, E. Wolf, Optical Coherence and Quantum Optics, Cambridge University Press, Cambridge, 1995.
[2] J.L. Gall, M. Olivier, J.J. Greffet, Phys. Rev. B 55 (1997) 10105.
[3] R. Carminati, J.-J. Greffet, Phys. Rev. Lett. 82 (1999) 1660.
[4] A.V. Shchegrov, K. Joulain, R. Carminati, J.-J. Greffet, Phys. Rev. Lett. 85 (2000) 1548.
[5] E.M. Lifshitz, Sov. Phys. JETP 2 (1956) 73 [J. Exp. Theor. Phys. USSR 29 (1955) 94].
[6] D. Polder, M.V. Hove, Phys. Rev. B 4 (1971) 3303.
[7] J. Schwinger, J. Lester, L. DeRaad, K.A. Milton, Ann. Phys. (NY) 115 (1978) 1.
[8] S.M. Rytov, Y.A. Kravtsov, V.I. Tatarskii, Principles of Statistical Radiophysics, vol. 3, Springer, Berlin, 1989 (Chapter 3).
[9] P.J. Feibelman, Prog. Surf. Sci. 12 (1982) 287.
[10] G.W. Ford, W.H. Weber, Phys. Rep. 113 (1984) 195.
[11] G.S. Agarwal, Phys. Rev. A 11 (1975) 230.
[12] S. Scheel, L. Knöll, D.-G. Welsch, Phys. Rev. A 58 (1998) 700.
[13] A.A. Maradudin, D.L. Mills, Phys. Rev. B 11 (1975) 1392.
[14] C. Henkel, J.-Y. Courtois, Eur. Phys. J. D 3 (1998) 129.
[15] E. Palik, Handbook of Optical Constants of Solids, Academic Press, San Diego, 1985.
[16] V.M. Agranovich, D.L. Mills (Eds.), Surface Polaritons, North-Holland, Amsterdam, 1982.
[17] H. Raether, Surface Plasmons on Smooth and Rough Surfaces and on Gratings, vol. 111, Springer Tracts in Modern Physics, Springer, Berlin, 1988.

[18] M. Abramowitz, I.A. Stegun, (Eds.), Handbook of Mathematical Functions, ninth ed., Dover Publications, New York, 1972.
[19] J.-J. Greffet, R. Carminati, Prog. Surf. Sci. 56 (1997) 133.
[20] C. Henkel, V. Sandoghdar, Opt. Commun. 158 (1998) 250.
[21] C. Henkel, S. Pötting, M. Wilkens, Appl. Phys. B 69 (1999) 379.
[22] J.-J. Greffet, R. Carminati, Heat Technol. 18 (2000) 81.
[23] J.P. Dowling, J. Gea-Banacloche, in: P.R. Berman (Ed.), Adv. At. Mol. Opt. Phys., vol. 37, Academic Press, New York, 1997, pp. 1–94 (Suppl. 3).
[24] V.I. Balykin, in: B. Bederson, H. Walther, (Eds.), Adv. At. Mol. Opt. Phys., vol. 41, Academic Press, San Diego, 1999, pp. 181–260.
[25] J. Schmiedmayer, Eur. Phys. J. D 4 (1998) 57.
[26] M. Key, et al., Phys. Rev. Lett. 84 (2000) 1371.
[27] J. Reichel, W. Hänsel, T.W. Hänsch, Phys. Rev. Lett. 83 (1999) 3398.
[28] R. Folman, P. Krüger, D. Cassettari, B. Hessmo, T. Maier, J. Schmiedmayer, Phys. Rev. Lett. 84 (2000) 4749.
[29] N.H. Dekker, et al., Phys. Rev. Lett. 84 (2000) 1124.
[30] D. Müller, D.Z. Anderson, R.J. Grow, P.D.D. Schwindt, E.A. Cornell, Phys. Rev. Lett. 83 (1999) 5194.
[31] C. Henkel, M. Wilkens, Acta Phys. Slov. 50 (2000) 293. quant-ph/0005038.
[32] C. Henkel, S. Pötting, Coherent transport of matter waves, Appl. Phys. B., accepted for publication, eprint quant-ph/0007083.

Nanoscale radiative heat transfer between a small particle and a plane surface

J.-P. Mulet, K. Joulain, R. Carminati et J.-J. Greffet

Applied Physics Letters, vol 78, pp2931–2933 (2001)

Nanoscale radiative heat transfer between a small particle and a plane surface

Jean-Philippe Mulet,[a] Karl Joulain, Rémi Carminati, and Jean-Jacques Greffet
Laboratoire d'Energétique Moléculaire et Macroscopique, Combustion, Ecole Centrale Paris, Centre National de la Recherche Scientifique, 92295, Châtenay-Malabry Cedex, France

(Received 20 December 2000; accepted for publication 7 March 2001)

We study the radiative heat transfer between a small dielectric particle, considered as a point-like dipole, and a surface. In the framework of electrodynamics and using the fluctuation-dissipation theorem, we can evaluate the energy exchange in the near field, which is dominated by the contribution of tunneling waves. The transfer is enhanced by several orders of magnitude if the surface or the particle can support resonant surface waves. An application to local heating is discussed. © *2001 American Institute of Physics.* [DOI: 10.1063/1.1370118]

Questions about radiative heat transfer (RHT) at nanoscales have been raised by recent developments of nanotechnology.[1] Design of micro- and nanostructures requires a thorough understanding of physical phenomena involved in radiative energy exchange, when their sizes become comparable to the thermal mean free path or the thermal radiation wavelength.[2,3] Modeling RHT between two semi-infinite bodies[4–7] or between a tip and a substrate[8] is a challenging problem for all near-field microscopes (scanning tuneling microscope, atomic force microscope) or for scanning thermal microscopes.[9] Our work deals with the problem of RHT between a small particle—considered as a point-like dipole—and a very close plane interface. This particle could be a single molecule, a dust particle, or a model for the tip of a microscope probe. Using an electromagnetic approach, in the dipolar approximation, we have derived the expression of the radiative heat power exchanged between the particle and the semi-infinite medium. We show that the transfer increases at small distances and can be enhanced by several orders of magnitude (in comparison with the transfer at large distances) if the particle or the bulk support resonant surface waves. Results of numerical simulations are presented and an application to local heating is discussed.

In this part, we focus on the derivation of the radiative power exchanged between a small particle (of spherical shape) and a semi-infinite medium. The geometry of the problem is presented in Fig. 1: the upper medium $z>0$ is vacuum ($\varepsilon=1$). A particle (P) of radius a and dielectric constant (frequency dependent) $\varepsilon_P(\omega)=\varepsilon'_P(\omega)+i\varepsilon''_P(\omega)$ is held at temperature T_P. The lower medium $z<0$, is filled by a homogeneous, isotropic material (bulk) of dielectric constant $\varepsilon_B(\omega)=\varepsilon'_B(\omega)+i\varepsilon''_B(\omega)$ and held at temperature T_B. The center of the particle is at a distance d above the interface.

We first calculate the mean power $P^{B\rightarrow P}_{\mathrm{abs}}(\omega)$ radiated by the bulk at a given frequency ω and absorbed by the particle. We assume that the bulk is in local thermodynamic equilibrium at uniform temperature $T_B\neq 0$, so that there are fluctuating currents inside the bulk due to thermal fluctuations. These currents inside the bulk radiate an electromagnetic field that illuminates the particle. An elementary fluctuating current $\mathbf{j}_f(\mathbf{r}',\omega)$ at frequency ω, radiates at point $\mathbf{r}$ inside the particle, an incident electric field $\mathbf{E}_{\mathrm{inc}}(\mathbf{r},\omega)$ given by

$$\mathbf{E}_{\mathrm{inc}}(\mathbf{r},\omega)=(i\omega\mu_0)\int_B \overleftrightarrow{\mathbf{G}}(\mathbf{r},\mathbf{r}',\omega)\mathbf{j}_f(\mathbf{r}',\omega)d^3\mathbf{r}', \tag{1}$$

where μ_0 is the magnetic permeability of vacuum and $\overleftrightarrow{\mathbf{G}}$ is the Green tensor[10] of a system constituted by two semi-infinite media whose dielectric constants are either 1 if $z\geqslant 0$ or $\varepsilon_B(\omega)$ if $z<0$. Let us now assume that $\mathbf{E}_{\mathrm{inc}}(\mathbf{r},\omega)$ is uniform inside the particle. This amounts to use a dipolar approximation, whose validity in the near field has already been discussed.[11] Provided that this condition is satisfied, the small particle behaves as a point-like dipole $\mathbf{p}_{\mathrm{ind}}(\mathbf{r}_P,\omega)$ induced by the incident field $\mathbf{E}_{\mathrm{inc}}(\mathbf{r}_P,\omega)$. These quantities are related by: $\mathbf{p}_{\mathrm{ind}}(\mathbf{r}_P,\omega)=\varepsilon_0\alpha(\omega)\mathbf{E}_{\mathrm{inc}}(\mathbf{r}_P,\omega)$, where ε_0 is the dielectric permittivity of vacuum and $\alpha(\omega)$ is the particle polarizability. For a spherical particle of dielectric constant $\varepsilon_P(\omega)$, we used the Clausius–Mossotti polarizability[12]

$$\alpha(\omega)=4\pi a^3\left[\frac{\varepsilon_P(\omega)-1}{\varepsilon_P(\omega)+2}\right]. \tag{2}$$

A more precise model,[13] taking into account the interaction between the dipole and its image through the interface, leads to the introduction of an effective polarizability. We have verified that, when the distance d is larger than the particle radius a, the correction to Eq. (2) is negligible. Since

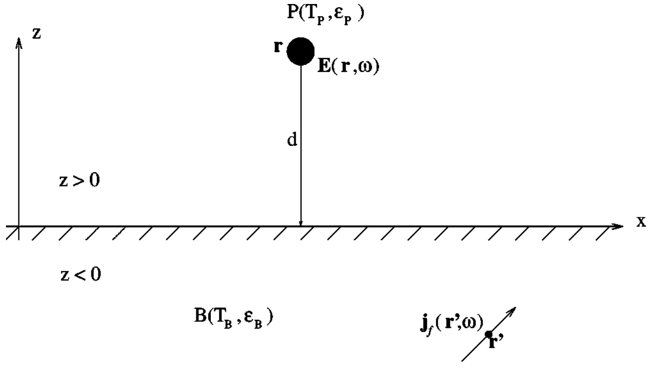

FIG. 1. Geometry of the system.

---

[a] Electronic mail: jpmulet@em2c.ecp.fr

we did our calculation for a distance d larger than $2a$, we will consider that Eq. (2) is a good approximation for the polarizability in our problem.

We now evaluate the mean radiative power $P_{\text{abs}}^{B\rightarrow P}(\omega)$ dissipated inside the particle. Since the scattered power is negligible,[14] this quantity is given by: $P_{\text{abs}}^{B\rightarrow P}(\omega) = \text{Re}\{\langle -i\omega \mathbf{p}_{\text{ind}}(\mathbf{r}_P,\omega)\cdot \mathbf{E}_{\text{inc}}^{*}(\mathbf{r}_P,\omega)\rangle\}$, where the brackets denote a statistical ensemble average over the fluctuations of the currents inside the bulk. The components $\langle |E_{\text{ind},i}(\mathbf{r}_P,\omega)|^2\rangle$ $(i=x,y,z)$ depend only on the distance d and are given by[10,15,16]

$$\langle |E_{\text{inc},i}(\mathbf{r}_P,\omega)|^2\rangle = 2\,\frac{\mu_0^2\varepsilon_0\omega^3}{\pi}\,\text{Im}[\varepsilon_B(\omega)]\Theta(\omega,T_B) \times \sum_{j=x,y,z}\int_B |G_{i,j}(\mathbf{r}_P,\mathbf{r}',\omega)|^2 d^3\mathbf{r}', \tag{3}$$

where $\Theta(\omega,T_B)=\hbar\omega/[\exp(\hbar\omega/k_BT_B)-1]$ is the mean energy of a quantum oscillator in thermal equilibrium at temperature T_B, $2\pi\hbar$ is Planck's constant, and k_B is Boltzmann's constant. Finally, we find the expression of the mean power radiated by the bulk and absorbed by the particle at frequency ω

$$P_{\text{abs}}^{B\rightarrow P}(\mathbf{r}_P,\omega)=\frac{2}{\pi}\frac{\omega^4}{c^4}\text{Im}[\varepsilon_B(\omega)]\text{Im}[\alpha(\omega)]\Theta(\omega,T_B) \times \sum_{i,j=x,y,z}\int_B |G_{i,j}(\mathbf{r}_P,\mathbf{r}',\omega)|^2 d^3\mathbf{r}'. \tag{4}$$

We now consider the fluctuating currents inside the particle at temperature T_P that illuminate the bulk. Using the same formalism, we can calculate the power *locally* dissipated per unit volume, at a point $\mathbf{r}$ inside the bulk, by the following relation: $P_{\text{abs}}^{P\rightarrow B}(\mathbf{r},\omega)=\text{Re}\{\langle \mathbf{j}_{\text{ind}}(\mathbf{r},\omega)\cdot \mathbf{E}_{\text{inc}}^{*}(\mathbf{r},\omega)\rangle\}$. It reads

$$P_{\text{abs}}^{P\rightarrow B}(\mathbf{r},\omega)=\frac{2}{\pi}\frac{\omega^4}{c^4}\text{Im}[\varepsilon_B(\omega)]\text{Im}[\alpha(\omega)]\Theta(\omega,T_P) \times \sum_{i,j=x,y,z}|G_{i,j}(\mathbf{r},\mathbf{r}_P,\omega)|^2. \tag{5}$$

In this part, we present some numerical results obtained with a particle and a surface of silicon carbide (SiC). The optical properties of this material can be described using an oscillator model[17]

$$\varepsilon_B(\omega)=\varepsilon_P(\omega)=\varepsilon(\omega)=\varepsilon_\infty\left(1+\frac{\omega_L^2-\omega_T^2}{\omega_T^2-\omega^2-i\Gamma\omega}\right) \tag{6}$$

with $\varepsilon_\infty=6.7$, $\omega_L=969\,\text{cm}^{-1}$, $\omega_T=793\,\text{cm}^{-1}$, and $\Gamma=4.76\,\text{s}^{-1}$. The bulk can support resonant surface waves, called surface phonon polaritons, that produce a peak in the density of states at frequency ω_B where $\varepsilon(\omega_B)$ satisfies the relation $\varepsilon'(\omega_B)=-1$. The spherical particle supports volume phonon polaritons at ω_P where $\varepsilon(\omega_P)$ satisfies the relation $\varepsilon'(\omega_P)=-2$. Using Eq. (6), we find: $\omega_B=178.7\times 10^{12}\,\text{rad}\,\text{s}^{-1}$ and $\omega_P=175.6\times 10^{12}\,\text{rad}\,\text{s}^{-1}$.

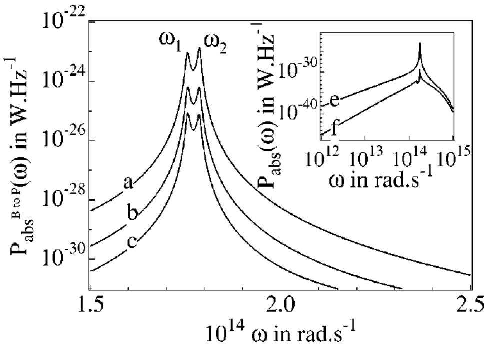

FIG. 2. Mean power radiated by the bulk (at $T_B=300$ K) and absorbed by the particle (of radius $a=5$ nm) vs frequency: (a) $d=20$ nm; (b) $d=50$ nm; (c) $d=100$ nm. The inset (log–log scale) shows the spectrum of the absorbed power between 10^{12} and 10^{15} rad s^{-1}; (e) $d=20$ nm; and (f) $d=1$ mm.

In Fig. 2, we plot $P_{\text{abs}}^{B\rightarrow P}(\omega)$ for a spherical particle of radius $a=5$ nm at different distances d above the surface, held at temperature $T_B=300$ K. We note that the figure displays two remarkable peaks at frequency $\omega_1\approx 175.6\times 10^{12}\,\text{rad}\,\text{s}^{-1}$ and $\omega_2\approx 178.7\times 10^{12}\,\text{rad}\,\text{s}^{-1}$. These two peaks are related to the resonant surface waves: the first corresponds to the resonance of the particle which presents a larger absorption at this frequency; the second is due to a huge increase of electromagnetic energy density close to the surface, demonstrated recently.[16] An asymptotic expansion of Eq. (4) for small distance d yields the radiative power spectrum

$$P_{\text{abs}}^{B\rightarrow P}(d,\omega)\sim\frac{1}{4\pi^2d^3} \times 4\pi a^3 \underbrace{\frac{3\varepsilon''(\omega)}{|\varepsilon(\omega)+2|^2}}_{\text{particle}}\underbrace{\frac{\varepsilon''(\omega)}{|\varepsilon(\omega)+1|^2}}_{\text{bulk}}\Theta(\omega,T_B). \tag{7}$$

At this point, we must emphasize that, whereas those surface waves are evanescent waves, an energy exchange between the bulk and the particle takes place because the particle lies in the region (up to many micrometers) where the evanescent field is large, so that there is an efficient coupling between them. The inset of the figure shows (in log–log scale) the spectrum of the absorbed power between 10^{12} and $10^{15}\,\text{rad}\,\text{s}^{-1}$ at two different distances $d=20$ nm and $d=1$ mm. It is seen that the RHT is almost monochromatic and is larger in the near field. If the particle and the bulk

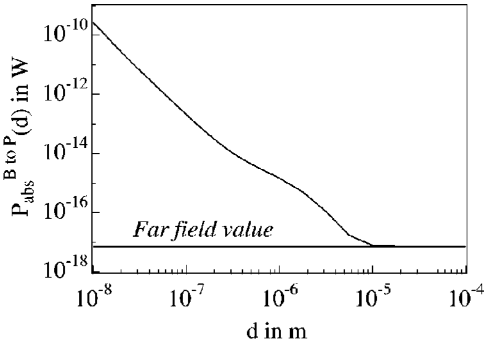

FIG. 3. Total power radiated by the bulk (at $T_B=300$ K) and absorbed by the particle (of radius $a=5$ nm) vs distance.

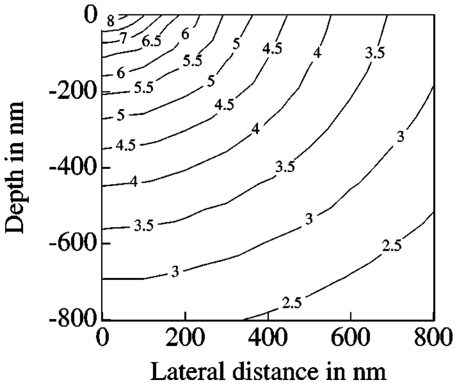

FIG. 4. Deposited power per unit volume inside the bulk. The particle has a radius $a=5$ nm and is held at temperature $T_P=300\,\mathrm{K}$.

were constituted by two different materials, the RHT spectrum would feature two separate sharp peaks at two different resonance frequencies.

Figure 3 shows the integrated power absorbed by the same particle versus distance d (the substrate is still held at temperature $T_B=300\,\mathrm{K}$). The near-field RHT increases as $1/d^3$ and is larger at small distances by several orders of magnitude than the far-field one. Indeed, for $d=10\,\mathrm{nm}$, $P_{\mathrm{abs}}\approx 2.6\times 10^{-10}\,\mathrm{W}$ and for $d=10\,\mu\mathrm{m}$, $P_{\mathrm{abs}}\approx 8.9\times 10^{-18}$ W. This enhancement comes from the contribution of evanescent waves to the energy exchange. Therefore, this contribution cannot be neglected in a near-field calculation. This phenomenon occurs when the materials can support resonant surface waves like III–V or II–VI semiconductors and because the resonant frequencies take place in the far IR region (up to 10 μm) where the characteristic wavelength of thermal emission at $T\approx 300\,\mathrm{K}$ is 10 μm. A lot of materials, like oxides or glass, can also support resonant surface waves in the IR or the visible region.

Reciprocity requires that the same enhanced RHT appears when the particle illuminates the surface. This situation may help us in understanding the radiative heat exchange between a nanotip (like those used in near-field microscopy) and a sample. It is interesting to study how the energy radiated by the tip is dissipated in the sample. To answer this question, we calculated—using Eq. (5)—the total power (integrated over the frequencies) dissipated per unit volume for different points in the sample. Figure 4 displays a map, in log scale, of the dissipation rate in the case of a 10 nm diameter sphere of SiC at $T_P=300\,\mathrm{K}$ situated at 100 nm above a sample of SiC. It is seen that the energy is dissipated on a scale comparable to the tip–sample distance. The dissipation per unit volume decreases very fast (as $1/r^6$) with the distance r between the source and the point of the sample where the dissipation is considered (the isocontour labeled with a ''6'' corresponds to the points where the dissipation per unit volume is $10^6\,\mathrm{W\,m^{-3}}$). The amount of energy locally deposited is as large as $100\,\mathrm{MW\,m^{-3}}$.

In this letter, we have shown that nanoscale RHT between a sample and a small particle is almost monochromatic and can be enhanced by several orders of magnitude when the materials involved support resonant surface waves. When illuminated by the particle, the distribution of power inside the sample extends over distances of the same order as the particle-sample separation. These results should have broad applications in near-field microscopy, in design of nanostructures and in high density storage processes by local heating.

[1] A. R. Abramson and C. L. Tien, Microscale Thermophys. Eng. **3**, 229 (1999).
[2] G. Chen, Microscale Thermophys. Eng. **1**, 215 (1997).
[3] J. B. Pendry, J. Mod. Opt. **45**, 2389 (1998).
[4] E. G. Cravalho, C. L. Tien, and R. P. Caren, J. Heat Transfer **89**, 351 (1967).
[5] C. M. Hargreaves, Phys. Rev. Lett. **30A**, 491 (1969).
[6] D. Polder and M. Van Hove, Phys. Rev. B **4**, 3303 (1971).
[7] J. L. Loomis and H. J. Maris, Phys. Rev. B **50**, 18 517 (1994).
[8] K. Dransfeld and J. Xu, J. Microsc. **152**, 35 (1988).
[9] C. C. Williams and H. K. Wickramasinghe, Appl. Phys. Lett. **49**, 1587 (1986).
[10] R. Carminati and J. J. Greffet, Phys. Rev. Lett. **82**, 1660 (1999).
[11] P. C. Chaumet, A. Rahmani, F. de Fornel, and J. P. Dufour, Phys. Rev. B **58**, 2310 (1998).
[12] J. D. Jackson, *Classical Electrodynamics*, 2nd Ed. (Wiley, New York, 1975), Sec. 4.4.
[13] F. Pincemin, A. Sentenac, and J. J. Greffet, J. Opt. Soc. Am. A **11**, 1117 (1994).
[14] B. T. Draine, Astrophys. J. **333**, 848 (1988).
[15] S. M. Rytov, Yu. A. Kravtsov, and V. I. Tatarskii, *Principles of Statistical Radiophysics* (Springer, Berlin, 1989).
[16] A. V. Shchegrov, K. Joulain, R. Carminati, and J. J. Greffet, Phys. Rev. Lett. **85**, 1548 (2000).
[17] E. W. Palik, *Handbook of Optical Constants of Solids* (Academic, San Diego, CA, 1985).

Enhanced radiative heat transfer at nanometric distances

J.-P. Mulet, K. Joulain, R. Carminati et J.-J. Greffet

Microscale Thermophysical Engineering, vol 6, pp209–222 (2002)

Enhanced radiative heat transfer at nanometric distances

Jean-Philippe Mulet, Karl Joulain, Rémi Carminati and Jean-Jacques Greffet
Laboratoire d'Energétique Moléculaire et Macroscopique, Combustion, Ecole Centrale Paris
Centre National de la Recherche Scientifique, 92295, Châtenay-Malabry Cedex, France

Abstract

We study in this article the radiative heat transfer between two semi-infinite bodies at subwavelength scale. We show that this transfer can be enhanced by several orders of magnitude when the surfaces support resonant surface waves. In these conditions, we show that the transfer is almost monochromatic.

1 Introduction

New questions about the heat transfer at nano-scales have been raised by the recent development of nano-technology. Examples of these new questions can be found in different fields. The number of transistors in a microprocessor is now so high that the distance between them is nanometric. The heat transfer and temperature control in a microprocessor is a major issue but is not very well understood [1]. Control of temperature at nanometric scales is also essential in the writing process for information storage on magnetic materials. Thermal microscopes with nanometric resolution have been designed [2]. They consist of a small thermocouple attached at the end of an atomic force microscope. Understanding the mechanisms that produce temperature enhancement when it is approaching a surface is a challenging problem. More generally, all near-field microscopes are concerned with the problem of heat transfer between a sample and a tip.

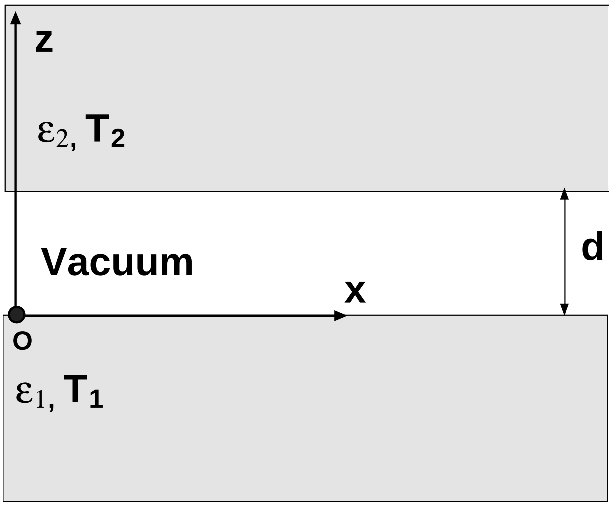

Fig. 1. System studied : two semi-infinite media at different temperatures and separated by a distance d

In this contribution we deal with the problem of radiative heat transfer between two opaque semi-infinite bodies separated by a small vacuum gap (Fig. 1), particularly when the distance between the bodies is nanometric. Our purpose is to show that under certain conditions, the radiative heat transfer due to surface phonon-polaritons can be larger than the classical radiative heat transfer by several orders of magnitude. In addition, most of the transfer is done in a very narrow range of frequencies. We also propose a generalized emissivity valid for evanescent waves.

2 Ab initio calculation of the radiative heat transfer

Let us first remind how the radiative heat transfer between two semi-infinite bodies separated by a vacuum is usually calculated. The heat transfer is equal to the energy flux going from medium 1 to medium 2 ($\phi_{1\to2}$) minus the flux going from medium 2 to medium 1 ($\phi_{2\to1}$). Note that the medium separating the heated media being transparent, it does not emit nor absorb. $\phi_{1\to2}$ and $\phi_{2\to1}$ can be easily calculated with a ray light approach. Note that this implies that geometrical optics is used and that wave effects are thus not taken into account. The elementary energy flux $d\phi_{1\to2}$ from 1 to 2 in a solid angle $d\Omega = 2\pi\sin\theta d\theta$ around the direction θ at frequency ω is the sum of the multiple reflected rays (Fig. 2) :

$$\begin{aligned} d\phi_{1\to2}(\theta) = {} & [\varepsilon'_{1\omega}\varepsilon'_{2\omega} + \varepsilon'_{1\omega}\rho'_{1\omega}\rho'_{2\omega}\varepsilon'_{2\omega} \\ & +\varepsilon'_{1\omega}\rho'_{1\omega}\rho'_{2\omega}\rho'_{1\omega}\rho'_{2\omega}\varepsilon'_{2\omega} + \cdots]\, I^0_\omega(T_1)\cos\theta d\Omega d\omega, \end{aligned} \tag{1}$$

where $\varepsilon'_{1\omega}$ and $\varepsilon'_{2\omega}$ are the monochromatic and directional emissivities of media 1 and 2, $\rho'_{1\omega}$ and $\rho'_{2\omega}$ the specular reflectivities. $I^0_\omega(T_1)$ is the intensity of equilibrium radiation at temperature T_1 :

$$I_\omega^0(T_1) = \frac{\hbar\omega^3}{4\pi^3c^2}\frac{1}{\exp[\hbar\omega/k_BT_1]-1} \tag{2}$$

where $2\pi\hbar$ is the Planck constant and k_B the Boltzmann constant. Equation (1) can be written as a sum of a geometrical series so that

$$\phi_{1\to2} = \int_0^{2\pi}\cos\theta d\Omega\int_0^\infty d\omega\frac{\varepsilon'_{1\omega}\varepsilon'_{2\omega}}{1-\rho'_{1\omega}\rho'_{2\omega}}I_\omega^0(T_1). \tag{3}$$

Doing the same calculation for $\phi_{2\to1}$, one finds the classical radiative heat exchange

$$\begin{aligned}\phi_{1\to2}-\phi_{2\to1} &= \int_0^{2\pi}\cos\theta d\Omega\int_0^\infty d\omega\frac{\varepsilon'_{1\omega}\varepsilon'_{2\omega}}{1-\rho'_{1\omega}\rho'_{2\omega}}\\ &\times\ \left[I_\omega^0(T_1)-I_\omega^0(T_2)\right]\end{aligned} \tag{4}$$

Note here that, as the materials are opaque, the result would be the same if T_1 and T_2 were surface temperatures instead of the uniform materials temperatures.

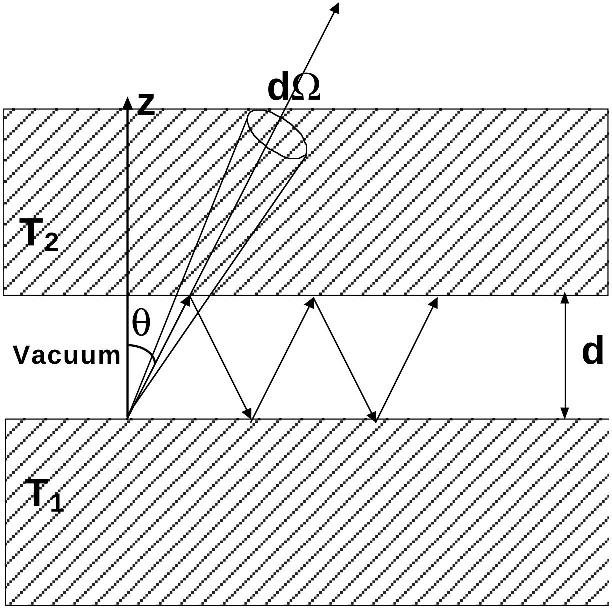

Fig. 2. The energy transfer in a solid angle $d\Omega$ comes from the multiply reflected rays issued form a first ray pointing in the solid angle $d\Omega$

The above calculation does not take into account interference effects. When the radiation is not monochromatic, these effects disappear as soon as the distance d is large compared to the temporal coherence length l_{coh}. This is given $c/\Delta\nu$ where $\Delta\nu$ is the inverse of the frequency width of the radiation. Note that the same behaviour is observed when looking at interferences rings in a Michelson illuminated with partially incoherent light. For an optical path difference larger than the coherence length l_{coh}, the contrast of the interference fringes goes to zero. However for distances smaller than l_{coh}, the interferences have to be taken into account.

There is another shortcut in the ray picture : the evanescent waves are not taken into account. To illustrate the nature of an evanescent wave, let us take the example of a plane wave of linear polarization $\mathbf{E} = \mathbf{E}_0 \exp[i(\mathbf{k}.\mathbf{r} - \omega t)]$ propagating in vacuum. The Maxwell equations impose a relation on the wave vector components $k_z = (\omega^2/c^2 - k_x^2 - k_y^2)^{1/2}$. An evanescent wave is a wave for which $k_x^2 + k_y^2 > \omega^2/c^2$ so that k_z is a pure imaginary number. It does not propagate anymore in the z-direction but decays exponentially. The simplest example of an evanescent wave is the wave produced by total internal reflection when an incident in glass illuminates an interface glass-air at an angle larger than the critical angle. An evanescent wave is then produced in the air. The evanescent wave does not carry energy in the vacuum along Oz except when it is in presence of another evanescent wave going in the opposite direction. This latter situation happens when a second prism is brought close to the first so that an evanescent wave produced by total internal reflection can reach the second prism. Then, light is partially reflected and partially transmitted at the second interface. This is the so-called frustrated total internal reflection which is formally identical to the tunnel effect. From these considerations, one can infer that at small distances, the radiative heat transfer will be enhanced due to the tunnelling of evanescent waves between the two materials. These two effects have been discussed already in the litterature. Cravalho et al. [3] were the first to point out the role of tunneling by introducing a generalized transmission coefficient. Yet, they did not include all the contributions. They only took into account tunneling waves which have $n\omega/c < \sqrt{k_x^2 + k_y^2} < \omega/c$. In other words, they have accounted for the frustration of the total internal reflection. However, they did not realize that there are evanescent waves with larger wavevectors that also contribute to the heat transfer. This can be done by doing an ab-initio calculation of the emitted radiation starting from the sources, namely the random currents due to the thermal motion.

Such an approach has been first introduced by Rytov [4], Polder and Van Hove [5] and later by Loomis and Maris [6]. They did a complete calculation based on classical electrodynamics. However, they only considered the case of metals. The main contribution of this paper is to apply this formalism to the case of dielectrics that can support surface phonon-polaritons. These are surface waves which are electromagnetic modes of the interface. Thus, they that can be resonantly excited. Their excitation produces a strong enhancement of the density of energy in the near field [7]. It will be shown here that their presence dramatically modifies the heat transfer between two interfaces. Surface plasmons polaritons are similar surface waves. However their contribution to the heat transfer is generally much smaller just because they exist in the near UV so that they can hardly be excited thermally.

Let us first describe in simple words the physical mechanism responsible of the emission of radiation by thermal sources. In any material, thermal fluctuations induce fluctuating currents. Their mean value is zero so that the mean radiated fields are zero. Yet the correlation function of these currents is not zero so that the Poynting vector which is a quadratic quantity is not zero. The correlation function of the currents can be calculated using the fluctuation dissipation theorem. Let us now take a look at the heat transfer due to radiation. For example, the currents in medium 1 (see Fig. 1) produce fields in the whole space, in particular in medium 2. Part of this energy is dissipated by Joule effect in medium 2. This is the contribution of medium 1 to the radiation heat exchange between the two media. An analogous contribution finds its origin in the thermal fluctuating currents excited in medium 2 and radiating fields that are dissipated in medium 1. The difference between the two terms gives the total radiative heat transfer. The important point is that this approach includes not only the far field terms that decay as $1/r$ but also the near-field terms that decay as $1/r^2$ and $1/r^3$. When using a plane wave representation of the fields, this amounts to say that we not only use the propagating waves but also the evanescent waves. In the approach of Cravalho, the near-field contributions are not taken into account because only propagating waves with a wave vector that has a maximum value of $n\omega/c$ are retained. To derive the radiative flux emitted by medium 1 and dissipated in medium 2, we compute the flux of the Poynting vector $\langle \mathbf{S} \rangle = \langle Re(\mathbf{E} \times \mathbf{H}^*) \rangle$ through a plane just above the interface separating medium 2 and a vacuum. Note that the symbol $<>$ denotes an average over an ensemble of realizations of the random currents. $\mathbf{E}$ and $\mathbf{H}^*$ are respectively the electric field and the complex conjugate of the magnetic field. Note also that this definition of the Poynting vector is 2 times larger than the usual definition. This factor comes from the fact that the signals considered here have only positive frequencies so that $\mathbf{E}(\mathbf{r}, t)$ and $\mathbf{H}(\mathbf{r}, t)$ are analytic signals [8]. The fields $\mathbf{E}$ and $\mathbf{H}$ are given in terms of the thermal currents $\mathbf{j}$ by the following expressions:

$$\mathbf{E}(\mathbf{r}, \omega) = i\mu_0\omega \int_V \overleftrightarrow{\mathbf{G}}_E(\mathbf{r}, \mathbf{r}', \omega) \cdot \mathbf{j}(\mathbf{r}', \omega) d^3\mathbf{r}' \tag{5}$$

$$\mathbf{H}(\mathbf{r}, \omega) = \int_V \overleftrightarrow{\mathbf{G}}_H(\mathbf{r}, \mathbf{r}', \omega) \cdot \mathbf{j}(\mathbf{r}', \omega) d^3\mathbf{r}' \tag{6}$$

where $\overleftrightarrow{\mathbf{G}}_E$ and $\overleftrightarrow{\mathbf{G}}_H$ are the Green dyadics of the electric and magnetic fields and obey the vector Helmholtz equation in the geometry of the problem. They respectively relate a source current at point $\mathbf{r}'$ to the electric and magnetic field at point $\mathbf{r}$. The volume V denotes the volume where the sources are present i.e. medium 1 when the heat transfer from medium 1 to medium 2 is computed. When an ensemble average is taken on the Poynting vector, it is easy to see that an ensemble average will be taken on the spatial correlation function of the thermal current fluctuations. This quantity is given by the fluctuation-dissipation theorem. In the frequency domain:

$$\begin{aligned} \langle j_n(\mathbf{r}, \omega) j_m^*(\mathbf{r}', \omega') \rangle &= \frac{2\omega}{\pi} \epsilon_0 \epsilon''(\omega) \Theta(\omega, T) \\ &\times \; \delta(\mathbf{r} - \mathbf{r}') \delta_{nm} \delta(\omega - \omega') \end{aligned} \tag{7}$$

where $\Theta(\omega, T) = \hbar\omega/[\exp(\hbar\omega/k_B T) - 1]$ is the mean energy of an oscillator in thermal equilibrium at temperature T and ϵ'' the imaginary part of the dielectric constant ϵ. This expression of the fluctuation dissipation theorem is valid as long as the medium is continuous and the dielectric constant local. The expression of the Green dyadic for the electric field relating a source in medium 1 to the electric field in medium 2 is [9] :

$$\begin{aligned} \overleftrightarrow{\mathbf{G}}_E(\mathbf{r}, \mathbf{r}', \omega) &= \frac{i}{8\pi^2} \int \frac{1}{\gamma_1} (\hat{s} t_{12}^s \hat{s} + \hat{p}_1 t_{12}^p \hat{p}_2) \\ \times \exp[i\mathbf{K}(\mathbf{R} - \mathbf{R}')] &\times \exp(i\gamma_2 z - i\gamma_1 z') d^2\mathbf{K} \end{aligned} \tag{8}$$

where $\mathbf{r} = (\mathbf{R}, z)$, $\hat{s} = \hat{\mathbf{K}} \times \hat{z}$, $\hat{p}_j = (|\mathbf{K}|\hat{z} - \gamma_j \hat{\mathbf{K}})/k_j$, the symbol $\hat{}$ denoting unit vectors, $k_j = \sqrt{\epsilon_j}\omega/c$, $\gamma_j = (k_j^2 - \mathbf{K}^2)^{1/2}$ with $Re(\gamma_j) > 0$, $Im(\gamma_j) > 0$. The coefficient t_{12}^s and t_{12}^p denotes the amplitude transmission coefficient between medium 1 and 2, for the s and p polarization. They can be expressed in terms of the Fresnel reflection and transmission coefficients [9] :

$$t_{12}^{s,p} = \frac{t_{13}^{s,p} t_{32}^{s,p} \exp(i\gamma_3 d)}{1 - r_{31}^{s,p} r_{32}^{s,p} \exp(2i\gamma_3 d)} \tag{9}$$

The Green function $\overleftrightarrow{\mathbf{G}}_H$ is deduced from $\overleftrightarrow{\mathbf{G}}_E$ with the help of the Maxwell equations [9]. One then finds the expression of the heat transfer per unit surface $P(T_1, T_2) = \langle S_z(d^+, T_1) \rangle - \langle S_z(0^-, T_2) \rangle$:

$$\begin{aligned} P(T_1,T_2) = \frac{4}{\pi^2} \int_0^\infty & d\omega (\Theta(\omega, T_1) - \Theta(\omega, T_2)) \int_0^\infty K dK \\ \times \left| e^{i\gamma_3 d} \right|^2 & \left[\frac{|\gamma_3|^2}{|1 - r_{31}^s r_{32}^s e^{2i\gamma_3 d}|^2} \frac{Re(\gamma_1) Re(\gamma_2)}{|(\gamma_3 + \gamma_1)(\gamma_3 + \gamma_2)|^2} \right. \\ + & \left. \frac{|\epsilon_3|^2 |\gamma_3|^2}{|1 - r_{31}^p r_{32}^p e^{2i\gamma_3 d}|^2} \frac{Re(\epsilon_1 \gamma_1^*) Re(\epsilon_2 \gamma_2^*)}{|(\epsilon_1 \gamma_3 + \epsilon_3 \gamma_1)(\epsilon_2 \gamma_3 + \epsilon_3 \gamma_2)|^2} \right] \end{aligned} \tag{10}$$

where $K = |\mathbf{K}|$. Note that in this expression, the integration over K goes from 0 to ∞. Integration from 0 to ω/c corresponds to waves propagating in the vacuum between the two media. When K is greater than ω/c, one includes the contribution to the heat transfer of the evanescent waves in vacuum. Let us make some comments on the validity of this approach. First, we are interested in small distances so we may question the validity of a result based on macroscopic electrodynamics. The main approximation made here is that we do not account for non-local effects. This is a reasonable approximation as far as the distances involved are larger than the Fermi length.

The heat transfer can actually be cast in a suggestive form which permits a comparison with expression (4). To do so, let us consider now the heat transfer $\phi_{1\to 2}$ due to the dissipation in medium 2 of the fields initiated by the currents in medium 1. $\phi_{1\to 2}$ is the sum of the contribution of propagating waves $\phi_{1\to 2}^{prop}$ and evanescent waves $\phi_{1\to 2}^{evan}$. Let θ be the angle of propagation of the energy flux in medium 3 with respect to the z-axis. We consider now the energy flux in a solid angle $d\Omega = 2\pi c^2 K dK/(\omega^2 \cos\theta)$ due to the propagating waves $\phi_{1\to 2}^{prop}$:

$$\begin{aligned} \phi_{1\to 2}^{prop} &= \int \frac{d\omega d\Omega \cos\theta}{2} \left[\frac{(1 - |r_{31}^s|^2)(1 - |r_{32}^s|^2)}{|1 - r_{31}^s r_{32}^s e^{2i\gamma_3 d}|^2} \right. \\ &+ \left. \frac{(1 - |r_{31}^p|^2)(1 - |r_{32}^p|^2)}{|1 - r_{31}^p r_{32}^p e^{2i\gamma_3 d}|^2} \right] I_\omega^0(T_1) \end{aligned} \tag{11}$$

In the preceding expression, $1 - |r_{31}^{s,p}|^2$ and $1 - |r_{32}^{s,p}|^2$ are the coefficients of transmission in energy between media 3 and 1 and 3 and 2 for the corresponding polarization. This expression is similar to (3). In Eq. (11), the denominator is due to interferences that exist for a monochromatic light. But noting that the evolution of the reflection coefficient with the frequency is slower than the evolution of $e^{i\gamma_3 d}$ and that the mean average of $1/|1 - r_{31} r_{32} e^{2i\gamma_3 d}|^2$ is $1/(1 - |r_{31}|^2 |r_{32}|^2)$ ($|r_{31} r_{32}| < 1$), (11) reduces to (3). For each polarisation, we can identify the emissivity of medium 1 with the energy transmission coefficient

$1-|r_{31}^{s,p}|^2$ and the reflectivity with the energy reflection coefficient $|r_{31}^{s,p}|^2$. For surface waves, we cannot define a directional emissivity since all the evanescent waves propagate along the interface. However, each of them is characterized by a well defined wave vector $\mathbf{K}$. We can thus introduce a generalized emissivity function of $\mathbf{K}$ instead of θ. To proceed, we start from the following expression of the energy flux $\phi_{1\to 2}^{evan}$ due to evanescent waves :

$$\phi_{1\to 2}^{evan} = \int_0^\infty d\omega I_\omega^0(T_1) \int_{\omega/c}^\infty 2KdK e^{-2Im(\gamma_3)d}$$
$$\times \left[\frac{Im(r_{31}^s)Im(r_{32}^s)}{|1-r_{31}^s r_{32}^s e^{-2Im(\gamma_3)d}|^2} + \frac{Im(r_{31}^p)Im(r_{32}^p)}{|1-r_{31}^p r_{32}^p e^{-2Im(\gamma_3)d}|^2} \right]. \tag{12}$$

Upon comparison with Eq.(3) the quantity $Im(r_{31}^{s,p})$ which is a function of $\mathbf{K}$ can be used as a generalized emissivity for medium 1 whereas $Im(r_{32}^{s,p})$ would be the emissivity of medium 2. Note that in this case the reasoning of Eq. (1) is still valid provided that one adds *amplitudes* instead of intensities and one introduces an additional exponential decay $\exp(-2Im(\gamma_3)d)$ in each term of the series. This decay accounts for the evanescent nature of the waves involved.

3 Contribution of resonant surface waves

We now evaluate the total contribution of radiation to the heat transfer. First of all, let us remark that for most materials, when a gas at atmospheric pressure is present between the two media, the radiative heat transfer remains lower than the conductive heat transfer due to the ballistic flight of molecules between the two bodies [10]. At ambient temperature and pressure and for small distances between the two media, a conductive heat transfer coefficient h^C can be evaluated. It reads [11]

$$h^C = 1.85\ 10^{-5} \frac{c_p/c_v+1}{c_p/c_v-1} a_0 \frac{p}{M^{1/2}\bar{T}^{1/2}} \tag{13}$$

where h^C is expressed in W.m^{-2}.K^{-1}, c_p and c_v are the specific heat of the gas respectively at constant pressure and volume, p is the pressure in Pa, a_0 is a factor related to the accomodation factor of the surfaces, M is the molecular weight of the gas. At ambient pressure and for air, h^C is about 4. 10^4 W m^{-2} K^{-1}. Following the approach of Ref. [5], a radiative heat transfer coefficient h^R (in W m^{-2} K^{-1}) is defined by $\lim_{T_1\to T_2}\ P(T_1,T_2)\ /\ (T_1\ -\ T_2)$. For most media, h^R remains much lower than h^C.

We consider now materials that can support a surface wave in the infrared range of interest in thermal transfer, namely between 2μm and 50μm. First of all, let us explain what is a resonant surface wave. It is a wave that propagates along the interface and that decays exponentially on both sides of the interface. This wave is an electromagnetic mode of the interface. It can thus be excited resonantly. These surface waves are polarized and exist only in p polarization. It appears whenever the real part of the dielectric constant is lower than -1. Two types of surface waves exist. The surface-plasmon polaritons which appears in the visible wavelength and near-UV domain and the surface phonon-polaritons which exist in the infrared. A surface-plasmon polariton is a charge density wave due to the presence of electrons. It can be viewed as an acoustic type wave in an electron gas. Since electrons carry a charge, this mechanical density wave is necessarily coupled to an electromagnetic wave. The surface-phonon polaritons appear in polar materials. They are also coupled mechanical and electromagnetic vibrations. The mechanical vibration involved is the usual phonon. If the medium is polar, then the atoms are charged and their mechanical oscillatory movement may produce an electromagnetic wave. Materials such as glass, SiC, II-VI and III-V semi-conductors do support surface phonon-polaritons in the infrared. We are specifically interested in surface phonon-polaritons case because these resonances occurs in the infrared so that they can be thermally excited.

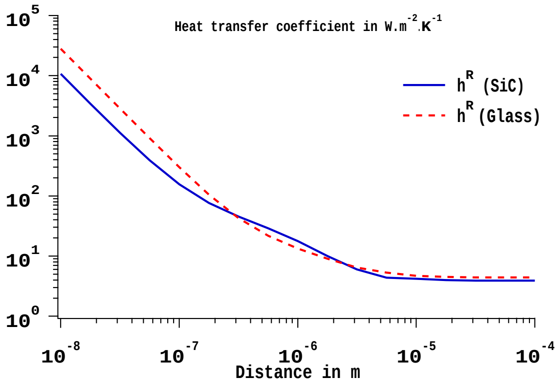

Fig. 3. Radiative heat transfer coefficient versus the distance between two semi-infinite bodies of SiC or glass at $T = 300$ K.

Fig. 3 displays $h^R(T = 300K, d)$ versus the distance separating two surfaces of same material, either SiC or glass. When d is much larger than the wavelength of the maximum of the Planck spectrum (here 10μm) , h^R does not depend on d. One finds the results given by the classical heat transfer theory : the heat transfer coefficient is equal to 5W.m^{-2}.K^{-1} at ambient temperature and is proportionnal to T^3. When d is lower than 1μm, the heat transfer increases as d^{-2} [6]. For SiC or glass surfaces, h^R reaches the value of the conductive heat transfer coefficient when d is approximately equal to 10 nm. At a pressure lower than the ambient one, the radiative heat transfer will be predominant. Xu [10] tried to measure this near-field radiative contribution in the case of two metals but did not achieve it. The transfer between a metal and a material exhibiting a surface wave, or better between two materials exhibiting surface waves would make the detection easier. Indeed, the radiative heat transfer for $d = 10$ nm is four orders of magnitude larger in the case of two media made of glass than in the case of two media made of Chromium.

Let us mention that this increase in $1/d^2$ has been recently questioned [12] with the argument that the heat flux cannot diverge. This is not actually a problem because this divergence means that the thermal resistance of the vacuum gap tends to zero so that a thermal contact is established. The difference of temperature between the two media has then to be zero. This is similar to the situation of a short circuit at the end of which it is impossible to impose a potential difference. This brings us to the question of the validity of the assumption of having a uniform temperature in the media. Let us assume that there is a gap of 10 nm between the two interfaces with a difference of temperature of 1 K. According to Fig. 3, the heat transfer coefficient is around 10^4. If we use a conservative estimate for the thermal conductivity of 1, we find that there will be a decay of temperature of 1 K in the solid over a distance which is $10^{-4}m$. This is four orders of magnitude more than the gap width. It means that the conduction is much more efficient than radiation. It also means that the temperature can be considered to be uniform over the skin depth (a fraction of wavelength) which is involved in the emission-absorption process.

This near-field radiative heat transfer contribution might find important applications in processes requiring rapid and highly confined heat transfer. Indeed, the presence of evanescent waves means that the radiative space distribution can be higly confined in space. It should be possible to heat locally the temperature of a sample by approaching a heated probe at an appropriate distance. Alternatively, it should be possible to do a high spatial resolution detection of the temperature.

The basic physical mechanism responsible of the enhancement of radiative transfer has been studied in Refs. [13, 14]. It was shown that the density of electromagnetic energy above an interface separating a lossy medium from vacuum increases exponentially when approaching the interface in a range of the order of the wavelength and diverges as $1/z^3$ at nanometer scale. This enhancement can be related to the existence of additional electromagnetic states due to surface waves. Indeed, the energy density can be cast in the following form:

$$I(\mathbf{r},\omega) = \Theta(\omega) N(\mathbf{r},\omega). \tag{14}$$

$N(\mathbf{r},\omega)$ is the density of electromagnetic modes of frequency ω at point $\mathbf{r}$. In the example of the equilibrium blackbody radiation in a cavity of volume V, $N(\mathbf{r},\omega)$ does not depend on $\mathbf{r}$ and is calculated by counting the number of propagating modes per unit volume in the cavity. It takes the value $N(\omega) = \omega^2/(\pi^2 c^3)$. When an interface is present, additional modes exist as discussed previously. This explains why the energy density may increase. The energy density is calculated by means of the cross-spectral density tensor following Carminati and Greffet [13]. The density of modes is then deduced from the energy density and depends only on the distance z. When the distance to the interface becomes much lower than the maximum wavelength of Planck function, the density of modes can be expanded asymptotically:

$$N(z,\omega) = \frac{\epsilon''}{|1+\epsilon|^2} \frac{1}{\pi^2 \omega z^3} \tag{15}$$

We see in this equation that the density of modes increases as $1/z^3$ at small distances. This behaviour had already been noticed by Rytov [4]. The novel interesting feature is the effect of surface waves. We take here the example of SiC, but the following discussion is valid for any material supporting surface waves.

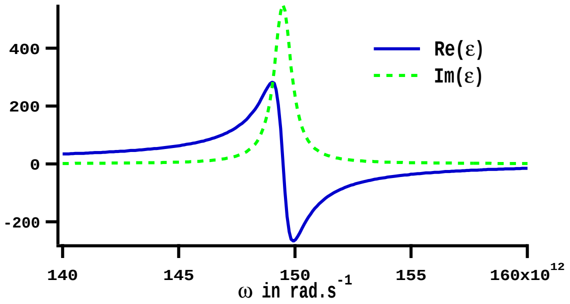

Fig. 4. Real and imaginary part variation of the SiC dielectric constant with the frequency ω.

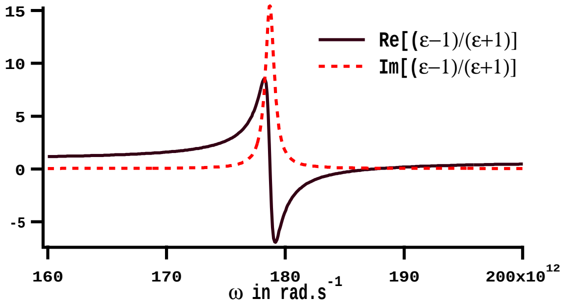

Fig. 5. Real and imaginary part varaition of the quantity $(\epsilon-1)/(\epsilon+1)$ with the frequency ω.

We see on Fig. 4 that the real part of the dielectric constant reaches -1 for a certain frequency denoted by ω_{max}. We see also that at this frequency the imaginary part of the dielectric constant is not too large. The quantity $Im[(\epsilon-1)/(\epsilon+1)]$ which is equal to $2\epsilon''/|\epsilon+1|^2$ exhibits a peak (Fig. 5) at ω_{max} and the density of modes also as we see in Eq. (15). The physical interpretation of this phenomenon can be inferred from the analysis of the dispersion relation of the surface modes [14]. The wave number parallel to the interface is given by $[k_{||}^{SW}(\omega)]^2 = (\omega^2/c^2)\epsilon(\omega)/[\epsilon(\omega)+1]$. Note that these waves cannot radiate in the vacuum since $|k_{||}| > \omega/c$ and that they decrease exponentially away from the interface. Near the frequency ω_{max}, there exists a large number of surface modes so that the energy density increases. Therefore, the energy density being larger near a material exhibiting surface waves, an important radiative energy transfer will take place if these additional surface electromagnetic modes can be coupled to a second material.

It is important to notice that this radiative heat transfer enhancement exhibits strong spectral effects. The increase of the density of modes exists at all frequencies but is much larger in the presence of surface waves and near the frequency ω_{max}. To analyse the spectral effects in the radiative near-field heat transfer, we introduced a monochromatic radiative heat transfer coefficient h_{ω}^{R}. It is plotted in Fig. 6 for two semi-infinite surfaces separated by d = 10nm in the case of SiC or glass.

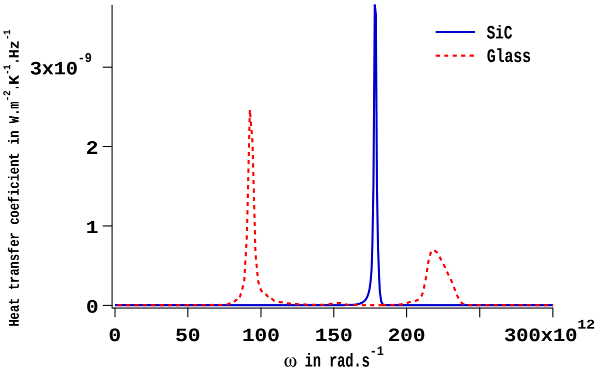

Fig. 6. Monochromatic radiative heat transfer coefficient versus frequency for two semi-infinite bodies of SiC or glass separated by a distance d=10 nm at T = 300 K.

The remarkable feature shown on this plot is that the heat transfer exhibits large peaks for some frequencies and is almost monochromatic. These peaks appear at frequencies where the energy density is enhanced near a material. An asymptotic expansion of the monochromatic radiative heat transfer coefficient can be done in the same way the expansion had been done for the density of modes. It takes actually a similar form:

$$\begin{aligned} h^R_\omega &= \frac{1}{\pi^2 d^2} \frac{\epsilon_1'' \epsilon_2''}{|1+\epsilon_1|^2 |1+\epsilon_2|^2} \\ &\times \; k_B \left(\frac{\hbar\omega}{k_B T} \right)^2 \frac{\exp[\hbar\omega/(k_B T)]}{(\exp[\hbar\omega/(k_B T)] - 1)^2} \end{aligned} \tag{16}$$

We see in this equation that the heat transfer is enhanced at the resonant frequencies of each material. The enhancement is particularly strong when the materials are identical because the resonances amplify each other. Let us discuss a possible application of this property in the field of thermophotovoltaic energy conversion. The major fundamental limit of efficiency of photovoltaic energy conversion is the mismatch between the photon energy and the gap of the semiconductor. If the energy of the incident radiation is below the gap, all the energy is lost. If the energy of the incident photon is higher than the gap width, all the extra energy is lost. This is reponsible for a large part of the low efficiency of the photovoltaic cells. Thermophotovoltaic energy conversion is based on the realization of a thermal source of radiation using a gas heater for instance. The radiation is then converted into electricity by a photovoltaic cell with a low gap so that infrared light can be used. Using a material with a band gap that matches the resonant frequency of the material used to fabricate the thermal source could increase significantly the efficiency of the system.

The presence of these strong resonances also explain why the integrated radiative heat transfer coefficient h^R does depend on the distance between the two media as $1/d^2$. In Eq. (16), it is seen that the spacing dependence appears as a factor $1/d^2$ independent of frequency. Let us now consider the temperature dependence of the heat transfer coefficient. If the pole at ω_{max} yields the leading contribution, then the temperature dependence is the same as for the monochromatic coefficient for $\omega = \omega_{max}$. This behaviour is very different from the $1/T^3$ of the blackbody radiation. Finally, let us remark that if $x = \hbar\omega/(k_B T) \gg 1$, the monochromatic radiative heat transfer coefficient decays as $x^2 \exp(-x)$. This is tipically the situation of metals which support surface plasmons in the visible or near UV. As shown on the figures 7 and 8, the nanoscale radiative heat transfer does not show any monochromatic peak because the Planck's function takes very low values in this part of the spectrum. However, there is still an enhancement of the transfer due to the near-field contributions (the $1/r^2$ and $1/r^3$ terms in the dipole radiation).

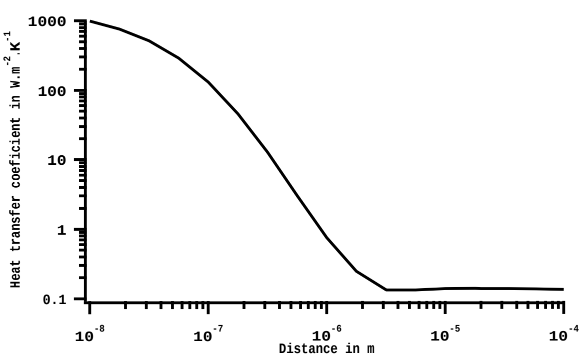

Fig. 7. Radiative heat transfer coefficient versus the distance between two semi-infinite bodies of Gold at $T = 300$ K.

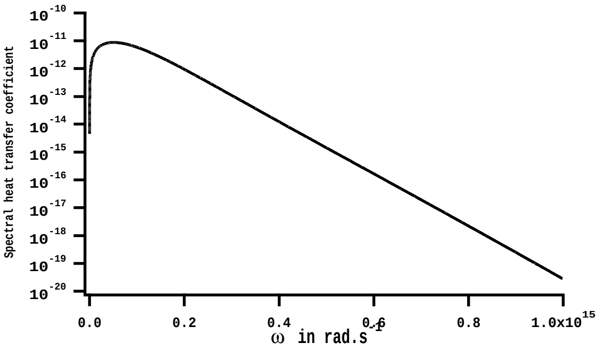

Fig. 8. Monochromatic radiative heat transfer coefficient (in W.m^{-2}.K^{-1}.Hz^{-1}) versus frequency for two semi-infinite bodies of Gold separated by a distance d=10 nm at $T = 300$ K.

We may wonder how the model can be applied to a system with some roughness. Let us consider roughnesses with different transverse length scales. If we consider variations of the spacing between the two interfaces over transverse distances of the order of $50\mu m$ or more, then, the present model can be used locally. Indeed, although the calculations have assumed an infinite interface, the result is expected to be locally valid on a scale on the order of the decay length of the surface waves. This is tipically on the order of 5 to 20 wavelengths. Since the spacing dependence of the heat transfer coefficient is very strong $(1/d^2)$, we may expect significant inhomogeneities in the heat transfer. If we now consider smaller transverse features in the roughness, we have to consider the problem of scattering of a surface wave by some surface features. This has been studied in the past[15]. It appears that the scattering cross section of structures much smaller than the wavelength is rather small. For example, the transmission of a surface plasmon polariton impinging on a rectangular protuberance of height $\lambda/20$ and width $\lambda/4$ is 97%[15]. Note that this is a rather large structure as compared to the typical spacing distances that we are using.

4 Conclusion

To summarize, it has been shown that the heat transfer between two semi-infinite bodies increases at short distances due to the presence of evanescent waves close to the interface. When the materials constituting the bodies support surface-phonon polaritons, the radiative heat transfer is enhanced by several orders of magnitude. The density of electromagnetic modes exhibits in that case a peak at a frequency ω_{max} and is responsible of a large increase of the heat tranfer at this particular frequency. We think that this nanoscale behaviour may have important applications. It is certainly necessary to properly model the radiative thermal exchanges between a sample and an atomic force microscope probe. This might also have applications for high density storage where the local control of temperature is essential in the writing process. The monochromatic behaviour of the heat transfer through the gap could also be used to dramatically increases the efficiency of thermophotovoltaic devices.

References

[1] A.R Abramson and C.L. Tien, *Microscale thermophysical engineering*, **3**, 229-244 (1999)

[2] C.C. Williams and K. Wickramasinghe, *Appl. Phys. Lett.*, **49**, 1587 (1986)

[3] E.G. Cravalho, C.L. Tien and R.P. Caren, *Journal of Heat Transfer*, **89**, 351, (1967)

[4] S. M. Rytov, Yu. A. Kravtsov, and V. I. Tatarskii, *Principles of Statistical Radiophysics vol. 3*, (Springer-Verlag, Berlin, 1989), p. 118

[5] D. Polder and M. Van Hove, *Phys. Rev. B*, **4**, 3303, (1971)

[6] J.L. Loomis and H.J. Maris, *Phys. Rev. B*, **50**, 18517-18524, (1994)

[7] A. Shchegrov, K. Joulain, R. Carminati and J.-J. Greffet, *Phys. Rev. Lett.*, **85**, 1548 (2000).

[8] L. Mandel and E. Wolf, *Optical coherence and quantum optics*, Cambridge University Press (Cambridge, U.K., 1995)

[9] J.E. Sipe, *J. Opt. Soc. Am. B*, **4**, 481, (1987)

[10] J. Xu, Heat Transfer between Two Metallic Surfaces at Small Distance, Ph.D thesis, (Konstanz, 1993)

[11] R.J. Coruccini, *Vacuum*, **7-8**,19, (1959)

[12] J.L. Pan, *Opt. Lett.*, **25**, 369, (2000)

[13] R. Carminati and J.-J. Greffet, *Phys. Rev. Lett.*, **82**, 1660 (1999).

[14] A. Shchegrov, K. Joulain, R. Carminati and J.-J. Greffet, *Phys. Rev. Lett.*, **85**, 1548, (2000).

[15] F. Pincemin, A.A. Maradudin, A.D. Boardman and J.J. Greffet, *Phys. Rev. B*, **50**, 15261 (1994).

Nomenclature

a_0 Global accomodation factor. Dimensionless.

c Velocity of light. In m s^{-1}.

c_p Specific heat at constant pressure. In J mol^{-1} K^{-1} or kg m^2 s^{-2} mol^{-1} K^{-1}.

c_v Specific heat at constant volume. In J mol^{-1} K^{-1} or kg m^2 s^{-2} mol^{-1} K^{-1}.

d Distance of separation between the two media. In m.

$\mathbf{E}$ Electric field. In V m^{-1} or kg m s^{-3} A^{-1}.

$\overleftrightarrow{\mathbf{G}}_E$ Green dyadic of the electric field. In m^{-1}.

$\overleftrightarrow{\mathbf{G}}_H$ Green dyadic of the magnetic field. In m^{-1}.

$\mathbf{H}$ Magnetic field. In A m^{-1}.

h Heat transfer coefficient. In W m^{-2} K^{-1} or kg s^{-3} K^{-1}.

$\hbar$ Planck constant divided by 2π. In J s or kg m^2 s^{-1}.

$I^0_\omega(T)$ Intensity of equilibrium radiation at temperature T. In W m^{-2} Hz^{-1} ster^{-1} or kg s^{-2}.

$\mathbf{j}$ Electric current density. In A m^{-2}.

$\mathbf{k}$ Wave vector. In m^{-1}.

$\mathbf{K}$ Wave vector component on the interface. In m^{-1}.

k_B Boltzmann constant. In J K^{-1} or kg m^2 s^{-2} K^{-1}.

M Molecular weight. Dimensionless.

N Density of electromagnetic modes. In m^{-3}.

p Pressure. In kg m^{-3} s^{-2}.

$P(T_1, T_2)$ Radiative heat transfer per unit surface between two semi-infinite media at temperature T_1 and T_2. In W m^{-2} or kg s^{-3}.

$\mathbf{r}$ Position vector. In m.

$\hat{p_j}$ Unit vector carrying the electric field in p polarization in the medium j. Dimensionless.

$\mathbf{R}$ Component of $\mathbf{r}$ on the interface. In m.

r^p_{ij} Amplitude reflection coefficient for the electric field in p polarization at the interface of media i and j, the incoming field coming from the medium i. Dimensionless.

r^s_{ij} Amplitude reflection coefficient for the electric field in s polarization at the interface of media i and j, the incoming field coming from the medium i. Dimensionless.

$\hat{s}$ Unit vector carrying the electric field in s polarization. Dimensionless.

$\mathbf{S}$ Poynting vector. In W m^{-2} or kg s^{-3}.

t^p_{ij} Amplitude transmission coefficient for the electric field in p polarization at the interface of media i and j, the incoming field coming from the medium i. Dimensionless.

t^s_{ij} Amplitude transmission coefficient for the electric field in s polarization at the interface of media i and j, the incoming field coming from the medium i. Dimensionless.

T Temperature. In K.

z Vertical component of $\mathbf{r}$. In m.

γ Vertical component of $\mathbf{k}$. In m^{-1}.

δ_{nm} Kronecker symbol.

$\delta(\mathbf{r})$ Dirac function.

ϵ Dielectric constant. Dimensionless.

ϵ' Real part of the dielectric constant. Dimensionless.

ϵ'' Imaginary part of the dielectric constant. Dimensionless.

ϵ_0 Permittivity of vacuum. In kg^{-1} m^{-3} s^4 A^2.

ε'_ω Monochromatic and directional emissivity. Dimensionless.

θ Angle of propagation in the vaccum with the normal to the interfaces. In rad.

$\Theta(\omega, T)$ Mean energy of an oscillator of frequency ω in thermal equilibrium at temperature T. In J or kg m^2 s^{-2}.

λ Wavelength. In m.

μ_0 Permeability of vacuum. In kg m s^{-2} A^{-2}.

ρ'_ω Monochromatic and directional reflectivity. Dimensionless.

$\phi_{1\to 2}$ Energy flux from medium 1 into medium 2. In W m^{-2} or kg s^{-3}.

$\phi_{2\to 1}$ Energy flux from medium 2 into medium 1. In W m^{-2} or kg s^{-3}.

ω Frequency. In rad s^{-1}.

Ω Solid angle. In steradian.

Coherent emission of light by thermal sources

J.-J. Greffet, R. Carminati, K. Joulain, J.-P. Mulet, S. Mainguy et Y. Chen

Nature, vol 416, pp61–64 (2002)

because the actual masses of massive protostars are poorly determined. Our approach is to predict the properties of some well studied massive protostars in terms of their bolometric luminosities. The bolometric luminosity L_{bol} has contributions from main-sequence nuclear burning L_{ms}, deuterium burning L_D, and accretion L_{acc}. The accretion luminosity $L_{acc} = f_{acc} G m_* \dot{m}_* / r_*$, where f_{acc} is a factor of order unity accounting for energy radiated by an accretion disk, advected into the star or converted into kinetic energy of outflows, and where the stellar radius r_* may depend sensitively on the accretion rate $\dot{m}_*$. Massive stars join the main sequence during their accretion phase at a mass that also depends on the accretion rate[23]. To treat accelerating accretion rates, we have developed a simple model for protostellar evolution based on that of refs 6 and 24. The model accounts for the total energy of the protostar as it accretes and dissociates matter and, if the central temperature $T_c \gtrsim 10^6$ K, burns deuterium. We have modified this model to include additional processes, such as deuterium shell burning, and we have calibrated these modifications against the more detailed calculations of refs 23 and 25.

Our model allows us to make predictions for the masses and accretion rates of embedded protostars that are thought to power hot molecular cores (C.F.M. and J.C.T., manuscript in preparation). Figure 2 compares our theoretical tracks with the observed bolometric luminosities of several sources. We find that uncertainties in the value of the pressure create only small uncertainties in m_* for L_{bol} in excess of a few times 10^4 solar luminosities.

The infrared and submillimetre spectra of accreting protostars and their surrounding envelopes have been modelled in ref. 5, modelling the same sources shown in Fig. 2. We note that uncertainties in the structure of the gas envelope and the possible contributions from additional surrounding gas cores or diffuse gas will affect the observed spectrum. Comparing results, our inferred stellar masses are similar, but our accretion rates are systematically smaller by factors of ~2–5. The modelled[5] high accretion rates of $\sim 10^{-3} M_\odot \mathrm{yr}^{-1}$ for stars with $m_* \approx 10 M_\odot$ would be difficult to achieve unless the pressure was increased substantially; for example, if the stars are destined to reach $m_{*f} \approx 30 M_\odot$, pressure increases of a factor ~40 are required. ☐

Received 17 September 2001; accepted 2 January 2002.

1. Bernasconi, P. A. & Maeder, A. About the absence of a proper zero age main sequence for massive stars. *Astron. Astrophys.* **307,** 829–839 (1996).
2. McLaughlin, D. E. & Pudritz, R. E. Gravitational collapse and star formation in logotropic and nonisothermal spheres. *Astrophys. J.* **476,** 750–765 (1997).
3. Stahler, S. W., Palla, F. & Ho, P. T. P. in *Protostars & Planets IV* (eds Mannings, V., Boss, A. P. & Russell, S. S.) 327–351 (Univ. Arizona Press, Tucson, 2000).
4. Behrend, R. & Maeder, A. Formation of massive stars by growing accretion rate. *Astron. Astrophys.* **373,** 190–198 (2001).
5. Osorio, M., Lizano, S. & D'Alessio, P. Hot molecular cores and the formation of massive stars. *Astrophys. J.* **525,** 808–820 (1999).
6. Nakano, T., Hasegawa, T., Morino, J.-I. & Yamashita, T. Evolution of protostars accreting mass at very high rates: Is Orion IRc2 a huge protostar? *Astrophys. J.* **534,** 976–983 (2000).
7. Plume, R., Jaffe, D. T., Evans, N. J. II, Martin-Pintado, J. & Gomez-Gonzalez, J. Dense gas and star formation: Characteristics of cloud cores associated with water masers. *Astrophys. J.* **476,** 730–749 (1997).
8. Bertoldi, F. & McKee, C. F. Pressure-confined clumps in magnetized molecular clouds. *Astrophys. J.* **395,** 140–157 (1992).
9. Hillenbrand, L. A. & Hartmann, L. W. A preliminary study of the Orion nebula cluster structure and dynamics. *Astrophys. J.* **492,** 540–553 (1998).
10. van der Tak, F. F. S., van Dishoeck, E. F., Evans, N. J. II & Blake, G. A. Structure and evolution of the envelopes of deeply embedded massive young stars. *Astrophys. J.* **537,** 283–303 (2000).
11. Vázquez-Semadeni, E., Ostriker, E. C., Passot, T., Gammie, C. F. & Stone, J. M. in *Protostars & Planets IV* (eds Mannings, V., Boss, A. P. & Russell, S. S.) 3–28 (Univ. Arizona Press, Tucson, 2000).
12. Richer, J. S., Shepherd, D. S., Cabrit, S., Bachiller, R. & Churchwell, E. in *Protostars & Planets IV* (eds Mannings, V., Boss, A. P. & Russell, S. S.) 867–894 (Univ. Arizona Press, Tucson, 2000).
13. Matzner, C. D. & McKee, C. F. Efficiencies of low-mass star and star cluster formation. *Astrophys. J.* **545,** 364–378 (2000).
14. McLaughlin, D. E. & Pudritz, R. E. A model for the internal structure of molecular cloud cores. *Astrophys. J.* **469,** 194–208 (1996).
15. Larson, R. B. Turbulence and star formation in molecular clouds. *Mon. Not. R. Astron. Soc.* **194,** 809–826 (1981).
16. Stahler, S. W., Shu, F. H. & Taam, R. E. The evolution of protostars. I—Global formulation and results. *Astrophys. J.* **241,** 637–654 (1980).
17. Crutcher, R. M. Magnetic fields in molecular clouds: Observations confront theory. *Astrophys. J.* **520,** 706–713 (1999).
18. Jijina, J. & Adams, F. C. Infall collapse solutions in the inner limit: Radiation pressure and its effects on star formation. *Astrophys. J.* **462,** 874–887 (1996).
19. Shu, F. H. Self-similar collapse of isothermal spheres and star formation. *Astrophys. J.* **214,** 488–497 (1977).
20. Palla, F. & Stahler, S. W. Star formation in the Orion nebula cluster. *Astrophys. J.* **525,** 772–783 (1999).
21. Wolfire, M. G. & Cassinelli, J. Conditions for the formation of massive stars. *Astrophys. J.* **319,** 850–867 (1987).
22. Bonnell, I. A., Bate, M. R., Clarke, C. J. & Pringle, J. E. Competitive accretion in embedded stellar clusters. *Mon. Not. R. Astron. Soc.* **323,** 785–794 (2001).
23. Palla, F. & Stahler, S. W. The evolution of intermediate-mass protostars. II—Influence of the accretion flow. *Astrophys. J.* **392,** 667–677 (1992).
24. Nakano, T., Hasegawa, T. & Norman, C. The mass of a star formed in a cloud core: Theory and its application to the Orion A cloud. *Astrophys. J.* **450,** 183–195 (1995).
25. Palla, F. & Stahler, S. W. The evolution of intermediate-mass protostars. I—Basic results. *Astrophys. J.* **375,** 288–299 (1991).
26. Schaller, G., Schaerer, D., Meynet, G. & Maeder, A. New grids of stellar models from 0.8 to 120 solar masses at Z = 0.020 and Z = 0.001. *Astron. Astrophys. Suppl.* **96,** 269–331 (1992).
27. Hunter, T. R. *et al.* G34.24+0.13MM: A deeply embedded proto-B-star. *Astrophys. J.* **493,** L97–L100 (1998).
28. Molinari, S., Testi, L., Brand, J., Cesaroni, R. & Palla, F. IRAS 23385+6053: A prototype massive class 0 object. *Astrophys. J.* **505,** L39–L42 (1998).
29. Kaufman, M. J., Hollenbach, D. J. & Tielens, A. G. G. M. High-temperature molecular cores near massive stars and application to the Orion hot core. *Astrophys. J.* **497,** 276–287 (1998).
30. Wyrowski, F., Schilke, P., Walmsley, C. M. & Menten, K. M. Hot gas and dust in a protostellar cluster near W3(OH). *Astrophys. J.* **514,** L43–L46 (1999).

Acknowledgements

We thank S. Stahler, R. Pudritz, M. Walmsley and M. Krumholz for discussions. This work was supported by the NSF, by NASA (which supports the Center for Star Formation Studies) and (for J.C.T.) by a Spitzer-Cotsen fellowship from Princeton University.

Correspondence and requests for materials should be addressed to C.F.M.
(e-mail: cmckee@mckee.berkeley.edu).

Coherent emission of light by thermal sources

Jean-Jacques Greffet*¶, Rémi Carminati*, Karl Joulain*, Jean-Philippe Mulet*, Stéphane Mainguy† & Yong Chen‡

* *Laboratoire EM2C, CNRS, Grande Voie des Vignes, Châtenay-Malabry 92295 Cedex, France*
† *CEA CESTA, Le Barp, 33114, France*
‡ *Laboratoire de Microstructures et de Microélectronique, CNRS, av. H. Ravera, 92220 Bagneux, France*
¶ *Present address: The Institute of Optics, University of Rochester, New York 14627, USA*

A thermal light-emitting source, such as a black body or the incandescent filament of a light bulb, is often presented as a typical example of an incoherent source and is in marked contrast to a laser. Whereas a laser is highly monochromatic and very directional, a thermal source has a broad spectrum and is usually quasi-isotropic. However, as is the case with many systems, different behaviour can be expected on a microscopic scale. It has been shown recently[1,2] that the field emitted by a thermal source made of a polar material is enhanced by more than four orders of magnitude and is partially coherent at a distance of the order of 10 to 100 nm. Here we demonstrate that by introducing a periodic microstructure into such a polar material (SiC) a thermal infrared source can be fabricated that is coherent over large distances (many wavelengths) and radiates in well defined directions. Narrow angular emission lobes similar to antenna lobes are observed and the emission spectra of the source depends on the observation angle—the so-called Wolf effect[3,4]. The origin of the coherent emission lies in the diffraction of surface-phonon polaritons by the grating.

It is usually taken for granted that light spontaneously emitted by

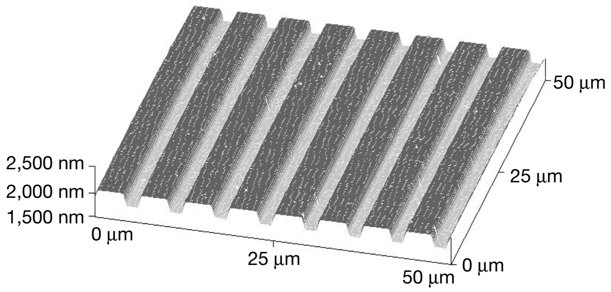

Figure 1 Image of the grating obtained by atomic force microscopy. Its period $d = 0.55\lambda$ ($\lambda = 11.36\,\mu$m) was chosen so that a surface wave propagating along the interface could be coupled to a propagating wave in the range of frequencies of interest. The depth $h = \lambda/40$ was optimized so that the peak emissivity is 1 at $\lambda = 11.36\,\mu$m. It was fabricated on SiC by standard optical lithography and reactive ion-etching techniques.

different points of a thermal source cannot interfere. In contrast, different points of an antenna emit waves that interfere constructively in particular directions producing well defined angular lobes. The intensity emitted by a thermal source is the sum of the intensities emitted by different points so that it cannot be directional. However, it has been shown[1,2] recently that some planar sources may have a spectral coherence length in the plane much larger than a wavelength and can be quasi-monochromatic in the near-field. This paves the way for the construction of a thermal source that could radiate light within narrow angular lobes as an antenna instead of having the usual quasi-lambertian angular behaviour.

Here we report experimental measurements demonstrating that it is possible to build an infrared antenna by properly designing a periodic microstructure on a polar material. Such an antenna radiates infrared light in a narrow solid angle when it is heated. Another unusual property of this source is that its emission spectrum depends on the observation direction. This property was first predicted by Wolf as a consequence of spatial correlations for random sources[3,4]. This effect has been demonstrated experimentally for artificial secondary sources[4,5] but has never been observed for direct thermal emission. In addition, the emissivity of the source is enhanced by a factor of 20 compared to the emissivity of a flat surface.

Using theories developed recently[6] to interpret the emission data by gratings, we have designed and optimized a periodic surface profile that produces a strong peak of the emissivity around a wavelength $\lambda = 11.36\,\mu$m. The grating (see Fig. 1) has been ruled on a SiC substrate. A similar grating of doped silicon with very deep depths has been investigated[7]. The authors attributed the particular properties observed to organ pipe modes in the microstructure[7]. However, the role of coherence induced by surface waves and the exact mechanism were not understood at that time[2,6].

The measurements of the thermal emission in a plane perpendicular to the lines of the grating are shown in Fig. 2. Emission is highly directional and looks very similar to the angular pattern of an antenna. We have also plotted (see Fig. 2) the calculated emission pattern. The qualitative discussion of the introduction suggests that the small angular width of the emission pattern is a signature of the local spatial coherence of the source. A proof of this stems from the fact that the source has a width $L = 5$ mm and a spectral coherence length $l \ll L$ and that its temperature is uniform. Hence, we can assume that the source is a quasi-homogeneous source[8]. With this assumption, it is known that the radiant intensity and the spectral degree of coherence in the plane of the source are related by a Fourier transform relationship[8]. Therefore, the angular width θ of the lobe emission varies qualitatively with λ/l for this locally coherent source instead of with λ/L, as for a globally coherent source. Thus a small angular aperture of the far-field radiation is the signature of a spectral coherence length in the source much larger than the wavelength. To overcome the experimental resolution limit of our direct emissivity measurement, we measured the reflectivity R. From Kirchhoff's law[9], we know that the polarized directional spectral emissivity ϵ is given by $\epsilon = \alpha = 1 - R$ where α is the absorptivity and R is the reflectivity of the grating. Results are plotted in Fig. 3. There is a remarkable quantitative agreement between the data taken at room temperature and theoretical calculations. We note that the peak at 60° has an angular width θ as narrow as 1° so that the corresponding spectral coherence length is as large as $\lambda/\theta \approx 60\lambda \approx 0.6$ mm. This suggests that a thermal source with a size L on the order of the spectral coherence length l, namely a globally coherent thermal source, could be achieved.

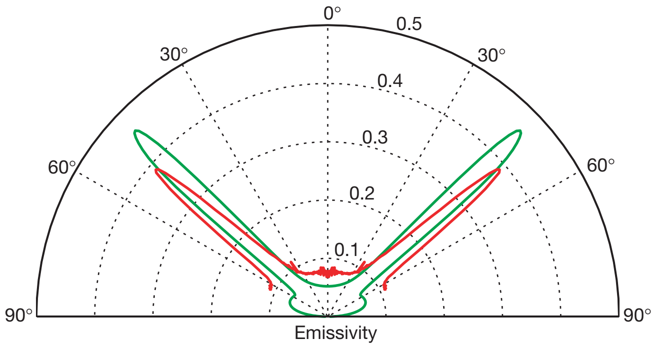

Figure 2 Polar plot of the emissivity of the grating depicted in Fig. 1 at $\lambda = 11.36\,\mu$m and for p-polarization. Red, experimental data; green, theoretical calculation. The measurements were taken by detecting the intensity emitted by the sample in the far field as a function of the emission angle. A HgCdTe detector placed at the focal length of a ZnSe lens was used. The sample was mounted on a rotation stage. The theoretical result was obtained by computing the reflectivity of the sample and using Kirchhoff's law ($\epsilon = \alpha = 1 - R$). To fit the data, we took into account the spectral resolution (0.22 µm) and the angular resolution (3°) of the measurements. The disagreement is due to the fact that for the calculation, the index at room temperature is used whereas emission data were taken with a sample in a local thermal equilibrium situation at a temperature of 773 K. Comparison between the two curves illustrates the validity of Kirchhoff's law for polarized monochromatic directional quantities. The surrounding medium was at 300 K and the background signal was subtracted. The emissivity for s-polarization (not shown) does not show any peak and is very close to its value for a flat surface. Note that most of the emitted light is emitted in the narrow lobe (that is, coherently).

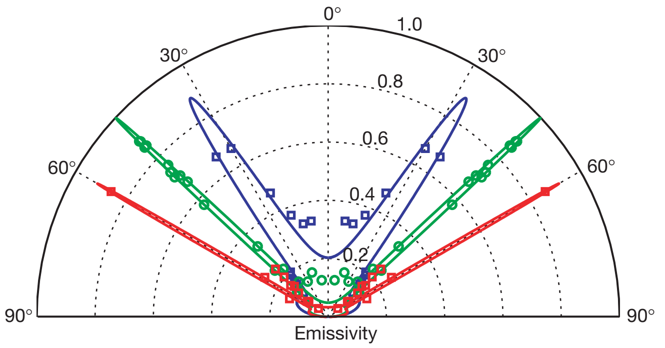

Figure 3 Emissivity of a SiC grating in p-polarization. Blue, $\lambda = 11.04\,\mu$m; red, $\lambda = 11.36\,\mu$m; green, $\lambda = 11.86\,\mu$m. The emissivity was deduced from measurements of the specular reflectivity R using Kirchhoff's law. The data have been taken at ambient temperature using a Fourier transform infrared (FTIR) spectrometer as a source and a detector mounted on a rotating arm. The angular acceptance of the spectrometer was reduced to a value lower than the angular width of the dip. The experimental data are indicated by circles; the lines show the theoretical results. An excellent agreement is obtained when the data are taken at ambient temperature, which supports our interpretation of the slight disagreement in Fig. 1 being due to the variation of index with temperature.

A surprising property of the emissivity patterns of Fig. 3 is that they depend strongly on the wavelength. This suggests that the emission spectra depend on the emission direction. This would be a manifestation of the Wolf effect[3,4]. To observe this effect, we have taken several spectra of the reflectivity of the surface at different angles. Fig. 4 shows experimental and theoretical spectra for different observation angles. The position of the peaks of emissivity (dips of reflectivity) depends strongly on the observation angle. It is important to emphasize that this property is not merely a scattering effect but is a consequence of the partial spatial coherence of the source. The value of the reflectivity is also remarkable. By ruling a grating onto a material which is essentially a mirror, we were able to produce a perfect absorber. This behaviour has already been observed for metallic gratings and attributed to the resonant excitation of surface plasmons. This is the first time, to our knowledge, that total absorption in the infrared owing to excitation of surface-phonon polaritons has been reported.

In order to prove experimentally the role of the surface wave, we have done spectral measurements of the emissivity for *s*- and *p*-polarization. The peaks are never observed for *s*-polarization nor for *p*-polarization in the spectral region where surface waves cannot exist. In order to characterize quantitatively the role of the surface waves, we have obtained the dispersion relation from reflectivity measurements[6]. The results are displayed in Fig. 5 and compared with theory. We note that the interaction of the surface wave with the grating produces the aperture of a gap close to the band edge. Figure 5 shows that our experiment allows us to directly see surface-phonon polaritons. It also yields additional insight into the Wolf-effect[3,4] mechanism. Emission of infrared light has already been used to study surface excitations, but using prisms to couple the surface waves to propagating modes[10].

We now discuss the physical origin of coherent thermal emission. We wish to understand how random thermal motion can generate a coherent current along the interface. The key lies in the coherent properties of surface waves (either surface-plasmon polaritons or surface-phonon polaritons) demonstrated in refs 1 and 2. Both are mechanical delocalized collective excitations involving charges. Surface-phonon polaritons are phonons in a polar material, whereas surface-plasmon polaritons are acoustical-type waves in an electron gas. In both cases, these waves have the following two properties: (1) they are mechanical modes of the system that can be resonantly excited; (2) they are charge-density waves, that is, they generate electromagnetic fields. Because these excitations are delocalized, so are the corresponding electromagnetic fields.

From a classical point of view, each volume element of the thermal source can be modelled by a random point-like source that excites an extended mode: the surface wave. This is similar to some extent to the emission of sound by a string of a piano. The source is a hammer that strikes the string at a particular point. Then the modes of the string are excited producing a vibration along the full length of the string. At that point of the analogy, as anyone can hear the vibrations of a piano string, we may wonder why the coherent electromagnetic surface waves are not usually observed. The reason is that surface modes have a wavevector larger than $2\pi/\lambda$ so that they are evanescent. Their effect is not seen in the far-field.

However, by ruling a grating on the interface, we are able to couple these surface modes to propagating modes. The relationship between the emission angle θ and the wavelength λ is simply given by the usual grating law

$$\frac{2\pi}{\lambda}\sin\theta = k_{\parallel} + p\frac{2\pi}{d}$$

where p is an integer and $k_{\parallel}$ is the wavevector of the surface wave. Thus, by modifying the characteristics of the surface profile, it is possible to modify the direction and the value of the emissivity of the surface at a given wavelength. It is also possible to modify the emission spectrum in a given direction. Such gratings can be used to design infrared sources with specific properties.

This may also have interesting applications such as modifying the radiative heat transfer for a given material. Indeed, we have demonstrated that a reflectivity of 94% can be reduced to almost zero in the infrared for SiC. This could also be done for glass, which

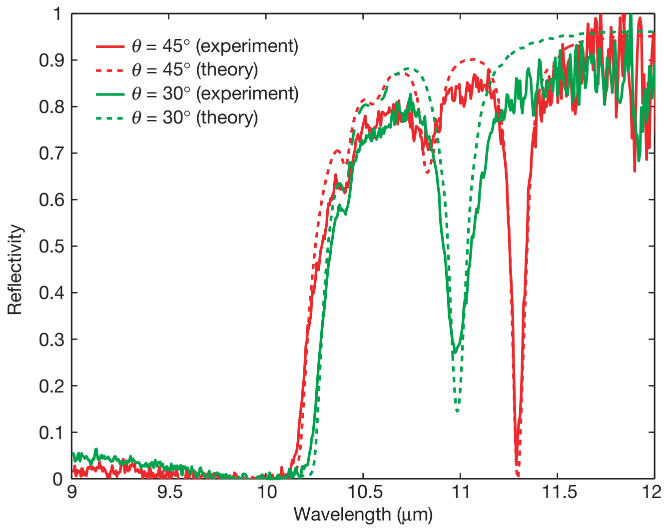

Figure 4 Comparison between measured and calculated spectral reflectivities of a SiC grating at room temperature. The incident light is *p*-polarized. The dip observed at 45° and $\lambda = 11.36\,\mu$m coincides with the emission peak observed in Figs 2 and 3. The figure shows clearly that the reflectivity spectra depend on the observation angle. Using Kirchhoff's law, it follows that the emission spectra depend on the observation angle. This is a manifestation of the Wolf effect[3,4].

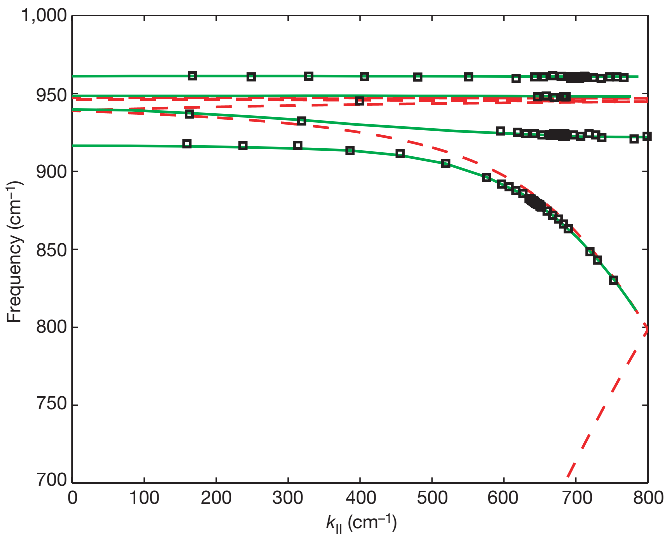

Figure 5 Dispersion relation wavevector, $\omega(k_{\parallel})$, of surface-phonon polaritons. Data points, experimental dispersion relation. Solid green curve, theoretical dispersion relation for the grating. Dotted red curve, theoretical dispersion relation for the flat surface. This figure explains the mechanism of the Wolf effect[3,4] for this particular source. The spatial coherence in the plane of the source is due to the presence of a surface wave. For a fixed frequency ω, it can be seen that there is only one possible wavevector $k_{\parallel}(\omega)$. Thus the spectral degree of coherence at ω oscillates[2] with a particular wavelength $2\pi/k_{\parallel}(\omega)$. When observing in the far field at an angle θ such that $ck_{\parallel}(\omega)/\omega = \sin\theta$ there is a strong contribution of the surface wave at frequency ω. By varying the observation angle, the frequency varies according to the dispersion relation of the surface wave. It is seen that the strong Wolf effect produced by this source is due to (1) the thermal excitation of surface waves which produce the spatial coherence and (2) the propagation in vacuum which selects one particular wavevector.

is a polar material that has a large reflectivity in the infrared owing to the presence of resonances. This would allow us to increase the radiative cooling of the material if the emission is enhanced in a region where absorption is low, because the atmosphere does not emit. Another promising application of our results is the possibility of modifying the heat transfer in the near-field. Materials that are separated by distances smaller than the typical wavelength exchange radiative energy through evanescent waves. When surface waves are resonantly excited, they provide the leading contribution[11]. Thus, the heat transfer is almost monochromatic. This may be used to enhance the efficiency of infrared photovoltaic cells[12]. □

Received 25 June; accepted 20 December 2001.

1. Shchegrov, A., Joulain, K., Carminati, R. & Greffet, J. J. Near-field spectral effects due to electromagnetic surface excitations. *Phys. Rev. Lett.* **85,** 1548–1551 (2000).
2. Carminati, R. & Greffet, J. J. Near-field effects in spatial coherence of thermal sources. *Phys. Rev. Lett.* **82,** 1660–1663 (1999).
3. Wolf, E. Non-cosmological red-shifts of spectral lines. *Nature* **326,** 363–365 (1987).
4. Wolf, E. & James, D. F. Correlation-induced spectral changes. *Rep. Prog. Phys.* **59,** 771–818 (1996).
5. Morris, G. M. & Faklis, D. Effects of source correlation on the spectrum of light. *Opt. Commun.* **62,** 5–11 (1987).
6. Le Gall, J., Olivier, M. & Greffet, J. J. Experimental and theoretical study of reflection and coherent thermal emission by a Sic grating supporting a surface photon polariton. *Phys. Rev. B* **55,** 10105–10114 (1997).
7. Hesketh, P. J., Zemel, J. N. & Gebhart, B. Organ pipe radiant modes of periodic micromachined silicon surfaces. *Nature* **325,** 549–551 (1986).
8. Mandel, L. & Wolf, E. *Optical Coherence and Quantum Optics.* Sec. 5.3 (Cambridge Univ. Press, New York, 1995).
9. Greffet, J. J. & Nieto-Vesperinas, M. Field theory for the generalized bidirectional reflectivity: derivation of Helmholtz's reciprocity principle and Kirchhoff's law. *J. Opt. Soc. Am. A* **10,** 2735–2744 (1998).
10. Zhizhin, G. N., Vinogradov, E. A., Moskalova, M. A. & Yakovlev, V. A. Applications of surface polaritons for vibrational spectroscopic studies of thin and very thin films. *Appl. Spectrosc. Rev.* **18,** 171–263 (1982).
11. Mulet, J. P., Joulain, K., Carminati, R. & Greffet, J. J. Nanoscale radiative heat transfer between a small particle and a plane surface. *Appl. Phys. Lett.* **78,** 2931–2933 (2001).
12. Whale, M. D. in *Proc. Conf. on 'Heat Transfer and Transport Phenomena in Microscale'* (ed. Celata, G. P.) 339–346 (Begell House, New York, 2000).

Competing interests statement

The authors declare that they have no competing financial interests.

Correspondence and requests for materials should be addressed to J.-J.G.
(e-mail: greffet@em2c.ecp.fr).

....

A general process for *in situ* formation of functional surface layers on ceramics

Toshihiro Ishikawa, Hiroyuki Yamaoka, Yoshikatsu Harada, Teruaki Fujii & Toshio Nagasawa

Ube Research Laboratory, Corporate Research & Development,
Ube Industries Ltd, 1978-5 Kogushi, Ube City, Yamaguchi 755-8633, Japan

....

Ceramics are often prepared with surface layers of different composition from the bulk[1,2], in order to impart a specific functionality to the surface or to act as a protective layer for the bulk material[3,4]. Here we describe a general process by which functional surface layers with a nanometre-scale compositional gradient can be readily formed during the production of bulk ceramic components. The basis of our approach is to incorporate selected low-molecular-mass additives into either the precursor polymer from which the ceramic forms, or the binder polymer used to prepare bulk components from ceramic powders. Thermal treatment of the resulting bodies leads to controlled phase separation ('bleed out') of the additives, analogous to the normally undesirable outward loss of low-molecular-mass components from some plastics[5–9]; subsequent calcination stabilizes the compositionally changed surface region, generating a functional surface layer. This approach is applicable to a wide range of materials and morphologies, and should find use in catalysts, composites and environmental barrier coatings.

To avoid the concentration of thermomechanical stress at the interface between the surface layer and the bulk material, many materials have been developed that have gradually varying properties as the distance into the material increases[10]. Such materials can contain gradients in morphology or in composition. Gradients in morphology can, for example, result in materials that have a graded distribution of pore sizes on a monolith of silica aerogel, and a type of integral plastic. These materials have been created by strictly controlling the vaporization of the volatile during the production process[11,12]. Gradients in chemical composition have been achieved, for example: (1) chemical vapour deposition[13,14], (2) powder methods such as slip cast or dry processing[15], (3) various coating methods[16], and (4) thermal chemical reaction[2,17]. Of these, (1) and (4) are relatively expensive, complicated and result in damage to bulk substrates. (2) and (3) produce stepped gradient structures, and it is difficult to control the thickness of each layer to less than 100 nm. Furthermore, most of these processes are not easily adapted to coating samples in the form of fibre bundles, fine powders or other materials with complicated shapes.

We have addressed the issue of establishing an inexpensive and widely applicable process for creating a material with a compositional gradient and excellent functionality. A schematic representative of our new *in situ* formation process for functional surface layers, which have a gradient-like structure towards the surface, is shown in Fig. 1. The important feature of our method is that the surface layer of the ceramic is not deposited on the substrate, but is formed during the production of the bulk ceramic. We confirmed that our process is applicable to any type of system as long as, in the green-body (that is, not-calcined) state, the system contains a resin and a low-molecular-mass additive that can be converted into a functional ceramic at high temperatures. Here, the resin is a type of precursor polymer (polycarbosilane, polycarbosilazane, polysilastyrene, methylchloropolysilane, and so on) or binder polymer used for preparing green bodies from ceramic powders[18]. Although the former case (using precursor polymers) is explained in detail in this Letter, the latter case using binder polymers was also confirmed by treating a Si_3N_4 body with a TiN surface layer. Si_3N_4 can exhibit excellent thermal stability and wear resistance in the high-speed machining of cast iron, but shows poor chemical wear resistance in the machining of steel[19]. In order to avoid this problem, TiN coating, by means of expensive chemical vapour deposition, has often been performed on previously prepared Si_3N_4 substrates. But if our process is appropriately applied, formation of the TiN surface layer could be achieved during the sintering process of the Si_3N_4 green body. In this case, titanium(IV) butoxide and polystyrene are used as the low-molecular-mass additive and binder polymer, respectively. By a combination of sufficient maturation (in air at 100 °C) and subsequent sintering (in NH_3+H_2+N_2 at 1,200 °C), Si_3N_4 covered with TiN is successfully produced. This technology would be very useful for producing ceramic materials with complicated shapes and various coating layers. Moreover, our process is advantageous for preparing precursor ceramics (particularly fine particles, thin fibrous ceramics and films). The systems to which our concept is applicable are shown in Fig. 1.

Here we give a detailed account of the results for the precursor ceramic obtained using polycarbosilane. Polycarbosilane $(-SiH(CH_3)-CH_2-)_n$ is a representative pre-ceramic polymer for preparing SiC ceramics—for example, Hi-Nicalon fibre[20] and Tyranno SA fibre[21]. Furthermore, oxide or nitride can also be produced from the polycarbosilane by firing in air or ammonia, respectively. Our new technology makes full use of the bleed-out

Definition and measurement of the local density of electromagnetic states close to an interface

K. Joulain, R. Carminati, J.-P. Mulet et J.-J. Greffet

Physical Review B, vol 68, pp245405 (2003)

PHYSICAL REVIEW B **68**, 245405 (2003)

Definition and measurement of the local density of electromagnetic states close to an interface

Karl Joulain,[1,2] Rémi Carminati,[2] Jean-Philippe Mulet,[2] and Jean-Jacques Greffet[2]
[1]*Laboratoire d'Études Thermiques, ENSMA, 1 Avenue Clément Ader, 86960 Futuroscope Cedex, France*
[2]*Laboratoire EM2C, Ecole Centrale Paris CNRS, Grande Voie des Vignes, 92295 Châtenay-Malabry, France*
(Received 2 July 2003; published 10 December 2003)

We propose in this article an unambiguous definition of the local density of electromagnetic states (LDOS) in a vacuum near an interface in equilibrium at temperature *T*. We show that the LDOS depends only on the electric-field Green function of the system but does not reduce in general to the trace of its imaginary part, as often is used in the literature. We illustrate this result by a study of the LDOS variations with the distance to an interface and point out deviations from the standard definition. We show nevertheless that this definition remains correct at frequencies close to the material resonances such as surface polaritons. We also study the feasibility of detecting such a LDOS with apertureless scanning near-field optical microscope (SNOM) techniques. We first show that a thermal near-field emission spectrum above a sample should be detectable and that this measurement could give access to the electromagnetic LDOS. It is further shown that the apertureless SNOM is the optical analog of the scanning tunneling microscope, which is known to detect the electronic LDOS. We also discuss some recent SNOM experiments aimed at detecting the electromagnetic LDOS.

DOI: 10.1103/PhysRevB.68.245405 PACS number(s): 73.20.Mf, 03.50.De, 07.79.Fc, 44.40.+a

I. INTRODUCTION

The density of states (DOS) is a fundamental quantity from which many macroscopic quantities can be derived. Indeed, once the DOS is known, the partition function can be computed yielding the free energy of the system. It follows that the heat capacity, forces, etc., can be derived. A well-known example of a macroscopic quantity that follows immediately from the knowledge of the electromagnetic DOS is the Casimir force.[1,2] Other examples are shear forces[3] and heat transfer[4] between two semi-infinite dielectrics. Recently, it has been shown that unexpected coherence properties of thermal emission at short distances from an interface separating vacuum from a polar material are due to the contribution to the density of states of resonant surface waves.[5] It has also been shown that the Casimir force can be interpreted as essentially due to the surface wave contribution to the DOS.[1,2]

Calculating and measuring the local density of states (LDOS) in the vicinity of an interface separating a real material from a vacuum is therefore necessary to understand many problems currently studied. The density of states is usually derived from the Green function of the system by taking the imaginary part of the Green function.[6,7] In solid-state physics, the electronic local density of states at the Fermi energy at the surface of a metal can be measured with a scanning tunneling microscope (STM).[8] This has been proved by several experiments, in particular the so-called quantum corral experiments.[9] Although one can formally generalize the definition of the electromagnetic LDOS by using the trace of the imaginary part of the Green tensor,[10] it turns out that this definition does not yield the correct equilibrium electromagnetic energy density.

Recently, it has been shown theoretically that the STM and the scanning near-field optical microscope (SNOM) have strong analogies.[11] More precisely, in the weak tip-sample coupling limit, it was demonstrated that a unified formalism can be used to relate the STM signal to the electronic LDOS and the SNOM signal to electromagnetic LDOS. SNOM instruments[12] have been used to perform different kinds of emission spectroscopy, such as luminescence,[13] Raman spectroscopy,[14] or two-photon fluorescence.[15] For detection of infrared light, apertureless techniques[16] have shown their reliability for imaging[17] as well as for vibrational spectroscopy on molecules.[18] Moreover, recent calculations and experiments have shown that an optical analog of the quantum corral could be designed, and that the measured SNOM images on such a structure present strong similarities with the calculated electromagnetic LDOS.[19,20] These results suggest that the electromagnetic LDOS could be directly measured with a SNOM.

The purpose of this article is to show how the electromagnetic LDOS can be related to the electric Green function, and to discuss possible measurements of the LDOS in SNOM. We first introduce a general definition of the electromagnetic LDOS in a vacuum in the presence of materials, possibly lossy objects. Then, we show that under some well-defined circumstances, the LDOS is proportional to the imaginary part of the trace of the electrical Green function. The results are illustrated by calculating the LDOS above a metal surface. We show next that the signal detected with a SNOM measuring the thermally emitted field near a heated body is closely related to the LDOS and conclude that the natural experiment to detect the LDOS is to perform a near-field thermal emission spectrum. We discuss the influence of the tip shape. We also discuss whether standard SNOM measurements using an external illumination can detect the electromagnetic LDOS.[19,20]

II. LOCAL DENSITY OF ELECTROMAGNETIC STATES IN A VACUUM

As pointed out in the Introduction, the LDOS is often defined as being the imaginary part of the trace of the electric-field Green dyadic. This approach seems to give a correct description in some cases,[19,20] but to our knowledge this definition has never been derived properly for electromagnetic fields in a general system that includes an arbitrary distribution of matter with possible losses. The aim of this section is to propose an unambiguous definition of the LDOS.

Let us consider a system at equilibrium temperature T. Using statistical physics, we write the electromagnetic energy $U(\omega)$ at a given *positive* frequency ω, as the product of the DOS by the mean energy of a state at temperature T, so that

$$U(\omega)=\rho(\omega)\frac{\hbar\omega}{\exp(\hbar\omega/k_BT)-1}, \tag{1}$$

where $2\pi\hbar$ is Planck's constant and k_B is Boltzmann's constant. We can now introduce[21] a *local* density of states by starting with the local density of electromagnetic energy $U(\mathbf{r},\omega)$ at a given point $\mathbf{r}$ in space and at a given frequency ω. This can be written by definition of the LDOS $\rho(\mathbf{r},\omega)$ as

$$U(\mathbf{r},\omega)=\rho(\mathbf{r},\omega)\frac{\hbar\omega}{\exp(\hbar\omega/k_BT)-1}. \tag{2}$$

The density of electromagnetic energy is the sum of the electric energy and of the magnetic energy. At equilibrium, it can be calculated using the system Green function and the fluctuation-dissipation theorem. Let us introduce the electric- and magnetic-field correlation functions for a stationary system:

$$\begin{aligned}\mathcal{E}_{ij}(\mathbf{r},\mathbf{r}',t-t')&=\frac{1}{2\pi}\int d\omega\,\mathcal{E}_{ij}(\mathbf{r},\mathbf{r}',\omega)e^{-i\omega(t-t')}\\&=\langle E_i(\mathbf{r},t)E_j^*(\mathbf{r}',t')\rangle,\end{aligned} \tag{3}$$

$$\begin{aligned}\mathcal{H}_{ij}(\mathbf{r},\mathbf{r}',t-t')&=\frac{1}{2\pi}\int d\omega\,\mathcal{H}_{ij}(\mathbf{r},\mathbf{r}',\omega)e^{-i\omega(t-t')}\\&=\langle H_i(\mathbf{r},t)H_j^*(\mathbf{r}',t')\rangle.\end{aligned} \tag{4}$$

Note that here the integration over ω goes from $-\infty$ to ∞. If $\mathbf{j}(\mathbf{r})$ is the electric current density in the system, the electric field reads $\mathbf{E}(\mathbf{r},\omega)=i\mu_0\omega\int\overleftrightarrow{\mathbf{G}}^E(\mathbf{r},\mathbf{r}',\omega)\cdot\mathbf{j}(\mathbf{r}')d^3\mathbf{r}'$. In the same way, the magnetic field is related to the density of magnetic currents $\mathbf{m}(\mathbf{r})$ by $\mathbf{H}(\mathbf{r},\omega)=\int\overleftrightarrow{\mathbf{G}}^H(\mathbf{r},\mathbf{r}',\omega)\mathbf{m}(\mathbf{r}')d^3\mathbf{r}'$. In these two expressions, $\overleftrightarrow{\mathbf{G}}^E$ and $\overleftrightarrow{\mathbf{G}}^H$ are the dyadic Green functions of the electric and magnetic field, respectively. The fluctuation-dissipation theorem yields[22,23]

$$\mathcal{E}_{ij}(\mathbf{r},\mathbf{r}',\omega)=\frac{\hbar\omega}{[\exp(\hbar\omega/k_BT)-1]}\frac{\mu_0\omega}{2\pi}\operatorname{Im}G_{ij}^E(\mathbf{r},\mathbf{r}',\omega), \tag{5}$$

$$\mathcal{H}_{ij}(\mathbf{r},\mathbf{r}',\omega)=\frac{\hbar\omega}{[\exp(\hbar\omega/k_BT)-1]}\frac{\epsilon_0\omega}{2\pi}\operatorname{Im}G_{ij}^H(\mathbf{r},\mathbf{r}',\omega). \tag{6}$$

If one considers only the positive frequencies,

$$U(\mathbf{r},\omega)=4\left((\epsilon_0/2)\sum_{i=1,3}\mathcal{E}_{ii}(\mathbf{r},\mathbf{r},\omega)+(\mu_0/2)\sum_{i=1,3}\mathcal{H}_{ii}(\mathbf{r},\mathbf{r},\omega)\right)$$

so that

$$U(\mathbf{r},\omega)=\frac{\hbar\omega}{[\exp(\hbar\omega/k_BT)-1]}\frac{\omega}{\pi c^2}\operatorname{Im}\operatorname{Tr}[\overleftrightarrow{\mathbf{G}}^E(\mathbf{r},\mathbf{r},\omega)+\overleftrightarrow{\mathbf{G}}^H(\mathbf{r},\mathbf{r},\omega)]. \tag{7}$$

It is important to note that the magnetic-field Green function and the electric-field Green function are not independent. In fact, one has

$$\frac{\omega^2}{c^2}\overleftrightarrow{\mathbf{G}}^H(\mathbf{r},\mathbf{r}',\omega)=[\boldsymbol{\nabla}_{\mathbf{r}}\times]\cdot\overleftrightarrow{\mathbf{G}}^E(\mathbf{r},\mathbf{r}',\omega)\cdot[\boldsymbol{\nabla}_{\mathbf{r}'}\times]. \tag{8}$$

A comparison of Eqs. (2) and (7) shows that the LDOS of the electromagnetic field reads

$$\rho(\mathbf{r},\omega)=\frac{\omega}{\pi c^2}\operatorname{Im}\operatorname{Tr}[\overleftrightarrow{\mathbf{G}}^E(\mathbf{r},\mathbf{r},\omega)+\overleftrightarrow{\mathbf{G}}^H(\mathbf{r},\mathbf{r},\omega)]=f(\overleftrightarrow{\mathbf{G}}^E) \tag{9}$$

in which $f(\overleftrightarrow{\mathbf{G}}^E)$ is an operator that will be discussed more precisely in the next section.

III. DISCUSSION

The goal of this section is to study the LDOS behavior for some well-characterized physical situations, based on the result in Eq. (9).

A. Vacuum

In a vacuum, the imaginary part of the trace of the electric- and magnetic-field Green functions are equal. Indeed, the electric- and magnetic-field Green functions obey the same equations and have the same boundary conditions in this case (radiation condition at infinity). In a vacuum, the LDOS is thus obtained by considering the electric-field contribution only, and multiplying the result by a factor of 2. One recovers the familiar result

$$\rho_v(\mathbf{r},\omega)=\rho_v(\omega)=\frac{\omega^2}{\pi^2c^3}, \tag{10}$$

which shows in particular that the LDOS is homogeneous and isotropic.

B. Plane interface

Let us consider a plane interface separating a vacuum (medium 1, corresponding to the upper half-space) from a semi-infinite material (medium 2, corresponding to the lower half-space) characterized by its complex dielectric constant $\epsilon_2(\omega)$ (the material is assumed to be linear, isotropic, and nonmagnetic). Inserting the expressions of the electric and magnetic-field Green functions for this geometry[24] into Eq. (9), one finds the expression of the LDOS at a given frequency and at a given height z above the interface in vacuum. In this situation, the magnetic- and electric-field Green functions are not the same. This is due to the boundary conditions at the interface which are different for the electric and magnetic fields. In order to discuss the origin of the different contributions to the LDOS, we define and calculate an electric LDOS $[\rho^E(z,\omega)]$ due to the electric-field Green function only, and a magnetic LDOS $[\rho^H(z,\omega)]$ due to the magnetic-field Green function only. The total LDOS $\rho^E(z,\omega)=\rho^E(z,\omega)+\rho^H(z,\omega)$ has a clear physical meaning unlike $\rho^E(z,\omega)$ and $\rho^H(z,\omega)$. Note that $\rho^E(z,\omega)$ is the quantity that is usually calculated and considered to be the true LDOS. In the geometry considered here, the expression of the electric LDOS is[25]

$$\rho^E(z,\omega)=\frac{\rho_v(\omega)}{4}\left\{\int_0^1\frac{\kappa\,d\kappa}{p}\left[2+\mathrm{Re}(r_{12}^s e^{2ip\omega z/c})+\mathrm{Re}(r_{12}^p e^{2ip\omega z/c})(2\kappa^2-1)\right]+\int_1^\infty\frac{\kappa\,d\kappa}{|p|}\left[\mathrm{Im}(r_{12}^s)+(2\kappa^2-1)\mathrm{Im}(r_{12}^p)\right]e^{-2|p|\omega z/c}\right\}. \tag{11}$$

This expression is actually a summation over all possible plane waves with wave number $\mathbf{k}=\omega/c(\kappa,p)$, where $p=\sqrt{1-\kappa^2}$ if $\kappa\leqslant 1$ and $p=i\sqrt{\kappa^2-1}$ if $\kappa>1$. r_{12}^s and r_{12}^p are the Fresnel reflection factors between media 1 and 2 in s and p polarizations, respectively, for a parallel wave vector $\omega\kappa/c$.[26] $0\leqslant\kappa\leqslant 1$ corresponds to propagating waves, whereas $\kappa>1$ corresponds to evanescent waves. A similar expression for the magnetic LDOS can be obtained:

$$\rho^H(z,\omega)=\frac{\rho_v(\omega)}{4}\left\{\int_0^1\frac{\kappa\,d\kappa}{p}\left[2+\mathrm{Re}(r_{12}^p e^{2ip\omega z/c})+\mathrm{Re}(r_{12}^s e^{2ip\omega z/c})(2\kappa^2-1)\right]+\int_1^\infty\frac{\kappa\,d\kappa}{|p|}\left[\mathrm{Im}(r_{12}^p)+(2\kappa^2-1)\mathrm{Im}(r_{12}^s)\right]e^{-2|p|\omega z/c}\right\}. \tag{12}$$

Adding the electric and magnetic contributions yields the total LDOS:

$$\rho(z,\omega)=\frac{\rho_v(\omega)}{2}\left\{\int_0^1\frac{\kappa\,d\kappa}{p}\{2+\kappa^2[\mathrm{Re}(r_{12}^s e^{2ip\omega z/c})+\mathrm{Re}(r_{12}^p e^{2ip\omega z/c})]\}+\int_1^\infty\frac{\kappa^3 d\kappa}{|p|}\left[\mathrm{Im}(r_{12}^s)+\mathrm{Im}(r_{12}^p)\right]e^{-2|p|\omega z/c}\right\}. \tag{13}$$

It is important to note that the electric and magnetic LDOS have similar expressions, but are in general not equal. The expression of $\rho^H(\mathbf{r})$ is obtained by exchanging the s and p polarizations in the expression of $\rho^E(\mathbf{r})$. As a result, the two polarizations have a symmetric role in the expression of the total LDOS $\rho(\mathbf{r})$.

The vacuum situation can be recovered from the previous expression by setting the values of the Fresnel reflection factors to zero. The same result is also obtained by taking the LDOS at large distance from the interface, i.e., for $z\gg\lambda$ where $\lambda=2\pi c/\omega$ is the wavelength. This means that at large distances, the interface does not perturb the density of electromagnetic states. In fact, $e^{-2|p|\omega z/c}$ becomes negligible for the evanescent waves and $e^{2ip\omega z/c}$ is a rapidly oscillating function for the propagating waves when integrating over κ. The result is that all the terms containing exponential do not contribute to the integral giving the LDOS in the vacuum.

Conversely, at short distance from the interface, $\rho(\mathbf{r},\omega)$ is drastically modified compared to its free-space value. Equations (11)–(13) show that the Fresnel coefficients and therefore the nature of the material play a crucial role in this modification. For example, as pointed out by Agarwal,[23] in the case of a perfectly conducting surface, the contribution of the electric and magnetic LDOS vanish, except for their free-space contribution. In this particular case, one also retrieves the vacuum result.

We now focus our attention on real materials such as metals and dielectrics. We first calculate $\rho(\omega)$ for aluminum at different heights. Aluminum is a metal whose dielectric constant is well described by a Drude model for near-uv, visible, and near-ir frequencies:[27]

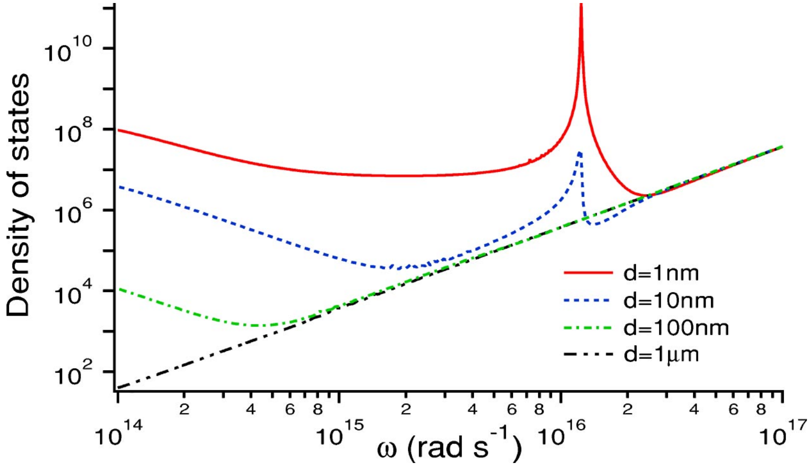

FIG. 1. LDOS versus frequency at different heights above a semi-infinite sample of aluminum.

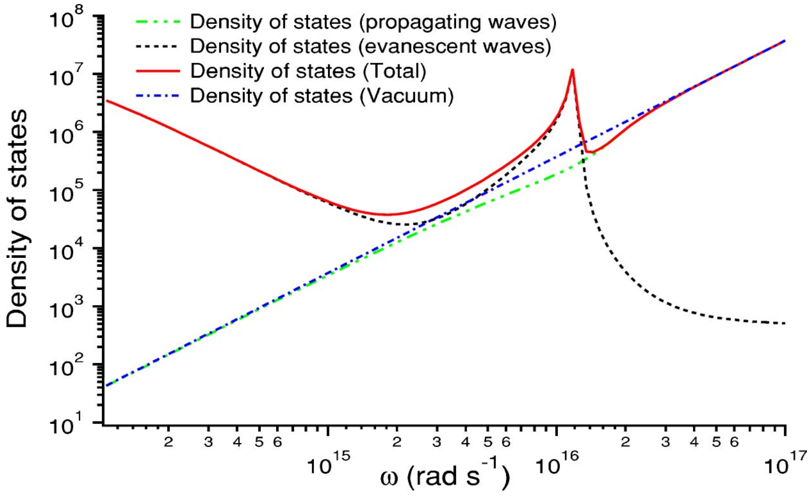

FIG. 2. Density of states contributions due to the propagating and evanescent waves compared to the total density of states and the vacuum density of states. These quantities are calculated above an aluminum sample at a distance of 10 nm.

$$\epsilon(\omega)=1-\frac{\omega_p^2}{\omega(\omega+i\gamma)} \tag{14}$$

with $\omega_p=1.747\times10^{16}$ rad s^{-1} and $\gamma=7.596\times10^{13}$ rad s^{-1}.

We plotted in Fig. 1 the LDOS $\rho(\mathbf{r},\omega)$ in the near-uv–near-ir frequency domain at four different heights. We first note that the LDOS increases drastically when the distance to the material is reduced. As discussed in the previous paragraph, at a large distance from the material, one retrieves the vacuum density of states. Note that at a given distance, it is always possible to find a sufficiently high frequency for which the corresponding wavelength is small compared to the distance so that a far-field situation is retrieved. When the distance to the material is reduced, additional modes are present: these are the evanescent modes that are confined close to the interface and that cannot be seen in the far field. Moreover, aluminum exhibits a resonance around $\omega=\omega_p/\sqrt{2}$. Below this frequency, the material supports resonant surface waves (surface-plasmon polaritons). Additional modes are therefore seen in the near field. This produces an increase of the LDOS close to the interface. The enhancement is particularly important at the resonant frequency that corresponds to $\mathrm{Re}[\epsilon(\omega)]=-1$. This behavior is analogous to that previously described in Ref. 21 for a SiC surface supporting surface-phonon polaritons. Also note that in the low frequency regime, the LDOS increases. Finally, Fig. 1 shows that it is possible to have a LDOS smaller than that of vacuum at some particular distances and frequencies. Figure 2 shows the contributions of propagating and evanescent waves to the LDOS above an aluminum sample at a distance of 10 nm. The propagating contribution is very similar to that of the vacuum LDOS. As expected, the evanescent contribution dominates at low frequency and around the surface-plasmon polariton resonance, where pure near-field contributions dominates.

We now turn to the comparison of $\rho(z,\omega)$ with the usual definition often encountered in the literature, which corresponds to $\rho^E(z,\omega)$. In Fig. 3 we plot ρ, ρ^E, and ρ^H above an aluminum surface at the distance $z=10$ nm. In this figure, it is possible to identify three different domains for the LDOS behavior. We note again that in the far-field situation (corresponding here to high frequencies, i.e., $\lambda/2\pi\ll z$), the LDOS reduces to the vacuum situation. In this case $\rho(z,\omega)=2\rho^E(z,\omega)=2\rho^H(z,\omega)$. Around the resonance, the LDOS is dominated by the electric-field Green contribution. Conversely, at low frequencies, $\rho^H(z,\omega)$ dominates. Thus, Fig. 3 shows that we have to be very careful when using the expression $\rho(z)=\rho^E(z,\omega)$. Above aluminum and at a distance $z=10$ nm, this approximation is only valid in a small range between $\omega=10^{16}$ rad s^{-1} and $\omega=1.5\times10^{16}$ rad s^{-1}.

C. Asymptotic form of the LDOS in the near field

In order to get more physical insight, we have calculated the asymptotic LDOS behavior in the three regimes mentioned above. As we have already seen, the far-field regime ($\lambda/2\pi\ll d$) corresponds to the vacuum case. To study the near-field situation, we focus on the evanescent contribution, as suggested by the results in Fig. 2. When $\lambda=2\pi c/\omega\gg z$, the exponential term $\exp(-|p|\omega z/c)$ is small only for $\kappa\gg\lambda/(4\pi z)\gg1$. In this (quasistatic) limit, the Fresnel reflection factors reduce to

$$\lim_{\kappa\to\infty} r_{12}^s=\frac{\epsilon-1}{4\kappa^2}, \tag{15}$$

$$\lim_{\kappa\to\infty} r_{12}^p=\frac{\epsilon-1}{\epsilon+1}. \tag{16}$$

Asymptotically, the expressions of $\rho^E(z,\omega)$ and $\rho^H(z,\omega)$ are

$$\rho^E(z,\omega)=\frac{\rho_v}{|\epsilon+1|^2}\frac{\epsilon''}{4k_0^3z^3}, \tag{17}$$

$$\rho^H(z,\omega)=\rho_v\left[\frac{\epsilon''}{16k_0z}+\frac{\epsilon''}{4|\epsilon+1|^2k_0z}\right]. \tag{18}$$

At a distance $z=10$ nm above an aluminum surface, these asymptotic expressions matches almost perfectly with the full evanescent contributions ($\kappa>1$) of ρ^E and ρ^H. These expressions also show that for a given frequency, one can always find a distance to the interface z below which the

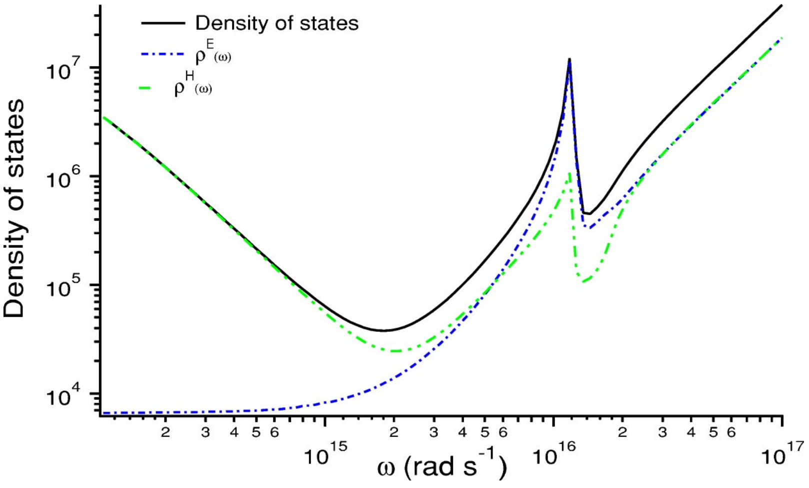

FIG. 3. LDOS at a distance $z=10$ nm above a semi-infinite aluminum sample. Comparison with $\rho^E(\omega)$ and $\rho^H(\omega)$.

dominant contribution to the LDOS will be the one due to the imaginary part of the electric-field Green function that varies like $(k_0 z)^{-3}$. But for aluminum at a distance $z=10$ nm, this is not the case for all frequencies. As we mentioned before, this is only true around the resonance. For example, for low frequencies, and for $z=10$ nm, the LDOS is actually dominated by $\rho_v \epsilon''/(16 k_0 z)$.

D. Spatial oscillations of the LDOS

Let us now focus on the LDOS variations at a given frequency versus the distance z to the interface. There are essentially three regimes. First, as discussed previously, at distances much larger than the wavelength the LDOS is given by the vacuum expression ρ_v. The second regime is observed close to the interface where oscillations are observed. Indeed, at a given frequency, each incident plane wave on the interface can interfere with its reflected counterpart. This generates an interference pattern with a fringe spacing that depends on the angle and the frequency. Upon adding the contributions of all the plane waves over angles, the oscillating structure disappears except close to the interface. This leads to oscillations around distances on the order of the wavelength. This phenomenon is the electromagnetic analog of Friedel oscillations that can be observed in the electronic density of states near the interfaces.[7,28] As soon as the distance becomes small compared to the wavelength, the phase factors $\exp(2ip\omega z/c)$ in Eq. (13) are equal to unity. For a highly reflecting material, the real part of the reflecting coefficients are negative so that the LDOS decreases while approaching the surface. These two regimes are clearly observed for aluminum in Fig. 4. The third regime is observed at small distances as seen in Fig. 4. The evanescent contribution dominates and ultimately the LDOS always increases as $1/z^3$, following the behavior found in Eq. (17). This is the usual quasistatic contribution that is always found at short distances.[26] At a frequency slightly smaller than the resonant frequency, surface waves are excited on the surface. These additional modes increase the LDOS according to an exponential law as seen in Fig. 5, a behavior which was already found for thermally emitted fields.[5,26] At low frequency, the LDOS dependance is given by Eq. (18). The $1/z$ magnetic term dominates because the $1/|\epsilon+1|^2$ takes large values. The $1/z^3$ contribution equals the $1/z$ contribution for distances much smaller than the nanometer scale, a distance for which the model is no longer valid.

The main results of this section can be summarized as follows. The LDOS of the electromagnetic field can be unambiguously and properly defined from the local density of

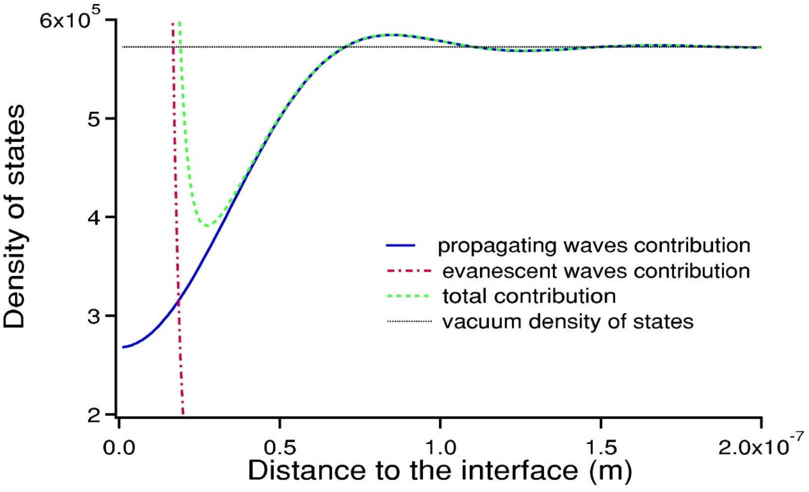

FIG. 4. LDOS versus the distance z from an aluminum-vacuum interface at the aluminum resonant frequency.

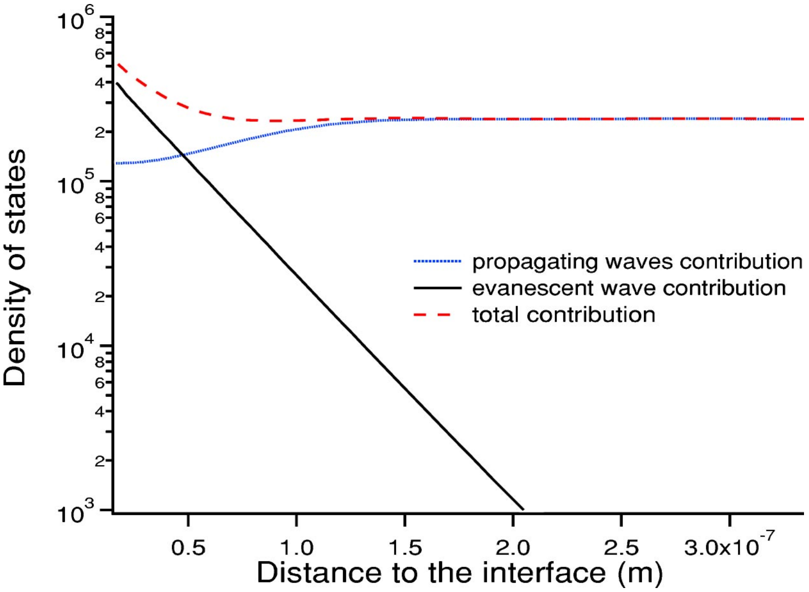

FIG. 5. LDOS versus the distance z from an aluminum-vacuum interface at frequency $\omega=8\times10^{15}$ rad s^{-1}.

electromagnetic energy in a vacuum above a sample at temperature T in equilibrium. The LDOS can always be written as a function of the electric-field Green function only, but is in general not proportional to the trace of its imaginary part. An additional term proportional to the trace of the imaginary part of the magnetic-field Green function is present in the far-field and at low frequencies. At short distances from the surface of a material supporting surface modes (plasmon or phonon-polaritons), the LDOS presents a resonance at frequencies such that $\mathrm{Re}[\epsilon(\omega)]=-1$. Close to this resonance, the approximation $\rho(z,\omega)=\rho^E(z,\omega)$ holds. In the next section, we discuss how the LDOS can be measured.

IV. MEASUREMENT OF THE LDOS

A. Near-field thermal emission spectroscopy with an apertureless SNOM

In this section we shall consider how the LDOS can be measured using a SNOM. We consider a frequency range where ρ is dominated by the electric contribution ρ^E. We note that for an isotropic dipole, a lifetime measurement yields the LDOS, as discussed by Wijnands *et al.*[10] However, if the dipole has a fixed orientation $\mathbf{x}$, the lifetime is proportional to G_{xx} and not to the trace of $\overleftrightarrow{\mathbf{G}}$. In order to achieve a direct SNOM measurement of the LDOS, we have to fulfill two requirements. First, all the modes must be excited. The simplest way to achieve this is to use the thermally emitted radiation by a body at equilibrium. The second requirement is to have a detector with a flat response to all modes. To analyze this problem we use a formalism recently introduced.

We consider a SNOM working in the detection mode, and detecting the electromagnetic field thermally emitted by a sample held at a temperature T. The system is depicted in Fig. 6. The microscope tip is scanned at close proximity of the interface separating the solid body from a vacuum. The signal is measured in the far field, by a point detector sensitive to the energy flux carried by the electromagnetic field. We assume that an analyzer is placed in front of the detector (polarized detection). The direction of polarization of the analyzer is along the direction of the vector $\mathbf{j}_{rec}$. If the solid angle $d\Omega$ under which the detector is seen from the tip is small (a condition we assume for simplicity), the signal $\langle S(\omega)\rangle$ at the detector, at a given frequency ω, reads

$$\langle S(\omega)\rangle=\frac{\epsilon_0 c}{2}|\mathbf{E}_d(\omega)|^2 r^2 d\Omega, \tag{19}$$

where ϵ_0 is the permittivity of vacuum, c is the speed of light in vacuum, r is the distance between the tip and the detector, and $\mathbf{E}_d$ is the electric field at the position of the detector. Let us denote by $\mathbf{E}_{expt}$ (experimental field) the thermal field, emitted by the sample, in the gap region between the tip and the sample. This field can be, in principle, calculated following the approach recently used in Refs. 5 and 21. For simplicity, we shall neglect the thermal emission from the tip itself (which is assumed to be cold) compared to that of the heated sample. But we do not need, at this stage, to assume a weak coupling between the tip and the sample. In particular, in the expressions derived in this section, the experimental field $\mathbf{E}_{expt}$ is the field emitted by the sample alone, in the presence of the detecting tip. Following the approach of Ref. 29 based on the reciprocity theorem of electromagnetism,[30] an exact relationship between the signal $\langle S(\omega)\rangle$ and the ex-

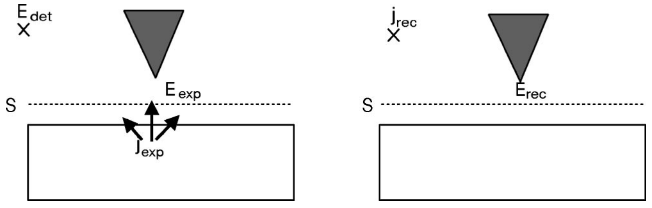

FIG. 6. Scheme of a scanning near-field optical microscope measuring a thermally emitted field. (a) Experimental situation. (b) Reciprocal (fictitious) situation.

perimental field $\mathbf{E}_{expt}$ can be established. It can be shown that the signal is given by an overlapping integral.

To proceed, one considers a fictitious situation in which the sample is removed, and a point source, represented by a monochromatic current $\mathbf{j}_{rec}$ oscillating at frequency ω, is placed at the position of the detector [see Fig. 6(b)]. The orientation of this reciprocal source is chosen along the direction of polarization of the analyzer used in the experimental situation. The field created around the tip in this reciprocal situation is denoted by $\mathbf{E}_{rec}$. Using the reciprocity theorem, the field at the detector can be written[29]

$$\mathbf{E}_d(\omega)\cdot\mathbf{j}_{rec}=\frac{-2i}{\mu_0\omega}\int_S\frac{\partial\mathbf{E}_{rec}(\mathbf{R},z,\omega)}{\partial z}\cdot\mathbf{E}_{expt}(\mathbf{R},z,\omega)d\mathbf{R}, \tag{20}$$

where the integration is performed in a plane $z=z_0$ between the tip and the sample and $\mathbf{R}=(x,y)$ are the coordinates along this plane. Equation (20) connects the field above the surface $\mathbf{E}_{expt}$ to the field in the detector $\mathbf{E}_d$ along the direction of the analyzer. Note that the reciprocal field $\mathbf{E}_{rec}$ encodes all the information about the detection system (tip and collection optics). Reporting the expression of the field at the detector (20) in Eq. (19), one finds the expression for the measured signal:

$$\langle S(\omega)\rangle=\frac{\epsilon_0 c}{8\pi^2}\int_S\int_S H_{ij}(\mathbf{R},\mathbf{R}',z,\omega)W_{ij}(\mathbf{R},\mathbf{R}',z,\omega)d\mathbf{R}\,d\mathbf{R}'. \tag{21}$$

Equation (21) establishes a linear relationship between the signal and the cross-spectral density tensor W_{ij} of the electric field defined by

$$\langle E_{expt,i}(\mathbf{R},z,\omega)E^*_{expt,j}(\mathbf{R}',z,\omega')\rangle = W_{ij}(\mathbf{R},\mathbf{R}',z,\omega)\,\delta(\omega-\omega'). \tag{22}$$

The response function H_{ij} only depends on the detection system (in particular the tip geometry and composition), and is given by

$$H_{ij}(\mathbf{R},\mathbf{R}',\omega)=\frac{\partial\mathbf{E}_{rec,i}(\mathbf{R},z,\omega)}{\partial z}\,\frac{\partial\mathbf{E}_{rec,j}(\mathbf{R}',z,\omega)}{\partial z}. \tag{23}$$

The cross-spectral density tensor W_{ij} describes the electric-field spatial correlation at a given frequency ω. For the thermal emission situation considered here, it depends only on the dielectric constant, on the geometry, and on the temperature of the sample.

Equation (21) is a general relationship between the signal and the cross-spectral density tensor. It is nonlocal and strongly polarization dependent. This shows that one does not measure in general a quantity that is proportional to $W_{kk}(\mathbf{r},\mathbf{r},\omega)$, and thus to $\rho^E(\mathbf{r},\omega)$. Nevertheless Eq. (21) suggested that $\rho^E(\mathbf{r},\omega)$ can be recovered if the response function H_{ij} is localized. Indeed, in that case the signal is proportional to $W_{ij}(\mathbf{R},\mathbf{R},z,\omega)$, thus to $\rho^E(\mathbf{r},\omega)$. As shown in the next section, a dipole tip (small sphere) would exhibit such a response function.

B. Detection of the LDOS by an ideal point-dipole probe

Let us see what would be measured by an ideal probe consisting of a single electric dipole described by a polarizability $\alpha(\omega)$. Note that such a probe was proposed as a model for the uncoated dielectric probe sometimes used in photon scanning tunneling microscopy (PSTM), and gives good qualitative prediction.[31] We assume that the thermally emitting medium occupies the half-space $z<0$, and that the probe is placed at a point $\mathbf{r}_t$. As in the preceding section, the detector placed in the far field measures the field intensity at a given point $\mathbf{r}_d$, through an analyzer whose polarization direction is along the vector $\mathbf{j}_{rec}$. In this case, Eq. (20) simplifies to read

$$\mathbf{j}_{rec}\cdot\mathbf{E}_d =\alpha(\omega)\frac{\omega^2}{4\pi c^2}\frac{\exp(ik|\mathbf{r}_d-\mathbf{r}_t|)}{|\mathbf{r}_d-\mathbf{r}_t|}\mathbf{j}_{rec}\cdot\overleftrightarrow{\mathbf{h}}(\mathbf{u}_d)\cdot\mathbf{E}_{expt}(\mathbf{r}_t,\omega), \tag{24}$$

where $k=\omega/c$, $\mathbf{u}_d=(\mathbf{r}_d-\mathbf{r}_t)/|\mathbf{r}_d-\mathbf{r}_t|$ is the unit vector pointing from the probe towards the detector and $\overleftrightarrow{\mathbf{h}}(\mathbf{u}_d)=\overleftrightarrow{\mathbf{I}}-\mathbf{u}_d\mathbf{u}_d$ is the dyadic operator that projects a vector on the direction transverse to $\mathbf{u}_d$, $\overleftrightarrow{\mathbf{I}}$ being the unit dyadic operator. The dyadic $\overleftrightarrow{\mathbf{h}}(\mathbf{u}_d)$ being symmetric, the scalar product in the right-hand side in Eq. (24) can be transformed using the equality $\mathbf{j}_{rec}\cdot\overleftrightarrow{\mathbf{h}}(\mathbf{u}_d)\cdot\mathbf{E}_{expt}(\mathbf{r}_t,\omega)=\mathbf{E}_{expt}(\mathbf{r}_t,\omega)\cdot\overleftrightarrow{\mathbf{h}}(\mathbf{u}_d)\cdot\mathbf{j}_{rec}$. Finally, the signal at the detector writes

$$\langle S\rangle=|\alpha(\omega)|^2\frac{\omega^4}{4\pi c^4}\mathrm{d}\Omega\sum_{i,j}A_iA_j^*W_{ij}(\mathbf{r}_t,\mathbf{r}_t,\omega), \tag{25}$$

where $\mathbf{A}=\overleftrightarrow{\mathbf{h}}(\mathbf{u}_d)\cdot\mathbf{j}_{rec}$ is a vector depending only on the detection conditions (direction and polarization). Note that if $\mathbf{j}_{rec}$ is transverse with respect to the direction $\mathbf{u}_d$, which is approximately the case in many experimental setups, then one simply has $\mathbf{A}=\mathbf{j}_{rec}$.

Equation (25) shows that with an ideal probe consisting of a signal dipole with an isotropic polarizability $\alpha(\omega)$, one locally measures the cross-spectral density tensor at the position $\mathbf{r}_t$ of the tip. Nevertheless, polarization properties of the detection still exist so that the trace of W_{ij}, and therefore $\rho^E(\mathbf{r},\omega)$, is not directly measured. A possibility of measuring the trace would be to measure a signal $\langle S_1\rangle$ in the direction normal to the surface with an unpolarized detection, and a signal $\langle S_2\rangle$ in the direction parallel to the surface, with an analyzer in the vertical direction. $\langle S_1\rangle$ would be a sum of the two signals obtained with $\mathbf{j}_{rec}$ along the x direction and along the y direction. $\langle S_2\rangle$ would correspond to the signal measured with $\mathbf{j}_{rec}$ along the z direction. Using Eq. (25), we see that the signal $\langle S\rangle=\langle S_1\rangle+\langle S_2\rangle$ is proportional to the trace $W_{kk}(\mathbf{r}_t,\mathbf{r}_t,\omega)$, and thus to $\rho^E(\mathbf{r},\omega)$. Measuring the thermal spectrum of emission with an apertureless SNOM whose probe is dipolar is thus a natural way to achieve the measurement of $\rho^E(\mathbf{r},\omega)$. Close to the material resonances, i.e., in the frequency domain where $\rho^E(\mathbf{r},\omega)$ matches $\rho(\mathbf{r},\omega)$, such a near-field thermal emission spectrum gives the electromagnetic LDOS.

C. Analogy with scanning (electron) tunneling microscopy

The result in this section shows that a SNOM measuring the thermally emitted field with a dipole probe (for example, a sphere much smaller than the existing wavelengths) measures the electromagnetic LDOS of the sample in the frequency range situated around the resonant pulsation. As discussed above, the measured LDOS is that of the modes that can be excited in the thermal emission process in a cold vacuum. This result was obtained from Eq. (20) assuming a weak tip-sample coupling, i.e., the experimental field is assumed to be the same with or without the tip.

The same result could be obtained starting from the generalized Bardeen formula derived in Ref. 11. Using this formalism for a dipole probe, one also ends up with Eq. (25), which explicitly shows the linear relationship between the signal and $\rho^E(\mathbf{r},\omega)$. This derivation is exactly the same as that used in the Tersoff-Hamann theory of the STM.[8] This theory showed, in the weak tip-sample coupling limit, that the electron-tunneling current measured in STM was proportional to the electronic LDOS of the sample, at the tip position, and at the Fermi energy. This result, although obtained under some approximations, was a breakthrough in understanding the STM signal. In the case of near-field optics, the present discussion, together with the use of the generalized Bardeen formula,[11] shows that under similar approximations, a SNOM using an ideal dipole probe and measuring the field thermally emitted by the sample is the real optical analog to the electron STM. We believe that this situation provides for SNOM a great potential for local solid-surface spectroscopy, along the directions opened by STM.

D. Could the LDOS be detected by standard SNOM techniques?

Before concluding, we will discuss the ability of standard SNOM techniques (by ‘‘standard’’ we mean techniques using laser-light illumination) to image the electromagnetic LDOS close to a sample. Recent experiments[32] have shown that an *illumination-mode* SNOM using metal-coated tips and working in transmission produce images that reproduce calculated maps of $\rho^E(\mathbf{r},\omega)$ (which is the adopted definition of the LDOS in this experimental work; see also Ref. 19). We shall now show that this operating mode bears strong similarities to that corresponding to a SNOM working in *collection mode*, and measuring thermally emitted fields. This will explain why the images reproduce (at least qualitatively) the electric LDOS $\rho^E(\mathbf{r},\omega)$.

Let us first consider a collection-mode technique, in which the sample (assumed to be transparent) is illuminated in transmission by a monochromatic laser with frequency ω, and the near-field light is collected by a local probe. If we assume the illuminating light to be spatially incoherent and isotropic in the lower half-space (with all incident directions included), then this illumination is similar to that produced by thermal fluctuations (except that only the modes corresponding to the frequency ω are actually excited). Note that this mode of illumination corresponds to that proposed in Ref. 33. This similarity, together with the discussion in the preceding paragraph, allows us to conclude that under these operating conditions, a collection-mode SNOM would produce images that closely resemble the electric LDOS $\rho^E(\mathbf{r},\omega)$.

We now turn to the discussion of images produced using an illumination-mode SNOM as used in Ref. 20. The use of the reciprocity theorem allows us to derive an equivalence between illumination and collection-mode configurations, as shown in Ref. 34. Starting from the collection-mode instrument described above, the reciprocal illumination-mode configuration corresponds to a SNOM working in transmission, the light being collected by an integrating sphere over all possible transmission directions (including those below and above the critical angle). Under such conditions, the illumination-mode SNOM produces exactly the same image as the collection-mode SNOM using isotropic, spatially incoherent, and monochromatic illumination. This explains why this instrument is able to produce images that closely follow the electric LDOS $\rho^E(\mathbf{r},\omega)$. Finally, note that in Ref. 20, the transmitted light is collected above the critical angle only, which in principle should be a drawback regarding the LDOS imaging. In these experiments, it seems that the interpretation of the images as maps of the electric LDOS remains nevertheless qualitatively correct, which shows that in this case, the main contribution to the LDOS comes from modes with wave vector corresponding to propagation directions above the critical angle.

V. CONCLUSION

In this paper, we have introduced a definition of the electromagnetic LDOS $\rho(\mathbf{r},\omega)$. We have shown that it is fully determined by the electric-field Green function, but that in general it does not reduce to the trace of its imaginary part $\rho^E(\mathbf{r},\omega)$. We have studied the LDOS variations versus the distance to a material surface and have explicitly shown examples in which the LDOS deviates from $\rho^E(\mathbf{r},\omega)$. Nevertheless, we have shown that around the material resonances (surface polaritons), the near-field LDOS reduces to $\rho^E(\mathbf{r},\omega)$. Measuring the LDOS with an apertureless SNOM using a point-dipole tip should be feasible. The principle of the measurement is to record a near-field thermal emission spectrum. Under such conditions, the instrument behaves as an optical analog of the STM, in the weak-coupling regime, which is known to measure the electronic LDOS on a metal surface. Finally, we have discussed recent standard SNOM experiments in which the LDOS seems to be qualitatively measured. Using general arguments, we have discussed the relevance of such measurements and compared them to measurements based on thermal-emission spectroscopy.

ACKNOWLEDGMENTS

We thank Y. De Wilde, F. Formanek, and A.C. Boccara for helpful discussions.

APPENDIX: CALCULATION OF THE FIELD AT THE DETECTOR FOR AN IDEAL POINT-DIPOLE PROBE

Let $\mathbf{e}_{rec}(\mathbf{K})$ and $\mathbf{e}_{expt}(\mathbf{K})$ be the two-dimensional Fourier component of $\mathbf{E}_{rec}(\mathbf{r})$ and $\mathbf{E}_{expt}(\mathbf{r})$. In the configuration chosen in our problem the reciprocal field propagates to the negative z whereas the experimental fields propagates to the positive z. Thus

$$\mathbf{E}_{rec}(\mathbf{r})=\int \mathbf{e}_{rec}(\mathbf{K})\exp\{i[\mathbf{K}\cdot\mathbf{R}-\gamma(\mathbf{K})z]\}d\mathbf{K}, \quad \text{(A1)}$$

$$\mathbf{E}_{expt}(\mathbf{r})=\int \mathbf{e}_{expt}(\mathbf{K})\exp\{i[\mathbf{K}\cdot\mathbf{R}+\gamma(\mathbf{K})z]\}d\mathbf{K}, \quad \text{(A2)}$$

where $\gamma(\mathbf{K})=\sqrt{\omega^2/c^2-K^2}$. Putting Eqs. (A1) and (A2) into Eq. (20) gives

$$\mathbf{E}_d(\omega)\cdot\mathbf{j}_{rec}=-\frac{8\pi^2}{\omega\mu_0}\int \gamma(\mathbf{K})\mathbf{e}_{rec}(-\mathbf{K})\cdot\mathbf{e}_{expt}(\mathbf{K})d\mathbf{K}. \quad \text{(A3)}$$

$\mathbf{e}_{expt}(K)$ can be evaluated by calculating the field $\mathbf{E}_{expt}(\mathbf{r})$. This last field is the field radiated by the reciprocal current $\mathbf{j}_{rec}$ and diffused by the ideal probe. It can also be seen as the field radiated by the dipole induced at the position $\mathbf{r}_t=(\mathbf{R}_t,z_t)$ of the probe. If $\mathbf{p}$ is the dipole induced at the position of the ideal probe, the reciprocal field at a position situated below the probe is written

$$\begin{aligned}\mathbf{E}_{rec}(\mathbf{r})&=\mu_0\omega^2\overleftrightarrow{\mathbf{G}}(\mathbf{r},\mathbf{r}_t)\cdot\mathbf{p}\\ &=\frac{i\mu_0\omega^2}{8\pi^2}\int\frac{d^2Ke^{i[\mathbf{K}\cdot(\mathbf{R}-\mathbf{R}_t)+\gamma(z_t-z)]}}{\gamma}\left[\overleftrightarrow{\mathbf{I}}-\frac{\mathbf{kk}}{k_0^2}\right]\cdot\mathbf{p},\end{aligned} \quad \text{(A4)}$$

where $k_0^2=\omega^2/c^2$. Comparing this expression and Eq. (A1), then

$$\mathbf{e}_{rec}(\mathbf{K})=\frac{i\mu_0\omega^2}{8\pi^2\gamma(\mathbf{K})}e^{i[-\mathbf{K}\cdot\mathbf{R}_t+\gamma(\mathbf{K})z_t]}\overleftrightarrow{\mathbf{h}}(\mathbf{k}^-)\cdot\mathbf{p}, \quad \text{(A5)}$$

where $\mathbf{k}^-=(\mathbf{K},-\gamma)$. Furthermore, using the fact that $\overleftrightarrow{\mathbf{h}}(\mathbf{k})=\overleftrightarrow{\mathbf{h}}(-\mathbf{k})$ and defining $\mathbf{k}^+=(\mathbf{K},\gamma)$,

$$\mathbf{e}_{rec}(-\mathbf{K})=\frac{i\mu_0\omega^2}{8\pi^2\gamma}e^{i(\mathbf{K}\cdot\mathbf{R}_t+\gamma z_t)}\overleftrightarrow{\mathbf{h}}(\mathbf{k}^+)\cdot\mathbf{p}. \quad \text{(A6)}$$

Let us denote $\mathbf{E}(\mathbf{j}_{rec}\rightarrow\mathbf{r}_t)$ the field radiated by the reciprocal current in $\mathbf{r}_t$. The dipole induced is then written $\mathbf{p}=\alpha(\omega)\epsilon_0\mathbf{E}(\mathbf{j}_{rec}\rightarrow\mathbf{r}_t)$ and

$$\mathbf{E}(\mathbf{j}_{rec}\rightarrow\mathbf{r}_t)=\frac{i\omega\mu_0}{4\pi}\frac{e^{i|\mathbf{r}_d-\mathbf{r}_t|}}{|\mathbf{r}_d-\mathbf{r}_t|}\overleftrightarrow{\mathbf{h}}(\mathbf{u}_d)\cdot\mathbf{j}_{rec}. \quad \text{(A7)}$$

Using the fact that for all dyadic $\overleftrightarrow{\mathbf{A}}$ and for all vectors $\mathbf{a}$ and $\mathbf{b}$,

$$[\overleftrightarrow{\mathbf{A}}\cdot\mathbf{a}]\cdot\mathbf{b}=\mathbf{a}\cdot[\overleftrightarrow{\mathbf{A}}^T\cdot\mathbf{b}] \quad \text{(A8)}$$

that $\overleftrightarrow{\mathbf{h}}$ is a symmetric dyadic ($\overleftrightarrow{\mathbf{h}}=\overleftrightarrow{\mathbf{h}}^T$), that $\mathbf{e}_{expt}(\mathbf{K})$ is transverse to the direction $\mathbf{k}^+$ and the definition of $\mathbf{E}_{expt}(\mathbf{r})$,

$$\begin{aligned}&\mathbf{j}_{rec}\cdot\mathbf{E}_d\\ &=\alpha(\omega)\frac{\omega^2}{4\pi c^2}\frac{\exp(ik|\mathbf{r}_d-\mathbf{r}_t|)}{|\mathbf{r}_d-\mathbf{r}_t|}\mathbf{j}_{rec}\cdot\overleftrightarrow{\mathbf{h}}(\mathbf{u}_d)\cdot\mathbf{E}_{expt}(\mathbf{r}_t,\omega).\end{aligned} \quad \text{(A9)}$$

---

[1] N.G. Van Kampen, B.R.A. Nijboer, and K. Schram, Phys. Lett. A **26**, 307 (1968).

[2] E. Gerlach, Phys. Rev. B **4**, 393 (1971).

[3] J.-B. Pendry, J. Phys.: Condens. Matter **9**, 10301 (1997).

[4] J.P. Mulet, K. Joulain, R. Carminati, and J.-J. Greffet, Microscale Thermophys. Eng. **6**, 209-222 (2002).

[5] R. Carminati and J.-J. Greffet, Phys. Rev. Lett. **82**, 1660 (1999).

[6] E. N. Economou, *Green's Functions in Quantum Physics* (Springer, Berlin, 1983).

[7] W.A. Harrison, *Solid State Theory* (Dover, New York, 1980).

[8] J. Tersoff and D.R. Hamann, Phys. Rev. B **31**, 805 (1985).

[9] M.F. Crommie, C.P. Lutz, and D.M. Eigler, Science **262**, 218 (1993).

[10] F. Wijnands, J.B. Pendry, F.J. Garcia-Vidal, P.J. Roberts, and L. Martin Moreno, Opt. Quantum Electron. **29**, 199 (1997).

[11] R. Carminati and J.J. Sáenz, Phys. Rev. Lett. **84**, 5156 (2000).

[12] *Near-Field Optics*, edited by D.W. Pohl and D. Courjon (Kluwer, Dordrecht, 1993); M.A. Paesler and P.J. Moyer, *Near Field Optics: Theory, Instrumentation and Applications* (Wiley-Interscience, New York, 1996); *Near-field Nano/Atom Optics and Technology*, edited by M. Ohtsu (Springer-Verlag, Tokyo, 1998).

[13] P.J. Moyer, C.L. Jahnckle, M.A. Paesler, R.C. Reddick, and R.J. Warmack, Phys. Lett. A **45**, 343 (1990).

[14] C.L. Jahnckle, M.A. Paesler, and H.D. Hallen, Appl. Phys. Lett. **67**, 2483 (1995); J. Grausem, B. Humbert, A. Burenau, and J. Oswalt, *ibid.* **70**, 1671 (1997).

[15] E.J. Sanchez, L. Novotny, and X.S. Xie, Phys. Rev. Lett. **82**, 4014 (1999).

[16] F. Zenhausern, M.P. O'Boyle, and H.K. Wickramasinghe, Appl. Phys. Lett. **65**, 1623 (1994); Y. Inouye and S. Kawata, Opt. Lett. **19**, 159 (1994); P. Gleyzes, A.C. Boccara, and R. Bachelot, Ultramicroscopy **57**, 318 (1995).

[17] A. Lahrech, R. Bachelot, P. Gleyzes, and A.C. Boccara, Appl. Phys. Lett. **71**, 575 (1997).

[18] B. Knoll and F. Keilman, Nature (London) **399**, 134 (1999).

[19] G. Colas des Francs, C. Girard, J.-C. Weeber, C. Chicanne, T. David, A. Dereux, and D. Peyrade, Phys. Rev. Lett. **86**, 4950 (2001).

[20] C. Chicanne, T. David, R. Quidant, J.C. Weeber, Y. Lacroute, E.

Bourillot, A. Dereux, G. Colas des Francs, and C. Girard, Phys. Rev. Lett. **88**, 097402 (2002).

[21] A.V. Shchegrov, K. Joulain, R. Carminati, and J.-J. Greffet, Phys. Rev. Lett. **85**, 1548 (2000).

[22] S.M. Rytov, Yu.A. Kravtsov, and V.I. Tatarskii, *Principles of Statistical Radiophysics* (Springer-Verlag, Berlin, 1989), Vol. 3.

[23] G.S. Agarwal, Phys. Rev. A **11**, 230 (1975).

[24] J.E. Sipe, J. Opt. Soc. Am. B **4**, 481 (1987).

[25] C. Henkel, S. Pötting, and M. Wilkens, Appl. Phys. B: Lasers Opt. **69**, 379 (1999).

[26] C. Henkel, K. Joulain, R. Carminati, and J.-J. Greffet, Opt. Commun. **186**, 57 (2000).

[27] E.D. Palik, *Handbook of Optical Constants* (Academic Press, San Diego, 1985).

[28] A. Ashcroft and D. Mermin, *Solid State Physics* (Saunders College, Philadelphia, 1976).

[29] J.A. Porto, R. Carminati, and J.-J. Greffet, J. Appl. Phys. **88**, 4845 (2000).

[30] J.-J. Greffet and R. Carminati, Prog. Surf. Sci. **56**, 133 (1997).

[31] D. Van Labeke and D. Barchiesi, J. Opt. Soc. Am. A **10**, 2193 (1993).

[32] L. Aigouy, F.X. Andreani, A.C. Boccara, J.C. Rivoal, J.A. Porto, R. Carminati, J.-J. Greffet, and R. Megy, Appl. Phys. Lett. **76**, 397 (2000).

[33] R. Carminati, J.-J. Greffet, N. García, and M. Nieto-Vesperinas, Opt. Lett. **21**, 501 (1996).

[34] E.R. Méndez, J.-J. Greffet, and R. Carminati, Opt. Commun. **142**, 7 (1997).

Coupled surface polaritons and the Casimir force

C. Henkel, K. Joulain, J.-P. Mulet et J.-J. Greffet

Physical Review A, vol 69, pp023808 (2004)

PHYSICAL REVIEW A **69**, 023808 (2004)

Coupled surface polaritons and the Casimir force

C. Henkel*
Institut für Physik, Universität Potsdam, Am Neuen Palais 10, 14469 Potsdam, Germany

K. Joulain,[†] J.-Ph. Mulet,[‡] and J.-J. Greffet
Laboratoire EM2C, Ecole Centrale Paris, 92295 Châtenay-Malabry Cedex, France

(Received 24 July 2003; revised manuscript received 6 November 2003; published 17 February 2004)

The Casimir force between metallic plates made of realistic materials is evaluated for distances in the nanometer range. A spectrum over real frequencies is introduced and shows narrow peaks due to surface resonances (plasmon polaritons or phonon polaritons) that are coupled across the vacuum gap. We demonstrate that the Casimir force originates from the attraction (repulsion) due to the corresponding symmetric (antisymmetric) eigenmodes, respectively. This picture is used to derive a simple analytical estimate of the Casimir force at short distances. We recover the result known for Drude metals without absorption and compute the correction for weakly absorbing materials.

DOI: 10.1103/PhysRevA.69.023808 PACS number(s): 42.50.Pq, 42.50.Lc, 73.20.Mf

I. INTRODUCTION

Van der Waals and Casimir forces are among the few macroscopic manifestations of vacuum fluctuations. Since the seminal paper by Casimir [1] showing the existence of an attraction between two perfect conductors separated by a vacuum gap, an abundant literature has been devoted to this effect. In particular, the relevance of retardation, finite conductivity, and finite temperature have been studied (see, e.g., Ref. [2]). Exhaustive lists of references can be found in several review papers such as Refs. [3–5].

In the last five years, the interest in Casimir forces has increased due to the existence of new measurements with improved accuracy [6,7]. This has challenged theoreticians to quantify the corrections to the ideal case (zero temperature, perfect conductors, flat interfaces) that must be taken into account for an accurate comparison with experiments [8–13]. Furthermore, the developments of microelectromechanical systems (MEMS), for example, have shown that the Casimir effect is becoming an issue in nanoengineering [14,15]. Indeed, these short-range forces could seriously disturb the performances of MEMS [16].

From a theoretical point of view, different methods exist to calculate Casimir forces. Casimir himself [1] determined the electromagnetic eigenfrequencies of the system and summed them in order to obtain the system's zero-point energy. The force is found by a differentiation of this energy with respect to the geometrical distance separating the bodies [1,17]. Ingenious subtraction procedures are often required to obtain a finite value for the Casimir energy, and realistic dispersive or absorbing materials can be dealt with using contour integrals over complex frequencies [18]. Another method, used by Lifshitz [19], considers fluctuating currents driven by thermal or vacuum fluctuations in the whole space. These currents, whose spatial correlations are known through the fluctuation dissipation theorem, interact via the electromagnetic fields they radiate. The force is obtained by calculating the flux of the Maxwell stress tensor across a surface separating the bodies. One thus gets an integral over all possible partial wave contributions. For two parallel plates separated by a vacuum gap, for example, the partial waves can be labeled by their frequency, wave vector parallel to the interface, and polarization. By using clever contour deformation, Lifshitz greatly simplified the calculation of the Casimir force integral. The principal drawback of this approach is that the integrand can no longer be interpreted as a force spectrum.

In this paper, we use an alternative approach and study the force integral over real frequencies and wave vectors. We show for generic materials (semiconductors and real metals) that in the near-field regime (separation distance small compared to the wavelengths considered), the frequency spectrum of the force exhibits peaks located close to surface-polariton frequencies. These peaks give the essential contribution to the Casimir force in this regime. We identify two types of resonant surface modes, binding and antibinding, that contribute respectively with attractive and repulsive terms to the force. This substantiates early suggestions [20,21] that the Casimir force is due to surface modes; also see the recent papers by Genet and co-workers [13,22].

We finally focus on materials whose dielectric function is modeled by a Lorentzian resonance, including a nonzero absorption. We are able to use the qualitative suggestions mentioned above and propose a quantitative estimation of the Casimir force in terms of coupled surface resonances. The dominant contribution of these resonances at nanometer distances allows us to perform exactly the integral over the mode frequencies, whereas the integral over the wave vector is computed to first order in the absorption. We show that the respective contributions of binding/antibinding modes give a simple and accurate analytical estimate for the short-distance Casimir force, recovering previous results for nonabsorbing

---

*Electronic address: Carsten.Henkel@quantum.physik.uni-potsdam.de

[†] Present address: Laboratoire d'études thermiques, ENSMA, 86960 Futuroscope Cedex, France.

[‡] Present address: The Institute of Optics, University of Rochester, Rochester New York 14627, USA.

Drude materials [10]. In the corresponding Hamaker constant, we include corrections due to material losses. The accuracy of our results is established by comparing to numerical evaluations of Lifshitz theory, using tabulated data for the dielectric functions [23]. The paper concludes with a discussion of possibilities to ‘‘tune’’ the Casimir force that are suggested by our approach.

II. SURFACE RESONANCES IN THE FREQUENCY SPECTRUM

The starting point for our calculation of the Casimir force is Rytov's theory of fluctuating electrodynamics in absorbing media [24] that was used by Lifshitz in his seminal paper [19]. This scheme applies to dispersive or absorbing materials, as long as their dielectric response is linear. It has also been shown to provide a suitable framework for a consistent quantization procedure of the macroscopic Maxwell equations (see Refs. [25,26] and references therein).

In the following, we focus on the standard geometry of two planar half-spaces made from identical material [of local complex dielectric constant $\varepsilon(\omega)$] and separated by a vacuum gap of width d. In the Rytov-Lifshitz method, the Casimir force is computed from the expectation value of the Maxwell stress tensor at an arbitary position in the gap. At zero temperature and after subtraction of divergent contributions, Lifshitz gets a force per unit area given by [19]

$$F = \int_0^\infty \frac{d\omega}{2\pi} \int_0^\infty \frac{du}{2\pi} F(u,\omega), \tag{1}$$

$$F(u,\omega) = \frac{2\hbar\omega^3 u}{c^3} \operatorname{Im}\left(v \sum_{\mu=s,p} \frac{r_\mu^2(u,\omega) e^{-2\omega v d}}{1 - r_\mu^2(u,\omega) e^{-2\omega v d/c}} \right), \tag{2}$$

where $v = (u^2-1)^{1/2}(\operatorname{Im} v \leqslant 0)$, and r_μ is the Fresnel reflection coefficient for a plane wave with polarization μ and wave vector $K = \omega u/c$ parallel to the vacuum-medium interface. We use the convention that an attractive force corresponds to $F > 0$. We note that Rytov's approach allows for an easy generalization to different media held at different nonzero temperatures. The radiation force on a small polarizable sphere above a heated surface has been discussed previously in Ref. [27]. Results for the nonequilibrium Casimir force will be reported elsewhere.

Lifshitz evaluated integrals (1) by deforming an integration contour in the complex plane to arrive at an integral over imaginary frequencies $\omega = i\xi$. The integration then requires the continuation of the dielectric function from real-frequency data to $\varepsilon(i\xi)$, using analyticity properties as discussed in Refs. [9,10]. Here we follow a different route and continue to work with real ω and u, taking advantage of the fact that Lifshitz's results provides us with an expression for the frequency spectrum $F(\omega) = \int F(u,\omega) du/2\pi$ of the Casimir force. Note that the force spectrum is more difficult to define in a calculation based on mode summation; see, e.g., Refs. [28,29].

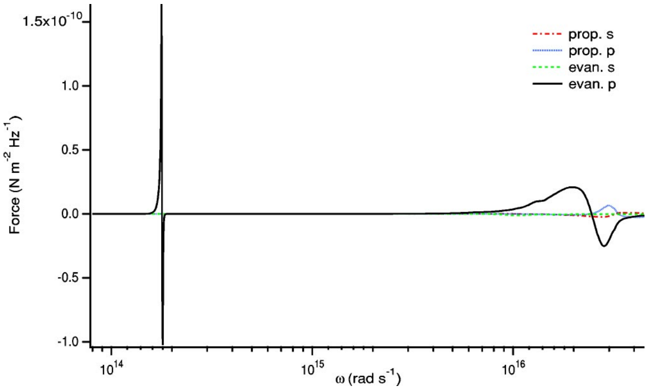

FIG. 1. Contributions of *s*- and *p*-polarized propagating and evanescent modes to the force spectrum [Eq. (2), integrated over the wave vector u]. Distance $d = 10$ nm. Material: SiC, dielectric function taken from tabulated data [23]. The corresponding surface resonances [$\operatorname{Re}\varepsilon(\omega) = -1$] are located at $1.78 \times 10^{14}\ \mathrm{s}^{-1}$ in the IR and $2.45 \times 10^{16}\ \mathrm{s}^{-1}$ in the UV.

For a polar material like SiC, the spectrum of the force is dominated by narrow peaks in the ultraviolet (UV) and in the infrared (IR) (Fig. 1) when the distance d is reduced to the nanometer range. These peaks can be ascribed to the surface phonon polaritons in the IR and to surface plasmon polaritons (SPPs) in the UV. The largest contribution comes from the UV surface plasmon polariton even though larger losses make it broader. The large difference between the UV and IR contributions in Fig. 1 is due to the factor ω^3 in Eq. (2). In Fig. 2, we plot the spectrum of the force between two aluminum half-spaces, using tabulated data for the dielectric function [23]. The dominant contribution to the force is clearly due to the surface plasmon polaritons. Indeed, the frequency of the peaks corresponds to the frequency Ω of the asymptote of the SPP dispersion relation [30] (see Fig. 3),

$$u_{\mathrm{SPP}} = \left(\frac{\varepsilon(\omega)}{\varepsilon(\omega)+1} \right)^{1/2}, \tag{3}$$

where the sign of the square root is chosen such that $\operatorname{Re} u_{\mathrm{SPP}} > 1$. It is seen in Eq. (3) that the frequency Ω is given by the condition $\operatorname{Re}\varepsilon(\Omega) = -1$. This corresponds to a large increase of the density of states and therefore to a peak in the

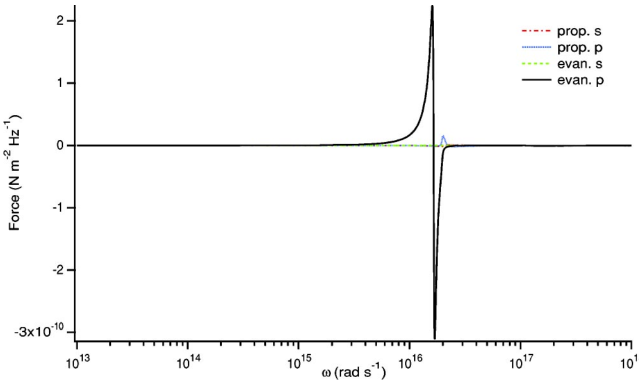

FIG. 2. Contributions of *s*- and *p*-polarized propagating and evanescent modes to the force spectrum [Eq. (2), integrated over the wave vector u]. Distance $d = 10$ nm. Material: aluminum, described by tabulated optical data [23].

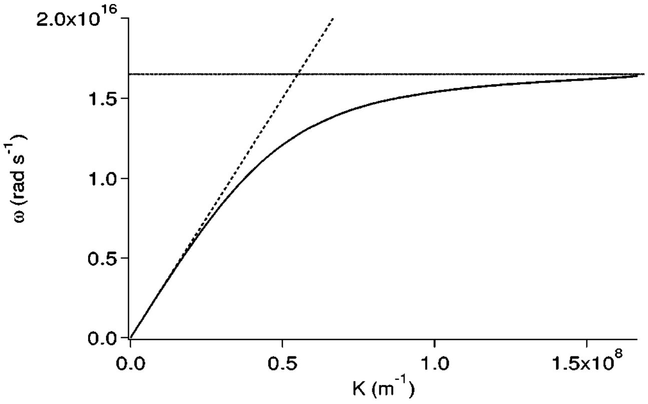

FIG. 3. Dispersion relation [Eq. (3)] of the surface plasmon polariton on a flat interface vacuum/aluminum. The dielectric function is taken from the data tabulated in Ref. [23]. We plot the real part of ω vs the real part of the parallel wave vector $K=u\omega/c$.

energy density [31,32]. The polarization dependence of the force spectrum provides a second argument in favor of a surface plasmon polariton. In Figs. 1 and 2, we have separated the contributions to the spectrum according to the mode polarization (s or p). The modes in the cavity can further be classified into evanescent (surface) modes ($u>1$) and propagating (guided) modes ($0\leqslant u\leqslant 1$). Among the four contributions it is seen that the leading one comes from the p-polarized surface modes, of which the SPP is a special case.

It is worthwhile pointing out that for a perfectly conducting metal, the spectrum of the force would be completely different because of the lack of SPPs. The usual picture of the Casimir effect in that case is based on the modified density of states for propagating waves between the two plates. This picture includes only what we have called guided modes and ignores surface (or evanescent) modes.

We observe from Figs. 1 and 2 that the contribution of the force is either positive or negative depending on the frequency. We analyze this behavior in Sec. III.

III. BINDING AND ANTIBINDING RESONANCES

In order to further analyze the role of SPPs for the Casimir force, in Fig. 4(a) we plot the integrand $F(u,\omega)$ as given by Eq. (2) for two aluminum half-spaces separated by a distance of $d=10$ nm. Two branches emerge with dominant contributions, the higher-frequency branch yielding a negative contribution whereas the lower branch gives a positive (attractive) contribution. These two branches are reminiscent of the dispersion relation of a SPP on a two-interface system. It is given by the complex poles of the reflection factor of the two interfaces system in the (u,ω) plane:

$$1-r_p^2 e^{-2\omega v d/c}=0. \tag{4}$$

In order to illustrate the influence of the SPP dispersion relation on the force, in Fig. 4(b) we plot the quantity $1/|1-r_p^2 e^{-2\omega v d/c}|^2$ in the real (u,ω) plane. Comparing Figs. 4(b) and 4(a), it is clearly seen that the main contribution to the force is due to the SPP. In addition, in Fig. 4(b) we observe a dark line which corresponds to minima of $1/|1-r_p^2 e^{-2\omega v d/c}|^2$. This can be attributed to very large values of the reflection factor r_p. Thus, the dark line is the dispersion relation of the SPP on a single flat interface. Note that the Casimir force shows no prominent feature in this region.

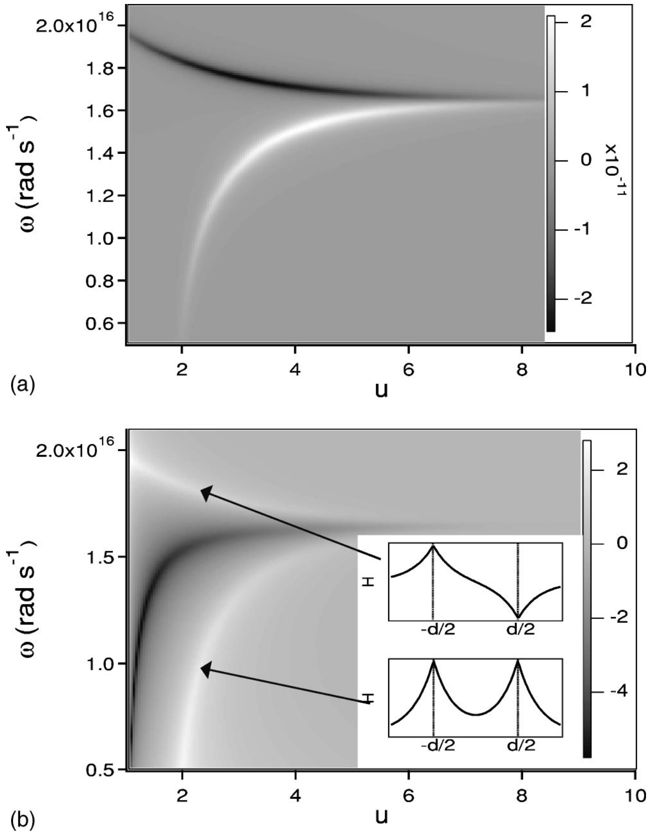

FIG. 4. (a) Wave-vector resolved spectrum of the Casimir force [Eq. (2)] in the (u,ω) plane between two aluminum half spaces separated by a distance of 10 nm. The frequency of the flat asymptote corresponds to the peaks of the force spectrum (Fig. 2). Light (dark) areas: attractive (repulsive) force. (b) Resonant denominator $1/|1-r_p^2 e^{-2\omega v d/c}|^2$ in the (u,ω) plane, the grayscale giving the logarithm to base 10. The dispersion relation of the coupled surface resonance corresponds to the light areas; dark area: dispersion relation for a single interface [Eq. (3)]. The dielectric function is extracted from tabulated data [23]. The inset sketches the magnetic field of the coupled surface resonances (antisymmetric and symmetric combinations).

In Fig. 5, we plot the force for a spacing $d=100$ nm: the two branches tend to merge with the flat interface dispersion relation. The following interpretation thus emerges: when the surfaces approach each other, the overlapping of the two SPP leads to a splitting of the polariton frequencies [33,34]. The frequency splitting can be found from the solutions of Eq. (4) which are implicitly defined by (also see Ref. [22])

$$r_p(u,\omega)=\pm e^{\omega v d/c}. \tag{5}$$

The signs correspond to either symmetric or antisymmetric mode functions (for the magnetic field), as shown in the Appendix and sketched in Fig. 4(b). The symmetric (antisymmetric) branch corresponds to a lower (higher) resonance

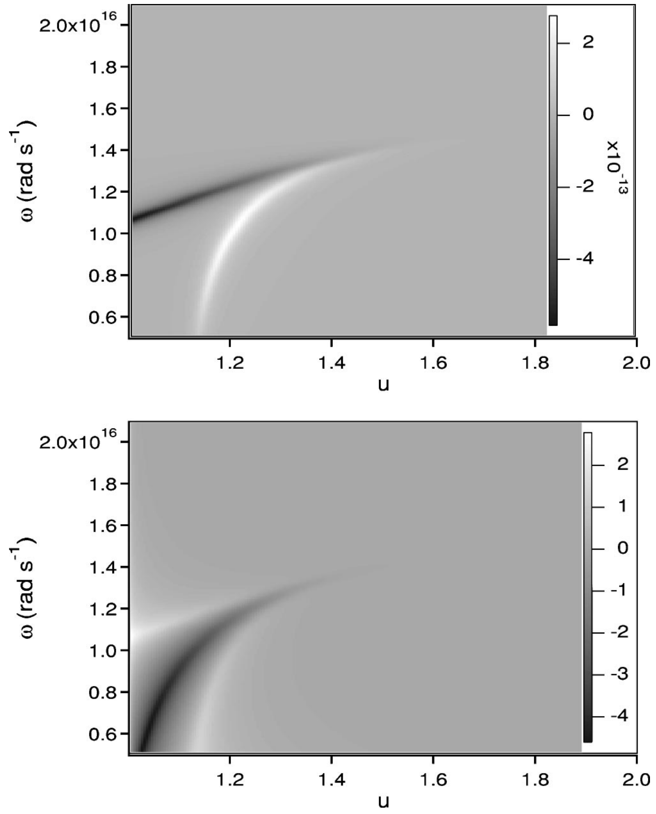

FIG. 5. Same as Fig. 4, but for a separation $d=100$ nm.

frequency, respectively, similar to molecular orbitals and tunneling doublets [35]. These branches contribute with opposite signs to the Casimir force, due to the identity

$$\frac{2r_p^2(\omega,u)e^{-2\omega v d}}{1-r_p^2(\omega,u)e^{-2\omega v d}}=\frac{r_p(\omega,u)e^{-\omega v d}}{1-r_p(\omega,u)e^{-\omega v d}}-\frac{r_p(\omega,u)e^{-\omega v d}}{1+r_p(\omega,u)e^{-\omega v d}}, \tag{6}$$

where the first (second) term is peaked at the symmetric (antisymmetric) cavity mode. The symmetry of the resonance mode function hence determines the attractive or repulsive character of its contribution to the Casimir force. In the Appendix, we show by explicitly evaluating the Maxwell stress tensor, that *symmetric modes are binding* as in molecular physics.

We note that the splitting in Eq. (6) of the force spectrum gives meaningful results also after integration because for evanescent waves, both terms converge separately. We also point out that for a complex permittivity $\varepsilon(\omega)$ (as required by the Kramers-Kronig relations for a dispersive material), the SPP dispersion relation necessarily moves into the complex plane and is never satisfied in the real (u,ω) plane, thus excluding any singularities of integral (1).

IV. SHORT-DISTANCE LIMIT

The short-distance behavior of the Casimir force between nonperfect metals was computed in Refs. [9,10] using tabulated data for the dielectric function and integrating over imaginary frequencies. We show here that these results can also be recovered with a real frequency calculation. In particular, we prove that the interaction between SPPs across the vacuum gap quantitatively accounts for the short-distance Casimir force derived in Ref. [10], thus completing qualitative discussions put forward by Gerlach [21] and Genet, Lambrecht, and Reynaud [22].

For definiteness, let us adopt a Lorentz-Drude model for the dielectric function

$$\varepsilon(\omega)=1+\frac{2(\Omega^2-\omega_0^2)}{\omega_0^2-i\gamma\omega-\omega^2}, \tag{7}$$

with resonance frequency ω_0 and damping coefficient γ. The corresponding plasma frequency is $[2(\Omega^2-\omega_0^2)]^{1/2}$. With this convention, the large u asymptote of the SPP dispersion (3) occurs at $\omega\approx\Omega$. This model can be used to describe either dielectrics or metals when $\omega_0=0$. In the region of large wave vectors, the p-polarized reflection coefficient has a pole at Ω:

$$u\gg 1:\quad r_p(\omega,u)\approx\frac{\varepsilon(\omega)-1}{\varepsilon(\omega)+1}=\frac{\Omega^2-\omega_0^2}{\Omega^2-i\gamma\omega-\omega^2}. \tag{8}$$

From Figs. 1 and 2, we know that the force is significant only in a range around the SPP resonance. It follows that the model for $\varepsilon(\omega)$ is needed only in this limited range. We have checked that Eq. (8) with $\omega_0=0$ is well suited to describe the reflection data computed from tabulated data for aluminum. Note that the results of the fitted parameters (Ω and γ are indicated in the caption of Fig. 4) differ from the usual bulk plasma frequency and damping rates that we would get from a fit over the entire spectrum.

We have checked that this formula is well suited to describe the reflection coefficient computed from tabulated optical data in the frequency region around the SPP resonance. For aluminum, we get a good agreement with the values given in the caption of Fig. 6. These values do not correspond, of course, to the usual bulk plasma frequency and damping rates that enter in the Drude model of the dielectric function at low frequencies.

With this form of the reflection coefficient, Eq. (5) yields the following dispersion relation for the (anti)symmetric SPP resonances, neglecting for the moment the damping coefficient γ:

$$\omega_\pm^2\approx\Omega^2\mp e^{-\omega_\pm u d/c}(\Omega^2-\omega_0^2). \tag{9}$$

We have used $v\approx u$ for $u\gg 1$. For large u, we solve by iteration and find that $\omega_\pm\lessgtr\Omega$. As announced above, the symmetric mode (upper sign) occurs at a lower resonance frequency.

To derive an analytical estimate for the Casimir force, in Eq. (2) we retain only the contribution of p-polarized, evanescent waves, containing the SPP resonance. Introducing the new variable $x=\omega v d/c$, we get, using identity (6),

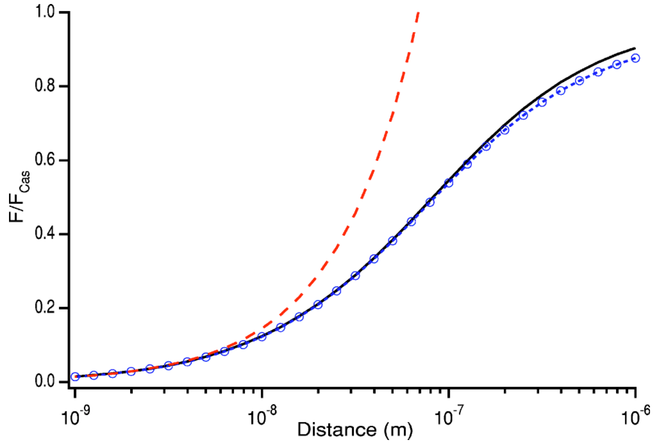

FIG. 6. (Color online) Comparison of different expressions for the Casimir force between aluminum surfaces. We plot the ratio $F(d)/F_{\mathrm{Cas}}(d)$, where $F_{\mathrm{Cas}}(d)=\hbar c\pi^2/(240d^4)$ is the Casimir force for perfect mirrors. Solid line (black): numerical integration of Eq. (2), using tabulated optical data [23,36]. Short-dashed line with circles (blue): same, with a model dielectric function of Drude form [Eq. (7)] with $\omega_0=0$, $\Omega=1.66\times10^{16}\ \mathrm{s}^{-1}$, and $\gamma/\Omega=0.036$. These parameters have been obtained from a plot of the reflection coefficient $[\varepsilon(\omega)-1]/[\varepsilon(\omega)+1]$ based on the tabulated data that has been fitted to the form given in Eq. (8). Long-dashed line (red): short-distance asymptotics (12) with the same values for ω_0, Ω, and γ.

$$F=\frac{\hbar}{4\pi^2 d^3}\,\mathrm{Im}\int_0^\infty d\omega\int_0^\infty x^2dx \times\sum_{\lambda=\pm1}\frac{\lambda e^{-x}}{r_p^{-1}(\omega,cx/(\omega d))-\lambda e^{-x}}, \tag{10}$$

where $\lambda=\pm1$ corresponds to symmetric (antisymmetric) modes, respectively. The integral is dominated by the range $x\sim1$ and $\omega\sim\Omega$. To leading order in $\Omega d/c\to0$, we can thus use the asymptotic form of r_p valid for large u given by Eq. (8). Performing the integral over ω analytically and including damping to first order in γ/Ω yields

$$F=\frac{\hbar\Omega}{4\pi d^3}\int_0^\infty dx\ \ x^2\sum_{\lambda=\pm1}\left(\frac{\lambda z e^{-x}}{2\sqrt{1-\lambda z e^{-x}}}-\frac{\gamma\lambda z e^{-x}}{2\pi\Omega(1-\lambda z e^{-x})}\right), \tag{11}$$

where $z=1-\omega_0^2/\Omega^2$. This result shows clearly that symmetric and antisymmetric modes give Casimir forces of opposite sign. The first term in the parenthesis can be computed by expanding the square root in a power series in $\lambda z e^{-x}$, leading to an infinite series given in Refs. [10,22]. The second term, the correction due to damping, can be integrated in terms of the polylogarithmic function, so that we finally have

$$F=\frac{\hbar\Omega}{4\pi d^3}\left(\alpha(z)-\frac{\gamma\mathrm{Li}_3(z^2)}{4\pi\Omega}\right), \tag{12}$$

where

$$\alpha(z)=\frac{1}{4}\sum_{n=1}^{\infty}z^{2n}\frac{(4n-3)!!}{n^3(4n-2)!!} \tag{13}$$

and

$$\mathrm{Li}_3(z^2)=\sum_{n=1}^{\infty}\frac{z^{2n}}{n^3}. \tag{14}$$

For completeness, we give the asymptotic series for small $\omega_0/\Omega(z\to1)$

$$\alpha(z)\approx0.1388-0.32(1-z)+0.4(1-z)^2 \tag{15}$$

$$\mathrm{Li}_3(z^2)\approx\zeta(3)-\frac{\pi^2}{3}(1-z)+\left[3-\frac{\pi^2}{6}-2\log[2(1-z)]\right]\times(1-z)^2, \tag{16}$$

with $\zeta(3)\approx1.202$. (The coefficient of the second order term in Eq. (15) is only accurate up to a logarithmic correction.)

Our result [Eq. (12)] for the short-distance Casimir force agrees with the formula given in Refs. [10,22] in the special case $\gamma=0$, $\omega_0=0$ (lossless Drude model). A very similar expression was found in Ref. [26]. We compare Eq. (12) in Fig. 6 to the full integral [Eq. (2)] for the case of aluminum: it turns out to be quite accurate for distances $d\leqslant0.1\,\lambda_{\mathrm{SPP}}$, where $\lambda_{\mathrm{SPP}}=115$ nm is the wavelength of the SPP with the largest frequency [36]. In the case of aluminum, the first order correction in γ/Ω is 2.5% of the zeroth order value of the force. The plot also shows that for the numerical integration, the tabulated data and the Lorentz-Drude model (7) with parameters fitted around the surface resonance give very close results over a large range of distances. This is another indication that the short-range Casimir force between real metals is dominated by a narrow frequency range. Differences of the order of a few percent appear at large distances where the Casimir force is dominated by the low-frequency behavior of the reflection coefficient that is not accurately modeled with the fitted parameters.

We finally note that the correction of order γ/Ω derived here introduces the effects of losses and must not be confused with the correction due to a finite real permittivity This is already taken into account by the finite value of the plasma frequency Ω and is responsible for the emergence of the short-distance regime $d\ll\lambda_{\mathrm{SPP}}$ where the Casimir force $\sim1/d^3$ [19]. At large distances, a finite Ω leads to a small correction to the well-known Casimir force $\sim1/d^4$ between perfect conductors [2,9,10].

V. CONCLUSION

We have pointed out that the Casimir attraction between realistic materials can be quantitatively understood, at short distances, in terms of the interaction between electromagnetic surface plasmon (or phonon) polaritons. The modes overlap across the vacuum gap and split into symmetric and antisymmetric combinations which contribute with different signs to the Maxwell stress tensor and hence to the Casimir force. We discussed in particular the short-distance regime of the Casimir force where $F=H/d^3$, and have given an analytical formula for the Hamaker constant H. We recover previous results for nonabsorbing materials and evaluate a correction due to absorption. Our results have been validated by comparing to a numerical calculation based on Lifshitz theory.

The approach presented here has the advantage of linking the Casimir force to the actual physical properties of the material surface in a transparent way. This suggests the possibility of engineering the surface plasmon polariton dispersion relation to modify the Casimir force. Indeed, as has been shown, the Casimir force at short distances is entirely due to the interaction between surface polaritons. Magnetic materials which exhibit Casimir repulsion [37] and support s-polarized surface waves when $\mathrm{Re}\,\mu<-1$ [38] are good candidates. The folding of the dispersion relation in reciprocal space by a grating, known to change the surface wave behavior [39] could also lead to a substantial modification of the Casimir force.

ACKNOWLEDGMENTS

This work has been supported by the bilateral French-German program ''Procope'' under Project Nos. 03199RH and D/0031079. We thank Christian Raabe for helpful comments.

APPENDIX: ANGULAR SPECTRUM ANALYSIS

In this appendix, we compute the Casimir force in terms of an angular spectrum representation of the electromagnetic fields that is adapted to the planar geometry at hand. Letting the vacuum gap occupy the region $-d<z<0$, we can expand the electric field in the gap as

$$\mathbf{E}(x,\omega)=\sum_{\mu=s,p}\int d^2K[E_-^\mu(\mathbf{K})e^{-ik_z z}e_\mu^- + E_+^\mu(\mathbf{K})e^{ik_z(z+d)}e_\mu^+]e^{i\mathbf{K}\cdot\mathbf{X}}, \tag{A1}$$

where $\mathbf{K}=(k_x,k_y)$ is the component of the wavevector parallel to the interfaces and $k_z=\sqrt{(\omega/c)^2-K^2}$ its perpendicular component. $\mathbf{e}_\mu^\pm(\mu=s,\ p)$ are unit polarization vectors, and $E_\pm^\mu(\mathbf{K})$ are the amplitudes of upward and downward propagating plane waves. A similar expansion holds for the magnetic field $\mathbf{H}(\mathbf{x},\omega)$ with amplitudes $H_\pm^\mu(\mathbf{K})$. We get the averaged Maxwell stress tensor by integrating incoherently over the contributions $T_{zz}^\mu(\mathbf{K})$ of individual modes. For the particular case of a p-polarized evanescent mode $(K>\omega)$, we get, by straightforward algebra,

$$T_{zz}^p(\mathbf{K})=2\mu_0 v^2\,\mathrm{Re}[H_+^{p*}(\mathbf{K})H_-^p(\mathbf{K})]. \tag{A2}$$

The upward and downward propagating amplitudes are of course related via the reflection coefficient from the upper interface. Taking the phase references in Eq. (A1) into account, we have

$$H_-^p=r_p e^{ik_z d}H_+^p=r_p e^{-\omega v d/c}H_+^p\approx\pm H_+^p, \tag{A3}$$

where the last equality applies in the vicinity of the coupled surface resonances defined by Eq. (5). The condition $r_p e^{-\omega v d/c}=+1$ thus corresponds to a symmetric magnetic field distribution on both interfaces, because $H_+^p=H_-^p$. In addition, with our sign convention, this mode gives an attractive contribution proportional to $+|H_-^p|^2$ to the stress tensor (A2). The opposite is true for antisymmetric modes.

The sign of the Casimir force due to the coupled polariton modes can also be understood in terms of the zero-point fluctuations of the charge densities on both surfaces, as pointed out by Gerlach [21]. The charge densities can be found from the normal component of the electric field. For a symmetric mode, we get surface charges with opposite sign, hence an attractive force, while an antisymmetric mode corresponds to equal surface charges.

---

[1] H. B. G. Casimir, Proc. Koninkl. Ned. Akad. Wetenschap. **51**, 793 (1948).

[2] J. Schwinger, J. Lester, L. DeRaad, and K. A. Milton, Ann. Phys. (N.Y.) **115**, 1 (1978).

[3] G. Plunien, B. Müller, and W. Greiner, Phys. Rep. **134**, 87 (1986).

[4] M. Bordag, U. Mohideen, and V. M. Mostepanenko, Phys. Rep. **353**, 1 (2001).

[5] S. K. Lamoreaux, Am. J. Phys. **67**, 850 (1999).

[6] S. K. Lamoreaux, Phys. Rev. Lett. **78**, 5 (1997).

[7] U. Mohideen and A. Roy, Phys. Rev. Lett. **81**, 4549 (1998).

[8] G. L. Klimchitskaya, A. Roy, U. Mohideen, and V. M. Mostepanenko, Phys. Rev. A **60**, 3487 (1999).

[9] G. L. Klimchitskaya, U. Mohideen, and V. M. Mostepanenko, Phys. Rev. A **61**, 062107 (2000).

[10] A. Lambrecht and S. Reynaud, Eur. Phys. J. D **8**, 309 (2000).

[11] C. Genet, A. Lambrecht, and S. Reynaud, Phys. Rev. A **62**, 012110 (2000).

[12] R. Tadmor, J. Phys.: Condens. Matter **13**, L195 (2001).

[13] C. Genet, A. Lambrecht, P. Maia Neto, and S. Reynaud, Europhys. Lett. **62**, 484 (2003); M. S. Tomaš, Phys. Rev. A **66**, 052103 (2002).

[14] H. B. Chan, V. A. Aksyuk, R. N. Kleiman, D. J. Bishop, and F. Capasso, Phys. Rev. Lett. **87**, 211801 (2001).

[15] H. B. Chan, V. A. Aksyuk, R. N. Kleiman, D. J. Bishop, and F. Capasso, Science **291**, 1941 (2001).

[16] E. Buks and M. L. Roukes, Phys. Rev. B **63**, 033402 (2001).

[17] P. W. Milloni, *The Quantum Vacuum: An Introduction to Quantum Electrodynamics* (Academic, London, 1994).

[18] V. M. Mostepanenko and N. N. Trunov, *The Casimir Effect and Its Applications* (Oxford Science Publications, Oxford, 1997).

[19] E. M. Lifshitz, Zh. Eksp. Teor. Fiz. **29**, 94 (1955) [Sov. Phys. JETP **2**, 73 (1956)].

[20] N. G. Van Kampen, B. R. A. Nijboer, and K. Schram, Phys. Lett. A **26**, 307 (1968).
[21] E. Gerlach, Phys. Rev. B **4**, 393 (1971).
[22] C. Genet, A. Lambrecht, and S. Reynaud, Ann. Fond. L. de Broglie (to be published); Phys. Rev. A **67**, 043811 (2003).
[23] E. D. Palik, *Handbook of Optical Constants of Solids* (Academic, San Diego, 1991).
[24] S. M. Rytov, Yu. A. Kravtsov, and V. I. Tatarskii, *Elements of Random Fields*, Principles of Statistical Radiophysics Vol. 3 (Springer, Berlin, 1989).
[25] L. Knöll, S. Scheel, and D.-G. Welsch, in *Coherence and Statistics of Photons and Atoms*, edited by J. Perina (Wiley, New York, 2001).
[26] C. Raabe, L. Knöll, and D.-G. Welsch, Phys. Rev. A **68**, 033810 (2003). Note that Eq. (82) in this paper is based on an inaccurate evaluation of the integral Eq. (E9). Once this is corrected, we find agreement with Eq. (12) reported here.
[27] C. Henkel, K. Joulain, J.-Ph. Mulet, and J.-J. Greffet, J. Opt. A: Pure Appl. Opt. **4**, S109 (2002).
[28] L. H. Ford, Phys. Rev. D **38**, 528 (1988).
[29] L. H. Ford, Phys. Rev. A **48**, 2962 (1993).
[30] H. Raether, *Surface Plasmons on Smooth and Rough Surfaces and on Gratings* (Springer, Berlin, 1988).
[31] A. V. Shchegrov, K. Joulain, R. Carminati, and J.-J. Greffet, Phys. Rev. Lett. **85**, 1548 (2000).
[32] K. Joulain, R. Carminati, J.-Ph. Mulet, and J.-J. Greffet, Phys. Rev. B **68**, 245405 (2003).
[33] D. Marcuse, *Theory of Dielectric Optical Waveguides*, 2nd ed. (Academic Press, San Diego, 1991).
[34] A. Krishnan, T. Thio, T. J. Kim, H. J. Lezec, T. W. Ebbesen, P. A. Wolff, J. Pendry, L. Martin-Moreno, and F. J. Garcia-Vidal, Opt. Commun. **200**, 1 (2001).
[35] A. Messiah, *Mécanique Quantique*, new ed. (Dunod, Paris, 1995), Vol. 1.
[36] The numerical integration uses the Lifshitz formula and proceeds along the imaginary frequency axis $\omega = i\xi$. The dielectric function $\varepsilon(i\xi)$ is constructed from the tabulated data at real frequencies using the sum rules given in Refs. [9], [10].
[37] O. Kenneth, I. Klich, A. Mann, and M. Revzen, Phys. Rev. Lett. **89**, 033001 (2002).
[38] R. Ruppin, Phys. Lett. A **277**, 61 (2000).
[39] J.-J. Greffet, R. Carminati, K. Joulain, J.-Ph. Mulet, S. Mainguy, and Y. Chen, Nature (London) **416**, 61 (2002).

Coherent spontaneous emission of light by thermal sources

F. Marquier, K. Joulain, J.-P. Mulet, R. Carminati, J.-J. Greffet et Y. Chen

Physical Review B, vol 69, pp155412 (2004)

PHYSICAL REVIEW B **69**, 155412 (2004)

Coherent spontaneous emission of light by thermal sources

F. Marquier, K. Joulain, J.-P. Mulet, R. Carminati, and J.-J. Greffet
Laboratoire d'Énergétique Moléculaire et Macroscopique; Combustion, École Centrale Paris,
Centre National de la Recherche Scientifique, Grande Voie des Vignes, 92295 Châtenay-Malabry Cedex, France

Y. Chen
Laboratoire de Photonique et Nanostructures, Centre National de la Recherche Scientifique, 91460 Marcoussis, France

(Received 21 November 2003; published 14 April 2004)

The emission of light by a material at temperature *T* has been shown recently to be coherent in the near field. These properties were attributed to the thermal excitation of surface polaritons. We review the origin of this phenomenon. We analyze the influence of the microstructure and temperature on the coherence properties and show how to engineer thermoradiative properties of surfaces. We report the design of a quasi-isotropic source and a very directional source of thermal light. We also report a measurement of the transverse coherence length of a thermal source of light.

DOI: 10.1103/PhysRevB.69.155412 PACS number(s): 73.20.Mf, 78.68.+m, 71.36.+c, 44.40.+a

I. INTRODUCTION

The tungsten filaments of light bulbs are certainly the most widely used sources of light. The microscopic mechanism of light generation is the spontaneous emission of a photon when an emitter thermally excited relaxes to a lower state. Such light sources are called thermal sources. They are usually almost isotropic sources of light with a broad spectrum. This contrasts with a laser that produces very directional and monochromatic light. The narrow spectrum is a measure of the temporal coherence of the source, whereas the directivity is a measure of its spatial transverse coherence. Recently, it has been realized[1–3] that a thermal source of light could be coherent in the near field, i.e., when analyzing the light at distances of the surface much smaller than the peak wavelength of the spectrum. Further work has led to the construction of a coherent thermal source of light.[4] It has thus been shown that a source based on spontaneous emission may produce light that is partially coherent, both spatially and temporally. In this paper, we shall report a detailed study of this type of source and discuss the role of surface waves in building coherent fields. We will report a measurement of the coherence length of the field along the source. We will also carefully study the role of the temperature on the emission. We will finally report measurements on a type of source that produces an isotropic emission of light.

The emission of light by hot bodies is usually discussed in the context of energy transfer or thermodynamics using phenomenological concepts such as absorptivity, emissivity, and specific intensity.[5,6] However, it is possible to address this problem in the framework of classical electrodynamics. This approach was first used by Lorentz[7] but, at that time, the statistical properties of the random currents were not known, so that it was impossible to obtain the Planck function following this route. This is why this type of approach has been abandoned in textbooks. Indeed, radiation in a vacuum, i.e., blackbody radiation, is usually derived using the Bose-Einstein statistics for photons. This approach can be used only if the electromagnetic states of the system are known and at thermodynamic equilibrium. Nonequilibrium phenomena such as emission by a specific material are usually described using a phenomenological theory. None of these theories allows one to derive the emitted fields starting from the basic principles of electrodynamics.

The basic idea of an electromagnetic treatment of thermal radiation is that each volume element of a body at temperature *T* can be viewed as a random electric dipole. Indeed, because of the random thermal motions of electrons and ions, there are random currents in the material. Therefore, each volume element can be viewed as an electric dipole that generates an electric field. Next, we have to derive the field generated by a dipole below an interface. This is a standard problem that was first solved by Sommerfeld. A detailed discussion can be found in the monograph by Banos.[8] Although the solution involves some integrals that may not be easy to evaluate analytically, the problem can be worked out numerically.[9] It is worthwhile to point out that all the optical properties of the medium and all the resonances of the interface are taken into account when computing the field emitted by a dipole below the interface (i.e., the Green tensor of the problem). Because the mean value of the current is null, the mean value of the electric field is also null. The quantity that is then needed is the correlation function of the current density which is given by the fluctuation-dissipation theorem derived in 1951.[10] The full treatment was first given by Rytov *et al.*[11] It was applied by these authors mostly to radio waves emission problems, but the framework is valid for any frequency. For instance, this approach allows one to derive rigorously the emissivity for a flat surface and thus to retrieve the usual phenomenological result. Furthermore it yields the field in the vicinity of the interface because surface modes are fully taken into account. When surface waves can exist, the field is completely dominated by these thermally excited surface waves. They produce unexpected results. First of all, the spectrum of the energy density becomes almost monochromatic.[2] Its Fourier transform yields the first order (i.e., amplitude) correlation function according to the Wiener-Khinchin theorem. It appears that the field has a long coherence time. Second, the density of energy increases by several orders of magnitude.[1,2] Third, the field can be shown to be spatially coherent over distances much larger than the wavelength along the interface.[1,3] These facts contradict the

0163-1829/2004/69(15)/155412(11)/$22.50

widely accepted point of view that a thermal source of light is incoherent. All these effects cannot be detected in the far field because they are due to surface waves which decay exponentially away from the interface. Yet, roughness can couple surface waves to propagating waves, and thus transfer the coherence properties into the far field.[4] Note that we do not claim that a thermal source produces a laserlike field. First of all, the mean occupancy number of each state is still given by the Bose-Einstein law. Second, the intensity statistics are very different for a laser and a thermal source. However, surface waves do produce a significant time and spatial second order coherence of the field in the near-field. This coherence can be used to modify significantly the radiative properties of surfaces.

To proceed, one can modify the surface profile. It has been known for a long time that microroughness modifies radiative properties. In particular, the influence of a grating on the absorption properties has been studied in great detail.[12] A spectacular effect was predicted and verified experimentally[13] in 1976: ruling a shallow sinusoidal grating on a gold surface may lead to a total absorption of visible light for a particular polarization. This behavior has been associated with the resonant excitation of a surface mode: a surface plasmon polariton. Due to its resonant character, this absorption takes place for a particular angle once the frequency is fixed.

Absorption is not the only radiative property that depends on the surface profile. According to Kirchhoff's law, the emissivity of a surface is equal to the absorptivity for the same frequency, same direction, and same polarization. Its validity has been a subject of debate for some time but the question was finally settled[5] when a proof was derived from the reciprocity theorem that follows from Maxwell's equations. Based on this argument, it is thus expected to observe a manifestation of surface waves on the emission of light by surfaces. This has indeed been observed recently by Kreiter *et al.*[14] on a gold surface heated at 700 °C. Because of the range of temperature needed, it is easier to observe these effects in the infrared. Although surface plasmon polaritons may exist for highly doped semiconductors, it is easier to observe these phenomena by taking advantage of a different type of surface waves. They are called surface phonon polaritons. They can be viewed schematically as phonons in an ionic crystal. The mechanical vibration of the ions generates a charge oscillation and therefore an electromagnetic wave.

In the early 1980s, Zhizhin *et al.* studied thermal emission of materials supporting surface phonon polaritons.[15] They worked with a ZnSe crystal sample including periodic inhomogeneities on its surface. The sample was heated at 150 °C in order to excite surface waves. Coupling these waves with the periodic profile, they observed emissivity spectra in the *p* polarization changing with the direction of observation. That observation was a signature of the excitation of a surface wave. It is worth mentioning that the emission assisted by the excitation of a surface wave has been used in a different context. In the late 1980s, Gruhlke, Holland, and Hall observed the luminescence by atoms placed in a film with a grating on top of it. They observed that the presence of the grating modified significantly the emission. The interpretation is that the emission of the atoms excited a surface mode that was subsequently diffracted by the grating.[16] It is interesting to compare the two emission phenomena because they have the same basic mechanism. The spontaneous emission of light by a metallic grating can be viewed as follows: (i) nonradiative decay of a thermally excited electron or phonon into a surface phonon polariton, and (ii) diffraction of the surface phonon polariton by the grating. Other authors have used this idea more recently. Let us mention the enhanced fluorescence of emitters (Eu^{3+}) located in close proximity to a metallic grating surface[17] and the extraction of light emitted by an active source located inside a modulated structure.[18]

Later on, Hesketh and Zemel measured thermal emission at 400 °C of doped silicon gratings. They observed resonances in the emission amplitude in the *p* polarization and different spectra when varying the grating period.[19–21] As we will see, the phenomenon reported by Hesketh and Zemel was related to the presence of surface plasmon polaritons and not to organ pipe modes, as first thought. Many other authors have experimentally explored the role of texture on emissivity. We will not mention here the works done on gratings with a period larger than the wavelength so that the geometric optics apply. In 1995, Auslander and Hava studied anomalous reflectance in doped silicon lamellar gratings due to the surface profile of a grating. Yet, they worked in *s* polarization,[22] so that these effects were not related to surface wave excitation. Nevertheless they noticed in 1998 an antireflective behavior in the *p* polarization for V-grooved silicon grating with a SiO_2 mask layer.[23] Sai *et al.* also made calculations and measurements on a three-dimensional V-grooved silicon grating with an SiO_2 mask layer and interpreted their observation in terms of resonance between the field and the grating.[24] Le Gall *et al.*[25] showed that the emissivity of SiC could be increased by ruling a grating. Finally, let us mention a recent attempt to use a photonic crystal structure of tungsten to modify the radiative properties.[26]

In this paper, we will report a detailed study of the thermal emission due to the thermal excitation of surface phonon polaritons. Recent papers[1,2] have shown that the presence of surface waves on a plane interface enhance the temporal and spatial coherence close to the interface (at distances smaller than the typical wavelength given by the Wien displacement law, 10 μm at 300 K, for example). This yields insight into the mechanism of light emission. We will first review these ideas. We will then study the interplay between the disorder of the microstructure of a material and the spatial coherence of the field by comparing amorphous and crystalline silica. We will then describe an experimental setup designed to enhance the angular and spectral resolution of emission measurements. We will report a detailed experimental study of the emission of a grating. We will, in particular, examine carefully the role of temperature in the results. We will also show that it is possible to engineer the radiative properties of a surface by a proper design of the grating profile using a rigorous coupled wave analysis (RCWA) algorithm.[27] Two thermal sources have been realized. The first source radiates almost isotropically but with an emissivity enhanced by more than an order of magnitude. The second source has an

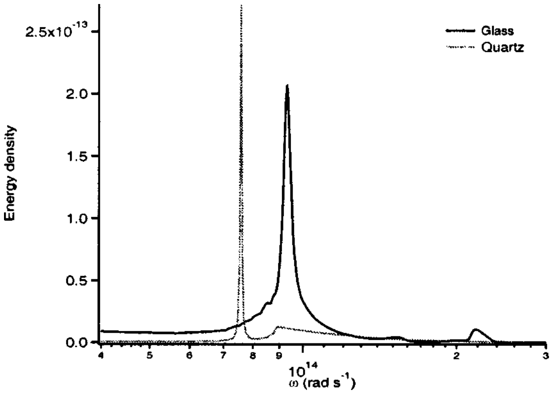

FIG. 1. Energy density above a vacuum-silica interface in the near field. Note the shift of the peak frequency depending on the microscopic structure.

emission pattern that displays two narrow lobes like an antenna. Finally, we will show how the coherence length along the source can be recovered from our far field emission measurements and discuss qualitatively the origin of the spatial coherence.

II. COHERENCE IN THE NEAR FIELD

A. Temporal coherence in the near field

In this section we consider the emission of light by a half space containing silica, either amorphous (glass) or crystalline (quartz). The upper half space is a vacuum. We plot the density of electromagnetic energy as a function of frequency in the near field in Fig. 1. We see that the spectrum is no longer a broad spectrum with an envelope given by the Planck function; instead, the spectrum has a narrow peak. This is a signature of the temporal coherence of the electromagnetic field close to the interface. A striking property is the numerical value of the density of energy. It is roughly larger than the density in vacuum by four orders of magnitude. Similar results for SiC were first reported in Ref. 2. These surprising results can be understood as follows. The energy density is proportional to the local density of electromagnetic states. Close to an interface, there are not only plane waves, which are the solutions of Maxwell equations in a vacuum, but also surface waves. These additional solutions produce a peak of the density of states at a particular frequency, as seen in the dispersion relation of Appendix A. In the case of ionic crystals, the origin of this peak is easy to understand. It is the frequency of the optical phonons which is basically the mechanical eigenfrequency of the atoms in a primitive cell. Since the atoms carry a partial charge, they produce an electromagnetic field. With this picture in mind, it is easy to understand why the density of energy increases when approaching the interface. Each primitive cell is equivalent to an oscillating dipole. As the distance is reduced, the electrostatic contributions in the dipole radiation become the dominating terms.

When comparing the two curves in Fig. 1, it is seen that the effect of the desorder of the amorphous glass is to broaden and to shift the resonance peak. This can be qualitatively understood. Indeed, (i) amorphous glass is a more disordered system so that surface phonon polariton are expected to be strongly damped, and (ii) the local environment of each cell varies from one cell to the other so that a broadening of the spectrum is expected.

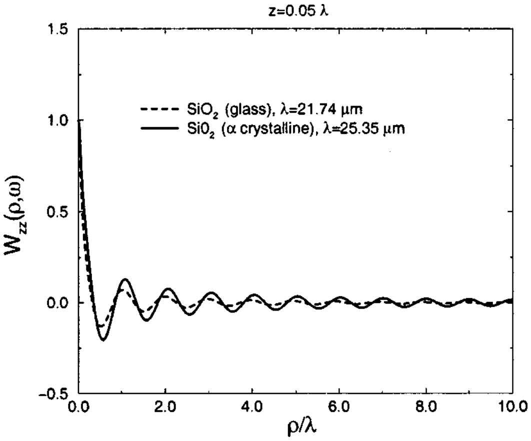

FIG. 2. Cross-spectral density of the z component of the electric field above a vacuum-glass interface. Note that the coherence length of the amorphous silica is smaller than for the crystalline form.

B. Spatial coherence

Since we have seen that the electromagnetic field is temporally coherent in the near field, it is natural to revisit its spatial coherence properties. It is also of interest to investigate the role of the structure of the material on the spatial coherence. To this end, we show in Fig. 2 the cross-spectral density of the z-component of the electric field along the interface at a distance of λ/20 for crystalline and amorphous silica. It has been calculated following the procedure outlined in Ref. 1. At a frequency that coincides with the peaks of the density of energy, there are many wave vectors excited so that the spatial spectrum is very broad. Accordingly, the correlation function has a very small range. In contrast, when looking at the cross-spectral density for a lower frequency, we observe a long range correlation of the electromagnetic field along the interface. Similar results were obtained previously for SiC and metals.[1] Not surprisingly, we observe that the coherence length of the amorphous glass is smaller than the coherence length for the crystalline quartz. Yet, it is seen that there exists a non-zero correlation over distances as large as four wavelengths (i.e., 88 μm) for the amorphous glass, indicating that there is still some order on this scale length. The origin of the long-range coherence of a thermal source that support a surface wave can be viewed as follows. The random electric dipole associated with each volume element of the medium excites a surface wave. Since the surface wave is a delocalized mode, the oscillations produced along the surface are coherent within a distance which is given by the decay length of the surface wave. In other words, each volume element is dressed by a surface wave that oscillates coherently over an area determined by the decay length of the surface wave along the interface. Thus each elementary source has an effective spatial extension along

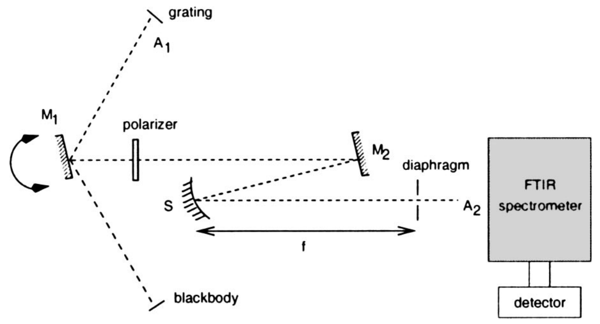

FIG. 3. Experimental setup used for measuring emissivity spectra.

the planar source which may be much larger than the wavelength in vacuum. In what follows, we will use these coherence properties to design sources with specific properties. Depending on the coherence properties, it is possible to design either a highly directional or a quasi isotropic source. In Sec. III, we describe the experimental setup that was built in order to measure the emission with high angular and spectral resolution.

III. EXPERIMENTAL SETUP

A. Optical system

The optical system is schematically shown in Fig. 3. Points A_1 and A_2 are conjugated. A_1 represents the grating or the blackbody and A_2 is the point which is conjugated with the detector through the spectrometer. Thus, the image of the detector determines the area of the sample which is observed. This allows to choose an isothermal area.

A diaphragm (diameter Φ) was placed in the Fourier plane of the spherical mirror. In this position, it makes an angular selection of the directions of emission which are observed. In other terms, we control the solid angle of observation by varying the diameter of the diaphragm. In our setup, $f=300$ mm and $\Phi=3$ mm, so that the solid angle of detection is $\Omega_{\text{detection}}\approx 8\times 10^{-5}$ sr. It is smaller than the solid angle of the natural emission of the grating due to a surface phonon polariton (SPP) $\Omega_{\text{emission}}\approx \pi(\lambda/L)^2$, where $L<1$ mm is the typical propagating length of the SPP on the plane interface. One sees that $\Omega_{\text{emission}}>3.10^{-4}$ sr.

The grating is heated by eight thermal electric resistances and its temperature is controlled by a regulator WEST4200. In the experiment, the target temperature for the grating is 773 K with a precision better than 1 K.

We used an infrared Fourier transform spectrometer DA8 BOMEM. The spectral resolution of this spectrometer varies between 0.01 and 4 cm^{-1}. The measurements have been made with a spectral resolution of 0.5 cm^{-1}, which corresponds to a precision of 5 nm at $\lambda=10$ μm. The detector is a HgCdTe detector cooled at 77 K. Each spectrum is an average of 500 scans: the noise is thus considerably reduced. The beamsplitter of the spectrometer is made of KBr, which is a transparent material in the working frequency range.

B. Experimental procedure

For each angle, we took several measurements of the emission of the sample, of a reference blackbody and of the ambiant radiation. For frequencies below 1500 cm^{-1}, the ambiant radiation reflected on the sample cannot be neglected. The emissivity spectrum S_ε is obtained by subtracting the background signal. The details of the procedure are given in Appendix B.

In order to obtain the emissivity spectrum, we need to know the exact value of the sample temperature. This is achieved by taking advantage of the Christiansen wavelength. At this point, the emissivity ε_λ of the SiC surface is equal to 1. The Christiansen frequency depends neither on the temperature nor on the roughness. We have the following relation:

$$I_{\lambda,T}=\varepsilon_\lambda I^0_{\lambda,T}, \tag{1}$$

where $I_{\lambda,T}$ is the specific intensity of the radiation emitted by the surface at wavelength λ and temperature T, and $I^0_{\lambda,T}$ is the blackbody specific intensity in the same conditions. At the wavelength λ, we can define a temperature T_λ such that $I_{\lambda,T}=I^0_{\lambda,T_\lambda}$. When $\varepsilon_\lambda=1$, we have

$$I_{\lambda,T}=I^0_{\lambda,T}=I^0_{\lambda,T_\lambda}, \tag{2}$$

i.e., $T=T_\lambda$. We can thus determine the exact temperature of the sample. For SiC $\lambda_{\text{Christiansen}}=10.034$ μm. We found that the temperature of the sample in our experiment was $T_S=770$ K.

IV. A QUASIMONOCHROMATIC AND ISOTROPIC THERMAL SOURCE

In this section, we show how to enhance the emissivity of the sample in all directions by taking advantage of the thermal excitation of the surface wave. To this end, we rule a grating on the surface so that the surface wave can be coupled to propagating waves. In order to be able to couple light to any direction, it is necessary to work at a frequency where the dispersion relation is flat (see Appendix A). For fabrication reasons, it is easier to work with a lamellar grating (i.e., with a rectangular surface profile). The characteristics of such a grating are the period Λ, the filling factor F, and the depth h. We optimized the grating parameters in order to maximise the emissivity using a rigorous coupled wave algorithm.[27] For SiC, we found the following characteristics: $\Lambda=3$ μm, $F=0.4$, and $h=0.35$ μm.

In Fig. 4(a), we show two experimental curves, obtained in the conditions described in Sec. III. We represent emissivity spectra for the grating and for the plane interface in p polarization in the normal direction of observation. One can see that a peak appears in the presence of a grating. This peak does not exist for s polarization [see Fig. 4(b)]. The polarization dependence suggests that the grating is not essential but serves to reveal an intrinsic property of the surface. It indicates the role of the SPP in this phenomenon since the SPP exists only for p polarization as discussed in

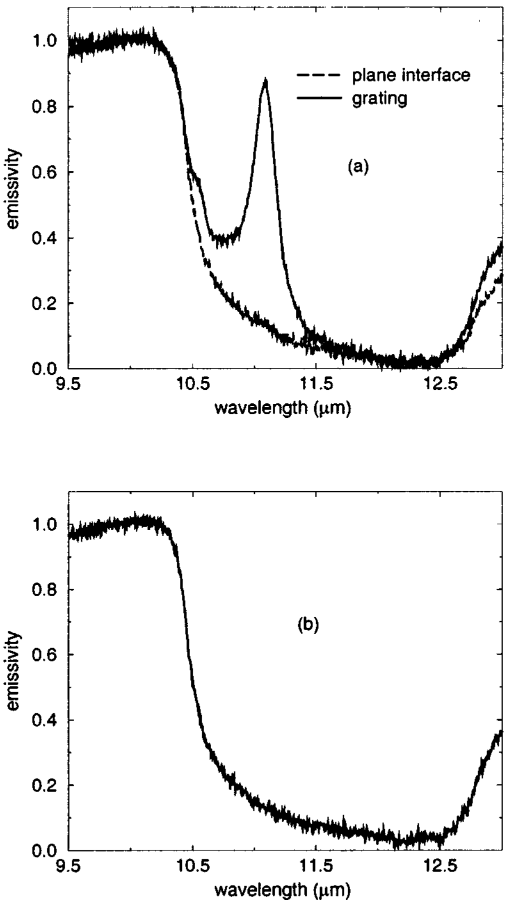

FIG. 4. Emissivity spectra of a smooth grating $\Lambda = 3.00\ \mu$m, $F = 0.4$, and $h = 0.35$. (a) Case of p polarization. (b) Case of s polarization.

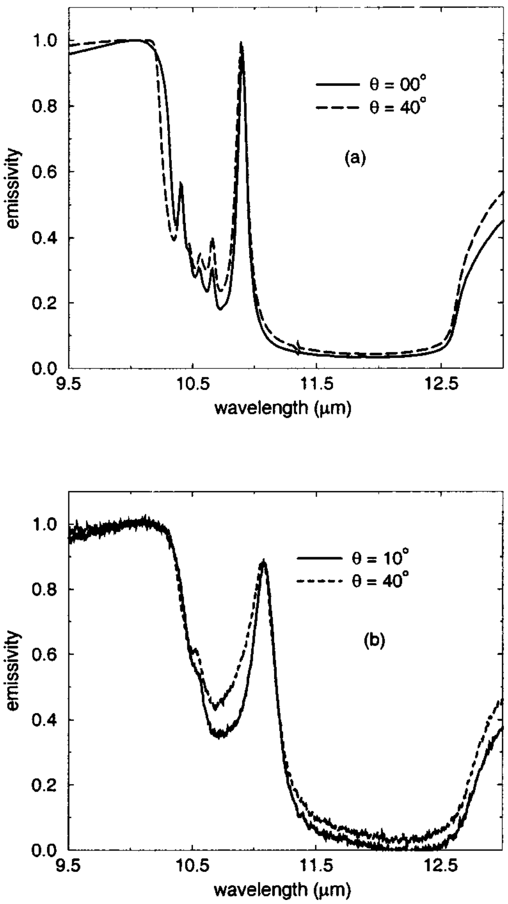

FIG. 5. Emissivity spectra in the p polarization of a smooth grating; $\Lambda = 3.00\ \mu$m, $F = 0.4$, and $h = 0.35$ for two direction of observation $\theta = 10°$ and $40°$. (a) Theoretical spectra. (b) Experimental spectra.

Appendix A. Further evidence of the role of the SPP will be given in Sec. V.

When the angle of observation changes, one can see in Fig. 5 that a peak still exists at the same wavelength. Figure 5(a) presents the theoretical spectra and Fig. 5(b) the experimental one. The experimental peak is lower and wider than the theoretical peak. It is also seen that the experimental peak appears at a wavelength $\lambda \approx 11.1\ \mu$m, instead of 10.9 μm in the calculation. We will explain this spectral shift and the broadening of the peak in the following sections.

In Fig. 6, we plot the emissivity versus the angle θ at a fixed wavelength $\lambda = 11.09\ \mu$m. We see that the emission at this wavelength is almost isotropic and increases from a value lower than 0.1 to a value larger than 0.8 at any angle. One can understand this phenomenon by inspection of the dispersion relation (see Appendix A). As a matter of fact the excited SPP lies on the asymptotic branch, characterized by $\omega = 946\ \mathrm{cm}^{-1}$ in the calculation. For a fixed wavelength, there are many SPPs with different wave vectors, i.e., different directions θ of emission. For all these directions the grating emits a quasimonochromatic radiation. Thus, using a SPP thermal excitation, we have succeeded in designing a thermal source which is both isotropic and quasimonochromatic. This concept can be extended to different materials. Tungsten, for instance, is a very good emitter in the visible but its emissivity in the infrared is low. The mechanism that we have described could be used to enhance its emissivity in the infrared, taking advantage of the surface plasmon polaritons.

V. A DIRECTIONAL THERMAL SOURCE

In this section, we consider a grating designed to emit light at a well-defined angle. In order to illustrate the role of the surface wave, we have calculated the emissivity as a function of angle of emission and frequency for a grating. This grating was designed to have a maximum absorption for

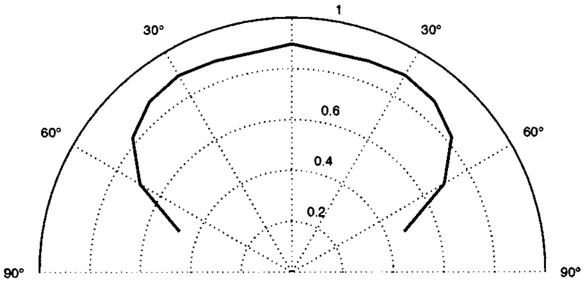

FIG. 6. Experimental emissivity diagram in polar coordinates of a smooth grating; $\Lambda = 3.00\ \mu$m, $F = 0.4$, and $h = 0.35$

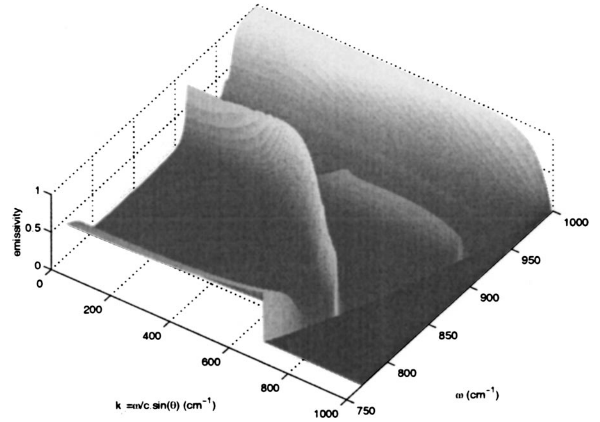

FIG. 7. Emissivity of a SiC grating as a function of frequency and angle of emission. It is seen that the peaks of emission coincide with the dispersion relation of the SPP in the (ω,k) plane.

11.36 μm. The result is displayed in Fig. 7. It is seen that the peaks of emissivity closely follow the dispersion relation of the SPP on a flat surface shown in Fig. 16. In this calculation, we see that the emissivity takes large values for any angle at a particular frequency on the order of 946 cm^{-1}, as already discussed. Furthermore, we see that for lower values of the frequency, the dispersion relation is no longer flat, so that for a given frequency, emission takes place for a well-defined angle. In this part of the spectrum, we expect an angle-dependent spectrum. In other terms, in each direction the grating emits at a different wavelength. We optimized the following characteristics for the grating: $\Lambda=6.25$ μm, $F=0.5$, and $h=0.285$ μm. Such a grating was already studied by Greffet *et al.*[4] In this work we report measurements of the emission spectrum and a quantitative analysis of the data. We will show that we can deduce the coherence length of the source from the emission data. We will also show that it is possible to obtain a quantitative agreement of measurement with theory at high temperature.

We plot the measured emissivity versus the angle θ in Fig. 8 for $\lambda=11.36$ and 11.89 μm. It is seen that the emission at a fixed wavelength is very directional: the heated grating behaves like an infrared antenna. This is a signature of the spatial coherence of the source. In previously reported measurements, the angular resolution was limited by our signal to noise ratio. We had to increase the aperture of the detection system. The spectral resolution was also limited by signal to noise ratio. In this measurement, we are no longer limited by the instrument in our measurement of the angular width. For instance, our measurement shows that the peaks are narrower when the angle θ increases as predicted by the theory. This will be fully discussed in the following section.

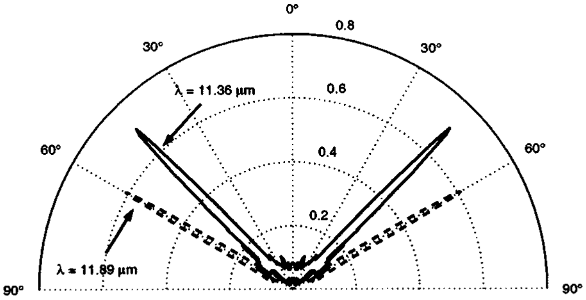

FIG. 8. Experimental emissivity diagram in polar coordinates of a smooth grating; $\Lambda=6.25$ μm, $F=0.5$, and $h=0.285$ at two different wavelengths $\lambda=11.36$ and 11.89 μm.

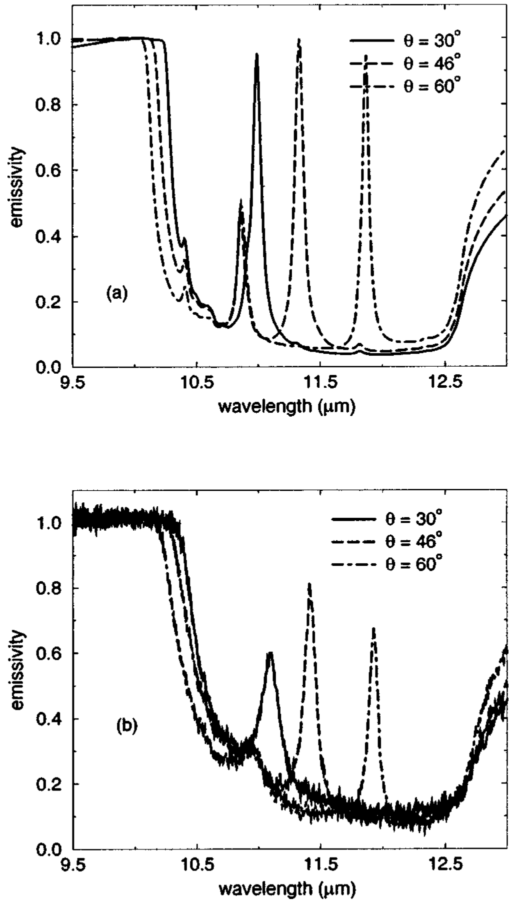

FIG. 9. Emissivity spectra in the p polarization of a smooth grating, $\Lambda=6.25$ μm, $F=0.5$, and $h=0.285$ for three directions of observation $\theta=30°$, 46°, and 60°. (a) Theoretical spectra. (b) Experimental spectra. The theoretical curve was calculated with the dielectric data at $T=300$ K, and a grating period of $\Lambda=6.28$ μm.

We now show the comparison between three theoretical and experimental spectra in Figs. 9(a) and 9(b), respectively, for the angles $\theta=30°$, 46°, and 60°. As we have seen in Sec. IV, the experimental emissivity is not equal to 1 at the peak wavelength and the peak wavelength is shifted by about 0.1 μm. As in Sec. IV, the experimental peak is wider than the theoretical one. However, the agreement between theory and experiment for reflectivity is excellent as shown in Ref. 4. Thus, we find that theory agrees with reflectivity data but not with emissivity data.

We are now going to analyze the origin of this discrepancy. A possible mechanism is that the grating period varies with the temperature T due to the thermal expansion of SiC as its temperature increases. We measured the period of the grating at 300 and 770 K using a diffraction method. We obtained $\Lambda=6.26$ and 6.28 μm, respectively, with a precision better than 1%. This variation does not affect signifi-

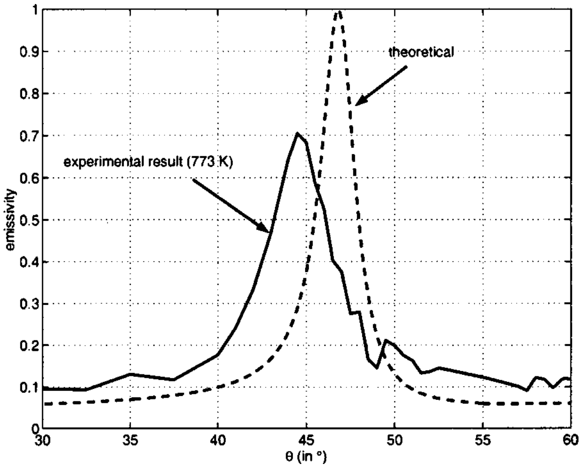

FIG. 10. Experimental emissivity vs the direction of observation θ ($\lambda = 11.36\ \mu$m).

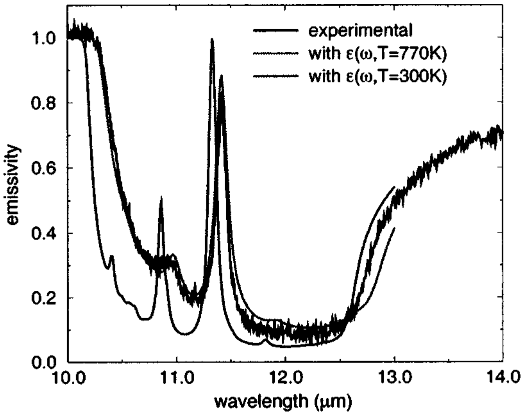

FIG. 11. Experimental and theoretical emissivity spectra. Calculations have been made with two different dielectric constants $\epsilon(\omega)$ at temperatures $T = 300$ and 770 K.

cantly the position of the peak. In Fig. 10 we show the theoretical and experimental emissivity versus the angle of observation θ for a SiC grating with a period $\Lambda = 6.28\ \mu$m at $\lambda = 11.36\ \mu$m. One can see that the thermal expansion of the grating does not explain the experimental result.

Another possible mechanism is the variation of the optical index with temperature. The position of the peak is mainly related to the dependence of the real part ϵ' of the dielectric constant with the temperature T; the width and the height are related to the material absorption, i.e., to the imaginary part ϵ''.

In order to find the dielectric constant at high temperature, we measured the emissivity of a flat surface at normal incidence. We then used a model for the dielectric constant with adjustable parameters. This calculation was made using a Lorentz model by varying ϵ_∞, ω_L, ω_T, and Γ so as to minimize the difference between theoretical and experimental emissivity ε (or reflectivity) as a function of ω. This is achieved by minimizing the following quantity:[28]

$$S = \sum_{i=1}^{N} [\varepsilon_{\mathrm{exp}}(\omega_i) - \varepsilon_{\mathrm{th}}(\omega_i)]^2, \tag{3}$$

where N is the number of experimental points. The number of experimental points was $N = 59$, taken between $\lambda = 9$ and 13 μm. We obtained $\epsilon_\infty = 6.8$, $\omega_L = 959\ \mathrm{cm}^{-1}$, $\omega_T = 779\ \mathrm{cm}^{-1}$, and $\Gamma = 11.7\ \mathrm{cm}^{-1}$. One can see that the variations are not very important (lower than 2%) except for Γ, which has been multiplied by about 2.5. This is not surprising. The main source of losses is phonon scattering. It obviously increases with T. Here we retrieve the increase of the absorption, which can explain the width and the height of the experimental peak.

Finally, we have used the new values of the oscillators parameters ϵ_∞, ω_L, ω_T, and Γ to derive the emission spectrum. In Fig. 11 we show the experimental spectrum at $\theta = 46°$ with the theoretical spectra at both ambiant and high temperature. It is seen that there is a very good agreement between the experiment and the calculation when the proper optical data are used. This confirms that the results depends on T through the parameter Γ. We made experiments at different temperatures between 450 and 770 K. In Fig. 12 we show the dependence of the coefficient Γ with the temperature in this range.

VI. MEASUREMENT OF THE COHERENCE LENGTH

We have seen in Sec. V that thermal emission by a SiC grating may become very directional at certain wavelengths. This can be interpreted in terms of spatial coherence: when a source is spatially coherent the radiation emitted by two different points of the source can interfere constructively in a given direction and destructively in the others producing angular lobes. The goal of this section is to use the far field data to recover the coherence length of the field in a plane placed just above the planar source.

We are interested here in the p-polarized emissivity, and the plane of detection is perpendicular to the grating lines. Thus the problem can be fully treated in terms of the scalar magnetic field at a given wavelength $\mathbf{H}(\mathbf{r},\lambda) = H_y(\mathbf{r},\lambda)\mathbf{e}_y$. In this case, we can characterize the spatial coherence with a coherence length calculated via the scalar cross-spectral den-

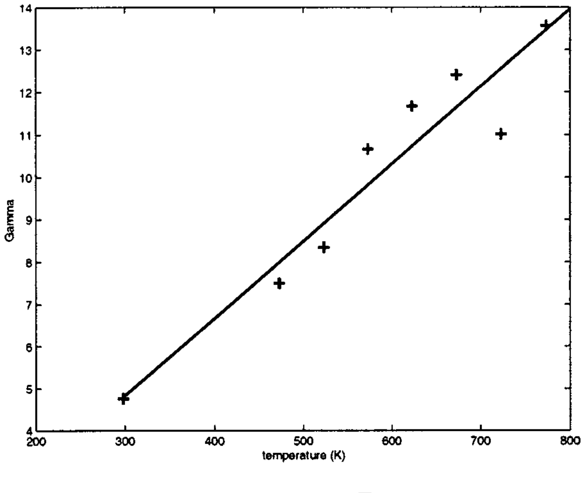

FIG. 12. Variation of the coefficient Γ in the dielectric constant with the temperature.

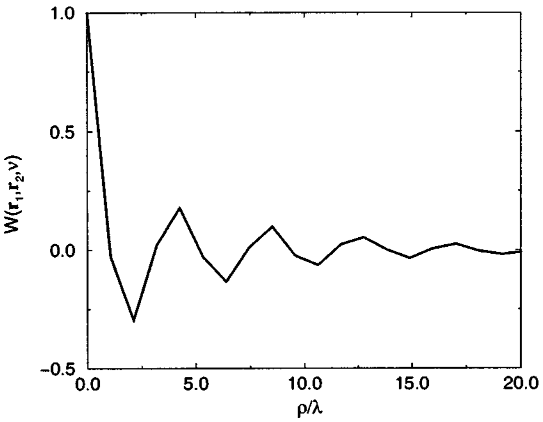

FIG. 13. Spectral degree of spatial coherence for a SiC grating; $\Lambda=6.25$ μm, $F=0.5$, and $h=0.285$ heated at $T=300$ K.

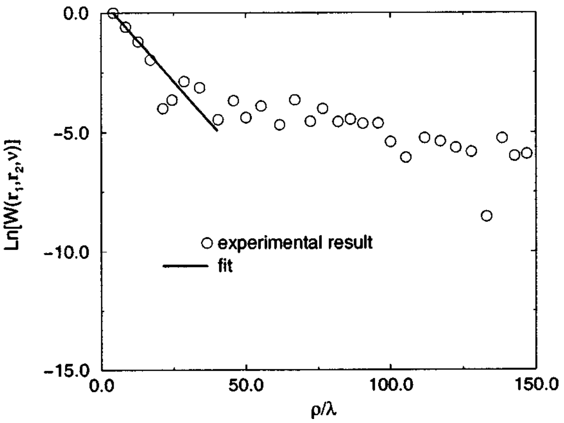

FIG. 14. Determination of the spatial coherence length.

sity function in the near-field $W(\mathbf{r}_1,\mathbf{r}_2,\lambda)$ defined by $W(\mathbf{r}_1,\mathbf{r}_2,\lambda)\,\delta(\lambda-\lambda')=\langle\widetilde{H_y}^*(\mathbf{r}_1,\lambda)\widetilde{H_y}(\mathbf{r}_2,\lambda')\rangle$ where $\widetilde{H_y}$ is the spectral Fourier transform of H_y.[29]

The emissivity diagram yields the radiant intensity in the far-field $J(\mathbf{s},\lambda)$, where $\mathbf{s}=\mathbf{k}/k$ and $\mathbf{k}$ is the wave vector of the incident wave on the detector. It can be shown that[29]

$$W(\mathbf{r}_1,\mathbf{r}_2,\lambda)\propto\int J(\mathbf{s},\lambda)\exp\left(i2\pi\mathbf{s}\cdot\frac{\mathbf{r}_2-\mathbf{r}_1}{\lambda}\right)d^3\mathbf{s}. \tag{4}$$

$W(\mathbf{r}_1,\mathbf{r}_2,\lambda)$ appears as a spatial Fourier transform of $J(\mathbf{s},\lambda)$ with respect to the variable $(\mathbf{r}_2-\mathbf{r}_1)\lambda$. One must take care that the radiant intensity is defined in the far-field so that we only have access to part of the spectrum of the cross-spectral density. More precisely, the field near the grating at a given wavelength can be split into four contributions:

$$\mathbf{H}=\mathbf{H}_{n-f}+\mathbf{H}_{sw-nr}+\mathbf{H}_{sw-r}+\mathbf{H}_{pw}, \tag{5}$$

where $\mathbf{H}_{n-f}$ is the very near-field (quasistatic) component of $\mathbf{H}$, $\mathbf{H}_{sw-nr}$ is the field associated with the part of the SPP which is not radiated (part of the dispersion relation lying below the light cone), $\mathbf{H}_{sw-r}$ is the field associated to the part of the SPP which is radiated by the grating and $\mathbf{H}_{pw}$ is the propagating wave contribution. The latter is the only contribution that is emitted in the far field by a flat surface. Only the last two components contribute to the signal received by the detector. These contributions are decorrelated and the cross-spectral density function can be splitted into four parts which are associated with the quasistatic near field, the radiative and nonradiative SPPs, and the natural emission of the sample. The cross-spectral density function reconstructed from the far-field data is thus $W_{\text{calculated}}=W_{sw-r}+W_{pw}$. Note that a flat surface would yield essentially W_{pw}.

In Fig. 13 we plot the reconstructed cross-spectral density function at the wavelength $\lambda=11.36$ μm versus the quantity ρ/λ, where $\rho=|\mathbf{r}_2-\mathbf{r}_1|$. As discussed above, it contains all the information on the radiated surface wave. This function is normalized by its value at $\rho=0$. Note that this normalization amounts to plotting the spectral degree of spatial coherence. One can see that the SPP is correlated in the near field over distances ρ of the order of several wavelengths. It is possible to show that the cross-spectral density function decreases exponentially. We define the coherence length as the value of ρ when the spectral degree of coherence is divided by e. In Fig. 14 we plot the neperian logarithm of the envelope of the last curve: it is clearly seen that there is a linear decay between $\rho=\lambda$ and 20λ. The slope yields the coherence length: we obtain on this particular case $L_{\text{coherence}}\approx7\lambda$. To our knowledge, this is the first measurement of the coherence length of a thermal source. We made the same analysis for the grating at $T=300$ K, using numerical simulations for the emissivity data. We obtained $L_{\text{coherence}}\approx11\lambda$. Another calculation was made in Ref. 1 for a plane interface of SiC, where the coherence length at $\lambda=11.36$ μm was 36λ. We see that the presence of the grating reduces the coherence length by a factor of 3 approximately because of the introduction of radiative losses. Another mechanism that reduces the coherence length is the increase of the damping of the surface phonon polariton due to the increase of the term Γ of the dielectric constant, as seen in Sec. V. This is due to the increase of the phonon-phonon collision as the temperature is increased.

VII. CONCLUSION

In this paper, the coherence properties of thermal near fields have been reviewed. The modification of the coherence properties of the electromagnetic field can be attributed to the presence of surface waves. We have discussed the influence of the microstructure of the material on the temporal and spatial coherence properties. We have shown how the near-field properties can be used to engineer the emission and absorption properties of surfaces. Taking advantage of the flat dispersion relation of the surface wave in a given spectral range, it is possible to produce a source of high emissivity which is almost isotropic and quasimonochromatic. In contrast, when working in the region where the coherence length is large, it is possible to realize a very directional source of light that behaves as an infrared antenna with well-defined lobes. Experimental and theoretical results have been reported showing an agreement better than 2% when proper temperature optical dependent data are used.

From these measurements, we were able to obtain a quantitative value of the coherence length of the thermal sources. This study has highlighted the role of surface waves in the process of light emission by thermal sources. A simple mechanism can be proposed: the first step is excitation of surface waves by thermally excited random dipoles, the second step is the diffraction of the surface waves by a grating. This analysis can have a large impact on the design of light sources. Indeed, the mechanism and the same concepts can be applied to design novel light sources using any physical process that excite surface waves. An advantage of this type of light source is the possibility of engineering the dispersion relation by modifying the surface profile. This allows one to produce either directional or isotropic sources. It also allows one to shift the emission frequency. Finally, we stress that the modification of the dispersion relation amounts to modify the local density of electromagnetic states and therefore, to modify the radiative decay of any type of excitation.

ACKNOWLEDGMENTS

We acknowledge support from Ministere de la recherche, contract Action Concertee Incitative Nanostructures N76-01.

APPENDIX A: SURFACE PHONON POLARITONS ON A PLANE INTERFACE

1. Surface waves at an air/material interface

In this appendix, we briefly review some characteristics of the surface waves which may propagate on a flat material/air interface. A surface wave has an exponential decay away from the interface and propagates along the interface. It is thus a wave that has the forms

$$z>0, \quad \mathbf{E}(x,z)=\mathbf{E}_0 \exp[i(k_{\parallel}x+\gamma_1 z)], \tag{A1}$$

$$z<0, \quad \mathbf{E}(x,z)=\mathbf{E}_0 \exp[i(k_{\parallel}x-\gamma_2 z)]. \tag{A2}$$

It can be shown[30,31] that such a solution exists at a vacuum/material interface for materials that have a dielectric constant whose real part is smaller than -1. This happens when the material structure has a resonant behavior. For metals, it corresponds to the plasma oscillation which is a collective oscillation of the electrons.[30,31] For dielectrics, it occurs for frequencies that are in the range of the optical phonons. In both cases, the excitations are delocalized damped modes.

The surface electromagnetic waves are actually charge density waves. Surface plasmon polaritons are due to an acoustic type of oscillation of the electron gas. This mechanical wave of charged particles generates an electric field. The term polariton means that the wave is half an acoustic vibration and half an electromagnetic vibration. In the case of polar dielectrics, the surface waves are called surface phonon polaritons. The underlying microscopic origin is a mechanical vibration of the atoms or phonon. If the phonon takes place in a medium where the atoms carry a partial charge (polar material), the mechanical oscillation is associated with an electromagnetic vibration. Thus, roughly speaking, the surface phonon polariton is half a phonon and half a photon. More precisely, the ratio of mechanical energy to the electromagnetic energy changes continuously as the frequency varies. The horizontal part of the dispersion relation is the phononlike part. In the case of SiC, surface waves are surface phonon polaritons. Other polar materials such as oxydes (e.g. SiO_2) or II-VI and III-V semiconductors for example can also support SPP's. An important property to keep in mind is that surface waves are modes of the interface. Therefore, they can be excited resonantly. It is also important to note that these waves exist only for *p* polarization, namely for electric fields in the plane (*x*,*z*).

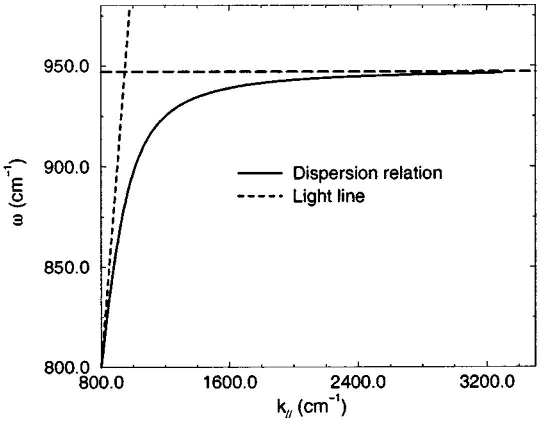

FIG. 15. Dispersion relation of a surface-phonon polariton on a plane surface.

In this paper, we study in detail silicon carbide. This material has interesting properties in the infrared range. Besides, its optical properties $\epsilon(\omega)$ can be described by a simple Lorentz model[28]

$$\epsilon(\omega)=\epsilon_\infty\left[1+\frac{\omega_L^2-\omega_T^2}{\omega_T^2-\omega^2+i\Gamma\omega}\right], \tag{A3}$$

where $\epsilon_\infty=6.7$, $\omega_L=969\ \mathrm{cm}^{-1}$, $\omega_T=793\ \mathrm{cm}^{-1}$, and $\Gamma=4.76\ \mathrm{cm}^{-1}$. The dispersion relation of the SPP has the following dispersion relation for a flat air/material interface:[25,31]

$$k_{\parallel}=\frac{\omega}{c}\left(\frac{\epsilon(\omega)}{\epsilon(\omega)+1}\right)^{1/2}, \tag{A4}$$

where $k_{\parallel}$ is the wave vector of the surface mode.

Solving this equation is not trivial. Indeed, $\epsilon(\omega)$ is complex, so in a general case $k_{\parallel}$ and ω are also complex. Although at first glance, the general choice is to have both quantities complex, it turns out that this is of no use for most cases. The possible choices are either real $k_{\parallel}$ and complex ω or vice versa. One can show[25] that, for this type of measurement, the dispersion relation is well described by assuming that the wave vector is real and the frequency is complex. In Fig. 15 we plot the dispersion relation for $793<\mathrm{Re}(\omega)<947\ \mathrm{cm}^{-1}$ which corresponds to $\mathrm{Re}[\epsilon(\omega)]<-1$. It is seen that there are two different domains: on the one hand, a linear branch $k_{\parallel}\approx\omega/c$, and on the other hand an asymptotic branch for $\omega\approx947\ \mathrm{cm}^{-1}$ which corresponds to $\epsilon(\omega)\approx-1$.

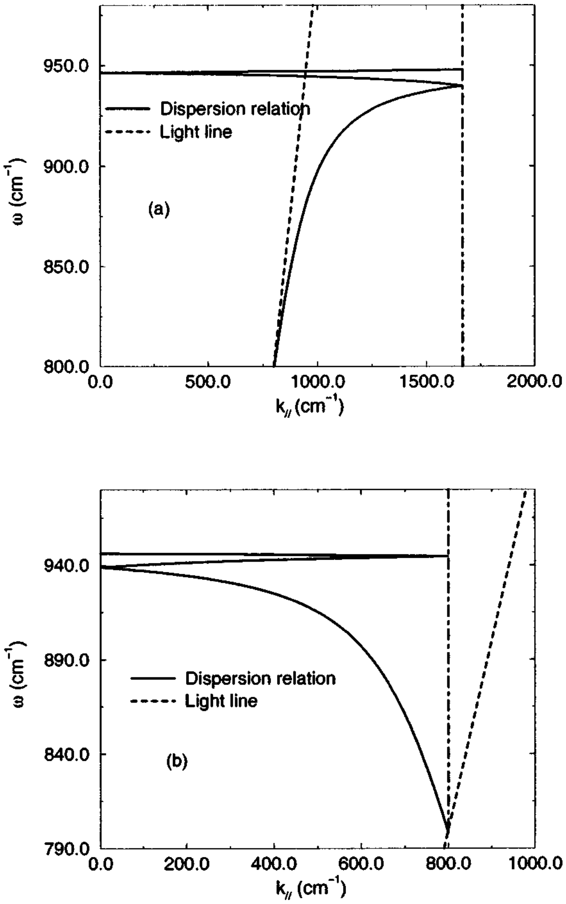

FIG. 16. Dispersion relation of a surface-phonon polariton on a smooth grating. (a) Period $\Lambda = 3.00$ μm. (b) Period $\Lambda = 6.25$ μm.

The curve is under the light line represented by $k = \omega/c$. This means that the solutions are evanescent waves.

2. Role of a smooth grating

As we have seen, the surface wave lies below the light line. All the propagating waves lie above the light line. Since the continuity conditions at the interface demand the frequency and the parallel wave vector to be equal, there cannot be excitation of a surface wave by a propagating plane wave. A well known solution to couple a propagating wave with a SPP is to use a periodic surface. The modes are then Bloch modes whose wave vector is given by

$$\frac{\omega}{c} \sin \theta = k_{\parallel} + m \frac{2\pi}{\Lambda}, \tag{A5}$$

where θ is the angle of propagation, Λ is the grating period and m is the diffraction order. The coupling of an incident propagating wave with a surface mode through the grating can produce up to total absorption.[12] The reciprocal situation is also possible. If a given grating can couple very efficiently the incident light into a surface wave, it can also couple efficiently a surface wave into a propagating mode. This can be used to emit light efficiently. This is the basic mechanism used to produce efficient and coherent thermal sources.

One can interpret Eq. (A5) in terms of dispersion relation. Here we consider that the grating is a smooth perturbation of the flat interface: relation (A4) is still valid. Nevertheless, the dispersion relation can be plotted in a reduced-zone scheme, limited by zero and π/Λ. This reduced-zone scheme depends on the period of the grating. We plot this relation for two different periods $\Lambda = 3$ and 6.25 μm in Figs. 16(a) and 16(b), respectively. It is seen that some parts of the dispersion relation lie in the light cone. These parts are leaky modes ($k_{\parallel} = \omega/c \sin \theta, \omega$) which are radiated in the direction θ.

In the first case [Fig. 16(a)], the upper asymptotic branch lies in the light cone. For each $k_{\parallel}$, only one frequency is possible $\omega \approx 947$ cm^{-1}. We can expect an emission at a single wavelength in each direction. In the second case [Fig. 16(b)], for a greater period, the linear branch of the dispersion relation lies in the light cone. We can expect a very directional emission at each frequency between $\omega = 793$ and 947 cm^{-1}.

Here we retrieve a feature of the Wolf effect:[32,33] the spectral content is linked to the direction of observation. The observed phenomenon is not only a diffractive effect, but an effect due to the strong spatial and temporal correlation of the SPP.

APPENDIX B: EXPERIMENTAL EMISSIVITY SPECTRUM

In this appendix, we describe the procedure used to obtain the emissivity spectrum from the emission measurements. We denote $S_S^{\mathrm{expt}}(\lambda, T_S)$ the experimental spectrum of the sample at temperature T_S. It can be cast in the form[34]

$$S_S^{\mathrm{expt}}(\lambda, T_S) = R(\lambda)[\varepsilon(\lambda) P(\lambda, T_S) + B(\lambda) + \rho(\lambda) P(\lambda, T_R)], \tag{B1}$$

where $R(\lambda)$ is the instrument response function, $\varepsilon(\lambda)$ the directional emissivity, $P(\lambda, T_S)$ the Planck function at the temperature T_S, $B(\lambda)$ the background radiation reaching the detector directly, and $\rho(\lambda) P(\lambda, T_R)$ the ambiant radiation at the temperature T_R reflected by the sample. $\rho(\lambda) = 1 - \varepsilon(\lambda)$ is the directional reflectivity. Using this relation, we can write

$$S_S^{\mathrm{expt}}(\lambda, T_S) = R(\lambda)\{\varepsilon(\lambda)[P(\lambda, T_S) - P(\lambda, T_R)] + B(\lambda) + P(\lambda, T_R)\}. \tag{B2}$$

When we remove the sample, we measure the spectrum of the room radiation denoted $S_R^{\mathrm{expt}}(\lambda, T_R)$. Eq. (B2) becomes

$$S_R^{\mathrm{expt}}(\lambda, T_R) = R(\lambda)[B(\lambda) + P(\lambda, T_R)]. \tag{B3}$$

We have

$$S_S^{\mathrm{expt}}(\lambda, T_S) - S_R^{\mathrm{expt}}(\lambda, T_R) = R(\lambda)\varepsilon(\lambda)[P(\lambda, T_S) - P(\lambda, T_R)]. \tag{B4}$$

The same procedure for a blackbody at temperature T_B, yields a signal denoted

$$S_B^{\mathrm{expt}}(\lambda,T_B)-S_R^{\mathrm{expt}}(\lambda,T_R)=R(\lambda)[P(\lambda,T_B)-P(\lambda,T_R)]. \tag{B5}$$

Finally, we can obtain the directional emissivity spectrum

$$\varepsilon(\lambda)=\left[\frac{S_S^{\mathrm{expt}}(\lambda,T_S)-S_R^{\mathrm{expt}}(\lambda,T_R)}{S_B^{\mathrm{expt}}(\lambda,T_B)-S_R^{\mathrm{expt}}(\lambda,T_R)}\right]\left[\frac{P(\lambda,T_B)-P(\lambda,T_R)}{P(\lambda,T_S)-P(\lambda,T_R)}\right]. \tag{B6}$$

---

[1] R. Carminati and J.-J. Greffet, Phys. Rev. Lett. **82**, 1660 (1999).

[2] A. V. Shchegrov, K. Joulain, R. Carminati, and J.-J. Greffet, Phys. Rev. Lett. **85**, 1548 (2000).

[3] C. Henkel, K. Joulain, R. Carminati, and J. J. Greffet, Opt. Commun. **186**, 57 (2000).

[4] J.-J. Greffet, R. Carminati, K. Joulain, J.-P. Mulet, S. Mainguy, and V. Chen, Nature (London) **416**, 61 (2002).

[5] J.-J. Greffet and M. Nieto-Vesperinas, J. Opt. Soc. Am. A **15**, 2735 (1998).

[6] R. Siegel and J. R. Howell, *Thermal Radiation Heat Transfer* (Hemisphere, Washington, D.C., 1981).

[7] A. K. Lorentz, *The Theory of Electrons* (Teibenr, Leipzig, 1916).

[8] A. Jr Banos, *Dipole Radiation in the Presence of a Conducting Half-Space* (Pergamon, Oxford, 1966).

[9] J. E. Sipe, J. Opt. Soc. Am. B **4**, 481 (1987).

[10] H. B. Callen and T. A. Welton, Phys. Rev. **83**, 34 (1951).

[11] S. M. Rytov, Y. A. Kravtsov, and V. I. Tatarskii, *Principles of Statistical Radiophysics* (Springer-Verlag, Berlin, 1989).

[12] R. Petit, *Electromagnetic Theory of Gratings* (Springer-Verlag, Berlin, 1980).

[13] D. Maystre and M. Hutley, Opt. Commun. **19**, 431 (1976).

[14] M. Kreiter, J. Oster, R. Sambles, S. Herminghaus, S. Mittler-Neher, and W. Knoll, Opt. Commun. **168**, 117 (1999).

[15] G. N. Zhizhin, E. A. Vinogradov, M. A. Moskalova, and V. A. Yakovlev, Appl. Spectrosc. Rev. **18**, 171 (1982).

[16] R. W. Gruhlke, W. R. Holland, and D. G. Hall, Phys. Rev. Lett. **56**, 2838 (1986).

[17] P. Andrew and W. L. Barnes, Phys. Rev. B **64**, 125405 (2001).

[18] H. Rigneault, F. Lemarchand, and A. Sentenac, J. Opt. Soc. Am. A **17**, 1048 (2000).

[19] P. J. Hesketh, J. N. Zemel, and B. Gebhart, Nature (London) **324**, 549 (1986).

[20] P. J. Hesketh, J. N. Zemel, and B. Gebhart, Phys. Rev. B **37**, 10795 (1988).

[21] P. J. Hesketh, J. N. Zemel, and B. Gebhart, Phys. Rev. B **37**, 10803 (1988).

[22] M. Auslender and S. Hava, Infrared Phys. Technol. **36**, 1077 (1995).

[23] M. Auslender, D. Levy, and S. Hava, Appl. Opt. **37**, 369 (1998).

[24] H. Sai, H. Yugami, Y. Akiyama, Y. Kanamori, and K. Hane, J. Opt. Soc. Am. A **18**, 1471 (2001).

[25] J. Le Gall, M. Olivier, and J.-J. Greffet, Phys. Rev. B **55**, 10105 (1997).

[26] S. Y. Lin, J.G. Fleming, D.L. Hetherington, B.K. Smith, R. Biswas, K.M. Ho, M.M. Sigalas, W. Zubrzycki, S.R. Kurtz, and J. Bur, Nature (London) **394**, 6690 (1998).

[27] N. Chateau and J.-P. Hugonin, J. Opt. Soc. Am. A **11**, 1321 (1994).

[28] E. D. Palik, *Handbook of Optical Constants of Solids* (Academic Press, San Diego, 1985).

[29] L. Mandel and E. Wolf, *Optical Coherence and Quantum Optics* (Cambridge University Press, Cambridge, 1995).

[30] C. Kittel, *Introduction to Solid State Physics* (Wiley, New York, 1996).

[31] H. Raether, *Surface Plasmons on Smooth and Rough Surfaces and on Gratings* (Springer-Verlag, Berlin, 1988).

[32] E. Wolf, Nature (London) **326**, 363 (1987).

[33] E. Wolf and D. F. James, Rep. Prog. Phys. **59**, 771 (1996).

[34] P. R. Griffiths and J. A. de Haseth, *Fourier Transform Infrared Spectrometry* (Wiley-Interscience, New York, 1986).

Engineering infrared emission properties of silicon in the near field and the far field

F. Marquier, K. Joulain, J.-P. Mulet, R. Carminati et J.-J. Greffet

Optics Communications, vol 69, pp155412 (2004)

Available online at www.sciencedirect.com
SCIENCE DIRECT®
Optics Communications 237 (2004) 379–388
OPTICS COMMUNICATIONS
www.elsevier.com/locate/optcom

Engineering infrared emission properties of silicon in the near field and the far field

F. Marquier *, K. Joulain, J.P. Mulet, R. Carminati, J.J. Greffet

Laboratoire d'Énergétique Moléculaire et Macroscopique, Combustion, École Centrale Paris, Centre National de la Recherche Scientifique, Grande Voie des Vignes, 92295 Châtenay-Malabry Cedex, France

Received 22 January 2004; accepted 19 April 2004

Abstract

We study numerically the thermal emission of highly doped silicon surfaces. We show that by modifying the doping, we can tune the frequency of emission. We also show that by taking advantage of the large local density of states due to surface-plasmon polaritons, radiative properties in the far field can be drastically modified. It is possible to realize a spatially partially coherent thermal source as well as a quasi-isotropic source. Finally, we study the radiative transfer between two doped silicon bodies. Surface-plasmon polaritons produce an enhancement of several orders of magnitude of the radiative energy transfer at nanometric distances.

PACS: 73.20.Mf; 71.36.+c; 44.40.+a; 78.68.+m

Keywords: Surface plasmon; Surface; Infrared; Near field; Emissivity

1. Introduction

Thermal sources are often considered as the archetype of incoherent sources as opposed to coherent sources such as lasers and antennas. Nevertheless, it has been shown recently [1–3] that thermal sources can emit coherent radiation in the near field. The near-field region corresponds to distances to the interface smaller than a tenth of a wavelength. We use as a typical wavelength the peak wavelength given by Wien's law, 10 μm at 300 K for example. In this distance range, radiation can be quasi-monochromatic [2]. This phenomenon is due to electromagnetic surface waves, and can be observed only on materials supporting them. Such surface waves are electromagnetic modes which propagate along the interface (separating, for example, the emitting material from a vacuum) and decrease exponentially in the perpendicular direction (evanescent waves). The

---

* Corresponding author. Tel.: +33141131078; fax: +33147028035.

E-mail address: Francois.Marquier@em2c.ecp.fr (F. Marquier).

doi:10.1016/j.optcom.2004.04.024

propagation length of these surface waves is important (about an hundred wavelengths). It has been shown that the propagation of these surface waves is the origin of a long-range correlation of the electromagnetic field along the interface [1,3].

There are different types of surface waves. Surface-phonon polaritons are observed for polar materials such as silicon carbide (SiC), glass, II–VI and III–V semiconductors. They are mechanical vibrations (phonons) propagating in a partially ionic material so that each unit cell becomes an oscillating electric dipole. Surface-plasmon polaritons are longitudinal electron oscillations (acoustic type wave in an electron gas) that can be observed with metals and doped semiconductors. They obviously generate electromagnetic fields with a longitudinal component. Surface waves due to excitons can also be observed. From an electromagnetic point of view, these surface modes are identical although the underlying microscopic mechanisms are very different. Surface polaritons appear as resonant modes when solving the Maxwell equations for the interface geometry. These modes have the same structure for polar materials, metals or semiconductors.

Studies have been reported with SiC which highlights the fact that a surface-phonon polariton can be coupled with a propagating wave through a grating [4]. Through this coupling, the near-field coherence properties modify the far-field emission. Spatial coherence leads to a high directionality of the thermal source that emits in angular lobes like an antenna. We will show that the same effects can be produced with a surface-plasmon polariton excited on doped silicon. Thermal emission mediated by surface plasmon has already been demonstrated with gold [5]. Doped silicon is very interesting because its permittivity ϵ can be tuned by modifying the carrier concentration N. This allows to tune the plasma frequency and therefore the emission frequency. This material is obviously very interesting because of the wealth of technological know-how. Many experiments have been already reported [6–11] on its radiative properties (reflectance, transmittance and emittance) by two active groups in this field. Let us also mention recent experiments [12] on silicon covered with a periodic metallic structure aimed at producing an infrared source. In these experiments, thermal emission is enhanced due to the excitation of a surface plasmon in the metallic structure. In the present work, we show, using numerical simulations, that surface-plasmon polaritons on doped silicon can be used to modify the radiative properties of the material in the infrared.

The paper is organized as follows. In Section 2, we shall present some optical properties of doped silicon and highlight the existence of evanescent modes (surface waves) close to the interface. The design of two types of thermal sources will be presented in Section 3. We have designed an infrared antenna that emits in narrow lobes and also a source that has a large quasi-isotropic emissivity. Finally, we will show in Section 4 that radiative heat transfer between two semi-infinite media of doped silicon is substantially enhanced due to the resonant excitation of a surface-plasmon polariton (SPP). This might have applications for the temperature control of silicon devices.

2. Optical properties of a doped silicon plane surface

In the infrared domain, the permittivity ϵ of a semiconductor can be described by the following well-known formula [6,10]:

$$\epsilon(\omega) = \epsilon_\infty \left(1 - \frac{\omega_p^2}{\omega\left(\omega + \frac{i}{\tau}\right)} \right), \tag{1}$$

where $\omega = 2\pi c/\lambda$, $\omega_p^2 = Ne^2/(m^*\epsilon_0\epsilon_\infty)$, and $\epsilon_\infty \approx 11.7$ for doped silicon.

The carrier concentration N, the electron or hole optical effective mass m^* (for n- or p-doped silicon) and the relaxation time τ are characteristic of the doping. τ can be calculated using the formula (2):

$$\tau = \frac{m^*}{Ne^2\rho} \tag{2}$$

where ρ is the dc resistivity of the material. We worked with both n- and p-doped silicon with N varying between 3×10^{19} and 5×10^{20} cm^{-3}. m^*, ρ (and thus τ) depend on N. We took $m^* = 0.27m_0$ (where m_0 is the free electron mass) for the n-doped silicon and $m^* = 0.34m_0$ for the p-doped silicon. These are certainly not the exact values for m^* at each concentration N, but are good approximations. We have checked that modifying these values does not affect significantly our results. The variation of the dc resistivity ρ of both n- and p-doped silicon with the impurity concentration (which is equal to the carrier concentration N assuming a full impurity ionization) was taken from the paper by Sze and Irvin [13].

Let us now turn to the near-field radiative properties of a flat air/doped-silicon interface. We show that the thermally emitted energy density drastically changes when approaching the interface. This can be interpreted in terms of enhancement of the local density of states [14]. In fact, at short distances z, the electromagnetic energy density u which depends on ω and z reads [2,3,14]:

$$u(\omega,z) \propto \frac{1}{z^3}\frac{\epsilon''(\omega)}{|1+\epsilon(\omega)|^2}\frac{\hbar\omega}{\exp\left(\frac{\hbar\omega}{k_B T}\right)-1}, \tag{3}$$

where ϵ'' is the imaginary part of the permittivity ϵ. The first part of this term exhibits a peak when $\mathrm{Re}[\epsilon(\omega)] \approx -1$. This corresponds to the surface-plasmon polariton resonance. It produces a peak in the local density of electromagnetic states [2,14].

Under these conditions, we plot in Fig. 1 $u(\omega)$ at different distances: $z = 100$ nm (Fig. 1(a)) and $z = 1$ nm (Fig. 1(b)) for the n-doped silicon with a carrier concentration $N = 3 \times 10^{19}$ cm^{-3} at $T = 800$ K. At close distance to the surface, a peak appears at a frequency $\omega_0 \approx 1.5 \times 10^{14}$ rad s^{-1}. This frequency corresponds to $\mathrm{Re}[\epsilon(\omega_0)] = -1$. Moreover, between $z = 100$ and $z = 1$ nm, the energy density $u(\omega)$ increases by almost six orders of magnitude (in agreement with the dependence on $1/z^3$ of Eq. (3)). Note that this peak is due to evanescent waves and thus cannot be observed at distances larger than the typical wavelength of the radiation. A SPP has the following dispersion relation for a flat air/material interface:

$$k_{//} = \frac{\omega}{c}\sqrt{\frac{\epsilon(\omega)}{\epsilon(\omega)+1}}, \tag{4}$$

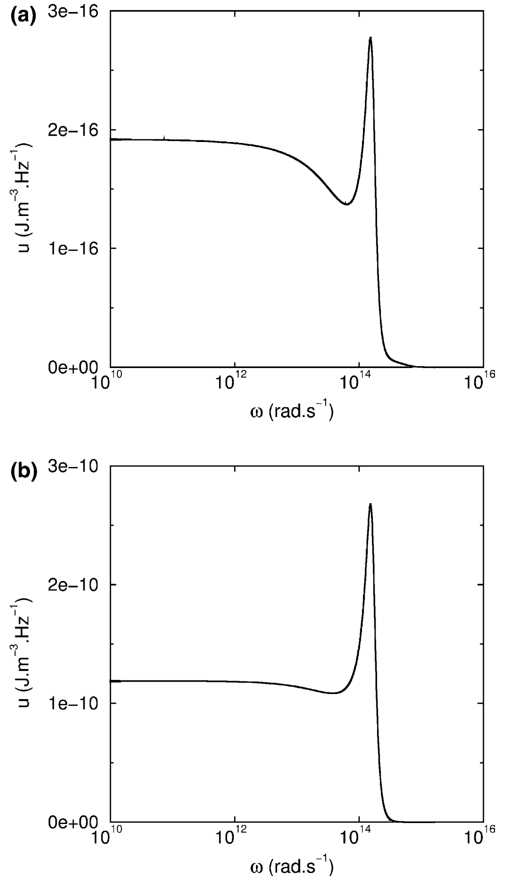

Fig. 1. Energy density $u(\omega)$ of a semi-infinite medium of n-doped silicon with $N = 3 \times 10^{19}$ cm^{-3} at $T = 800$ K, for two different heights z above the interface: (a) $z = 100$ nm, (b) $z = 1$ nm.

where $k_{//}$ is the wavevector parallel to the interface. Such waves exist for materials having $\epsilon'(\omega) < -1$ where ϵ' is the real part of ϵ [15]. Eq. (4) implies that $|k_{//}| > \omega/c$, i.e., that these are evanescent waves. Nevertheless, following ideas which have been developed in the case of SiC, it is possible to couple this evanescent wave with a propagating wave through a grating [4,16] of period Λ. The emission angle θ is then given by

$$\frac{\omega}{c}\sin\theta = \mathrm{Re}[k_{//}] + m\frac{2\pi}{\Lambda}, \tag{5}$$

where m is the diffraction order. The reciprocal situation is a propagating plane wave incident on such a grating. It can be coupled to a surface mode when the angle of incidence θ satisfies Eq. (5). This is a well-known phenomenon which can lead to total absorption (absorptivity $\alpha(\omega,\theta) = 1$) of the incident energy by the grating [16–18]. An emissivity $\varepsilon(\omega,\theta)$ of 1 can thus be expected from Kirchhoff's law $\varepsilon(\omega,\theta)=\alpha(\omega,\theta)$ [19].

3. Silicon infrared sources

In order to characterize the radiative thermal emission of a grating, we use its directional emissivity ε which depends on the frequency ω and on the direction θ (our calculations are made in a plane perpendicular to the grating lines). $\varepsilon(\omega,\theta)$ can be deduced from the absorptivity $\alpha(\omega,\theta)$ by Kirchhoff's law. Note that $\varepsilon(\omega,\theta)$ is a directional and polarized quantity. For example, the absorptivity is the ratio between the total absorbed flux and the flux transported by a polarized incident plane wave propagating in direction θ. In the same way, we can define a polarized directional reflectivity. For an opaque body, we have $\alpha(\omega,\theta)=1-\rho(\omega,\theta)$, where $\rho(\omega,\theta)$ is the hemispherical reflectivity for a given angle of incidence θ of the bulk [19]. We used an algorithm based on a rigorous coupled-wave analysis developed by Chateau and Hugonin [20] to calculate the reflectivity of lamellar gratings ruled on doped silicon.

To analyse these results, it is useful to derive the dispersion relation. As explained in [16], we choose a real wave vector and a complex frequency to solve the dispersion relation equation. The dispersion relation of the SPP on a grating (Re[ω] versus $k_{//}$) can be plotted in a reduced-zone scheme (Fig. 2). Some portions of the dispersion relation are above the light cone (defined by $k_{//}=\mathrm{Re}[\omega/c]$), therefore the corresponding SPP can be radiated by the grating.

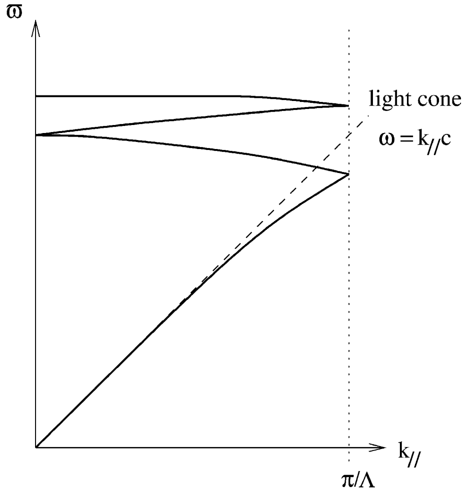

Fig. 2. Reduced-zone scheme of the dispersion relation for a surface wave on a smooth grating.

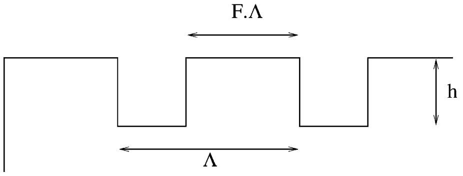

Fig. 3. Geometry of the grating: period Λ, filling factor F and depth h.

We have worked with two types of lamellar gratings (Fig. 3: period Λ, filling factor F and depth h). To show how the radiative properties of a material can be engineered by taking advantage of the coherence properties of the SPP, we designed two types of sources. These results were obtained with both n- and p-doped silicon.

3.1. First type of source: an infrared antenna

Our aim is to design a source that emits thermal light in narrow angular lobes like an antenna. This source is analog to the one demonstrated with SiC in [4] Instead of surface-phonon polaritons, we are using surface-plasmon polaritons to generate the spatial coherence along the interface. Note that Hesketh et al. [10] have already studied the emission of doped silicon gratings. In this work, we show how to optimize the grating to have intense narrow emission peaks. According to Fig. 2, we must excite a SPP lying on a linear portion of the dispersion relation above the light cone in order to produce such a source. This is possible provided that the grating has a sufficiently large period. We have optimized numerically a lamellar grating which has the following characteristics: period $\Lambda=6.3$ μm, filling factor $F=0.4$ and depth $h=0.6$ μm. We used p-doped silicon with a large carrier concentration $N=5\times10^{20}$ cm^{-3}. We plot its emissivity spectrum in Fig. 4 as a function of the angle of observation. Similar curves are obtained with n-doped silicon at the same carrier

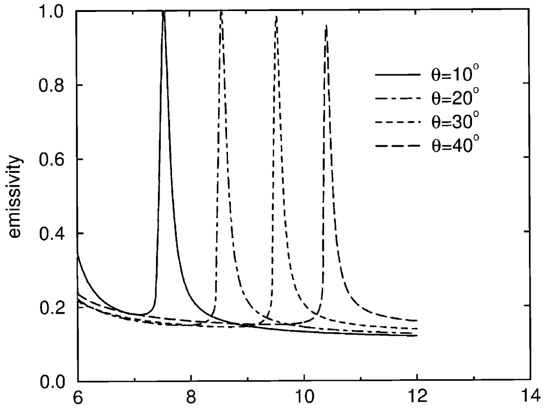

Fig. 4. Numerical emissivity spectrum of a p-doped silicon grating with $N = 5 \times 10^{20}$ cm^{-3} for different angles of observation (parameters of the grating: $\Lambda = 6.3$ μm, $F = 0.4$ and $h = 0.6$ μm).

concentration but with a filling factor $F = 0.5$ for the grating. One can see that in each direction there is a strong quasi-monochromatic peak of emission and that the spectral location of this peak changes with the observation direction.

In order to show that this phenomenon is due to the excitation of a SPP, we have compared the reduced-zone scheme of the dispersion relation of a SPP on a plane surface and the numerical results obtained with the grating when varying the angle of observation θ (Fig. 5). Each triangle in the figure represents a couple $(\omega/c \sin\theta, \omega/c)$ corresponding to a peak of emission. For $6 < \lambda < 12$ μm, i.e., $830 < \omega < 1700$ cm^{-1}, one can see that there is a good agreement between the two approaches. The small difference is due to the presence of the grating. Note in particular that a gap appears at the edge of the Brillouin zone. We have thus shown that a SPP is radiated by the grating. In other terms, we can build a coherent thermal source by ruling a grating on a plane surface.

We now study the influence of the doping on the emission peak. In a given direction of observation $\theta = 20°$, we plot the emissivity spectrum for different concentrations N in Fig. 6. One can see that the peak decreases and broadens when N decreases. In order to interpret this phenomenon, we can relate it to the evolution of the imaginary part of the permittivity ϵ'' at the plasma frequency. Indeed ϵ'' increases when N decreases. Losses increase in the grating so that the coupling between the SPP and the propagating wave is less effective and the peak becomes smaller and broader. We also see that the position of this peak remains globally the same in comparison with Fig. 4. Indeed the SPP excited is on a part of the dispersion relation very close to the light cone which is the same for every concentration. Therefore, the emission peak occurs at the same wavelength

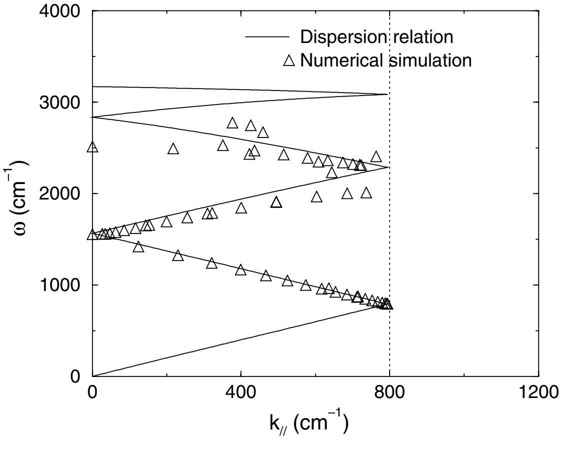

Fig. 5. Theoretical dispersion relation for a surface-plasmon polariton on a smooth grating and numerical simulation with the real grating (parameters of the grating: $\Lambda = 6.3$ μm, $F = 0.4$ and $h = 0.6$ μm).

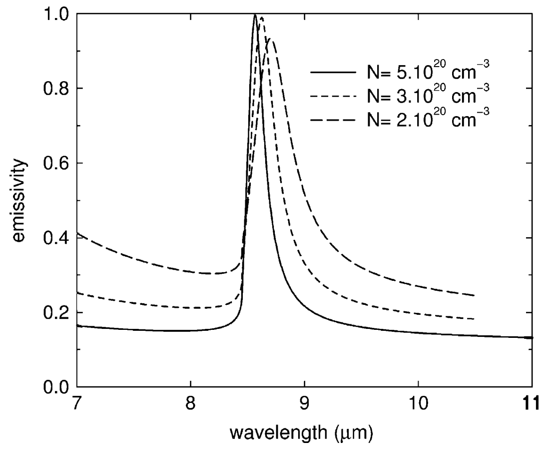

Fig. 6. Numerical emissivity spectra of a p-doped silicon grating at $\theta = 20°$ (parameters of the grating: $\Lambda = 6.3$ μm, $F = 0.4$ and $h = 0.6$ μm).

because the dispersion relation is almost not affected when N varies.

3.2. Second type of source: a quasi-lambertian source

In Section 3.1, we were interested in the coupling of a SPP lying on a linear branch of the dispersion relation with a propagating wave. Here, we excite a surface wave lying on the upper branch of the dispersion relation, i.e., the horizontal asymptote at the plasma frequency ω_0, corresponding to $\epsilon'(\omega_0) = -1$. In this case, we expect an emission at a single wavelength in any direction (quasi-isotropic emission) because the dispersion relation is flat. In order to have only this branch above the light cone, we must design a grating with a smaller period than in the previous section. The grating that we have optimized has the following characteristics: period $\Lambda = 2.5$ μm, filling factor $F = 0.8$ and depth $h = 0.6$ μm in the case of the p-doped silicon with $N = 3 \times 10^{20}$ cm^{-3}. We plot its emissivity spectrum in Fig. 7 for three directions of observation. The spectra obtained with the same grating but with n-doped silicon are remarkably close. One can see that there is a peak of emission around 5.5 μm which does not move when the direction of observation θ changes. We can remark that when $\theta = 50°$, a strong variation appears at $\lambda = 4.4$ μm. This is a Wood anomaly, well known in the case of the absorption of an incident beam by a grating [17,18]. The source designed here is different from that presented in Section 3.1: it emits in any direction for a particular wavelength. However, one can see that the peak has a large width indicating a low temporal coherence.

In s-polarization, this peak disappears. This suggests that a SPP, which exists only in p-polarization, is responsible for this effect. In order to further confirm the role of the SPP, we have plotted the theoretical and numerical dispersion relation as in the previous section (Fig. 8). Our numerical results do not agree with the reduced-zone scheme of the dispersion relation for the flat interface. This is not surprising: the grating dimensions are close to the typical wavelength and the grating is now a strong modification of the plane surface profile. Yet, when the depth h of the grating is decreased, the actual dispersion relation gets closer to the dispersion relation for a flat surface. The mechanism for the thermal emission is thus clearly due to the excitation of a surface-plasmon polariton. The thermal motion of the electrons excites the surface mode. This surface mode is then radiated by the grating. A slightly but more correct point of view is to consider that in the presence of a grating, the surface wave is transformed into a leaky wave with a modified disper-

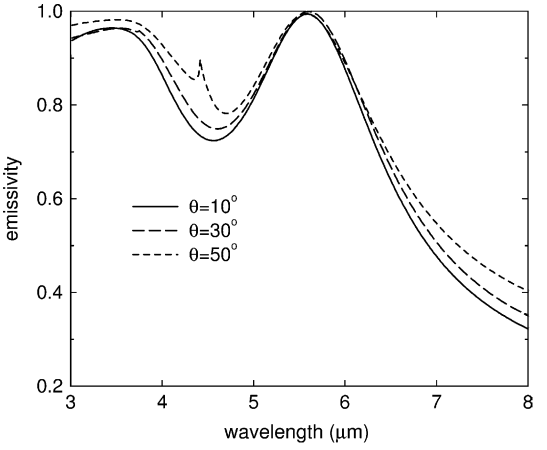

Fig. 7. Numerical emissivity spectra of a p-doped silicon grating with $N = 3 \times 10^{20}$ cm^{-3} for different angles of observation (parameters of the grating: $\Lambda = 2.5$ μm, $F = 0.8$ and $h = 0.6$ μm).

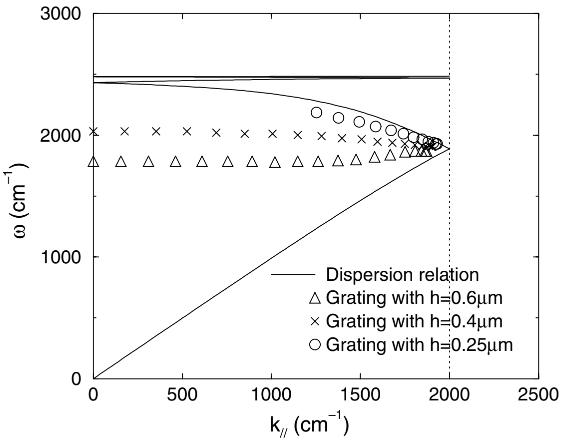

Fig. 8. Theoretical dispersion relation for a surface-plasmon polariton on a flat surface and numerical simulations with real gratings.

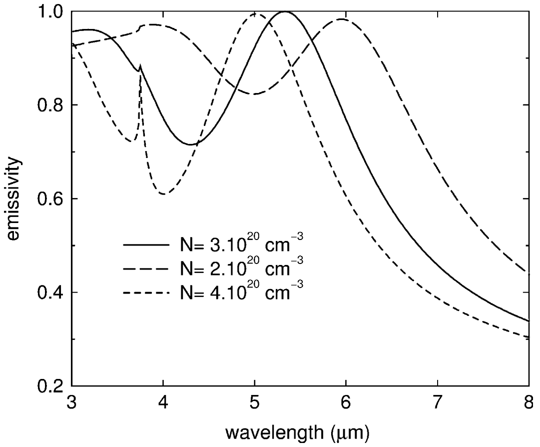

Fig. 9. Numerical emissivity spectra of a p-doped silicon grating for different concentration N at a fixed angle $\theta = 30°$. The characteristics of the grating are: $\Lambda = 2.5$ µm, $F = 0.8$ and $h = 0.6$ µm.

sion relation. This mode is excited by the random currents due to the thermal motion of the electrons. Since the dispersion relation has a quasi-horizontal branch at a given frequency, there is emission for all wave vectors and therefore all angles at this particular frequency. This frequency is essentially the plasma frequency divided by $\sqrt{2}$.

A remarkable property is that the emission frequency can be shifted by modifying the density of electrons. This can be easily done by changing the level of doping. As in the previous section, we plot the emissivity spectrum for different carrier concentrations N in a given direction of observation $\theta = 30°$ in Fig. 9. One can see that the location of the peak changes with N. When N decreases, the emission wavelength increases. This displacement shows that building an infrared source which could be tunable in wavelength when varying N seems to be possible. Note that the peak frequency ω_0 depends on the concentration and increases when N increases.

4. Enhanced radiative heat transfer at nanometric distances

The current development of nano-technology creates new challenges. Many macroscopic laws of physics are no longer valid in the mesoscopic regime. Transport of electrons has been widely studied and many new effects have been demonstrated [21]. Similar phenomena appear for the energy transfer [22,23] at nanoscale. It has been known for some time that the radiative heat transfer can be increased significantly at subwavelength distances due to interference effects and to the contribution of evanescent waves [24]. The first authors to introduce a complete formulation of the problem were Polder and van Hove [25] who used the type of formulation previously used to discuss the Casimir force (i.e. a momentum transfer). This problem has been discussed subsequently by many authors [26–30]. We have recently shown [31,32] that the presence of surface waves enhances by many orders of magnitude the radiative heat transfer at nanometric distances. In addition, most of the energy is transfered in a narrow range of frequencies. Those frequencies correspond to the resonances of the system, plasmons for electron systems, optical phonons for ionic crystals. In this section, we will examine the heat transfer through radiation tunelling for silicon and doped silicon. The importance of heat transfer for silicon nanostructures is well known. It is thus of interest to investigate what new phenomena can be obtained when modifying the doping.

We consider a simple configuration of two plane parallel media at temperature T_1 and T_2 separated by a small gap. In order to simplify the problem, the media are identical materials. Usually the conductive heat transfer due to the ballistic flight of molecules between the two bodies is very important and much larger than the radiative heat transfer [33]. Nevertheless, we will see that with doped silicon and at nanometric distances, the radiative heat transfer may be enhanced by the thermal excitation of a SPP. The derivation of the radiative heat transfer was already given by Polder and van Hove [25] and discussed extensively in [32]. In essence, one derives the field in the gap radiated by an ensemble of random currents in the media. Once, the field is formally known, the Poynting vector can be derived. Note that the field is linearly related to the current density. Since the mean value of the current is null, the mean value of the field is also null. Yet, the quadratic mean value does not vanish. This can be evaluated using the correlation function of the current density which is given by the fluctuation-dissipation theorem [34]. By assuming that temperatures of the two media are close enough, the flux can be linearized and cast in the form $h^R(T_1 - T_2)$ [25]. h^R can be split up in two parts: one due to propagating waves and the other to evanescent waves [32,35]. We plot these two contributions versus the distance d separating the two bodies for the n-doped silicon with $N = 3 \times 10^{19}$ cm^{-3} (Fig. 10) at $T = 300$ K. When $d < 1$ μm, the contribution of the evanescent waves becomes very important and larger than the contribution of the propagating waves by several orders of magnitude. This is due to the fact that the exponentially decaying evanescent waves can tunnel through the gap and transfer energy when the distance is smaller than the typical wavelength. This effect has already been observed and explained in the case of SiC. In particular, the role of surface-phonon polaritons has been shown [32,35]. In this case, the microscopic mechanism describing the energy transfer is a phonon–phonon collision. Indeed, atoms on each side of the gap can interact through a Coulomb potential if the gap width is small enough. For the doped silicon, we observe exactly the same effects with surface-plasmon polaritons. Surface plasmons on both sides of the gap can interact. This results in an enhancement of h^R when decreasing d. We find that h^R depends on the distance between the two media as $1/d^2$.

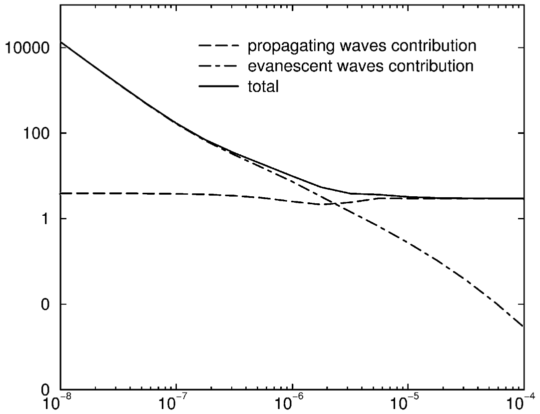

Fig. 10. Radiative heat transfer coefficient h^R versus the distance d between two bodies of n-doped silicon with $N = 3 \times 10^{19}$ cm^{-3} at $T = 300$ K.

We have seen in the previous sections that a surface wave introduces important spectral effects. In order to analyse the radiative heat transfer at small distances, a monochromatic radiative heat transfer coefficient h^R_ω has been introduced [33,35]. The product of this coefficient (in W m^{-2} K^{-1} Hz^{-1}) by the temperature difference between the materials yields the monochromatic heat flux per surface unit. We plot this coefficient in Fig. 11 for a temperature $T = 300$ K and two distances $d = 10$ μm (Fig. 11(a)) and $d = 10$ nm (Fig. 11(b)). We have separated the

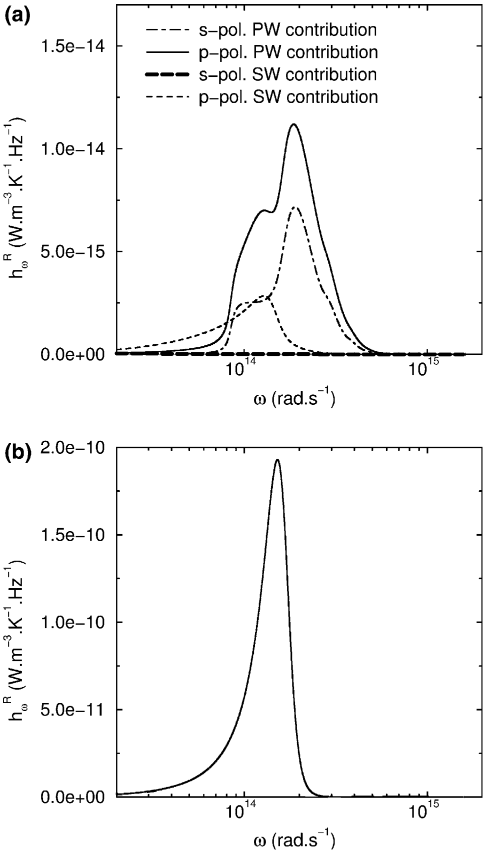

Fig. 11. Monochromatic radiative heat transfer coefficient h^R_ω versus frequency for two bodies of n-doped silicon with $N = 3 \times 10^{19}$ cm^{-3} at $T = 300$ K for two different distances d between the bodies. (a) $d = 10$ μm, (b) $d = 10$ nm, in this case we present only the p-polarized surface waves contribution. SW and PW stand for surface waves and propagating waves, respectively.

different contributions of the p- or s-polarized evanescent and propagating waves. One can see in Fig. 11(a) that the part due to the propagating waves is larger than the one due to the surface waves. The SPP is a p-polarized wave, therefore the contribution of the s-polarized evanescent wave does not appear in this figure. When $d = 10$ nm, the contribution of the propagating waves is negligible. The radiative heat transfer coefficient h^{R}_{ω} is enhanced by five orders of magnitude and becomes quasi-monochromatic. As mentioned above, we ascribe this peak to the surface-plasmon polariton. Indeed, the location ω_0 of this peak corresponds to $\epsilon'(\omega_0) \approx -1$ which is the frequency where the density of electromagnetic states becomes very large (cf. Section 2) due to the presence of a SPP.

5. Conclusion

In this paper, we explored the possibility of using surface-plasmon polaritons to generate intense and spatially coherent thermal fields on doped silicon. The key feature of doped silicon is that by controlling its doping, one can shift the plasma frequency. It is thus possible to shift the peak of the density of states in the near field. We have shown how this could be used to design efficient infrared sources of light. Particularly, the first type of infrared light source which we design in this paper is equivalent to the source produced in [4]. It produces narrow lobes of light, i.e. it is a spatially partially coherent source. The second type of source is a quasi-isotropic source of light with a large emissivity at a given frequency.

We also studied the problem of radiative transfer between two doped silicon surfaces held at subwavelength distances. The existence of surface-plasmon polaritons on the doped silicon enhances this radiative transfer at a particular wavelength: it becomes larger by several orders of magnitude and quasi-monochromatic. These results could be used to modify the radiative cooling of silicon devices.

References

[1] R. Carminati, J.J. Greffet, Phys. Rev. Lett. 82 (1999) 1660.
[2] A.V. Shchegrov, K. Joulain, R. Carminati, J.J. Greffet, Phys. Rev. Lett. 85 (2000) 1548.
[3] C. Henkel, K. Joulain, R. Carminati, J.J. Greffet, Opt. Commun. 186 (2000) 57.
[4] J.J. Greffet et al., Nature (London) 416 (2002) 61.
[5] M. Kreiter et al., Opt. Commun. 168 (1999) 117.
[6] M. Auslender, S. Hava, Infrared Phys. Technol. 36 (1995) 1077.
[7] S. Hava, J. Ivri, M. Auslender, J. Appl. Phys. 85 (1999) 7893.
[8] M. Auslender, D. Levy, S. Hava, Appl. Opt. 37 (1998) 369.
[9] P.J. Hesketh, J.N. Zemel, B. Gebhart, Nature (London) 324 (1986) 549.
[10] P.J. Hesketh, J.N. Zemel, B. Gebhart, Phys. Rev. B 37 (1988) 10795.
[11] P.J. Hesketh, J.N. Zemel, B. Gebhart, Phys. Rev. B 37 (1988) 10803.
[12] M.U. Pralle et al., Appl. Phys. Lett. 81 (2002) 4685.
[13] S.M. Sze, J.C. Irvin, Sol. State Electron. 11 (1968) 599.
[14] K. Joulain, R. Carminati, J.P. Mulet, J.J. Greffet, Phys. Rev. B 68 (2003) 245405.
[15] H. Raether, Surface Plasmons on Smooth and Rough Surfaces and on Gratings, Springer, Berlin, 1988.
[16] J. Le Gall, M. Olivier, J.J. Greffet, Phys. Rev. B 55 (1997) 10105.
[17] D. Maystre, M. Hutley, Opt. Commun. 19 (1976) 431.
[18] R. Petit, Electromagnetic Theory of Gratings, Springer, Berlin, 1980.
[19] J.J. Greffet, M. Nieto-Vesperinas, J. Opt. Soc. Am. A 15 (1998) 2735.
[20] N. Chateau, J.P. Hugonin, J. Opt. Soc. Am. A 11 (1994) 1321.
[21] N. Agrat, A. Levy Yeyati, J.M. van Ruitenbeek, Phys. Rep. 377 (2003) 81.
[22] C.L. Tien, G. Chen, J. Heat Transfer 114 (1994) 799.
[23] A.R. Abramson, C.L. Tien, Microscale Thermophys. Eng. 3 (1999) 229.
[24] E.G. Cravalho, C.L. Tien, R.P. Caren, J. Heat Transfer 89 (1967) 351.
[25] D. Polder, M. Van Hove, Phys. Rev. B 4 (1971) 3303.
[26] M.L. Levin, V.G. Polevoi, S.M. Rytov, Sov. Phys. JETP 52 (1980) 1054.
[27] J.J. Loomis, H.J. Maris, Phys. Rev. B 50 (1994) 18517.
[28] G. Chen, Microscale Thermophys. Eng. 1 (1997) 215.
[29] J.B. Pendry, J. Phys.: Condens. Matter 11 (1999) 6621.
[30] A.I. Volotikin, B.N.J. Persson, Phys. Rev. B 63 (2001) 205404.
[31] J.P. Mulet, K. Joulain, R. Carminati, J.J. Greffet, Appl. Phys. Lett. 78 (2001) 2931.
[32] J.P. Mulet, K. Joulain, R. Carminati, J.J. Greffet, Microscale Thermophys. Eng. 6 (2002) 209.
[33] J.J. Greffet et al., in: M. Allegrini, N. Garcia, O. Marti (Eds.), Nanometer Scale Science and Technology, Proceedings of the International School of Physics “Enrico Fermi”, Course CXLIV, Bologna, Italy, 2001, Società Italiana di Fisica, 2001, p. 375.

[34] S.M. Rytov, Y.A. Kravtsov, V.I. Tatarskii, Principles of Statistical Radiophysics, Springer, Berlin, 1989.
[35] J.P. Mulet, K. Joulain, R. Carminati, J.J. Greffet, in: G.P. Celata (Ed.), Heat Transfer and Transport Phenomena in Microscale, Proceedings of the International Conference on Heat Transfer and Transport Phenomena in Microscale, Banff, Canada, 2000, Begell House, Inc., New York, 2000, p. 352.

Heat Transfer between Two Nanoparticles Through Near Field Interaction

G. Domingues, S. Volz, K. Joulain et J.-J. Greffet

Physical Review Letters, vol 94, pp085901 (2005)

Heat Transfer between Two Nanoparticles Through Near Field Interaction

Gilberto Domingues,[1,*] Sebastian Volz,[2,†] Karl Joulain,[1] and Jean-Jacques Greffet[2]
[1]*Laboratoire d'Etudes Thermiques, 86961 Futuroscope Cedex, France*
[2]*Laboratoire d'Energétique Macroscopique, Moléculaire; Combustion, Grande Voie des Vignes, Châtenay Malabry 92295, France*

(Received 23 July 2004; revised manuscript received 8 November 2004; published 2 March 2005)

We introduce a thermal conductance by using the fluctuation-dissipation theorem to analyze the heat transfer between two nanoparticles separated by a submicron distance. Using either a molecular dynamics technique or a model based on the Coulomb interaction between fluctuating dipoles, we derive the thermal conductance. Both models agree for distances larger than a few diameters. For separation distances smaller than the particle diameter, we find a transition regime characterized by a thermal conductance larger than the contact conductance.

DOI: 10.1103/PhysRevLett.94.085901 PACS numbers: 65.80.+n, 82.60.Qr

Understanding and predicting the heat transfer between two bodies separated by a nanometric distance is a key issue both from the theoretical and applied points of view. Most near-field techniques involve bringing a tip close to an interface. In many cases, the tip and the interface temperatures are not equal so that a heat transfer is generated. Superinsulating materials such as aerogels and highly conductive media such as nanofluids also involve heat exchanges between neighboring particles. However, there is a lack of understanding of the physical mechanisms involved. The heat transfer in quantum wells and at nanoscale has been analyzed in the context of phonon transport [1]. The heat transfer, through constrictions [2] or linear chains [3–5], has been discussed in many papers. The quantized thermal conductance has been studied both theoretically [6,7] and experimentally [8]. Yet all these works rely on the concept of phonon, which is hardly valid for small aggregates. Heat transfer between two planes separated by subwavelength distances through electromagnetic interaction has been first investigated by Polder and van Hove [9] and later by many groups [10,11]. It has been shown recently that this mechanism has a very large resonance at the optical phonon frequency for polar materials [12,13]. When the distance is decreased, the heat transfer increases dramatically.

A still open question is how energy is exchanged between two objects, a tip and a surface for instance, just before contact. The mechanisms involved are unclear. Whereas radiative heat transfer (i.e., emission and absorption of photons) is negligible, near-field radiation (i.e., Coulomb interaction) may become important. Dipole-dipole energy transfer also known as Forster energy transfer is the dominant energy transfer mechanism between molecules [14]. In this Letter, we explore the heat transfer between two nanoparticles (NPs) separated by a distance on the order of a few nanometers. We introduce a thermal conductance that can be related to the fluctuations of the heat flux using the fluctuation-dissipation theorem. We then implement a molecular dynamics simulation to compute the thermal conductance as a function of the separation distance. An alternative approach is based on a direct derivation of the heat flux between the two nanoparticles modeled by fluctuating dipoles. We find that both models agree and yield a $1/d^6$ dependence for distances larger than a few diameters. Yet when the distance is further decreased, we observe a stronger enhancement of the conductance followed by a decay when the NPs are in contact.

Let us first define the linear response susceptibility, relating the net heat flux Q_{12} exchanged between the two NPs to the NPs temperature difference:

$$\frac{Q_{12}(\omega)}{T_0} = G_{12}^*(\omega)\Delta T(\omega), \tag{1}$$

where T_0 is the mean temperature and ω is the circular frequency. The fluctuations of ΔT and Q_{12} are characterized by their power spectral densities $P_{\Delta T}$ and $P_{Q_{12}}$. When combining Eq. (1) with the definition of the power spectral density of a random stationary process X, $P_X(\omega) = \lim_{r\to\infty} \frac{1}{T}\langle |X_T(\omega)|^2\rangle$, where X_T is the Fourier transform of the restriction of $X_{(t)}$, to the finite time interval $[0, T]$, we obtain

$$P_{\Delta T}(\omega) = \frac{P_{Q_{12}}(\omega)}{|G_{12}^* T_0|^2}. \tag{2}$$

We now apply the fluctuation-dissipation theorem considering ΔT as the force and G_{12}^* as the susceptibility. The power spectral density of the temperature fluctuation is given by the fluctuation-dissipation theorem [15]:

$$P_{\Delta T}(\omega) = \frac{\mathrm{Re}(G_{12}^*)}{|G_{12}^*(\omega)|^2}\Theta(\omega, T_0), \tag{3}$$

where $\Theta(\omega, T_0)$ is the mean energy of an oscillator $\hbar\omega/(e^{h\omega/k_B T} - 1)$, and Re indicates the real part.

Combining Eqs. (2) and (3) yields

$$\mathrm{R\,e}[G_{12}^*(\omega)] = \frac{P_{Q_{12}}(\omega)}{T_0^2\Theta(\omega, T_0)}. \tag{4}$$

From Eq. (1), it is obvious that the thermal conductance

$G_{12} = Q_{12}/\Delta T$ is given by $G_{12} = T_0 G^*_{12}$. The static limit ($\omega = 0$) of Eq. (4) indicates that the time integration of the flux autocorrelation is directly proportional to the static thermal conductance. From the Wiener-Khinchin theorem, we have $P_{Q_{12}}(\omega) = \int_{-\infty}^{+\infty} \langle Q_{12}(0) Q_{12}(t) \rangle e^{-i\omega t} dt$, so that we need to compute the temporal fluctuation of the flux between the two silica NPs. To this aim, we use the molecular dynamics (MD) technique. It consists of computing all the atomic positions and velocities as a function of time. Each atom is modeled by a mass point whose trajectory is described by the second Newton's Law [16]:

$$\sum_j \mathbf{f}_{ij} = m_i \ddot{\mathbf{r}}_i, \tag{5}$$

where m_i and $\ddot{\mathbf{r}}_i$ are the atomic mass and acceleration, and $\mathbf{f}_{ij}$ represents the force exerted by atoms j on atom i. The interatomic forces describe the interaction in polar materials such as silica. They are derived from the van Beest, Kramer, and van Santen (BKS) interaction potential [17] in order to provide the full physical picture of the long range electromagnetic and the repulsive-attractive short range interactions. Accordingly, the BKS potential can be decomposed into a Coulomb and a Buckingham potential. The Buckingham part includes an exponential term to describe the repulsive forces and a sixth power term that represents the short range van der Waals attractive forces. The Coulomb potential takes into account the interatomic electrostatic forces. Neither a potential cutoff nor a limited neighbors list are implemented in the force calculation. No boundary conditions are applied. A fourth order Gear integration scheme [16] was used to provide the velocities $\mathbf{v}_i$ and the positions $\mathbf{r}_i$ from Eq. (5). The time step of 0.7 fs that is proposed in the literature [18] appears to be sufficiently small to ensure the total energy conservation. The simulation starts with two cubes of β-cristobalite crystals separated by a few nanometers. The two NPs are heated up during 2000 time steps to the same temperature $T_0 = 300$ K by using a conventional Gaussian thermostat. The β-cristobalite is not stable at this temperature so that the NPs lose their crystalline structure to become amorphous, as illustrated in Fig. 1. Since the NPs positions are not frozen, the van der Waals forces drive them to stick together. In order to avoid the artifacts due to the variation of the inter-NP distance, we stop the simulation when a 10% variation of the initial distance is reached. The error is reduced by computing several phase ensembles for the same macroscopic experiment. We also *a posteriori* checked that the heat transfer is characterized by a relaxation time much smaller than the physical simulation time. After the NPs have reached equilibrium, the exchanged power Q_{12} between the nanoparticle noted NP1 and the nanoparticle noted NP2 is computed as the net work done by a particle on the ions of the other particle (see Fig. 2):

$$Q_{12} = \sum_{\substack{i\in \mathrm{NP1}\\ j\in \mathrm{NP2}}} \mathbf{f}_{ij} \cdot \mathbf{v}_j - \sum_{\substack{i\in \mathrm{NP1}\\ j\in \mathrm{NP2}}} \mathbf{f}_{ji} \cdot \mathbf{v}_i. \tag{6}$$

To provide a basis for comparison, we also derive the spectral dissipated power $Q_{1\to 2}$ in NP2 due to the electromagnetic interaction NP1 in the framework of fluctuational electrodynamics [11]. The power at a given frequency can be expressed as a Joule term generated by a monochromatic field [11,12]:

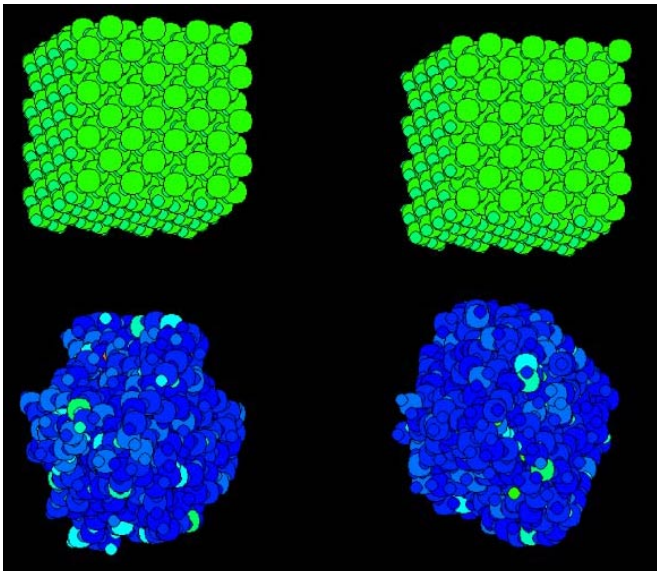

FIG. 1 (color online). Snapshots of the NPs at time $t = 0$ (top) and 1 ps after (bottom). The crystalline structure rapidly disappears and amorphous NPs are obtained. The color indicates the work done by the atom under the electrostatic field of the neighboring particle.

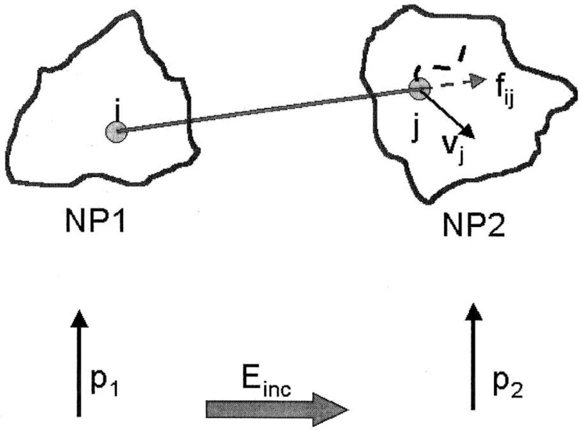

FIG. 2. Explanation schemes of the calculation of the power dissipated in the NP2 due to the field emitted by the NP1. In the MD computation (above), the power is computed as the work produced by the atomic motions of the NP2 atoms in the potential field generated by the NP1. In the electrostatic calculation (below), each NP is assimilated to one dipole (vectors $\mathbf{p}_1$ and $\mathbf{p}_2$) situated at the NP centers.

$$Q_{1\to 2}(\omega) = \frac{\omega\varepsilon_0}{2}\alpha_2''|\mathbf{E}_{\text{inc}}(\mathbf{r}_2)|^2, \tag{7}$$

where α_2'' is the imaginary part of the NP2 polarizability. The modulus of the incident electric field is evaluated simply by using a dipole approximation. Because the separation distance d is smaller than the wavelength, retardation effects can be neglected so that an electrostatic approximation is valid. If in addition, $d \gg R$, where R stands for the effective radius of the particle, each particle is equivalent to a dipole. The incident field then takes the form $\mathbf{E}_{\text{inc}} = \mathbf{G}\cdot\mathbf{p}$. $\mathbf{G}$ is the Green's dyadic given by $\mathbf{G} = \frac{1}{4\pi\varepsilon_0}\frac{1}{r^3}[\mathbf{1} - 3\mathbf{uu}]$, where $\mathbf{u}$ is the unit vector $\mathbf{r}/r$. Because of thermal fluctuations, each particle has a random electric dipole. The fluctuations-dissipation theorem yields the correlation function:

$$\langle p_k p_l\rangle = \frac{\varepsilon_0}{\pi\omega}\alpha_1''(\omega)\Theta(T_1,\omega)\delta(\omega-\omega')\delta_{kl}. \tag{8}$$

This equation yields α_1'' from a MD calculation of $\langle p_k p_l\rangle$. Using this result, and the form of the incident field produced by a dipole, we obtain

$$Q_{1\to 2} = \frac{3\alpha_1''\alpha_2''}{4\pi^3 d^6}\Theta(T_1,\omega). \tag{9}$$

The power exchanged between the NPs due to the dipole-dipole coupling can finally be written as [11]

$$Q_{12}(\omega) = \frac{3}{4\pi^3}\frac{\alpha_1''(\omega)\alpha_2''(\omega)}{d^6}[\Theta(\omega,T_1) - \Theta(\omega,T_2)]. \tag{10}$$

This is drastically different from the usual radiative heat transfer flux due to the emission and absorption of photons in the far field [11]:

$$Q_{12}^{\text{FF}}(\omega) = \frac{\omega^4\alpha_1''(\omega)\alpha_2''(\omega)}{32\pi^3 c^4 d^2}[\Theta(\omega,T_1) - \Theta(\omega,T_2)], \tag{11}$$

where c is the light velocity. We can linearize Eq. (10) to obtain the following form of the conductance:

$$G_{12}(T_0) = \frac{3}{4\pi^3}\int_0^\infty \Theta'(\omega,T_0)\alpha_1''(\omega)\alpha_2''(\omega)d\omega\frac{1}{d^6}, \tag{12}$$

where Θ' is the temperature derivative of the function Θ. The near-field and far-field contributions have the same order of magnitude when $d = 2\pi c/\omega$, but the dipole-dipole heat transfer is 12 orders of magnitude larger when $d = 10$ nm. In silica, the main contributions to the integral in Eq. (11) are the resonant phonon-polariton modes with frequencies equal to 20 and 33 THz . They appear as sharp peaks in the polarizability spectrum and therefore in the spectrum of the exchanged power. The polarizability is proportional to the NP volume and G_{12} is proportional to the product $\alpha_1''\alpha_2''$, so that the conductance should increase as the effective radius R to the power six. Equation (11) also provides the conductance dependence on the interparticle distance $d = |r_2 - r_1|$ as a d^{-6} law. The field produced by a dipole in the near field at a distance d is proportional to d^{-3}. It follows that the exchanged power is linearly dependent to d^{-6}. In Fig. 3, the thermal conductances are reported as a function of the internanoparticle distance. In the distance interval (8–100 nm), the MD (data points) and the dipole-dipole (thick lines) models are in very good agreement. This constitutes a validation of the molecular dynamics based near-field analysis and also shows that the polarizability is relevant up to nanometric sizes. At distances smaller than 8 nm (4 diameters), a deviation between the MD and the dipole-dipole model appears. This deviation reaches 4 orders of magnitude as compared to the dipole-dipole model. In order to understand the origin of the enhanced heat transfer, we have studied the contribution of the Buckingham potential which is not taken into account in the dipole-dipole model. We have evaluated separately the contributions of the three terms of the potential: repulsive and attractive parts of the Buckingham potential and Coulomb potential. The latter always dominate the transfer in the range of investigation. Thus, the increase of the conductance cannot be attributed to short range interactions. It appears to be due to the contribution of multipolar Coulomb interactions. Indeed, the field produced by a particle cannot be considered as uniform in the neighboring particle when the separation distance is on the order of the NP's diameter. This explanation is supported by Fig. 3. It is clearly seen that the deviation between both models

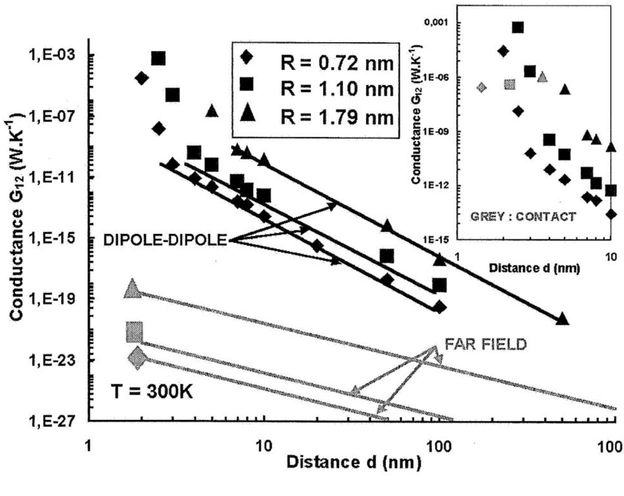

FIG. 3. Thermal conductance G_{12} vs distance d between the centers of mass. R corresponds to the nanoparticle radius and N is the number of atoms in each particle. While the MD (data points) and the analytical (thick lines) predictions agree very well when the interparticle distance is larger than the nanoparticle diameter, a deviation appears when $d < 4R$. The far-field conductance due to emission and absorption is reported for comparison. The inset highlights the conductance values when the NPs are in contact (gray data points). Their abscissa correspond to $2R$. The contact conductance is 2 to 3 orders of magnitude lower than the conductance just before contact.

occurs for a distance between particles which is between $4R$ and $5R$ for the three cases studied. These results show that the thermal conductance increases continuously when the distance between NPs is decreased. It entails that the strong coupling between the particles is responsible for a transition regime between far-field radiation and conduction.

We also have done calculations of the conductance when the particles are in contact. Surprisingly, we find that the contact conductance is smaller than the conductance for a separation distance of the order of the particle radius as seen in the insert of Fig. 3 for the two smallest particles. Since the Buckingham contribution is negligible before contact, the conductance is only due to the autocorrelation of the Coulomb power $\langle Q_{12}{}^{\mathrm{C}} Q_{12}{}^{\mathrm{C}}(t)\rangle$. At contact, this last quantity does not vary much but three other terms appear: the pure Buckingham contribution $\langle Q_{12}{}^{\mathrm{B}} Q_{12}{}^{\mathrm{B}}(t)\rangle$ and the cross terms $\langle Q_{12}{}^{\mathrm{C}} Q_{12}{}^{\mathrm{B}}(t)\rangle$ and $\langle Q_{12}{}^{\mathrm{B}} Q_{12}{}^{\mathrm{C}}(t)\rangle$. The calculation shows that the cross terms are negative and on the order of $\langle Q_{12}{}^{\mathrm{B}} Q_{12}{}^{\mathrm{B}}(t)\rangle$. Therefore the final sum is lower than $\langle Q_{12}{}^{\mathrm{C}} Q_{12}{}^{\mathrm{C}}(t)\rangle$. The origin of this decay is still an open question. It might be possible that the contact produces a correlation of the positions of the atoms of both particles that results in a smaller fluctuation of Q_{12}.

One can speculate on the properties of a chain of particles. It has been shown recently [20] that a chain of metallic particles can be used as a waveguide of electromagnetic energy due to the coupling of surface plasmons between neighboring particles. We have found that a similar coupling involving localized polaritons is responsible for the heat transfer at small distances. These results suggest that the thermal conductance of a chain of particles might be larger than the conductance of a continuous rod.

In conclusion, we have reported an analysis of heat transfer between two nanoparticles as a function of their separation distance. We have used a MD technique and the fluctuation-dissipation theorem to compute the thermal conductance between two nanoparticles. We have also introduced a model based on a dipole-dipole interaction. Both models agree for distances larger than 2 diameters. In all cases, the Coulomb potential and the resonant excitation of the polariton modes are responsible for the large heat transfer. At separation distances smaller than the diameter, the heat transfer due to multipolar contributions is enhanced by several orders of magnitude. The heat transfer before mechanical contact is found to be 2 to 3 orders of magnitude more efficient than when the NPs are in contact. These results show that the traditional separation between conduction and radiation is no longer meaningful at these length scales.

S.V. acknowledges a Grant from the French Commissariat à L'Energie Atomique (CEA).

---

*Electronic address: gilberto.domingues@let.ensma.fr
†Electronic address: volz@em2c.ecp.fr

[1] G. Chen, Phys. Rev. B **57**, 14958 (1998).
[2] K.R. Patton and M.R. Geller, Phys. Rev. B **64**, 155320 (2001).
[3] A. Dhar, Phys. Rev. Lett. **86**, 5882 (2001).
[4] P.L. Garrido, P.I. Hurtado, and B. Nadrowski, Phys. Rev. Lett. **86**, 5486 (2001).
[5] A. Ozpineci and S. Ciraci, Phys. Rev. B **63**, 125415 (2001).
[6] L.G.C. Rego and G. Kirczenow, Phys. Rev. Lett. **81**, 232 (1998).
[7] T. Yamamoto, S. Watanabe, and K. Watanabe, Phys. Rev. Lett. **92**, 75502 (2004).
[8] K. Schwab, E.A. Henrlksen, J.M. Worlock, and M.L. Roukes, Nature (London) **404**, 974 (2000).
[9] D. Polder and M. van Hove, Phys. Rev. B **4**, 3303 (1971).
[10] J.B. Pendry, J. Phys. Condens. Matter **11**, 6621 (1999); J.J. Loomis and H.J. Maris, Phys. Rev. B **50**, 18517 (1994); A. Narayanaswamy and G. Chen, Appl. Phys. Lett. **82**, 3544 (2003).
[11] A.I. Volokitin and B.N.J. Persson, Phys. Rev. B **63**, 205404 (2001).
[12] J.-P. Mulet, K. Joulain, R. Carminati, and J.-J. Greffet, Appl. Phys. Lett. **78**, 2931 (2001).
[13] J.-P. Mulet, K. Joulain, R. Carminati, and J.-J. Greffet, Microscale Thermophysical Engineering **6**, 209 (2002).
[14] Th. Förster, Ann. Phys. (Berlin) **2**, 55 (1948).
[15] H.B. Callen and T.A. Welton, Phys. Rev. **83**, 1 (1951).
[16] M.P. Allen and D.J. Tildesley, *Computer Simulation of Liquids* (Oxford University Press, New York, 1987).
[17] B.W.H. van Beest, G.J. Kramer, and R.A. van Santen, Phys. Rev. Lett. **64**, 1955 (1990).
[18] S. Volz, Phys. Rev. Lett. **87**, 74301 (2001).
[19] G. Domingues, J.-B. Saulnier, and S. Volz, Superlattices Microstruct. (to be published).
[20] S.A. Maier *et al.*, Nat. Mater. **2**, 229 (2003).

Surface electromagnetic waves thermally excited : Radiative heat transfer, coherence properties and Casimir forces revisited in the near field

K. Joulain, J.-P. Mulet, F. Marquier, R. Carminati et J.-J. Greffet

Surface Science Reports, vol 57, pp59–112 (2005)

Available online at www.sciencedirect.com

SCIENCE DIRECT®

Surface Science Reports 57 (2005) 59–112

surface science reports

www.elsevier.com/locate/surfrep

Surface electromagnetic waves thermally excited: Radiative heat transfer, coherence properties and Casimir forces revisited in the near field

Karl Joulain [a], Jean-Philippe Mulet [b], François Marquier [b],
Rémi Carminati [b], Jean-Jacques Greffet [b,*]

[a] *Laboratoire d'Études Thermiques, ENSMA, BP 109, 86960 Futuroscope Cedex, France*
[b] *Laboratoire d'Energétique Moléculaire, Macroscopique, Combustion, Ecole Centrale Paris,*
Grande Voie des Vignes, 92295 Châtenay-Malabry Cedex, France

Received 16 November 2004
Available online 8 April 2005

Abstract

We review in this article the influence of surface waves on the thermally excited electromagnetic field. We study in particular the field emitted at subwavelength distances of material surfaces. After reviewing the main properties of surface waves, we introduce the fluctuation–dissipation theorem that allows to model the fluctuating electromagnetic fields. We then analyse the contribution of these waves in a variety of phenomena. They give a leading contribution to the density of electromagnetic states, they produce both temporal coherence and spatial coherence in the near field of planar thermal sources. They can be used to modify radiative properties of surfaces and to design partially spatially coherent sources. Finally, we discuss the role of surface waves in the radiative heat transfer and the theory of dispersion forces at the subwavelength scale.

PACS: 73.20.Mf; 42.25.Kb; 44.40+a; 42.50.Lc

Keywords: Surface waves; Polaritons; Optical coherence; Heat transfer; Radiative transfer; Dispersion forces

---

* Corresponding author.
E-mail address: greffet@em2c.ecp.fr (J.-J. Greffet).

doi:10.1016/j.surfrep.2004.12.002

Contents

1. Introduction

Many condensed matter properties are determined by surface properties. Very often, surface waves, which are electromagnetic eigenmodes of the surface, play a key role. Let us mention a few examples. It has been demonstrated [1] that the lifetime of a molecule varies dramatically when a metallic surface is brought at a distance smaller than a micron. This effect is due to the resonant excitation of surface plasmons. The van der Waals force between a molecule and an interface is proportional to $1/|\varepsilon + 1|^2$, where ε is the dielectric constant of the medium. There is therefore a resonance for the particular frequency such that $\varepsilon = -1$. This condition coincides with a branch of the dispersion relation of a surface wave. It can be viewed as a resonant excitation of surface charge oscillations. It was shown in [2] that the van der Waals force between a molecule and a surface can become repulsive depending on the relative position of the molecule and the surface resonances. Enhanced scattering due to the resonant excitation of surface charges has also been demonstrated for SiC in the infrared: a tip brought close to a surface generates a very strong scattering signal for some particular frequencies corresponding to the excitation of surface waves [3]. Both experiments can be understood by replacing the interface by an image whose amplitude is very large owing to the excitation of a resonance of the surface charges. Surface enhanced Raman scattering (SERS) is partially due to the enhancement of the electromagnetic field at the interface due to the excitation of a surface wave. The resonance of the electromagnetic (EM) field at an interface is also responsible for the enhanced transmission of a metallic film with a periodic array of holes [4,5]. The resonance of the EM field associated with the surface mode is responsible for the so-called "perfect lens" effect [6]. A key feature of all the above examples is that they involve the interaction of a surface and an object in the near field of the structure. As it will be explained in detail in Section 2, surface waves are evanescent waves whose amplitude decreases away from the interface on a wavelength scale. In the far field, the influence of such modes is therefore negligible. In the near field on the contrary, their role is essential.

We will see in Section 3 that surface waves can be excited by thermal fluctuations inside a body. The role of surface waves in the modification of the density of EM states at the interface has a strong influence on the thermally emitted fields. Their intensity is many orders of magnitude larger in the near field than in the far field [7]. In addition, they are quasi-monochromatic in the vicinity of the surface. This entails that their coherence properties are extremely different from those of the blackbody radiation [8]. There have been recently several experiments that have probed these thermal fields in the near-field regime: heating of trapped atoms [9], realization of a spatially partially coherent thermal source [10]. After reviewing these experiments, we will show how an EM approach with random fluctuating thermal sources can be used to describe and analyse these effects. It is based on the fluctuation–dissipation theorem. We will see that the knowledge of the electromagnetic energy density gives access to a fundamental concept: the local density of EM states. In Section 4, we study the EM coherence properties near a material supporting surface waves and held at a temperature *T*. We will see that the emitted field has very peculiar spatial coherent properties in the near field. Indeed, the field can be spatially coherent over a length larger than several tens of wavelength. We then use this property to design coherent thermal sources. In Sections 5 and 6 we show that the radiative heat transfer is enhanced by several orders of magnitude in the near field when two material supporting surface waves are put face to face. We will consider three cases: two nanoparticles face to face, a nanoparticle near a plane interface and two semi-infinite half-spaces separated by a narrow gap. In the last section, we will analyse the role played by the surface waves in the Casimir force, i.e. in the force of interaction between two semi-infinite bodies. We will see that this force is dominated in the near field by the interaction between surface waves. Finally, we review the work done to analyse the contribution of fluctuating electromagnetic fields to the friction forces.

2. Introduction to surface electromagnetic waves

In this section, we give a brief introduction to the main properties of electromagnetic surface waves. This particular type of waves exists at the interface between two different media. An electromagnetic surface wave propagates along the interface and decreases exponentially in the perpendicular direction. Surface waves due to a coupling between the electromagnetic field and a resonant polarization oscillation in the material are called surface polaritons. From a microscopic point of view, the surface waves at the interface of a metal is a charge density wave or plasmon. It is therefore called surface-plasmon polariton. At the interface of a dielectric, the surface wave is due to the coupling of an optical phonon with the electromagnetic field. It is thus called surface-phonon polariton. Plasmon polaritons and phonon polaritons can also exist in the whole volume of the material. More details about this subject can be found in textbooks such as Kittel [11], Ashcroft and Mermin [12] and Ziman [13]. In what follows, we will focus our attention on surface polaritons propagating along a plane interface. Excellent reviews of the subject can be found in [14–17].

2.1. Surface polaritons

Let us now study the existence and the behaviour of surface polaritons in the case of a plane interface separating two linear, homogeneous and isotropic media with different dielectric constants. The system considered is depicted in Fig. 1.

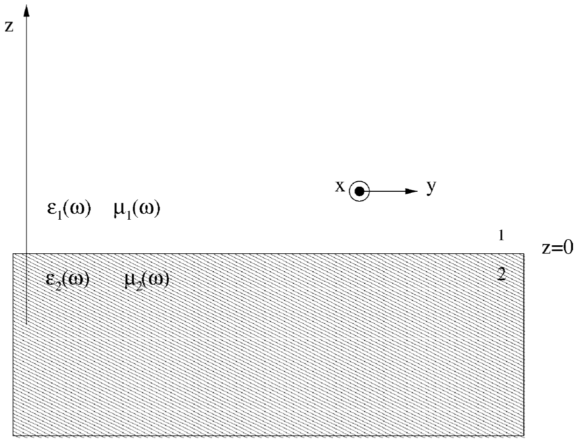

Fig. 1. A plane interface separating medium 1 (dielectric constant ε_1, magnetic constant μ_1) and medium 2 (dielectric constant ε_2, magnetic constant μ_2).

Medium 1 (dielectric constant ε_1 and magnetic constant μ_1) fills the upper half-space, $z > 0$, whereas medium 2 (dielectric constant ε_2 and magnetic constant μ_2) fills the lower half-space, $z < 0$. The two media are supposed to be local and dispersive so that their complex dielectric and magnetic constants only depend on ω.

The three directions x, y, z shown in Fig. 1 are characterized by their unit vectors $\hat{\mathbf{x}}, \hat{\mathbf{y}}, \hat{\mathbf{z}}$. A point in space will be denoted $\mathbf{r} = (x, y, z) = x\hat{\mathbf{x}} + y\hat{\mathbf{y}} + z\hat{\mathbf{z}} = (\mathbf{R}, z)$, where $\mathbf{R} = x\hat{\mathbf{x}} + y\hat{\mathbf{y}}$. Similarly, a wavevector $\mathbf{k} = (k_x, k_y, k_z)$ will be denoted by $\mathbf{k} = (\mathbf{K}, \gamma)$, where $\mathbf{K}$ is the component parallel to the interface and $\gamma = k_z$ the component in the z-direction.

A surface wave is a particular solution of Maxwell's equations which propagates along the interface and decreases exponentially in the perpendicular directions. Because of the translational invariance of the system, it can be cast in the form

$$\mathbf{E}_1(\mathbf{r}, \omega) = \begin{pmatrix} E_{x,1} \\ E_{y,1} \\ E_{z,1} \end{pmatrix} \exp\left[\mathrm{i}(\mathbf{K}\cdot\mathbf{R} + \gamma_1 z)\right] \quad \text{(medium 1)}, \tag{1}$$

$$\mathbf{E}_2(\mathbf{r}, \omega) = \begin{pmatrix} E_{x,2} \\ E_{y,2} \\ E_{z,2} \end{pmatrix} \exp\left[\mathrm{i}(\mathbf{K}\cdot\mathbf{R} - \gamma_2 z)\right] \quad \text{(medium 2)}, \tag{2}$$

where γ_1 and γ_2 are given by

$$\gamma_1^2 = \varepsilon_1\mu_1 k_0^2 - K^2 \quad \text{with}\, \mathrm{Im}(\gamma_1) > 0, \tag{3}$$

$$\gamma_2^2 = \varepsilon_2\mu_2 k_0^2 - K^2 \quad \text{with}\, \mathrm{Im}(\gamma_2) > 0. \tag{4}$$

Here $k_0 = \omega/c$, where c is the speed of light in vacuum. We now look for the existence of surface waves in s (TE) or p (TM) polarization. In what follows, we shall assume that the wave propagates along the y-axis.

2.1.1. s-Polarization (TE)

In s-polarization, the electric field is perpendicular to the plane (y, z). The electric field $\mathbf{E}$ is thus parallel to the x-direction

$$\mathbf{E}_1(\mathbf{r}, \omega) = E_{x,1}\hat{\mathbf{x}} \exp\left[\mathrm{i}(\mathbf{K}\cdot\mathbf{R} + \gamma_1 z)\right], \tag{5}$$

$$\mathbf{E}_2(\mathbf{r}, \omega) = E_{x,2}\hat{\mathbf{x}} \exp\left[\mathrm{i}(\mathbf{K}\cdot\mathbf{R} - \gamma_2 z)\right]. \tag{6}$$

The magnetic field is then derived from the Maxwell equation $\mathbf{H} = -\mathrm{i}\nabla \times \mathbf{E}/(\mu(\omega)\omega)$. The continuity conditions of the parallel components of the fields across the interface yield the following equations:

$$E_{x,1} - E_{x,2} = 0, \tag{7}$$

$$\frac{\gamma_1}{\mu_1} E_{x,1} + \frac{\gamma_2}{\mu_2} E_{x,2} = 0. \tag{8}$$

We search a mode of the system which is a solution of the homogeneous problem. The system has a non-trivial solution if and only if

$$\mu_2\gamma_1 + \mu_1\gamma_2 = 0. \tag{9}$$

Taking into account Eqs. (3) and (4), one obtains from (9) the surface-wave dispersion relation for s-polarization:

$$K^2 = \frac{\omega^2}{c^2}\frac{\mu_1\mu_2[\mu_2\varepsilon_1 - \mu_1\varepsilon_2]}{\mu_2^2(\omega) - \mu_1^2(\omega)}. \tag{10}$$

For the particular case where $\varepsilon_1 = \varepsilon_2 = \varepsilon$, the dispersion relation takes the simple form:

$$K^2 = \frac{\omega^2}{c^2}\varepsilon\frac{\mu_1(\omega)\mu_2(\omega)}{\mu_1(\omega) + \mu_2(\omega)}. \tag{11}$$

2.1.2. p-Polarization (TM)

For p-polarization, the electric field lies in the plane (y, z) and can be cast in the form:

$$\mathbf{E}_1(\mathbf{r}, \omega) = \begin{pmatrix} 0 \\ E_{y,1} \\ E_{z,1} \end{pmatrix} \exp[\mathrm{i}(\mathbf{K}\cdot\mathbf{R} + \gamma_1 z)], \tag{12}$$

$$\mathbf{E}_2(\mathbf{r}, \omega) = \begin{pmatrix} 0 \\ E_{y,2} \\ E_{z,2} \end{pmatrix} \exp[\mathrm{i}(\mathbf{K}\cdot\mathbf{R} - \gamma_2 z)]. \tag{13}$$

The continuity of the tangential electric field yields

$$E_{y,1} - E_{y,2} = 0. \tag{14}$$

The Maxwell equation $\nabla\cdot\mathbf{E} = 0$ imposes a relation between the two components of the electric field

$$KE_{y,2} - \gamma_2 E_{z,2} = KE_{y,1} + \gamma_1 E_{z,1} = 0. \tag{15}$$

The continuity of the z-component of D yields

$$\varepsilon_1 E_{z,1} = \varepsilon_2 E_{z,2}. \tag{16}$$

Inserting (16) and (14) into (15) yields

$$\varepsilon_1\gamma_2 + \varepsilon_2\gamma_1 = 0. \tag{17}$$

Taking into account Eqs. (3) and (4), one obtains from (17) the surface-wave dispersion relation for p-polarization:

$$K^2 = \frac{\omega^2}{c^2}\frac{\varepsilon_1\varepsilon_2[\varepsilon_2\mu_1 - \varepsilon_1\mu_2]}{\varepsilon_2^2 - \varepsilon_1^2}. \tag{18}$$

For the particular case where $\mu_1 = \mu_2 = \mu$, the dispersion relation takes the simple form

$$K^2 = \frac{\omega^2}{c^2}\mu\frac{\varepsilon_1(\omega)\varepsilon_2(\omega)}{\varepsilon_1(\omega) + \varepsilon_2(\omega)}. \tag{19}$$

2.1.3. Remarks

- When the media are non-magnetic, there are no surface waves in s-polarization. Indeed, the imaginary part of the z-components γ_i is always positive, so that $\gamma_1 + \gamma_2$ cannot be zero.

- At a material–vacuum interface ($\varepsilon_1 = \mu_1 = 1$), the dispersion relation reads in p-polarization.

$$K = \frac{\omega}{c}\sqrt{\frac{\varepsilon_2(\omega)}{\varepsilon_2(\omega)+1}}. \tag{20}$$

It follows that the wavevector becomes very large for a frequency such that $\varepsilon_2(\omega) + 1 = 0$.

- The conditions (9) and (17) correspond to the poles of the Fresnel reflection factors. To search these poles is an alternative and simple way to find the dispersion relation. This is particularly useful when searching the dispersion relation for multilayers system.
- For non-lossy media, one can find a real K corresponding to a real ω. This mode exists only if $\varepsilon_2 < -1$ in the case of an interface separating a vacuum from a material.
- In the presence of losses, the dispersion relation yields two equations but both frequency and wavevector can be complex so that there are four parameters. Two cases are of practical interest: (i) a real frequency and a complex wavevector and (ii) a complex frequency and a real wavevector. These two choices leads to different shapes of the dispersion relation as discussed in [18–21]. The imaginary part of ω describes the finite lifetime of the mode due to losses. Conversely, for a given real ω, the imaginary part of K yields a finite propagation length along the interface.
- The dispersion relation (20) shows that for a real dielectric constant $\varepsilon_1 < -1, K > \omega/c$. This mode cannot be excited by a plane wave whose wavevector is such that $K < \omega/c$. In order to excite this mode, it is necessary to increase the wavevector. One can use a prism [14,22,23] or a grating [18]. A scatterer can also generate a wave with the required wavevector.

2.2. *Dispersion relation*

In this section, we will consider two types of surface waves: surface-plasmon polaritons and surface-phonon polaritons. Surface-plasmon polaritons are observed at surfaces separating a dielectric from a medium with a gas of free electrons such as a metal or a doped semiconductor. The dielectric constant of the latter can be modelled by a Drude model:

$$\varepsilon(\omega) = \varepsilon_\infty - \frac{\omega_p^2}{\omega^2 + i\Gamma\omega}, \tag{21}$$

where ω_p is the plasma frequency and Γ accounts for the losses. Using this model and neglecting the losses, we find that the resonance condition $\varepsilon(\omega) + 1 = 0$ yields $\omega = \omega_p/\sqrt{2}$. For most metals, this frequency lies in the near UV so that these surface waves are difficult to excite thermally. By contrast, surface-phonon polaritons can be excited thermally because they exist in the infrared. They have been studied through measurements of emission and reflectivity spectra by Vinogradov et al. [24]. Let us study the dispersion relation of surface-phonon polaritons at a vacuum/silicon carbide (SiC) interface. SiC is a non-magnetic material whose dielectric constant is well described by an oscillator model in the 2–22 μm range [25]:

$$\varepsilon(\omega) = \varepsilon_\infty\left(1 + \frac{\omega_L^2 - \omega_T^2}{\omega_T^2 - \omega^2 - i\Gamma\omega}\right) \tag{22}$$

with $\omega_L = 969\ \mathrm{cm}^{-1}$, $\omega_T = 793\ \mathrm{cm}^{-1}$, $\Gamma = 4.76\ \mathrm{cm}^{-1}$ and $\varepsilon_\infty = 6.7$. The dispersion relation at a SiC/vacuum interface is represented in Fig. 2. This dispersion relation has been derived by assuming that the

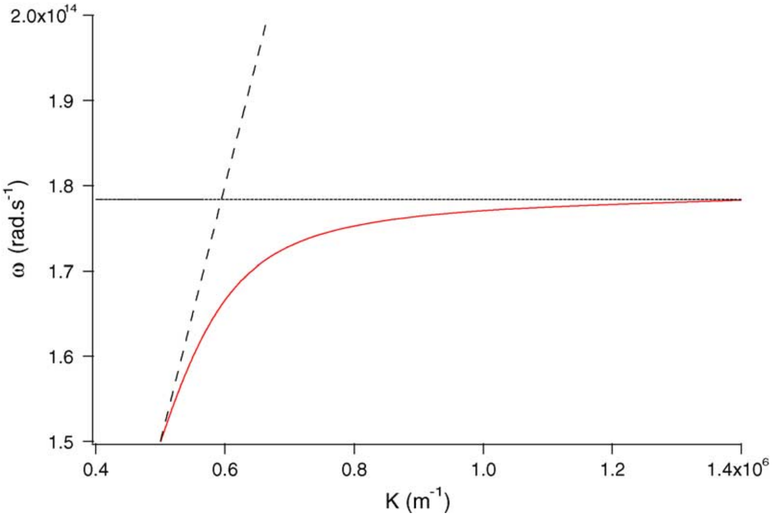

Fig. 2. Dispersion relation for surface-phonon polariton at a SiC/vacuum interface. The flat asymptote is situated at $\omega_{\text{asym}} = 1.784 \times 10^{14}$ rad s^{-1}. The slanting dashed line represents the light cone above which a wave is propagating and below which a wave is evanescent.

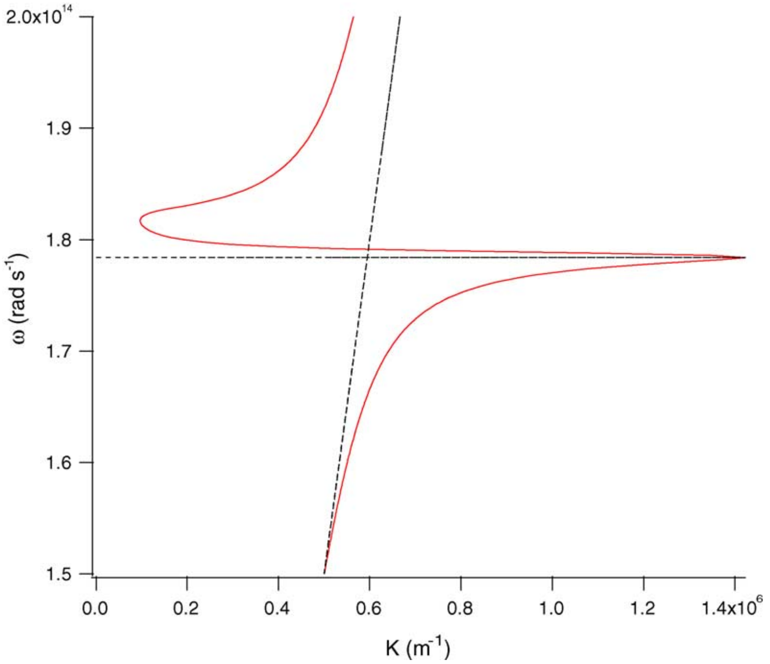

Fig. 3. Dispersion relation for surface-phonon polariton at a SiC/vacuum interface. Real ω chosen to obtain a complex K. The real part of K is represented. The horizontal asymptote is situated at $\omega_{\text{asym}} = 1.784 \times 10^{14}$ rad s^{-1}. The slanting dashed line represents the light line above which a wave is propagating and below which a wave is evanescent.

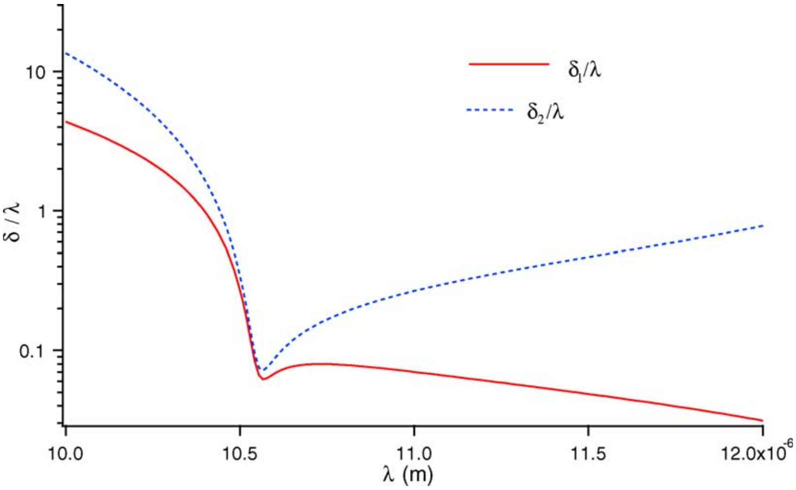

Fig. 4. Surface-wave decay length along the *z*-direction in mediums 1 and 2 vs. the wavelength for a SiC–vacuum interface.

frequency ω is complex and the parallel wavevector K is real. This choice is well suited to analyse experimental measurements of spectra for fixed angles. The width of the resonance peaks observed is related to the imaginary part of the frequency of the mode. We note that the curve is situated below the light cone $\omega = cK$ so that the surface wave is evanescent. We also observe a horizontal asymptote for $\omega_{\text{asym}} = 1.784 \times 10^{14}$ rad s^{-1} so that there is a peak in the density of electromagnetic states. We will see in the next sections that the existence of surface modes at a particular frequency plays a key role in many phenomena.

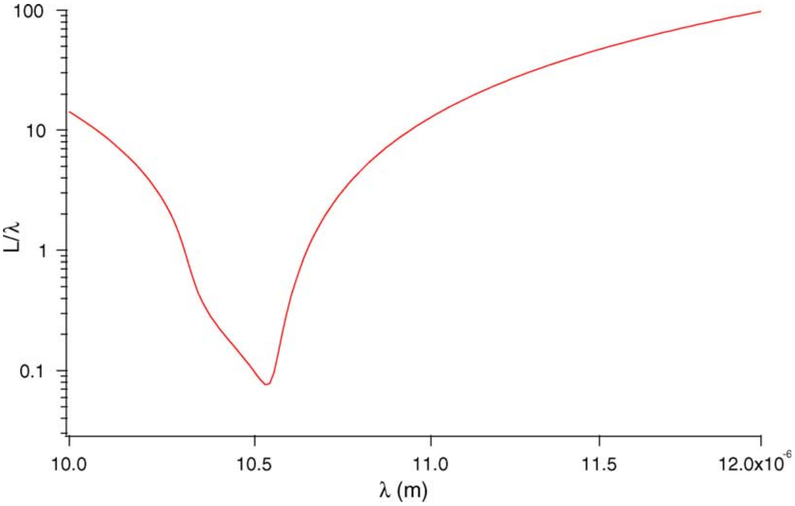

Fig. 5. Surface-wave propagation length along the interface vs. the wavelength λ.

In Fig. 3, we have shown the dispersion relation obtained when choosing a real frequency ω and a complex wavevector K. The real part of the complex wavevector is represented. It is seen that the shape of the dispersion relation is significantly changed. A backbending of the curve is observed. This type of behaviour is observed experimentally when performing measurements at a fixed frequency and varying the angle. Observed resonances in reflection or emission experiments have an angular width which is related to the imaginary part of the complex wavevector.

We have plotted in Fig. 4 the surface-wave decay length in the direction perpendicular to the interface versus the wavelength. From Eqs. (1) and (2), it is seen that the amplitude of the electromagnetic field decreases exponentially in the z-direction with a decay length $\delta_1 = 1/\mathrm{Im}(\gamma_1)$ in medium 1 and $\delta_2 = 1/\mathrm{Im}(\gamma_2)$ in medium 2. We note that the smallest penetration depth in SiC is obtained for the frequency ω_{asym}. At this frequency, losses are very large.

We study in Fig. 5 the surface-wave propagation length along a SiC–vacuum interface. It is given by the inverse of the imaginary part of the parallel wavevector $L = 1/\mathrm{Im}(K)$. Around ω_{asym}, L is minimum. It can be as large as several tens of wavelengths.

It will be seen below that the existence of these surface modes is responsible for a long coherence time and a long coherence length of the electromagnetic field in the near field.

3. Fluctuation–dissipation theorem: cross-spectral density

In this section, we introduce the tools and methods that are useful to derive the field radiated by a body in thermal equilibrium at temperature T both in the near field and in the far field. Whereas the phenomenological theory of radiometry based on geometrical optics describes correctly the field emitted in the far field, it fails to predict the behaviour of the emitted radiation in the near field. Indeed, geometrical optics does not include evanescent waves. A new framework to describe thermal radiation is thus needed. Such a framework has been introduced by Rytov [26,27] and is known as fluctuational electrodynamics. The key idea is that for any material in thermal equilibrium, charges such as electrons in metals, or ions in polar crystals undergo a random thermal motion. This generates fluctuating currents which radiate an electromagnetic field. A body at temperature T is thus viewed as a medium with random currents that radiate the thermal field. The statistical properties of this field can be determined provided that: (i) the statistical properties of the random currents are known and (ii) the radiation of a volume element below an interface is known. The first information is given by the fluctuation–dissipation theorem (FDT), the second is given by the Green's tensor of the system.

This approach is very similar to the Langevin model for Brownian motion. Langevin [28] introduced a random force as a source for the dynamical equations of the particles. This allows us to derive the statistical properties of their random motion. An important feature of the model is that the random force is not arbitrary. Its correlation function is related to the losses of the system by the FDT. In the case of random electromagnetic fields, the dynamic equations for the fields are Maxwell equations. We need to introduce an external random source to model the fluctuations of the field. These external sources are random currents. The key issue now is to know the statistical properties of these random sources. They are given by the FDT. The remaining of this section introduces the technical tools needed to derive the radiated field. The first part is devoted to the statistical properties of the random currents given by the FDT, the second part deals with the FDT applied to the EM fields. The Green's tensor are given in Appendix A.

3.1. Cross-spectral density

The spectral analysis of a signal is usually done using its Fourier transform. In the case of a stationary stochastic signal, the Fourier transform cannot be computed in the sense of a function because the integral is not square integrable. However, it is possible to compute the Fourier transform of the time-correlation function of the random signal. In what follows, we will be interested in the space–time-correlation function of the electromagnetic fields $\langle E_k(\mathbf{r},t)E_l(\mathbf{r}',t')\rangle$. For a stationary field, this correlation function depends only on $t-t'$. Its Fourier transform $\mathcal{E}_{kl}(\mathbf{r},\mathbf{r}',\omega)$ is called cross-spectral density:

$$\mathcal{E}_{kl}(\mathbf{r},\mathbf{r}',\omega)=\int_{-\infty}^{\infty}\langle E_k(\mathbf{r},t)E_l(\mathbf{r}',t')\rangle\,\mathrm{e}^{\mathrm{i}\omega(t-t')}\,\mathrm{d}(t-t'). \tag{23}$$

Note that for $\mathbf{r}=\mathbf{r}'$, the above equation reduces to the Wiener–Khinchin theorem that relates the power spectral density of a random stationary signal to the Fourier transform of its time-correlation function [29]. It is convenient to introduce a correlation function of the Fourier transforms using generalized functions:

$$\langle E_k(\mathbf{r},\omega)E_l^*(\mathbf{r}',\omega')\rangle=2\pi\delta(\omega-\omega')\mathcal{E}_{kl}(\mathbf{r},\mathbf{r}',\omega). \tag{24}$$

3.2. Fluctuation–dissipation theorem for the current density

The FDT derived by Callen and Welton [30] yields a general form of the symmetrised correlation function of a vector $\mathbf{X}(\mathbf{r},\omega)$. Whereas for classical quantities, the symmetrization does not change the results, it plays an important role in quantum mechanics for non-commuting observables. If the cross-spectral density of $\mathbf{X}$ is defined by $\mathcal{X}_{kl}$, we define the symmetrised correlation function of $\mathbf{X}$ by

$$\mathcal{X}_{kl}^{(\mathrm{S})}=\tfrac{1}{2}[\mathcal{X}_{kl}+\mathcal{X}_{lk}]. \tag{25}$$

The symmetrised correlation function of the dipole moment of a particle in thermodynamic equilibrium with polarizability α defined by $p_i=\varepsilon_0\alpha_{ij}E_j$ can be written as [30,31]:

$$\langle p_k(\omega)p_l^*(\omega')\rangle_{\mathrm{S}}=2\pi\delta(\omega-\omega')\mathcal{P}_{kl}^{(\mathrm{S})}(\omega)=\hbar\coth\left(\frac{\hbar\omega}{2k_{\mathrm{B}}T}\right)\mathrm{Im}[\varepsilon_0\alpha_{kl}(\omega)]2\pi\delta(\omega-\omega'), \tag{26}$$

where the brackets denote an ensemble average. In the preceding expression $\hbar$ is the reduced Planck constant and k_{B} the Boltzmann's constant.

For a bulk in thermodynamic equilibrium at temperature T, the symmetrised correlation function of the polarization density can be written as [30,31]:

$$\begin{aligned}\langle P_k(\mathbf{r},\omega)P_l^*(\mathbf{r}',\omega')\rangle_{\mathrm{S}}&=2\pi\delta(\omega-\omega')\mathcal{P}_{kl}^{(\mathrm{S})}(\mathbf{r},\mathbf{r}',\omega)\\&=\hbar\coth\left(\frac{\hbar\omega}{2k_{\mathrm{B}}T}\right)\mathrm{Im}[\varepsilon_0\varepsilon_{kl}(\mathbf{r},\mathbf{r}',\omega)]2\pi\delta(\omega-\omega'),\end{aligned} \tag{27}$$

where the spatial dependence of the dielectric constant accounts for a possible non-locality. From this equation, we can easily derive the correlation function of the current density $\mathbf{j} = -\mathrm{i}\omega\mathbf{P}$:

$$\langle j_k(\mathbf{r},\omega) j_l^*(\mathbf{r}',\omega')\rangle_{\mathrm{S}} = \hbar\omega^2 \coth\left(\frac{\hbar\omega}{2k_{\mathrm{B}}T}\right) \mathrm{Im}[\varepsilon_0\varepsilon_{kl}(\mathbf{r},\mathbf{r}',\omega)] 2\pi\delta(\omega-\omega'). \tag{28}$$

Note that if the medium is isotropic and local, the quantity $\mathrm{Im}[\varepsilon_{kl}(\mathbf{r},\mathbf{r}',\omega)]$ becomes $\mathrm{Im}[\varepsilon(\mathbf{r},\omega)]\delta_{kl}\delta(\mathbf{r}-\mathbf{r}')$. We also note that:

$$\frac{\hbar\omega}{2}\coth\left(\frac{\hbar\omega}{2k_{\mathrm{B}}T}\right) = \hbar\omega\left[\frac{1}{2} + \frac{1}{\exp(\hbar\omega/k_{\mathrm{B}}T) - 1}\right] \tag{29}$$

is the mean energy of a harmonic oscillator in thermal equilibrium. In the following we will also use the compact notation

$$\Theta(\omega,T) = \frac{\hbar\omega}{\exp(\hbar\omega/k_{\mathrm{B}}T) - 1} \tag{30}$$

for the mean energy of the harmonic oscillator without the zero point energy $\hbar\omega/2$.

3.3. Fluctuation–dissipation for the fields

Another very useful application of the fluctuation–dissipation theorem yields a relation between the cross-spectral density of the fluctuating fields at equilibrium and the Green's tensor of the system [31]. The Green's tensor appears as the linear response coefficient relating the fields to their sources. Note that these quantities are defined in classical electrodynamics. In what follows, we will use three different Green's tensors defined by

$$\mathbf{E}(\mathbf{r},\omega) = \mathrm{i}\mu_0\omega \int \mathrm{d}^3\mathbf{r}' \overset{\leftrightarrow}{\mathbf{G}}{}^{EE}(\mathbf{r},\mathbf{r}',\omega)\mathbf{j}(\mathbf{r}',\omega), \tag{31}$$

$$\mathbf{H}(\mathbf{r},\omega) = \int \mathrm{d}^3\mathbf{r}' \overset{\leftrightarrow}{\mathbf{G}}{}^{HE}(\mathbf{r},\mathbf{r}',\omega)\mathbf{j}(\mathbf{r}',\omega), \tag{32}$$

and

$$\mathbf{H}(\mathbf{r},\omega) = \int \mathrm{d}^3\mathbf{r}' \overset{\leftrightarrow}{\mathbf{G}}{}^{HH}(\mathbf{r},\mathbf{r}',\omega)\mathbf{M}(\mathbf{r}',\omega). \tag{33}$$

In this last equation G_{kl}^{HH} is the Green tensor relating the magnetic field to the *magnetization M*. Note that both $\overset{\leftrightarrow}{\mathbf{G}}{}^{HE}$ and $\overset{\leftrightarrow}{\mathbf{G}}{}^{HH}$ are related to $\overset{\leftrightarrow}{\mathbf{G}}{}^{EE}$ through the Maxwell equations [32].

$$\overset{\leftrightarrow}{\mathbf{G}}{}^{HE}(\mathbf{r},\mathbf{r}',\omega) = \frac{\mu_0}{\mu(\mathbf{r})}\nabla_{\mathbf{r}} \times \overset{\leftrightarrow}{\mathbf{G}}{}^{EE}(\mathbf{r},\mathbf{r}',\omega), \tag{34}$$

$$\overset{\leftrightarrow}{\mathbf{G}}{}^{HH}(\mathbf{r},\mathbf{r}',\omega) = \frac{\mu_0}{\mu(\mathbf{r})}\nabla_{\mathbf{r}} \times \overset{\leftrightarrow}{\mathbf{G}}{}^{EE}(\mathbf{r},\mathbf{r}',\omega) \cdot \nabla_{\mathbf{r}'} \times . \tag{35}$$

Explicit forms of the Green's tensors are given in Appendix A.

The cross-spectral correlation function of the electromagnetic field at equilibrium or blackbody radiation then reads [31]:

$$\mathcal{E}_{kl}^{(\mathrm{S})}(\mathbf{r},\mathbf{r}',\omega) = \mu_0\hbar\omega^2\coth\left[\frac{\hbar\omega}{2k_\mathrm{B}T}\right]\mathrm{Im}[G_{kl}^{EE}(\mathbf{r},\mathbf{r}',\omega)]. \tag{36}$$

This last equation is the FDT for the electric field. The cross-spectral correlation function of the magnetic field obeys a similar relation

$$\mathcal{H}_{kl}^{(\mathrm{S})}(\mathbf{r},\mathbf{r}',\omega) = \varepsilon_0\hbar\omega^2\coth\left[\frac{\hbar\omega}{2k_\mathrm{B}T}\right]\mathrm{Im}[G_{kl}^{HH}(\mathbf{r},\mathbf{r}',\omega)]. \tag{37}$$

These relations yield the coherence properties of the equilibrium field provided that the Green's tensor of the system are known. Note that the Green's tensor is a classical object so that the vacuum fluctuations are already included in the above formalism. It is also important to note that the Green's tensor can be computed including the losses of the system.

3.4. Relation between symmetrised correlation function and observables

In what follows, we will use the FDT either with $\Theta(\omega,T)$ or with $(\hbar\omega/2)\coth[\hbar\omega/2k_\mathrm{B}T] = \Theta(\omega,T)+\hbar\omega/2$. The former amounts to drop the vacuum energy $\hbar\omega/2$. This choice can be justified using a heuristic argument [27]. When it comes to the derivation of fluxes, the vacuum energy cancels when taking the difference between emission and absorption [27]. Instead, when computing the Casimir force, one has first to compute the energy variation of the electromagnetic field in the space between two parallel plates. In that case, the vacuum fluctuation energy $\hbar\omega/2$ plays a fundamental role and cannot be ignored so that it is kept in the calculation. This procedure may seem arbitrary. A more rigorous approach to the choice of the relevant form of the FDT can be derived from quantum electrodynamics as discussed by Agarwal [31]. It can be shown that when the process studied involves an absorption measurement, the relevant correlation function is the normally ordered correlation function [29]. If the measurement involves a quantum counter, then one needs to calculate the antinormally ordered correlation function [29]. The relevant forms of the FDT are given in the paper by Agarwal [31]. We show in Appendix B that one can end up with an *effective* cross-spectral density defined for positive frequencies only. This effective cross-spectral density depends on the type of measurement. The time-correlation function can be written as:

$$\langle E_k(\mathbf{r},t+\tau)E_l(\mathbf{r}',t)\rangle = \mathrm{Re}\left[\int_0^\infty \frac{\mathrm{d}\omega}{2\pi}\exp(\mathrm{i}\omega\tau)\mathcal{E}_{kl}^{\mathrm{eff}}(\mathbf{r},\mathbf{r}',\omega)\right], \tag{38}$$

where the effective cross-spectral density $\mathcal{E}_{kl}^{\mathrm{eff}}(\mathbf{r},\mathbf{r}',\omega)$ that should be used for an absorption measurement is given by:

$$\mathcal{E}_{kl}^{(\mathrm{N})}(\mathbf{r},\mathbf{r}',\omega) = 4\omega\mu_0\,\mathrm{Im}[G_{kl}^{EE}(\mathbf{r},\mathbf{r}',\omega)]\Theta(\omega,T), \tag{39}$$

and the cross-spectral density appropriate for a quantum-counter measurement is given by:

$$\mathcal{E}_{kl}^{(\mathrm{A})}(\mathbf{r},\mathbf{r}',\omega) = 4\omega\mu_0\,\mathrm{Im}[G_{kl}^{EE}(\mathbf{r},\mathbf{r}',\omega)][\Theta(\omega,T)+\hbar\omega]. \tag{40}$$

Only the latter includes the energy of vacuum fluctuations. For the sake of comparison, we also report the symmetrised form appropriate for positive frequencies only:

$$\mathcal{E}_{kl}^{(\mathrm{S})}(\mathbf{r},\mathbf{r}',\omega) = 4\omega\mu_0\,\mathrm{Im}[G_{kl}^{E}(\mathbf{r},\mathbf{r}',\omega)]\left[\Theta(\omega,T)+\frac{\hbar\omega}{2}\right]. \tag{41}$$

A simple rule can thus be used when starting with the usual symmetrised FDT as given by (36) in order to get the relevant correlation function for a process involving absorption: (1) restrict the spectrum to positive frequencies, (2) multiply the spectrum by 2, (3) remove the energy fluctuation contribution and (4) take the real part of the Fourier transform.

3.5. Fluctuational electrodynamics out of equilibrium

In the previous section, we have given the form of the cross-spectral densities of the fields and current densities at equilibrium. However, it is possible to derive the fields radiated by a system out of equilibrium. The approach is based on the FDT for the current density. Assuming local thermal equilibrium, we can derive the statistical properties of the currents. We can thus derive the fields radiated by a system with an inhomogeneous temperature field. Although the mean values of the fields are zero, their correlations are non-zero. Let us consider for instance the symmetrised cross-spectral correlation function of the electric field

$$\langle E_k(\mathbf{r},\omega)E_l^*(\mathbf{r}',\omega')\rangle_{\mathrm{S}} = \left\langle \mu_0^2\omega^2 \int \mathrm{d}^3\mathbf{r}_1\,\mathrm{d}^3\mathbf{r}_2\, G_{km}^{EE}(\mathbf{r},\mathbf{r}_1,\omega)G_{ln}^{EE*}(\mathbf{r}',\mathbf{r}_2,\omega)\,j_m(\mathbf{r}_1,\omega)\,j_n^*(\mathbf{r}_2,\omega')\right\rangle. \tag{42}$$

Using the FDT for the fluctuating currents (28), we obtain

$$\begin{aligned}\langle E_k(\mathbf{r},\omega)E_l^*(\mathbf{r}',\omega')\rangle_{\mathrm{S}} &= \frac{\mu_0\omega^3}{c^2}\int \mathrm{d}^3\mathbf{r}_1\,\mathrm{Im}[\varepsilon(\mathbf{r}_1)] \\ &\quad\times\left[\Theta[\omega,T(\mathbf{r}_1)]+\frac{\hbar\omega}{2}\right]G_{km}^{EE}(\mathbf{r},\mathbf{r}_1,\omega)G_{lm}^{EE*}(\mathbf{r}',\mathbf{r}_1,\omega')2\pi\delta(\omega-\omega').\end{aligned} \tag{43}$$

With the help of the FDT, we have seen that it is possible to calculate all kinds of cross-spectral spatial correlation functions involving the electric and the magnetic fields. With these functions, we are now able to calculate other quantities such as the energy density, the Poynting vector or the Maxwell stress tensor. In the case of thermal equilibrium situations, we will use the application of the FDT for the fields which give simpler expressions. Nevertheless, in non-equilibrium situation such as the study of heat transfer between materials held at different temperatures, these expressions are no longer valid. It is however still possible to use the fluctuation–dissipation theorem for the currents by assuming local thermal equilibrium. It will thus be possible to derive the fluxes for non-equilibrium situations.

4. Electromagnetic energy density and local density of states (LDOS)

In this section, we will study how the electromagnetic energy density is modified by the presence of material media. We shall first examine the amount of electromagnetic energy emitted by a half-space at temperature T. It will be shown that the density of energy is dramatically different in the near field and in the far field when surface waves are excited. The second point that we address is the general problem of the definition of the local density of electromagnetic states. Whereas it is possible to derive the density of electromagnetic states for a non-lossy system by searching the eigenmodes, the lossy case is more difficult. An alternative approach was introduced by Agarwal [33] based on the FDT. Using this approach, we will discuss the role of surface waves.

4.1. Density of emitted electromagnetic energy

Let us return to the configuration described in Fig. 1. We calculate the electromagnetic energy density in the vacuum above a material (medium 2) at temperature T due to the emission of this material. We do not take into account the energy incident on the medium. In order to retrieve the density of energy at equilibrium, we should include the energy incident on the surface. The density of energy in vacuum reads (see [34, p. 242])

$$\langle U \rangle = \frac{\varepsilon_0}{2}\langle |\mathbf{E}(\mathbf{r},t)|^2\rangle + \frac{\mu_0}{2}\langle |\mathbf{H}(\mathbf{r},t)|^2\rangle = \int_0^\infty \frac{\mathrm{d}\omega}{2\pi} u_{\mathrm{tot}}(z,\omega), \tag{44}$$

where we have introduced a spectral density of energy u_{tot}. The details of the derivation are given in [7,35]. The basic procedure amounts to derive the field radiated by the random currents in the lower half-space. Adding the electric and magnetic contributions, the total electromagnetic energy above a medium at temperature T in a vacuum at $T = 0$ K is

$$u_{\mathrm{tot}}(z,\omega) = \frac{\Theta(\omega,T)\omega^2}{2\pi^2 c^3}\left\{ \int_0^{\omega/c} \frac{K\,\mathrm{d}K}{k_0|\gamma_1|} \frac{(1-|r_{12}^{\mathrm{s}}|^2) + (1-|r_{12}^{\mathrm{p}}|^2)}{2} + \int_{\omega/c}^{\infty} \frac{4K^3\,\mathrm{d}K}{k_0^3|\gamma_1|} \frac{\mathrm{Im}(r_{12}^{\mathrm{s}}) + \mathrm{Im}(r_{12}^{\mathrm{p}})}{2}\, \mathrm{e}^{-2\,\mathrm{Im}(\gamma_1)z} \right\}, \tag{45}$$

where the Fresnel reflection factors are given in Appendix A.

4.2. Discussion

In order to illustrate this discussion, we study the density of electromagnetic energy above some specific materials. Let us first consider a material supporting surface waves in the infrared such as SiC. In Fig. 6, we plot the energy density $u_{\mathrm{tot}}(z,\omega)$ versus the frequency at different distances of a semi-infinite interface of SiC. The semi-infinite medium is at temperature $T = 300$ K whereas the vacuum is at $T = 0$ K. Note that at $T = 300$ K, Wien's law gives a peak wavelength for thermal radiation $\lambda_{\mathrm{Wien}} = 10\,\mu\mathrm{m}$. In the far field, i.e. for distances d larger than $\lambda_{\mathrm{Wien}}/2\pi$, the energy density spectrum resembles that of a blackbody. The difference with a Planck spectrum comes from the fact that SiC is a very reflecting material around $\lambda = 10\,\mu\mathrm{m}$ or $\omega = 1.7 \times 10^{14}$ rad s^{-1}. Thus, its emissivity is small in this frequency interval.

This property is easily recovered from the electromagnetic energy due to propagating waves only (first term in (45))

$$u_{\mathrm{tot}}^{\mathrm{prop}}(z,\omega) = u^0(\omega,T)\int \frac{\mathrm{d}\Omega}{4\pi} \frac{1-|r_{12}^{\mathrm{s}}|^2 + 1 - |r_{12}^{\mathrm{p}}|^2}{2}, \tag{46}$$

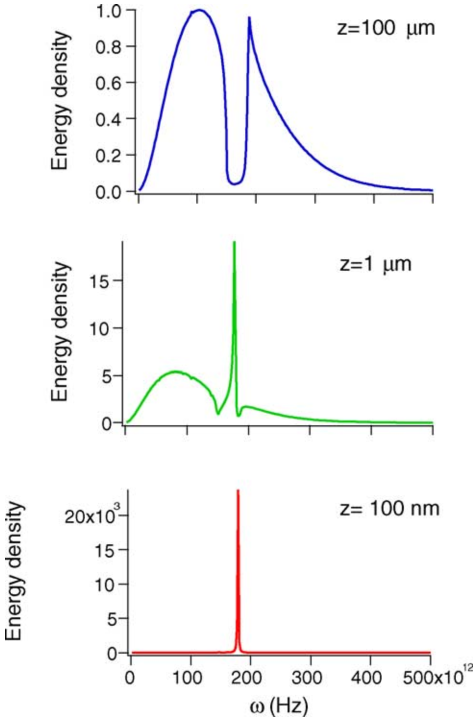

Fig. 6. Total electromagnetic energy density above a plane interface separating SiC at $T = 300$ K from vacuum at $T = 0$ K.

where we have used $2\pi K\,\mathrm{d}K = k_0^2 \cos(\theta)\,\mathrm{d}\Omega$, θ is the angle between the emission direction and the normal of the surface. The integral is performed over a half-space and

$$u^0(\omega, T) = \frac{\hbar\omega^3}{\pi^2 c^3}\frac{1}{\exp(\hbar\omega/kT) - 1} = \frac{\omega^2}{\pi^2 c^3}\Theta(\omega, T) \tag{47}$$

is the electromagnetic energy density in a cavity at thermal equilibrium T. In the far field, the evanescent waves do not contribute to the energy density because of the exponential decay ($\mathrm{e}^{-2\,\mathrm{Im}(\gamma_1)z}$). We note that if medium 2 is totally absorbing ($r_{12}^{\mathrm{s,p}} = 0$), the energy density due to propagating waves is half the energy calculated in a vacuum at thermal equilibrium. This is not surprising since we are computing only the emitted part of the radiation. In the case of equilibrium radiation, there is also the contribution of the radiation coming from the upper half-space. We note that in (46), the emissivity appears to be $(1 - |r_{12}^{\mathrm{s}}(\omega, \Omega)|^2 + 1 - |r_{12}^{\mathrm{p}}(\omega, \Omega)|^2)/2$. It is thus the half sum of the energy transmission factors for both polarizations. Thermal emission by a half-space can be viewed as a transmission process of a blackbody radiation in the material medium through an interface. This point of view yields insight in Kirchhoff's law. Indeed, the equality between emissivity and absorptivity appears to be a consequence of the equality of the transmission factor when interchanging source and detector.

At a distance $z = 3$ μm which is slightly larger than $\lambda_{\mathrm{Wien}}/2\pi$, the energy density spectrum changes drastically and a strong peak emerges. At 100 nm from the interface, one observes that the thermal emission is almost monochromatic around $\omega = 1.78 \times 10^{14}$ rad s^{-1}. At this frequency the energy density has increased by more than four orders of magnitude. The peak corresponds to the excitation of a surface wave. This distance is in agreement with the decay length of the surface waves as discussed in Section 2. At distances much smaller than the wavelength, we enter a regime that we call extreme near field. The leading contribution comes from the very large wavevectors K in the energy density integral. At large K, it can be shown that $\gamma_1 \sim \mathrm{i}K$, so that $\mathrm{Im}(r^{\mathrm{s}}_{12})$ tends to zero and $\mathrm{Im}(r^{\mathrm{p}}_{12})$ tends to its electrostatic limit $(\varepsilon_2 - 1)/(\varepsilon_2 + 1)$. We finally obtain a very simple asymptotic form of the energy density

$$u_{\mathrm{tot}} = \frac{\omega^2}{4\pi^2 c^3} \frac{\mathrm{Im}[\varepsilon_2(\omega)]}{|\varepsilon_2(\omega) + 1|^2} \frac{1}{(k_0 z)^3} \Theta(\omega, T), \tag{48}$$

showing that the energy density will diverge at the frequencies where $\varepsilon_1 = -1$. These are the frequencies where the dispersion relation has horizontal asymptotes. For lossy materials, a resonance will occur at the frequency where $\mathrm{Re}(\varepsilon_2) = -1$ provided that absorption (i.e. $\mathrm{Im}[\varepsilon_2]$) is not too large. Let us mention that the resonance of the reflection factor in the electrostatic limit has been observed experimentally by Hillenbrand et al. [3]. A spectrum of the light scattered by a tip very close to a surface shows a peak for the resonance frequency. This peak is due to the field emitted by the image of the tip. Indeed, its amplitude is proportional to the reflection factor $(\varepsilon_2 - 1)/(\varepsilon_2 + 1)$ and is therefore resonant when $\mathrm{Re}(\varepsilon_2) = -1$.

In order to prove that this surprising behaviour is not specific to SiC, we plot in Fig. 7, the energy density spectrum above a flat interface of glass. This material is amorphous so that the optical phonons are poorly defined. Here again, the energy density spectrum resembles that of a blackbody in the far field whereas peaks emerge while approaching the surface. The strongest peak is at $\omega = 9.2 \times 10^{13}$ rad s^{-1} and the weakest one

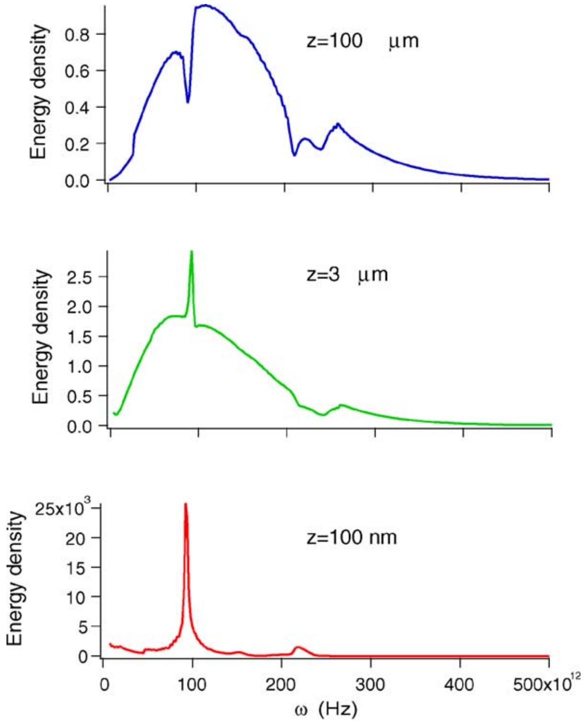

Fig. 7. Electromagnetic energy density above a plane interface separating glass at $T = 300$ K from vacuum at $T = 0$ K.

at $\omega = 2.2 \times 10^{14}$ rad s^{-1}. These frequencies are solution of $\mathrm{Re}[\varepsilon_2(\omega)] = -1$. Yet, the corresponding surface waves have a very short propagation length.

Not all materials supporting surface waves exhibit strong peaks in their near-field thermal energy density spectrum. Indeed, as it can be seen in (48), a peak is exhibited if the frequency where $\varepsilon_2(\omega)$ approaches -1 corresponds to a frequency range where $\Theta(\omega, T)$ is not too small. For example, metals exhibit surface-plasmon polariton in the UV or visible range where $\Theta(\omega, T)$ is exponentially small at ambient temperature. Thus metals do not exhibit strong peak in their thermal energy density spectrum in the near field.

4.3. Local density of states

The density of states (DOS) is a fundamental quantity from which many macroscopic quantities can be derived. In statistical physics, the DOS allows to calculate the partition function of a system from which all the macroscopic properties follow. The local density of states (LDOS) is useful to study a non-uniform system. The local density of electronic states is widely used in solid state physics. It has been shown [36] for instance that a scanning tunneling microscope images the electronic LDOS. The local character of the LDOS clearly describes the spatial distribution of electrons in the solid. A similar spatial dependence is also relevant for electromagnetic waves. Whereas the intensity is uniform in a vacuum in equilibrium, this is not the case in a waveguide or above an interface. The distribution of the energy is no longer uniform. Whereas LDOS is well defined for electrons in solid state physics [37], its electromagnetic counterpart is not very well defined in the literature. As compared to electronic systems, two differences must be taken into account: the vectorial nature of the fields and the existence of losses.

In electrodynamics, the LDOS is used in different contexts. From Fermi's golden rule, it is known that the DOS determines the radiation rate. It can be shown that the lifetime of an atom with an electric dipole along a unit vector $\mathbf{u}$ is inversely proportional to $\mathrm{Im}[\mathbf{u} \cdot G^{EE} \cdot \mathbf{u}]$. This is often referred to as the LDOS. To avoid confusion, we shall refer to this quantity as the projected LDOS. It is the relevant quantity that one needs to study when designing a microcavity or a photonic crystal to tailor emission properties. Yet, note that only those states that can be coupled to the dipole are taken into account. Thus it is not a good definition if one is interested in the total energy of the system. Such a quantity is required when computing dispersion forces [38,39] or shear forces [40] for instance. Those forces depend on the energy stored in all available modes. In a vacuum, the LDOS can be shown to be given by the imaginary part of the trace of the Green's tensor $\overset{\leftrightarrow}{\mathbf{G}}^{EE}$. This seems to be a straightforward extension of the scalar result which is proportional to the imaginary part of the Green function. The vacuum form is thus usually assumed to be valid for any other situations [41–43]. In what follows, we will summarize a recent analysis of the LDOS [44] that follows the original approach by Agarwal [33]. It will be seen that the LDOS is not given by the imaginary part of the trace of the Green's tensor $\overset{\leftrightarrow}{\mathbf{G}}^{EE}$. It will also appear that surface waves dominate the LDOS close to an interface.

We consider a system in thermal equilibrium at temperature T. In a vacuum, one can define the electromagnetic energy $U(\omega)$ by the product of the DOS $\rho(\omega)$ by the mean energy of each state at temperature T:

$$U(\omega) = \rho(\omega) \frac{\hbar\omega}{\exp(\hbar\omega/k_B T) - 1}. \qquad (49)$$

We can now introduce [7,44] a *local* density of states by using as a starting point the *local* density of electromagnetic energy $U(\mathbf{r},\omega)$ at a given point $\mathbf{r}$ in space, and at a given angular frequency ω. This can be written by definition of the LDOS $\rho(\mathbf{r},\omega)$ as

$$U(\mathbf{r},\omega) = \rho(\mathbf{r},\omega)\frac{\hbar\omega}{\exp(\hbar\omega/k_{\mathrm{B}}T) - 1}. \tag{50}$$

The density of electromagnetic energy is the sum of the density of electric energy and of the density of magnetic energy given in (44). In equilibrium, it can be calculated using the system Green's function and the fluctuation–dissipation theorem. We start from the electric and magnetic field correlation functions for a stationary system

$$\langle E_k(\mathbf{r},t)E_l(\mathbf{r}',t')\rangle = \mathrm{Re}\left[\int_0^\infty \frac{\mathrm{d}\omega}{2\pi}\mathcal{E}^{(\mathrm{N})}_{kl}(\mathbf{r},\mathbf{r}',\omega)\,\mathrm{e}^{-\mathrm{i}\omega(t-t')}\right], \tag{51}$$

$$\langle H_k(\mathbf{r},t)H_l(\mathbf{r}',t')\rangle = \mathrm{Re}\left[\int_0^\infty \frac{\mathrm{d}\omega}{2\pi}\mathcal{H}^{(\mathrm{N})}_{kl}(\mathbf{r},\mathbf{r}',\omega)\,\mathrm{e}^{-\mathrm{i}\omega(t-t')}\right], \tag{52}$$

with $t = t'$. The cross-spectral density for normally ordered fields is given by (39). It follows that the energy per unit volume can be cast in the form [33,44]:

$$U(\mathbf{r},\omega) = \frac{\hbar\omega}{\exp(\hbar\omega/k_{\mathrm{B}}T) - 1}\,\frac{\omega}{\pi c^2}\mathrm{Im}\ \mathrm{Tr}\left[\overset{\leftrightarrow}{\mathbf{G}}^{EE}(\mathbf{r},\mathbf{r},\omega) + \overset{\leftrightarrow}{\mathbf{G}}^{HH}(\mathbf{r},\mathbf{r},\omega)\right]. \tag{53}$$

A comparison of Eqs. (50) and (53) shows that the LDOS is the sum of an electric contribution ρ^E and a magnetic contribution ρ^H:

$$\rho(\mathbf{r},\omega) = \frac{\omega}{\pi c^2}\mathrm{Im}\ \mathrm{Tr}\left[\overset{\leftrightarrow}{\mathbf{G}}^{EE}(\mathbf{r},\mathbf{r},\omega) + \overset{\leftrightarrow}{\mathbf{G}}^{HH}(\mathbf{r},\mathbf{r},\omega)\right] = \rho^E(\mathbf{r},\omega) + \rho^H(\mathbf{r},\omega). \tag{54}$$

In what follows, we shall discuss a few examples to illustrate the modification of the LDOS. It will be seen that in some cases, the LDOS is accurately given by the trace of the electric Green's dyadic but it can also be very different.

4.4. Electromagnetic LDOS in simple geometries

4.4.1. Vacuum

In the vacuum, the Green's tensors $\overset{\leftrightarrow}{\mathbf{G}}^{EE}$ and $\overset{\leftrightarrow}{\mathbf{G}}^{HH}$ obey the same equation and have the same boundary conditions. Therefore, their contribution to the electromagnetic energy density are equal:

$$\mathrm{Im}[\overset{\leftrightarrow}{\mathbf{G}}^{EE}(\mathbf{r},\mathbf{r},\omega)] = \mathrm{Im}[\overset{\leftrightarrow}{\mathbf{G}}^{HH}(\mathbf{r},\mathbf{r},\omega)] = \frac{\omega}{6\pi c}\overset{\leftrightarrow}{\mathbf{I}}. \tag{55}$$

The LDOS is thus obtained by multiplying the electric-field contribution by 2. After taking the trace, the usual result for a vacuum is retrieved

$$\rho_{\mathrm{v}}(\mathbf{r},\omega) = \rho_{\mathrm{v}}(\omega) = \frac{\omega^2}{\pi^2 c^3}. \tag{56}$$

As expected, we note that the LDOS is homogeneous and isotropic.

4.4.2. Plane interface

We now consider a plane interface separating a vacuum (medium 1, in the upper half-space) from a semi-infinite material (medium 2, in the lower half-space) characterised by its complex dielectric constant $\varepsilon_2(\omega)$. The material is assumed to be homogeneous, linear, isotropic and non-magnetic. The expression of the LDOS at a given frequency and at a given height z above the interface in vacuum is obtained by inserting the expressions of the electric and magnetic Green's tensors for this geometry [45] into Eq. (54). Note that in the presence of an interface, the magnetic and electric Green's tensors are no longer the same. Indeed, the boundary conditions at the interface are different for the electric and magnetic fields.

Let us consider some specific examples for real materials like metals and dielectrics. We first calculate $\rho(z,\omega)$ for aluminum at different heights. Aluminum is a metal whose dielectric constant is well described by a Drude model for near-UV, visible and near-IR frequencies [46]:

$$\varepsilon(\omega) = 1 - \frac{\omega_p^2}{\omega(\omega + i\Gamma)}, \tag{57}$$

with $\omega_p = 1.747 \times 10^{16}$ rad s^{-1} and $\Gamma = 7.596 \times 10^{13}$ rad s^{-1}. We plotted in Fig. 8 the LDOS $\rho(\mathbf{r},\omega)$ in the near UV–near IR frequency domain at four different heights. We first note that the LDOS increases drastically when the distance to the material is reduced. As discussed in the previous section, at larger distances from the material, one retrieves the vacuum density of states. Note that at a given distance, it is always possible to find a sufficiently high frequency for which the corresponding wavelength is small compared to the distance so that a far-field situation is retrieved. This is clearly seen when looking at the curve for $z = 1$ μm which coincides with the vacuum LDOS. When the distance to the material is

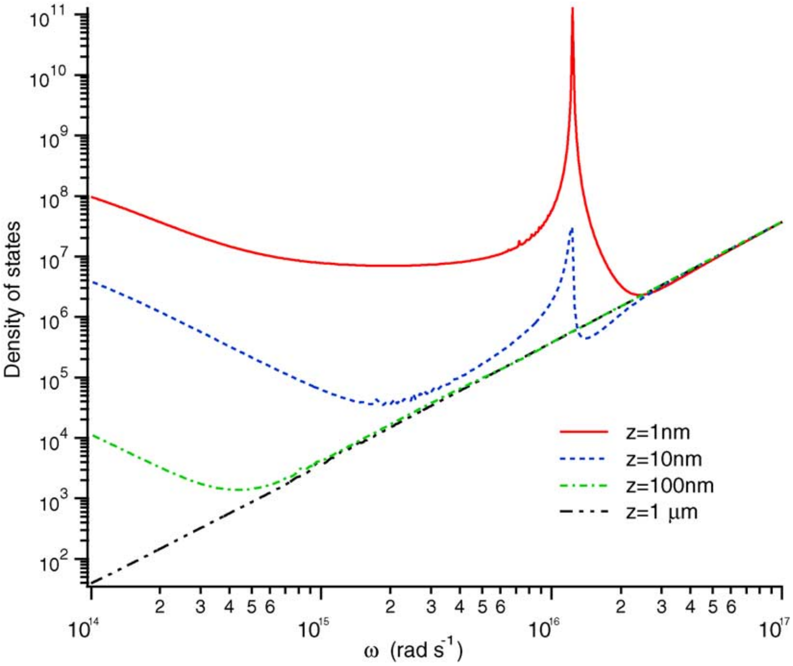

Fig. 8. LDOS vs. frequency at different heights above a semi-infinite sample of aluminum. From [44].

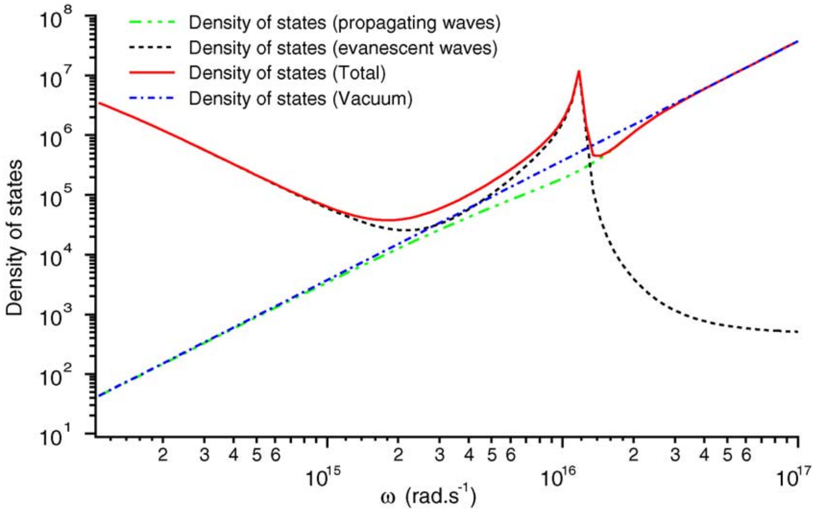

Fig. 9. Density of states contributions due to the propagating and evanescent waves compared to the total density of states and the vacuum density of states. These quantities are calculated above an aluminum sample at a distance of 10 nm. From [44].

decreased, additional modes are present: these are the evanescent modes which are confined close to the interface and which cannot be seen in the far field. Moreover, aluminum exhibits a resonance around $\omega = \omega_p/\sqrt{2}$. Below this frequency, the material supports surface-plasmon polaritons so that these additional modes are seen in the near field. This produces an increase of the LDOS close to the interface. The enhancement is particularly important at the resonant frequency which corresponds to $\mathrm{Re}[\varepsilon_2(\omega)] = -1$. This behaviour is analogous to that previously described in Section 4.1 for a glass surface supporting surface-phonon polaritons. Also note that in the low frequency regime, the LDOS increases. Finally, Fig. 8 shows that it is possible to have a LDOS smaller than that of vacuum at some

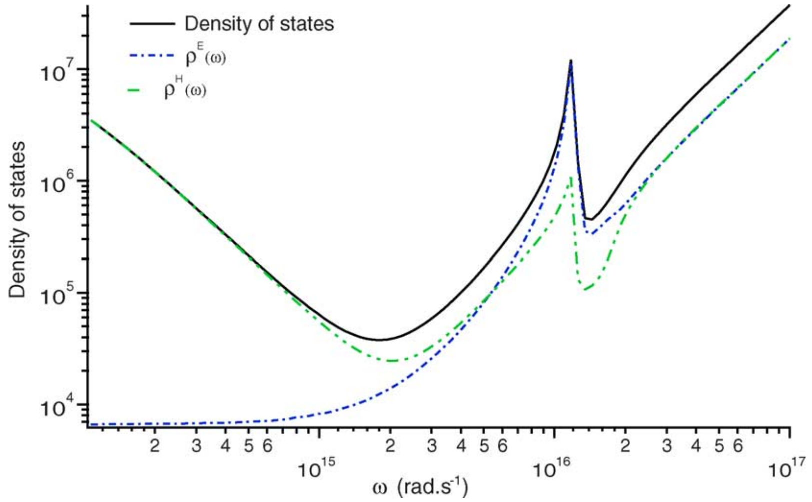

Fig. 10. LDOS at a distance $z = 10$ nm above a semi-infinite aluminum sample. Comparison with $\rho^E(z,\omega)$ and $\rho^H(z,\omega)$. From [44].

particular distances and frequencies. Fig. 9 shows the propagating and evanescent waves contributions to the LDOS above an aluminum sample at a distance of 10 nm. The propagating contribution is very similar to that of the vacuum LDOS. As expected, the evanescent contribution dominates at low frequency and around the surface-plasmon polariton resonance, where pure near-field contributions dominate.

Let us now turn to the comparison of $\rho(z,\omega)$ with the usual definition often encountered in the literature [41–43], which corresponds to $\rho^E(z,\omega)$. We plot in Fig. 10, ρ, ρ^E and ρ^H above an aluminum surface at a distance $z = 10$ nm. In this figure, it is possible to identify three different domains for the LDOS behaviour. We note again that in the far-field situation (corresponding here to high frequencies, i.e. $\lambda/2\pi \ll z$), the LDOS reduces to the vacuum situation. In this case $\rho(z,\omega) = 2\rho^E(z,\omega) = 2\rho^H(z,\omega)$. Around the resonance, the LDOS is dominated by the electric contribution ρ^E. Conversely, at low frequencies, $\rho^H(z,\omega)$ dominates. Thus, Fig. 10 shows that we have to be very careful when using the approximation $\rho(z,\omega) = \rho^E(z,\omega)$. Above aluminum and at a distance $z = 10$ nm, it is only valid in a narrow range between $\omega = 10^{16}$ and 1.5×10^{16} rad s^{-1}, i.e. around the frequency where the surface wave exists.

4.4.3. Asymptotic form of the LDOS in the near-field

In order to get more physical insight, we have calculated the asymptotic LDOS behaviour in the three regimes mentioned above. As we have already seen, the far-field regime ($\lambda/2\pi \ll z$) corresponds to the vacuum case. To study the near-field situation ($\lambda/2\pi \gg z$), we focus on the evanescent contribution due to the large wavevectors K as suggested by the results in Fig. 9. In this (quasi-static) limit, the Fresnel reflection factors reduce to

$$\lim_{K\to\infty} r_{12}^{\mathrm{s}} = \frac{\varepsilon_2 - 1}{4(K/k_0)^2}, \tag{58}$$

$$\lim_{K\to\infty} r_{12}^{\mathrm{p}} = \frac{\varepsilon_2 - 1}{\varepsilon_2 + 1}. \tag{59}$$

Asymptotically, the expressions of $\rho^E(z,\omega)$ and $\rho^H(z,\omega)$ are [44]:

$$\rho^E(z,\omega) = \frac{\rho_{\mathrm{v}}}{|\varepsilon_2 + 1|^2} \frac{\varepsilon_2''}{4k_0^3 z^3}, \tag{60}$$

$$\rho^H(z,\omega) = \rho_{\mathrm{v}} \left[\frac{\varepsilon_2''}{8k_0 z} + \frac{\varepsilon_2''}{2|\varepsilon_2 + 1|^2 k_0 z} \right]. \tag{61}$$

At a distance $z = 10$ nm above an aluminum surface, these asymptotic expressions matches almost perfectly with the evanescent contributions ($K > k_0$) of ρ^E and ρ^H. These expressions also show that for a given frequency, one can always find a distance z to the interface below which the dominant contribution to the LDOS will be the one due to the imaginary part of the electric-field Green function that varies like $(k_0 z)^{-3}$. But for aluminum at a distance $z = 10$ nm, this is not the case for all frequencies. As we mentioned before, this is only true around the resonance. For example, at low frequencies, and for $z = 10$ nm, the LDOS is actually dominated by $\rho_{\mathrm{v}}\varepsilon_2''/16k_0 z$.

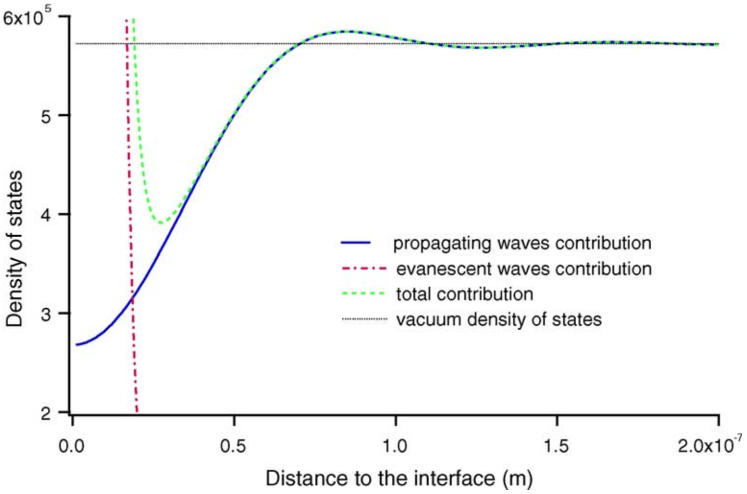

Fig. 11. LDOS vs. the distance z from an aluminum–vacuum interface at the aluminum resonant frequency. From [44].

4.4.4. *Spatial oscillations of the LDOS*

Let us now focus on the LDOS variations at a given frequency ω versus the distance z to the interface. There are essentially three regimes. First, for distances much larger than the wavelength, the LDOS is given by the vacuum expression ρ_V. The second regime is observed close to the interface where oscillations are observed. Indeed, at a given frequency, each incident plane wave on the interface can interfere with its reflected counterpart. This generates an interference pattern with a fringe spacing that depends on the angle and the frequency. Upon adding the contributions of all the plane waves over angles, the oscillating structure disappears except close to the interface. This leads to oscillations around distances on the order of the wavelength. This phenomenon is the electromagnetic analog of Friedel oscillations which can be observed in the electronic density of states near interfaces [12,47]. For a highly reflecting material, the real part of the reflection coefficients are negative so that the LDOS decreases while approaching the surface. These two regimes are clearly observed for aluminum in Fig. 11. The third regime is observed at small distances as seen in Fig. 11. It is due to the contribution of surface waves. Its behaviour is thus dependent on the frequency. Let us first consider the particular case of the frequency corresponding to the asymptote of the dispersion relation. It is seen that the evanescent contribution dominates and, ultimately, the LDOS always increases as $1/z^3$, following the behaviour found in (60). This is the usual quasi-static contribution that is always found at short distance [35]. At a frequency slightly lower than the resonance frequency, surface waves are still excited on the surface. These modes increase the LDOS according to an exponential law, a behaviour which was already found for thermally emitted fields [8,35].

4.4.5. *Conclusion about the LDOS*

The main results of this section can be summarized as follows. The LDOS of the electromagnetic field can be unambiguously and properly defined from the local density of electromagnetic energy in a vacuum above a sample at temperature T in equilibrium. The LDOS can still be written as a function of the electric-field Green's tensor only, but it is in general not proportional to the trace of its imaginary part.

An additional term proportional to the trace of the imaginary part of the magnetic-field Green's tensor is present in the far field and at low frequencies. At short distance from the surface of a material supporting surface modes (plasmon or phonon polaritons), the LDOS has a resonance at frequencies such that $\mathrm{Re}[\varepsilon(\omega)] = -1$. Close to this resonance, the approximation $\rho(z, \omega) = \rho^E(z, \omega)$ holds. If it is possible to measure the near-field thermal emission spectrum of a material, the local density of states can be retrieved [44].

5. Coherence properties of planar thermal sources in the near-field

In this section, we examine the second-order coherence properties of the fields due to thermal excitation in the presence of surface waves. We have shown that the density of energy is completely dominated by the contribution of surface waves in the near field. We shall see that they are also responsible for a deep modification of coherence properties. In what follows, we restrict ourselves to second-order coherence properties.

5.1. Spatial coherence in the near field

The spatial coherence of the electromagnetic field is characterized by its cross-spectral density $\mathcal{E}_{kl}(\mathbf{r}, \mathbf{r}', \omega)$. Roughly speaking, we study the correlation function of the electromagnetic field at two different points for a particular frequency. For a system in thermal equilibrium, this quantity is readily given by the fluctuation–dissipation theorem (36). The spatial dependence is thus included in the spatial dependence of the imaginary part of the Green's tensor. For the particular case of a vacuum, one finds the properties of the blackbody radiation. The vacuum Green's tensor is given in Appendix A.

It is more interesting to analyse what happens in the presence of an interface. It turns out that the coherence length may be either much larger or much smaller than the wavelength. This problem has been studied in [8,35] for a slightly different case. The authors considered the coherence properties of the field emitted by a solid. The difference with the above result is that in equilibrium, one has to consider two contributions: (i) the blackbody radiation illuminating the surface and reflected by the surface and (ii) the radiation emitted by the surface. In what follows, we focus only on the emitted part of the radiation so that we do not consider the equilibrium situation. The correlation is given by (43). This equation is valid inasmuch as the temperature T can be defined everywhere in a half-space. It requires a local thermal equilibrium. We have represented in Fig. 12 the cross-spectral density of the electric field for different metallic surfaces at a given distance $z = 0.05\lambda$ to the interface. It is seen that the correlation oscillates and has an exponentially decaying envelope. The decay length is much larger than the wavelength indicating that the fields are coherent over large distances. This surprising phenomenon is due to the excitation of surface waves along the interface. The physical mechanism is based on the fact that a small volume element contains random currents that excite a surface wave. This surface wave propagates along the interface over distances larger than the wavelength. It follows that different points may be illuminated by the same random source so that they are correlated. Accordingly, one does not expect any correlation between the s-polarized field since no surface wave exists for s-polarization. If one uses a material with a real part of the dielectric constant larger than -1, no surface wave can propagate so that no correlation should be observed. We have shown in Fig. 12 the case of tungsten in the visible that does not support

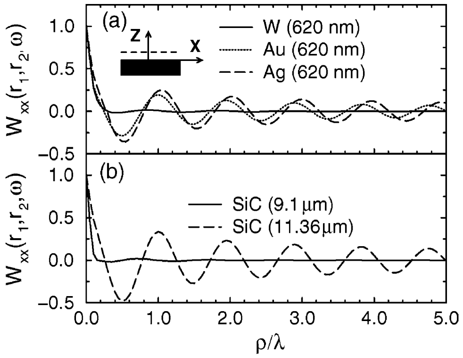

Fig. 12. Cross-spectral density function $\mathcal{E}_{xx}(\mathbf{r}_1, \mathbf{r}_2, \omega)$ (denoted as W_{xx} in the label of the figure) of the thermally emitted x-component of the electric field vs. ρ/λ, where $\rho = |\mathbf{r}_1 - \mathbf{r}_2|$ for different metals (a) and for SiC at different wavelengths (b). The long-range correlation is due to surface-plasmon polaritons for metals and to surface-phonon polaritons for SiC. From [8].

surface waves. It is seen that the coherence length is smaller than a wavelength so that the radiation field appears to be more incoherent than blackbody radiation. It has been shown in [35] that in the short-distance regime, the coherence length is given by z.

A similar behaviour is observed for SiC, a polar material that supports surface-phonon polaritons in a frequency band. Within this band, at a wavelength 11.36 μm the correlation is seen to be a long-range correlation whereas the correlation decays very rapidly for a wavelength (9.1 μm) that is not in the band where surface waves exist.

Let us discuss in simple terms the physical origin of these unusual coherence properties. The long-range coherence is unexpected because the fluctuating currents are δ-correlated as shown by the FDT. This is the reason why the fields are usually assumed to be δ-correlated in space. However, the fluctuating currents excite *induced currents* in the material. In the case of a metal, a surface plasmon can be excited. In the case of a polar crystal, a surface-phonon polariton can be excited. Both surface waves are extended modes along the surface. The induced currents associated with these extended modes are therefore coherent over large distances. More precisely, the coherence length is expected to be given by the decay length of these surface modes. This has been confirmed by a detailed asymptotic analysis in [35].

The other surprising property shown in Fig. 12 is that the coherence length defined as the FWMH of the cross-spectral density can be smaller than the wavelength. In other words, a source can be more spatially incoherent than the blackbody radiation. The key idea is that close to an interface, the field contains evanescent waves so that features smaller than the wavelength can exist. This is not the case in a vacuum so that the field has a minimum coherence length. Since the amplitude of evanescent waves of large wavevector K decays as $\exp(-Kz)$, it is clear that the distance z appears as a cutoff frequency. This explains that the coherence length increases as z in the near-field regime.

5.2. Temporal coherence in the near field

The temporal coherence of the electromagnetic field is characterized by the same-point time-correlation function of the electromagnetic field:

$$\langle E_k(\mathbf{r}, t+\tau) E_l(\mathbf{r}, t) \rangle. \tag{62}$$

This correlation function is a measurement of the memory of the random field. It is useful to introduce a typical decay time t_{coh} of the correlation function called coherence time. A Michelson interferometer with aligned mirrors performs a measurement of the correlation function. Indeed, the interference term of the signal can be written as $E(\mathbf{r}, t+\tau)E(\mathbf{r}, t)$, where τ is the flight time corresponding to the optical path length difference δ_{opt} between the two paths $\delta_{\text{opt}} = c\tau$. If the path length difference is larger than the longitudinal coherence length ct_{coh}, no interferences can be observed.

The temporal coherence of the EM field is related to its power spectral density. This is clearly seen by using the Wiener–Khinchin theorem [29,48] which shows that the power spectral density is the Fourier transform of the correlation function. Alternatively, we can start from (36). It follows that:

$$\langle E_k(\mathbf{r}, t+\tau)E_l(\mathbf{r}, t)\rangle = \text{Re}\left[\int_0^\infty 4\mu_0\omega\Theta(\omega, T)\,\text{Im}[G_{kl}^{EE}(\mathbf{r}, \mathbf{r}, \omega)]\,\text{e}^{\text{i}\omega\tau}\frac{\text{d}\omega}{2\pi}\right]. \tag{63}$$

Let us first consider the temporal coherence of the field in a vacuum. The imaginary part of the Green's tensor does not diverge and yields zero for non-diagonal terms and $\omega/6\pi c$ for diagonal terms. It follows that the time-correlation function of the blackbody radiation is given by:

$$\langle E_k(\mathbf{r}, t+\tau)E_l(\mathbf{r}, t)\rangle = \delta_{kl}\,\text{Re}\left[\int_0^\infty 4\mu_0\omega\Theta(\omega, T)\frac{\omega}{6\pi c}\,\text{e}^{\text{i}\omega\tau}\frac{\text{d}\omega}{2\pi}\right]. \tag{64}$$

Since the integrand has a large spectral width, it appears that the coherence time is on the order of the peak radiation period.

If we now consider the case of an interface, we know that the spectrum can be very different in the near field. We have seen previously that the contribution of the surface wave modifies dramatically the density of electromagnetic energy. In particular, we have seen that the density of energy becomes quasi-monochromatic which suggests a large coherence time. More specifically, in the extreme near field, we have seen in (59) that the Green's function has a resonant denominator $\varepsilon + 1$. Close to the resonance where $\text{Re}[\varepsilon(\omega_0)] = -1$, we can expand the dielectric constant as

$$\varepsilon(\omega) = -1 + \text{i}\varepsilon''(\omega_0) + (\omega - \omega_0)\frac{\text{d}\varepsilon}{\text{d}\omega}, \tag{65}$$

where we have used the notation $\varepsilon = \varepsilon' + \text{i}\varepsilon''$. The denominator $\varepsilon + 1$ can be cast in the form:

$$\varepsilon(\omega) + 1 = \left(\frac{\text{d}\varepsilon'}{\text{d}\omega}\right)[\omega - \omega_0 + \text{i}\Gamma], \tag{66}$$

where $\Gamma = \varepsilon''(\omega_0)/(\text{d}\varepsilon'/\text{d}\omega)$. It is seen that the Green's dyadic has a pole at the frequency corresponding to the asymptote of the dispersion relation of the surface wave. Its contribution to the integral (64) yields an exponential decay of the form $\exp[\text{i}\omega_0 t - \Gamma t]$. It follows that in the extreme near field, the thermally emitted field is partially temporally coherent with a coherence time given by Γ^{-1}. The origin of the temporal coherence of the electromagnetic field can thus be assigned to the very large density of states due to the asymptote of the surface wave. It follows that whereas the plane interface of a hot metallic surface is a temporally incoherent source for an atom located in the far field, it is a partially temporally coherent source for an atom located within a nanometric distance from the interface.

5.3. Polarization coherence in the near field

We have seen that the excitation of surface waves by δ-correlated currents produces both a spatial and a temporal coherence. The correlation of the field is characterized by the decay time and the decay length of the surface wave that propagates along the interface. There is a further interesting coherence effect that has been studied by Setälä et al. [49]. The basic idea is that surface waves are p-polarized waves. As shown in Section 2, a surface wave that propagates along the y-axis has an electric field with two components along the y- and z-axes. It follows that the y- and z-components of the field are correlated.

The study of correlation of the fields in the near field of the source cannot be performed using the standard formalism. Indeed, when dealing with a beam, it is usually possible to work with the two components of the field perpendicular to the propagation axis. This is no longer possible in the near field of a thermal source. A generalization of the degree of polarization has been introduced in [49]. It was found that the degree of polarization varies as a function of the distance to the interface. Like the coherence time, it increases when approaching the interface from the far field because the surface wave creates a correlation. When reaching the very near-field regime, the degree of polarization decays and tends to 1/4 for all the materials.

6. Spatially partially coherent thermal sources in the far field

6.1. Introduction

In this section, we will discuss the possibility of designing a source that is spatially partially coherent. In simple terms, a spatially partially coherent source is a source that radiates a field which has a narrow angular aperture at a given wavelength. The typical examples of coherent sources are lasers and antennas. These sources have well-defined emission angular lobes. In what follows, we will show that a narrow angular emission lobe is a signature of the spatial coherence of the field in the plane of the source.

We first introduce an analog of the Wiener–Khinchin theorem (WKT) (63) to analyse the spatial coherence of the field. In simple terms, WKT states that a quasi-monochromatic source with bandwidth $\Delta\nu$ has a coherence time roughly equal to $1/\Delta\nu$. Similarly, a quasi-parallel beam with a spatial frequency bandwidth Δk_x has a transverse coherence length $2\pi/\Delta k_x$. A formal proof is based on two properties: the relationship between the cross-spectral density of the field in the plane of the source $z = 0$ and the power spectral density of the field, the relationship between the power radiated in far field and the power spectral density. For a translationally invariant system, the Fourier transform of the field does not converge in the sense of a function. Yet, one can define a field equal to the random field in a square of area A and null outside. We can now define the Fourier transform of the field in the plane $z = 0$ as:

$$\mathbf{E}_A(\mathbf{r}_\parallel, \omega) = \int \frac{\mathrm{d}^2\mathbf{K}}{4\pi^2} \mathbf{E}_A(\mathbf{K}, \omega) \exp(\mathrm{i}\mathbf{K} \cdot \mathbf{r}_\parallel). \tag{67}$$

It can be shown [48] that the WKT yields a relation between the cross-spectral density and the power spectral density of the spectrum of the field:

$$\langle E_l(\mathbf{r}_\parallel, \omega) E_l^*(\mathbf{r}_\parallel + \mathbf{r}'_\parallel, \omega)\rangle = \int \frac{\mathrm{d}^2\mathbf{K}}{4\pi^2} \lim_{A\to\infty} \frac{1}{A} \langle E_{l,A}(\mathbf{K}, \omega) E_{l,A}^*(\mathbf{K}, \omega)\rangle \exp(\mathrm{i}\mathbf{K} \cdot \mathbf{r}'_\parallel). \tag{68}$$

This relation implies that if the spectrum has a bandwidth smaller than $2\pi/\lambda$, the coherence length is larger than λ. The second step is to show that the bandwidth of the spectrum power density $\langle \mathbf{E}_{l,A}(\mathbf{K},\omega)\mathbf{E}^{*}_{l,A}(\mathbf{K},\omega)\rangle/A$ is given by the emission pattern in the far field. Indeed, the field can be written everywhere as [50,29]:

$$\mathbf{E}_A(\mathbf{r},\omega) = \int \frac{\mathrm{d}^2\mathbf{K}}{4\pi^2}\mathbf{E}_A(\mathbf{K},\omega)\exp\left(\mathrm{i}\mathbf{K}\cdot\mathbf{r}_{\parallel} + \mathrm{i}\gamma z\right), \tag{69}$$

where $\mathbf{k} = (\mathbf{K},\gamma)$ and γ is given by $\gamma^2 = k_0^2 - \mathbf{K}^2$. This field can be evaluated asymptotically in the far field using the stationary phase approximation [29]. It can be cast in the form:

$$\mathbf{E}_A(\mathbf{r},\omega) = \frac{K\exp\left(\mathrm{i}k_0 r\right)}{r}\mathbf{E}_A\left(\mathbf{K} = \frac{2\pi}{\lambda}\hat{\mathbf{r}}_{\parallel},\omega\right), \tag{70}$$

where K is a constant. The power $\mathrm{d}P$ flowing through an element of surface $\mathrm{d}S = r^2\,\mathrm{d}\Omega$ is given by the flux of the Poynting vector. In far field, the Poynting vector has locally a plane wave structure so that its time averaged amplitude is given by $\varepsilon_0 c|\mathbf{E}|^2/2$:

$$\mathrm{d}P = \frac{\varepsilon_0 c}{2}|K|^2\left|\mathbf{E}_A\left(\mathbf{K} = \frac{2\pi}{\lambda}\hat{\mathbf{r}}_{\parallel},\omega\right)\right|^2\mathrm{d}\Omega, \tag{71}$$

where $\hat{\mathbf{r}}$ is the unit vector $\mathbf{r}/|\mathbf{r}|$. This relation completes the discussion of the link between the directivity of the emitted field and the coherence of the field in the plane of the source. It is clear that a directional source implies a narrow spectrum and therefore a large correlation length.

6.2. *Design of coherent thermal sources*

We have seen in the previous section that a source which supports a surface wave is partially spatially coherent along the surface. However, because these waves cannot propagate in a vacuum, the coherence remains confined in the vicinity of the surface. The question that we address now is whether it is possible to export the near-field coherence to the far field. In essence, that amounts to couple the surface waves to the propagating waves. This can be done in several ways. A practical way is to rule a grating on the surface. The grating can then diffract the surface wave. By properly choosing the period of the grating, it is possible to control the angle of propagation of the diffracted light. This was first observed in [51–53] for a very deep grating ruled on a doped silicon surface. Such a material supports surface-plasmon polaritons in the infrared. A more effective source was realized using a gold grating by Kreiter et al. [54]. Heinzel et al. [55] have also realized a source using surface plasmons on tungsten in the near infrared. A source based on the use of surface-phonon polaritons on SiC was reported by Le Gall et al. [18]. The first discussion of the spatial coherence of these sources was reported in [10]. An extended discussion of these properties has been recently reported [56] where transverse coherence lengths have been derived from experimental measurements of angular widths of emission peaks. Angular peaks as narrow as 1 ° can be obtained.

In order to have an efficient source of light, it is necessary to make sure that the coupling of the surface wave into a propagating wave is optimum. This can be accomplished by designing a surface with total absorption. From Kirchhoff's law, it follows that if absorption is unity, then emissivity is also unity. Another condition must be satisfied: the emission wavelength should lie in a region where Planck's function takes large values. The optimum choice of the wavelength thus depends on the temperature of the source. Fig. 13 shows the angular emission pattern of a SiC grating. It is clearly seen that the angular

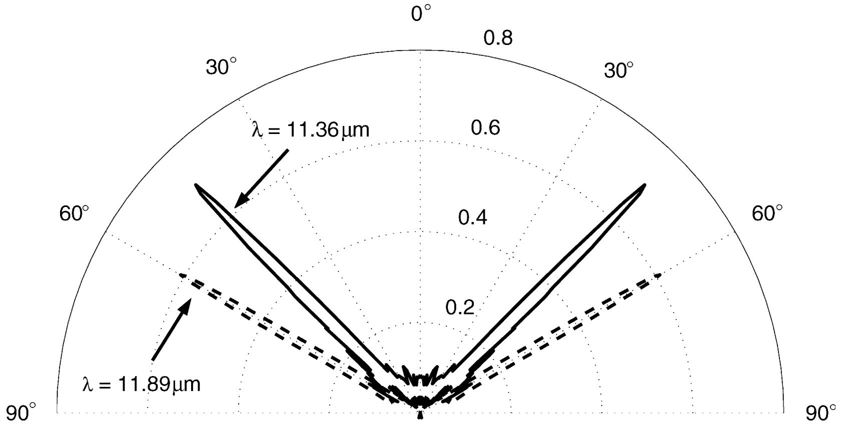

Fig. 13. Experimental angular emission of a SiC grating at two different wavelengths. The angular pattern has the characteristic shape of an antenna. It demonstrates the spatial coherence of the thermal source. Measurements are taken at 800 K. From [56].

aperture is very narrow indicating a large coherence length [56]. Let us emphasize that the coherence is not due to the grating but only to the surface wave. The role of the grating is merely to couple the surface wave into a propagating wave.

Different schemes have been proposed to produce partially coherent thermal sources. They are based on a filtering of the emission pattern in order to reduce the angular width of the emission pattern. The scheme that we have described so far is based on the use of a grating that couples a surface wave to propagating wave. It can be viewed as a device that increases the absorptivity or emissivity to 1 for a narrow set of angles. It can thus be viewed as a filtering process. A different type of filter can be designed using multilayers systems. Several authors [57,58] have reported a narrow angular pattern emission obtained by interferences between several layers. This mechanism leads to angular widths on the order of 10 °.

6.3. Engineering radiative properties of surfaces

For many applications, it is desirable to modify radiative properties of surfaces. An introduction to radiative properties of surfaces can be found in a review paper by Zhang [59]. Roughness has often been used to increase the emissivity. An analysis of the different mechanisms involved can be found in [60]. Further references on scattering by rough surfaces can be found in several reviews and monographs [50,61–65]. Microstructures can be used to design efficient selective absorbers and sources. The decay of reflectivity of a shallow rough surface due to the excitation of surface plasmons is addressed in [66]. Hava and coworkers have examined silicon microstructured surfaces [67–70]. Sai et al. [71] have designed silicon microstructured surfaces for thermophotovoltaics applications. Marquier et al. [72] have studied the effect of surface plasmon on highly doped silicon showing that the peak absorption frequency can be tuned by varying the doping. Kusunoki et al. [73] have reported emissivity measurements on tantalum surfaces with two-dimensional periodic structures. They observed peaks of emission due to the excitation of surface plasmons. Pralle et al. [74] have designed selective infrared emitters using periodic structures on silicon wafers coated with gold.

An interesting application of surface waves to the enhancement of light emission has been demonstrated by Marquier et al. [56,72]. The idea is to emit light in all directions at a given frequency. To this aim, it is

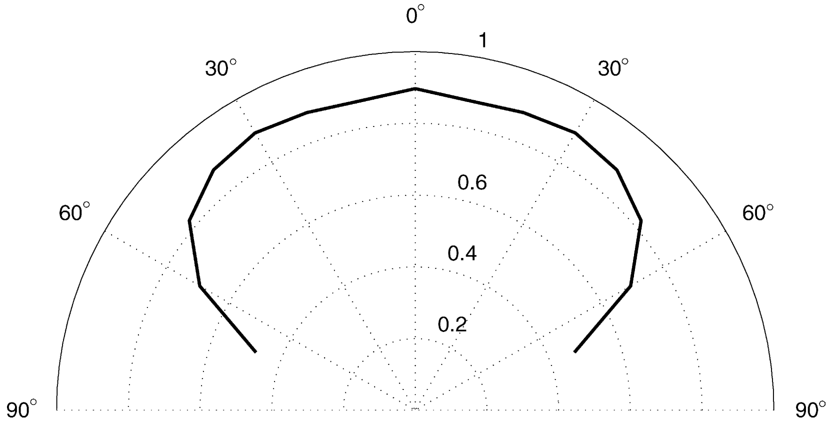

Fig. 14. Angular emissivity measurements of a SiC grating at the surface-phonon polariton frequency. The emissivity is above 0.9 and quasi-isotropic in the plane of incidence. The sample temperature is 800 K. From [56].

necessary to be able to couple light in all directions. When using a grating of period d, the emission angle θ is given by $(\omega/c)\sin(\theta) = K(\omega) + p(2\pi/d)$, where p is an integer. The key idea is to work at the resonance frequency taking advantage that the dispersion relation is flat. At that particular frequency, surface plasmons exist for a very large set of wavevectors K. It follows that one can design a source emitting in all directions. This has been demonstrated for a SiC surface on which a grating was ruled. Fig. 14 represents the angular emission pattern. It is seen that the emissivity is close to its maximum value 1 and almost isotropic. The mechanism of emission can be again viewed as a two-step process. First, each volume element is equivalent to a random dipole that can either emit a photon or excite a surface wave. The latter is a very efficient process so that usually, most of the de-excitation goes into surface waves and eventually into heat. The second step is the introduction of a grating that converts the surface wave into a propagating wave by diffraction. Thus, the excitation of a surface wave which usually tends to decrease the emission of light becomes a factor that enhances the emission of light. A similar mechanism has been proposed recently to use the surface waves in order to enhance the emission of light by quantum wells placed close to a metallic layer [75,76]. The idea is that the high density of states due to the surface plasmon enhances the emission. If the conversion of a surface wave into a propagating wave is efficient, the process enhances the emission.

7. Radiative heat transfer in the near field

We have shown previously that the density of electromagnetic energy increases in the near field due to the contribution of surface waves. We now address the question of heat transfer between bodies separated by distances smaller than the wavelength. In that case, contributions of the surface waves to the radiative heat transfer are expected. This topic has already a long history. Anomalous radiative heat transfer was observed in the 1960s. Cravalho et al. [77] and Boehm and Tien [78] studied that problem and took into account waves that are propagative in the materials and evanescent in the vacuum gap. Yet, this correction does not take into account all the evanescent waves. Waves that are evanescent on both sides of the interface (i.e. surface modes) were not taken into account in these early works. The first correct derivation of the flux between two plane parallel plates was reported by Polder and van Hove [79] in 1971. Their method allowed them to analyse the contributions of different polarizations and to compute separately the contributions of evanescent and propagating waves. Similar works were reported later on by different authors [80–85]. It is found in all these works that the flux diverges as the distance decreases. This point was considered to be unphysical in [86,87] where the increase in the density of states due to surface waves was not included. It is pointed out in [88,89] that when keeping the contribution of all the wavevectors, the flux diverges if the temperature difference is assumed to be kept to a constant value. This amounts to say that the thermal resistance goes to zero which does not violate any physical law. Only a few experiments [90–92] were reported on measurements of heat transfer due to near-field radiation.

Heat transfer between a plane and a small particle was first discussed by Dorofeyev [93] and later by Pendry [82] and Volokitin and Persson [83]. Practical results were derived for a metal using a Drude model and making the additional assumption that $|\varepsilon| \gg 1$. Mulet et al. [94] pointed out the resonant contribution of surface waves to the heat transfer. It was shown that the heat transfer is quasi-monochromatic at the frequency of the optical phonons for a polar crystal given by $\mathrm{Re}[\varepsilon(\omega)] + 1 = 0$. A similar effect is observed between metallic parallel surfaces [85] and for doped semiconductors [72]. For metals, this resonance does not play a significant role because the plasma frequency is in the UV domain so that the Bose–Einstein factor takes low values at usual temperatures. It was later suggested [10,95] that a quasi-monochromatic enhanced heat transfer could be used to increase the efficiency of thermophotovoltaics devices by matching the energy of the emitted photons with the absorption band gap of the photovoltaics cell. That might reduce the loss of excess energy of ultraviolet photons. The heat transfer between two small particles has been studied in [83]. It has been shown that the dipole–dipole interaction yields a large contribution to the heat transfer whereas the contribution of the photon emission and absorption process is negligible. This near-field heat transfer between nanoparticles is analogous to the energy transfer between molecules due to the dipole–dipole coupling known as Forster transfer [96]. It may also be resonant for surface-plasmon resonances. In what follows, we shall derive explicitly the heat transfer between nanoparticles and the emission by a surface plane.

7.1. Radiative power exchange between two spherical nanoparticles

We now calculate the heat transfer between two spherical nanoparticles held at different temperatures and separated in the vacuum. Such a calculation was first reported by Volokitin and Persson [83]. Let us consider two nanoparticles whose dielectric constants are ε_1 and ε_2 and whose temperatures are T_1 and T_2. We first calculate the power dissipated in particle 2 by the electromagnetic field induced by particle 1 using the dipolar approximation:

$$P_{1\to 2}(\omega) = \varepsilon_0 \frac{\omega}{2} \,\mathrm{Im}(\alpha_2)|\mathbf{E}_{\mathrm{inc}}(\mathbf{r}_2, \omega)|^2, \tag{72}$$

where $\mathbf{r}_2$ denotes the position of the particle 2 and α_2 is the polarizability of a sphere of radius a [97]:

$$\alpha_2 = 4\pi a^3 \frac{\varepsilon_2 - 1}{\varepsilon_2 + 2}. \tag{73}$$

The field incident on particle 2 created by the thermal fluctuating dipole of particle 1 located at $\mathbf{r}_1$ at temperature T_1 is given by:

$$\mathbf{E}_{\mathrm{inc}}(\mathbf{r}_2, \omega) = \mu_0\omega^2 \overleftrightarrow{\mathbf{G}}(\mathbf{r}_2, \mathbf{r}_1, \omega) \cdot \mathbf{p}, \tag{74}$$

where $\overset{\leftrightarrow}{\mathbf{G}}(\mathbf{r}_2, \mathbf{r}_1, \omega)$ is the vacuum Green's tensor given in Appendix A. To proceed, we need the correlation function of the dipole given by the fluctuation–dissipation theorem whose symmetrised form is given by (26). We finally obtain the heat exchange between two spherical nanoparticles at temperatures T_1 and T_2:

$$P_{1\leftrightarrow 2} = \frac{3}{4\pi^3} \frac{\mathrm{Im}[\alpha_1(\omega)]\,\mathrm{Im}[\alpha_2(\omega)]}{|\mathbf{r}_2 - \mathbf{r}_1|^6} [\Theta(\omega, T_1) - \Theta(\omega, T_2)]. \tag{75}$$

Let us note the $1/r^6$ spatial dependence of the heat transfer. This dependence is typical of the dipole–dipole interaction. It is actually a van der Waals type interactions that can be interpreted in the following way: fluctuations (thermal or not) distort the charge distribution of a nanoparticle producing a fluctuating dipole. This fluctuating dipole induces in turn an electromagnetic field on the other nanoparticle initiating a second dipole. This dipole interaction causes both an energy transfer and a momentum transfer or force. For molecules this energy transfer is known as Forster transfer and the force is called van der Waals force. We find that nanoparticles follow a similar behaviour with a resonance at the surface polariton resonance. Indeed, in the case of spherical particle with radius a, the polarizability has a resonance when the dielectric constant approaches -2 provided that the imaginary part of the dielectric constant is not too high. The particle resonances appear in the visible part of the spectrum for metals and in the infrared for polar materials. This phenomenon has been confirmed by a recent numerical simulation based on molecular dynamics [150]. It was also shown that at distances smaller than the diameter, the heat transfer deviates from the dipole–dipole interaction and increases before decaying at contact.

7.2. Thermal emitted flux by a planar interface

In this section, we analyse the emission by a plane interface. Let us consider the situation of a planar interface ($z = 0$) separating a dielectric ($z < 0$) at temperature T from a vacuum ($z > 0$). We shall derive the flux emitted from the interface.

7.2.1. Classical theory of radiation

In the classical theory of radiation, the power d^2Q emitted by an elementary opaque surface dS at temperature T, in a solid angle $d\Omega$ around a direction $\mathbf{u}$ making an angle θ with the normal to the surface (Fig. 15), whose monochromatic emissivity is $\varepsilon'(\theta)$ is

$$d^2Q(\omega, \theta) = \varepsilon'_\omega(\theta) I^0_\omega(T)\, d\Omega\, dS, \tag{76}$$

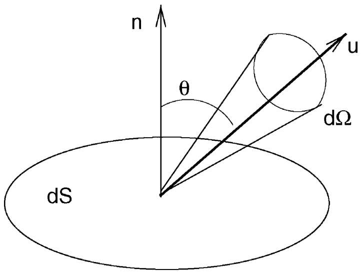

Fig. 15. Solid angle $d\Omega$ around a direction $\mathbf{u}$ making an angle θ with the normal of an elementary surface dS.

where

$$I^0_\omega(T) = \frac{\hbar\omega^3}{4\pi^3 c^2}\,\frac{1}{\mathrm{e}^{\hbar\omega/k_\mathrm{B}T}-1}$$

is the blackbody specific intensity. The power $\mathrm{d}Q$ emitted by the elementary surface is thus

$$\mathrm{d}Q(\omega) = \int \varepsilon'_\omega(\theta) I^0_\omega(T) \cos\theta \,\mathrm{d}\Omega\,\mathrm{d}S = \mathbf{q}\cdot\mathbf{n}\,\mathrm{d}S, \tag{77}$$

where the integral is performed over a half-space. We have introduced the radiative vector defined by

$$\mathbf{q}(\omega) = \int \varepsilon'_\omega(\theta) I^0_\omega(T)\mathbf{u}\,\mathrm{d}\Omega. \tag{78}$$

In the case of a blackbody, the integration over the angles is straightforward. The monochromatic heat flux is thus equal to $\pi L^0_\omega(T)$ and the total heat flux is equal to σT^4, where σ is the Stefan constant

$$\sigma = \frac{\pi^2 k_\mathrm{B}^4}{60 c^2 \hbar^3} = 5.67\times 10^{-8}\,\mathrm{W\,m^{-2}\,K^{-4}}.$$

7.2.2. *Fluctuational electrodynamics method*

We will follow Polder and van Hove [79] to show that the phenomenological form of the emitted flux can be derived in the framework of fluctuational electrodynamics. In the following sections, we use this approach to derive the expressions valid in the near field. Let us consider the situation of a planar interface ($z = 0$) separating a dielectric ($z < 0$) at temperature T from a vacuum ($z > 0$). The flux emitted by the half-space is given by the Poynting vector $\mathbf{S} = \mathbf{E}\times\mathbf{H}$. In the case of monochromatic quantities, the time average Poynting vector reads $\mathbf{S}(\mathbf{r},\omega) = (1/2)\,\mathrm{Re}(\mathbf{E}(\mathbf{r},\omega)\times\mathbf{H}^*(\mathbf{r},\omega))$. This quantity can be derived using the fluctuation–dissipation theorem. Thus, the electric and magnetic Green's tensor are needed. In this geometry, these tensors are given by (A.3) and (A.4). The Poynting vector reduces to its z-component $\langle S_z(\mathbf{r},\omega)\rangle = (1/2)\,\mathrm{Re}[\langle E_x H_y^* - E_y H_x^*\rangle]$. In order to obtain the Poynting vector, one calculates quantities like $\langle E_i(\mathbf{r},\omega) H_j^*(\mathbf{r},\omega)\rangle$. Using (31) and (32)

$$\langle E_i(\mathbf{r},\omega) H_j^*(\mathbf{r},\omega)\rangle = \langle \mathrm{i}\mu_0\omega \int G^{EE}_{ik}(\mathbf{r},\mathbf{r}') G^{HE*}_{jl}(\mathbf{r},\mathbf{r}'') j_k(\mathbf{r}') j_l^*(\mathbf{r}'')\,\mathrm{d}^3\mathbf{r}'\,\mathrm{d}^3\mathbf{r}''\rangle. \tag{79}$$

Using the effective FDT for the currents (28) defined for positive frequencies only, the preceding equation reduces to

$$\langle E_i(\mathbf{r},\omega) H_j^*(\mathbf{r},\omega)\rangle = \frac{\mathrm{i}\Theta(\omega,T)\omega^2}{\pi c^2} \int \varepsilon''(\mathbf{r}') G^{EE}_{ik}(\mathbf{r},\mathbf{r}') G^{HE*}_{jk}(\mathbf{r},\mathbf{r}')\,\mathrm{d}^3\mathbf{r}'. \tag{80}$$

Using the Green functions expressions (A.3) and (A.4) and the identities $\varepsilon'' = 0$ in the upper half-space and that $\varepsilon''_2\omega^2/c^2 = 2\,\mathrm{Re}(\gamma_2)\,\mathrm{Im}(\gamma_2)$, the Poynting vector can be cast in the form

$$\langle S_z(\mathbf{r},\omega)\rangle = \frac{\omega\Theta(\omega,T)}{16\pi^3 c}\,\mathrm{Re}\left\{\int \mathrm{d}^2\mathbf{K}\,\mathrm{e}^{-2\,\mathrm{Im}(\gamma_1)z}\frac{\gamma_1\,\mathrm{Re}(\gamma_2)}{k_0|\gamma_2|^2}\left[|t^\mathrm{s}_{21}|^2 + |t^\mathrm{p}_{21}|^2\frac{|\gamma_2|^2+K^2}{|n_2|^2 k_0^2}\right]\right\}. \tag{81}$$

Let us note that only γ_1 may not be real in the preceding expression. In fact, as the upper half-space is vacuum (medium 1), γ_1 can only be real ($K < \omega/c$) or pure imaginary ($K > \omega/c$). Therefore, the contribution of evanescent waves vanishes in the radiative flux expression. Using the identities (82–85),

$$\mathrm{Re}(\varepsilon^* \gamma) = \mathrm{Re}(\gamma) \frac{|\gamma|^2 + K^2}{k_0^2}, \tag{82}$$

$$\mathrm{Im}(\varepsilon^* \gamma) = \mathrm{Im}(\gamma) \frac{-|\gamma|^2 + K^2}{k_0^2}, \tag{83}$$

$$\mathrm{Re}(\gamma_2)|t^{\mathrm{s}}_{21}|^2 \frac{|\gamma_1|^2}{|\gamma_2|^2} = \mathrm{Re}(\gamma_1)(1 - |r^{\mathrm{s}}_{21}|^2) - 2\,\mathrm{Im}(\gamma_1)\,\mathrm{Im}(r^{\mathrm{s}}_{21}), \tag{84}$$

$$\frac{|n_1|^2}{|n_2|^2} \frac{|\gamma_1|^2}{|\gamma_2|^2} \mathrm{Re}(\varepsilon_2^* \gamma_2)|t^{\mathrm{p}}_{21}|^2 = [\mathrm{Re}(\varepsilon_1^* \gamma_1)(1 - |r^{\mathrm{p}}_{21}|^2) - 2\,\mathrm{Im}(\varepsilon_1^* \gamma_1)\,\mathrm{Im}(r^{\mathrm{p}}_{21})], \tag{85}$$

one finally obtains:

$$\langle S_z(\mathbf{r}, \omega) \rangle = \frac{\hbar \omega^3}{2\pi^2 c^2} \frac{1}{\mathrm{e}^{\hbar\omega/k_{\mathrm{B}}T} - 1} \int_0^{\omega/c} \frac{K\,\mathrm{d}K}{k_0^2} \frac{1 - |r^{\mathrm{s}}_{12}|^2 + 1 - |r^{\mathrm{p}}_{12}|^2}{2}. \tag{86}$$

As already mentioned, only propagating waves ($K < \omega/c$) contribute to this expression. This is not surprising because no waves come from the positive z-direction. Moreover, there is a revolution symmetry around the z-axis. Introducing $\mathrm{d}\Omega$ the elementary solid angle, we have the relation $K\,\mathrm{d}K/k_0^2 = \mathrm{d}\Omega \cos\theta / 2\pi$. The Poynting vector is then given by

$$\langle S_z(\mathbf{r}, \omega) \rangle = \frac{\hbar \omega^3}{2\pi^2 c^2} \frac{1}{\mathrm{e}^{\hbar\omega/k_{\mathrm{B}}T} - 1} \int_{\Omega = 2\pi} \frac{\cos\theta\,\mathrm{d}\Omega}{2\pi} \frac{1 - |r^{\mathrm{s}}_{12}|^2 + 1 - |r^{\mathrm{p}}_{12}|^2}{2}. \tag{87}$$

In the case of a blackbody, i.e. a body for which the reflection factors are null, the usual expression of the radiative flux $\pi I^0_\omega(T)$ is recovered. When the dielectric situated below the interface does not behave as a blackbody, the flux takes the usual form

$$q(\omega) = \langle S_z(\mathbf{r}, \omega) \rangle = \int \mathrm{d}\omega\, \varepsilon'_\omega(\theta) I^0_\omega(T) \cos\theta\,\mathrm{d}\Omega, \tag{88}$$

where we have identified the emissivity $\varepsilon'_\omega(\theta) = (1 - |r^{\mathrm{s}}_{12}|^2 + 1 - |r^{\mathrm{p}}_{12}|^2)/2$. In presence of a single interface, we note that the radiation emitted is not different from the usual one. The near field does not play any role in this situation.

7.3. Heat transfer between two semi-infinite polar materials: interference effects

We now focus on the heat transfer between two semi-infinite half-spaces separated by a vacuum gap and whose temperature T_1 and T_2 are uniform (Fig. 16). The main changes that occur at small distance is the fact that evanescent waves can contribute to the heat transfer through tunneling.

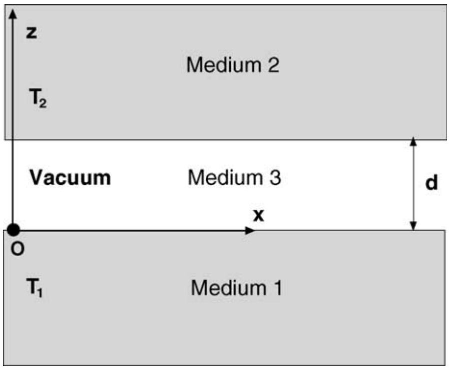

Fig. 16. Two semi-infinite half-spaces separated by a vacuum (distance d).

We summarize in the next sections the results. Detailed derivations can be found in [85] for instance. The radiative transfer is characterised by the radiative flux. In the phenomenological theory, this flux is given by

$$q(\omega) = \int_0^{2\pi} \cos\theta \, \mathrm{d}\Omega \int_0^{\infty} \mathrm{d}\omega \, \frac{\varepsilon'_{1\omega}\varepsilon'_{2\omega}}{1-\rho'_{1\omega}\rho'_{2\omega}} [I^0_\omega(T_1) - I^0_\omega(T_2)], \tag{89}$$

where the $\varepsilon'_{i\omega}$ are the directional monochromatic emissivities and the $\rho'_{i\omega}$ the directional monochromatic reflectivities.

Using a fluctuational electrodynamics model, the flux can be written as the sum of two terms $q(\omega) = q^{\mathrm{prop}}(\omega) + q^{\mathrm{evan}}(\omega)$.

The first term $q^{\mathrm{prop}}(\omega)$ is the propagating waves contribution:

$$q^{\mathrm{prop}}(\omega) = \sum_{q=\mathrm{s,p}} \int \mathrm{d}\omega \, \mathrm{d}\Omega \cos\theta \left[\frac{(1-|r^q_{31}|^2)(1-|r^q_{31}|^2)}{|1-r^q_{31} r^q_{32} \, \mathrm{e}^{2\mathrm{i}\gamma_3 d}|^2} \right] [I^0_\omega(T_1) - I^0_\omega(T_2)]. \tag{90}$$

Let us note that $1-|r^{\mathrm{s,p}}_{31}|^2$ and $1-|r^{\mathrm{s,p}}_{32}|^2$ are the transmission energy coefficients between media 1 and 3 and 2 and 3 for the s- or p-polarization. These coefficients can be identified as an emissivity in the same way that it has been defined for a single interface. Let us remark that this expression for the propagating waves contribution to the radiative flux between two semi-infinite media is very close to the usual one. Only the denominators are different because interferences are not taken into account in the phenomenological model. Nevertheless, if one considers a frequency interval small in comparison with the frequency but larger than c/d, the variation of $\mathrm{e}^{\mathrm{i}\gamma_3 d}$ with ω is much faster than the Fresnel reflection coefficient variations. The integration over this interval yields an average value of $|1-r^i_{31} r^i_{32} \, \mathrm{e}^{2\mathrm{i}\gamma_3 d}|^2$ which is exactly $1-|r^i_{31}|^2|r^i_{32}|^2$. Matching the reflectivity with the Fresnel reflection energy coefficient, one can then identify this expression for the radiative flux with the classical one.

7.3.1. Tunneling of evanescent waves

The second term $q^{\mathrm{evan}}(\omega)$ is the contribution of the evanescent waves. It reads:

$$q^{\mathrm{evan}}(\omega) = \sum_{q=\mathrm{s,p}} \int \mathrm{d}\omega \int_{\omega/c}^{\infty} \frac{2K \, \mathrm{d}K}{k_0^2} \, \mathrm{e}^{-2\,\mathrm{Im}(\gamma_3) d} \left[\frac{\mathrm{Im}(r^q_{31}) \, \mathrm{Im}(r^q_{32})}{|1-r^q_{31} r^q_{32} \, \mathrm{e}^{2\mathrm{i}\gamma_3 d}|^2} \right] [I^0_\omega(T_1) - I^0_\omega(T_2)]. \tag{91}$$

Contrary to the single interface case, this contribution does not vanish because of the existence of both upward and downward evanescent waves in the space between the two media [98]. When the distance reduces, this term is more and more important due to the presence of the exponential $e^{-2\,\mathrm{Im}(\gamma_3)d}$. When the materials involved are supporting surface waves, the imaginary part of the reflection coefficient in p-polarization becomes important around the resonant frequency, when the dielectric constant approaches -1. If the two media are sufficiently close to allow the interaction between the exponentially decaying surface waves bound to each interface, a transfer occurs due to the tunneling of evanescent waves.

Let us define a radiative heat transfer coefficient as the limit of the ratio of the radiative flux on the temperature difference between the two media when this temperature tends to zero:

$$h^{\mathrm{R}}(\omega) = \lim_{(T_1-T_2)\to 0} \frac{q(\omega)}{T_1 - T_2}. \tag{92}$$

In Fig. 17, $h^{\mathrm{R}}(\omega)$ is represented versus the distance between two semi-infinite media of glass or SiC. For a distance larger than the thermal radiation wavelength given by the Wien's law, i.e. for $d > 10\,\mu\mathrm{m}$, the transfer does not depend on the distance. We are then in the classical regime where the transfer occurs through the radiation of propagating waves. At shorter distances, the transfer increases as $1/d^2$. For a distance of 10 nm, the radiative heat transfer coefficient has increased by four orders of magnitude compared to its far-field value. If we now focus on the spectral dependence of the heat transfer coefficient at a 10 nm distance (Fig. 18), we note that the heat transfer is important for the frequencies corresponding to resonant surface waves. The heat transfer is therefore practically monochromatic in the near field. We can also expand asymptotically the radiative heat transfer coefficient for short distances:

$$h^{\mathrm{R}}(\omega) \sim \frac{1}{d^2} \frac{\mathrm{Im}(\varepsilon_1)\,\mathrm{Im}(\varepsilon_2)}{|1+\varepsilon_1|^2 |1+\varepsilon_2|^2} k_{\mathrm{B}} \left(\frac{\hbar\omega}{k_{\mathrm{B}}T}\right)^2 \frac{e^{\hbar\omega/k_{\mathrm{B}}T}}{(e^{\hbar\omega/k_{\mathrm{B}}T} - 1)^2}. \tag{93}$$

This expression yields the $1/d^2$ dependence of the transfer coefficient and its strong frequency dependence. Indeed, when the dielectric constant approaches -1, the radiative heat transfer coefficient exhibits a peak as well as the Fresnel reflection factor. This is the signature of the presence of a surface wave. The validity of the $1/d^2$ dependence has been questioned in [86] on the basis that an infinite flux is not physical. As a matter of fact, the flux is infinite if one assumes that the temperature difference is kept constant. This problem is analogous to the problem of an electron flux or intensity that goes to infinity if

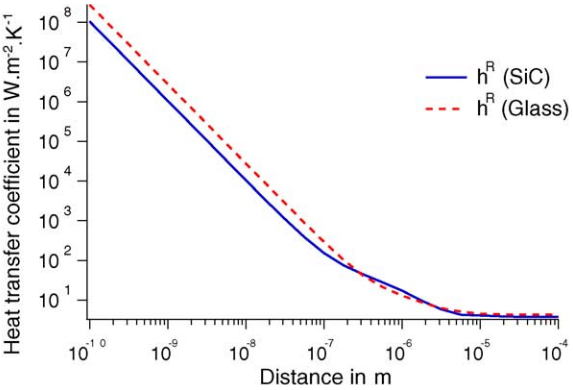

Fig. 17. Radiative heat transfer coefficient vs. distance for semi-infinite media of temperature $T = 300$ K. From [85].

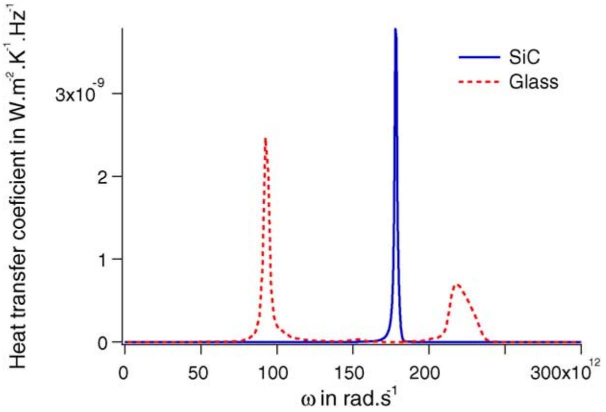

Fig. 18. Monochromatic heat transfer coefficient for a distance $d = 10$ nm and a temperature $T = 300$ K. From [85].

the resistance goes to zero at fixed voltage. This raises another question: in the case of heat transfer, the resistance across a vacuum gap on the order of 10 nm usually remains much larger than the bulk conduction resistance of solids over distances on the order of 100 nm. It is thus safe to assume that the temperature is uniform in the bulk over a skin depth so that the calculation is valid.

7.4. Calculation of the heat transfer between a dielectric sphere and a half-space

7.4.1. Introduction

We calculate in this part the radiative power exchanged between a small spherical particle and a semi-infinite medium. To this aim, we first calculate the power absorbed by the dielectric sphere placed above a heated half-space. We then calculate the power dissipated by the half-space situated below a heated sphere from reciprocity [94]. The geometry of the problem is presented in Fig. 19: the upper medium, $z > 0$, is vacuum. A particle (P) of radius a and dielectric constant $\varepsilon_P(\omega) = \varepsilon_P(\omega)' + \mathrm{i}\varepsilon_P(\omega)''$ is held at temperature T_P. The lower medium is filled by a homogeneous, isotropic material (bulk) of dielectric constant $\varepsilon_\mathrm{B}(\omega) = \varepsilon'_\mathrm{B}(\omega) + \mathrm{i}\varepsilon''_\mathrm{B}(\omega)$ and held at temperature T_B. The center of the particle is at a distance d above the interface.

7.4.2. Power absorbed by the bulk: near-field limit

A calculation following the procedures already introduced (see, e.g. [83,94]), yields the power absorbed by the particle when illuminated by the field radiated by a half-space:

$$P_\mathrm{abs}^{B\to P}(\omega) = \frac{2}{\pi}\frac{\omega^4}{c^4}\,\mathrm{Im}[\varepsilon_\mathrm{B}(\omega)]\,\mathrm{Im}[\alpha(\omega)]\Theta(\omega, T_\mathrm{B})\sum_{n,m}\int_\mathrm{B}|G_{nm}(\mathbf{r}_P, \mathbf{r}', \omega)|^2\,\mathrm{d}^3\mathbf{r}'. \tag{94}$$

If we consider the fluctuating currents inside the particle that radiates into the bulk and dissipates, one can calculate by the same formalism the power locally dissipated per unit volume at a point $\mathbf{r}$ inside the bulk. It reads

$$P_\mathrm{abs}^{P\to B}(\mathbf{r}, \omega) = \frac{2}{\pi}\frac{\omega^4}{c^4}\,\mathrm{Im}[\varepsilon_\mathrm{B}(\omega)]\,\mathrm{Im}[\alpha(\omega)]\Theta(\omega, T_P)\sum_{n,m}|G_{nm}(\mathbf{r}, \mathbf{r}_P, \omega)|^2. \tag{95}$$

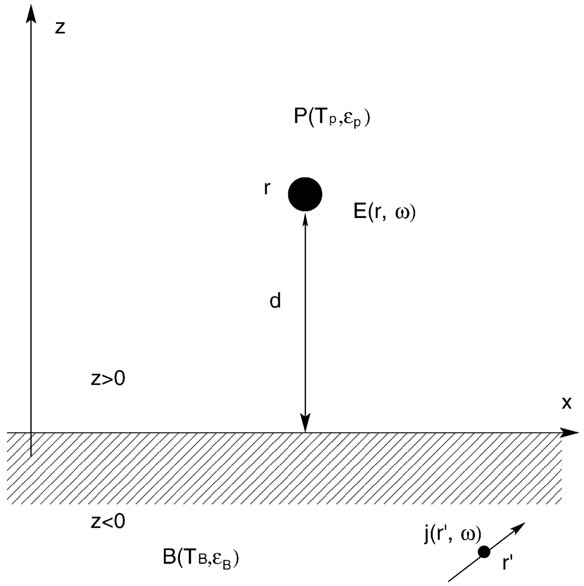

Fig. 19. Geometry of the system.

From the expression of the one-interface Green's tensor, it is possible to expand asymptotically the expression of the power absorbed by the particle. This quantity behaves as $1/d^3$ and reads

$$P_{\rm abs}^{B\to P}(d,\omega)\sim\frac{1}{4\pi^2d^3}4\pi a^3\frac{3\varepsilon_P''(\omega)}{|\varepsilon_P(\omega)+2|^2}\frac{\varepsilon_{\rm B}''(\omega)}{|\varepsilon_{\rm B}(\omega)+1|^2}\Theta(\omega,T_{\rm B}). \tag{96}$$

From this expression, we see that there is an enhancement of the power absorbed if the denominators vanish or approach zero. We have seen that it is the case if the material support resonant surface waves so that the dielectric constant of the material can take negative values. We study in the next section the case of SiC.

7.4.3. Example of SiC

As it has been said in the first part of the article, SiC is a polar material that can be described by an oscillator model (22). In Fig. 20, we plot $P_{\rm abs}^{B\to P}(\omega)$ for a spherical particle held at temperature $T_P = 300$ K of radius $a = 5$ nm at different distances above the surface. We note that the figure displays two remarkable peaks at frequency $\omega_1 \approx 1.756\times10^{14}$ rad s^{-1} and $\omega_2 \approx 1.787\times10^{14}$ rad s^{-1}. These two peaks correspond to the resonances of the system. The first one corresponds to a frequency where $\varepsilon_P(\omega)$ approaches -2: a volume phonon polariton is excited in the particle inducing a large electric dipole and a large dissipation. The second one is related to the resonant surface wave corresponding to a large increase of the electromagnetic LDOS. Thus, the radiative heat transfer in the near field can be considered as monochromatic. The electromagnetic waves associated with the resonant surface waves are evanescent. The energy transfer, which finds its origin in the presence of these waves, is important because the particle lies in the region (up to many micrometers) where the evanescent field is large, so

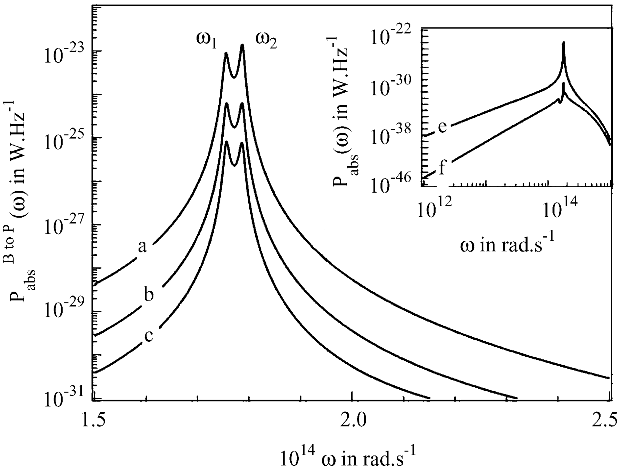

Fig. 20. Mean power radiated by the bulk (at $T_B = 300$ K) and absorbed by the particle (of radius $a = 5$ nm) vs. frequency: (a) $d = 20$ nm; (b) $d = 50$ nm; (c) $d = 100$ nm. The insert (log–log-scale) shows the spectrum of the absorbed power between 10^{12} and 10^{15} rad s^{-1}; (e) $d = 20$ nm; (f) $d = 1$ mm. From [94].

that there is an efficient coupling between the field and the particle. In the far field, evanescent waves are negligible and usual results are retrieved. Fig. 21 shows the integrated power absorbed by the same particle versus the distance d. The near-field radiative heat transfer increases as $1/d^3$ (as it was suggested by the asymptotic behaviour) and is larger at small distances by several orders of magnitude than the far field one. This enhancement comes from the contribution of evanescent waves. Reciprocity requires that the same enhanced radiative heat transfer appears when the particle illuminates the surface. This situation may help to understand the radiative heat exchange between a nano-tip (like those used in near-field microscopy) and a sample. To answer this question, we calculated from (95) the total power (integrated over frequencies) dissipated per unit volume for different points in the sample. Fig. 22 displays a map, in log-scale, of the dissipation rate in the case of a 10 nm diameter sphere of SiC at $T_P = 300$ K situated

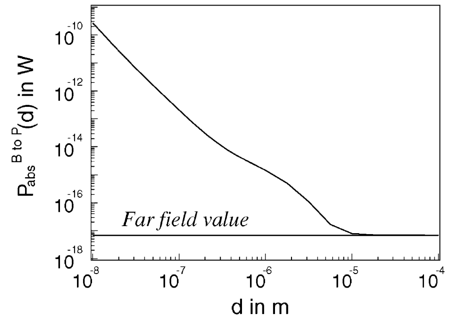

Fig. 21. Total power radiated by the bulk (at $T_B = 300$ K) and absorbed by the particle (of radius $a = 5$ nm) vs. distance. From [94].

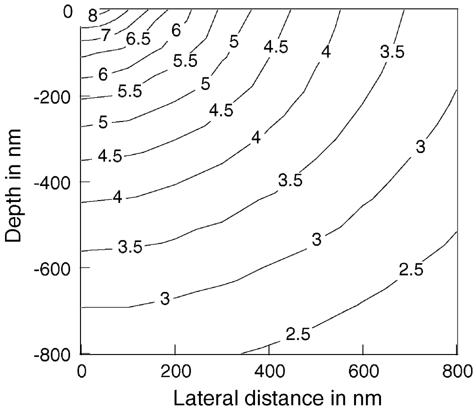

Fig. 22. Deposited power per unit volume inside the bulk. The particle has a radius $a = 5$ nm and is held at temperature $T_P = 300$ K. From [94].

100 nm above a sample of SiC. It is seen that the energy is dissipated on a scale comparable to the tip–sample distance. The dissipation per unit volume decreases very fast ($1/r^6$) with the distance r between the source and the point of the sample where the dissipation is considered (the isocontour labeled with a '6' corresponds to the points where the dissipation per unit volume is 10^6 W m^{-3}. The amount of energy locally deposited is as large as 100 MW m^{-3}. We note that the dependence of the heat deposited follows the same regime as in the two particles exchange in the vacuum. This is not surprising. Here also the phenomenon is due to an interaction between induced dipoles. This phenomenon is also at the origin of the force between macroscopic bodies at nanometric distances which is the subject of the next section.

8. Role of surface electromagnetic waves on the Casimir force

8.1. Introduction

After having considered the energy exchange due to the interaction in the near field between surface waves, it is natural to wonder what happens in terms of momentum exchange in the near field when two semi-infinite bodies are approached face to face. This situation is actually well known since 1948, when Casimir and Polder [99,100] first showed the existence of an attracting force between two parallel perfect conductors. A large body of literature has been devoted to this effect and several reviews are available [101–106]. The seminal paper of Lifshitz [107] occupies a special place because it was the first calculation of this force by means of the FDT for the currents. Agarwal [108] reported a similar calculation using the FDT for the fields. There has been an increasing interest in the Casimir force since it has been shown that this force could be measured with high accuracy [109–114] and that it should be considered in the design of micro-electromechanical systems (MEMS) [115,116]. Various corrections to this force have been studied such as finite conductivity [117] or temperature corrections [118,119]. In what follows, we discuss the role of surface waves in the Casimir force. We will show that they play a key role in the short-distance regime.

To get a simple picture of Casimir force, we recall that a system of two plane parallel reflecting planes is a waveguide. The number of electromagnetic modes in the waveguide is discrete and depends on the thickness of the waveguide. From quantum electrodynamics, it is known that each mode with frequency ω has a minimum energy $\hbar\omega/2$ referred to as vacuum fluctuations. If the thickness decreases, the number of modes decreases so that the electromagnetic energy decreases. Hence, the existence of vacuum fluctuations entails that there is an attractive force between the two plates. This phenomenon is clearly a macroscopic manifestation of the electromagnetic energy of the vacuum which is a pure quantum effect. Yet, its computation amounts to count the number of electromagnetic modes available and this is a pure classical problem. As has been discussed in the previous sections, the local density of electromagnetic states is completely dominated by the existence of surface modes. It follows that the role of surface waves is essential in the physics of the Casimir force in the short-distance regime.

In classical electrodynamics, the momentum transfer is given by the Maxwell stress tensor T_{ij}[34]. The fields can be derived using the FDT [120]. Using the system Green tensors for the electric and the magnetic field, it is possible to obtain this quantity. In the case of two semi-infinite bodies separated along the z-axis by a vacuum gap, the momentum flux reduces to the zz-component T_{zz} of the Maxwell stress tensor given by

$$T_{zz} = \frac{\varepsilon_0}{2}[|E_x|^2 + |E_y|^2 - |E_z|^2] + \frac{\mu_0}{2}[|H_x|^2 + |H_y|^2 - |H_z|^2]. \tag{97}$$

One has to subtract the infinite contribution to the force in the absence of bodies [121]. The force can be attractive or repulsive depending on the materials properties [122,123]. One obtains an attractive force in the case of dielectrics [124] and a force that might be repulsive in some configurations implying magnetic materials [125,126].

8.2. Spectrum of the force

Lifshitz [107] obtained a force per unit area given by

$$F = \int_0^\infty \frac{d\omega}{2\pi} \int_0^\infty \frac{du}{2\pi} F(u,\omega), \tag{98}$$

$$F(u,\omega) = -\frac{2\hbar\omega^3}{c^3}\, \mathrm{Im}\, uv \sum_{\mu=\mathrm{s,p}} \frac{r_\mu^2(u,\omega)\, e^{-2(\omega/c)vd}}{1 - r_\mu^2(u,\omega)\, e^{-2(\omega/c)vd}}, \tag{99}$$

where $v = (u^2-1)^{1/2}$ ($\mathrm{Im}\, v \le 0$), and r_μ is the Fresnel reflection coefficient for a plane wave with polarization μ and wavevector $K = (\omega/c)u$ parallel to the vacuum–medium interface. We use the convention that an attractive force corresponds to $F < 0$. The force appears as the contribution of elementary plane waves whose angular frequency is ω and whose wavevector parallel to the interface is $u\omega/c$. In his paper, Lifshitz used a deformation contour in the complex plane of frequencies to obtain a final formula where the summation over the wavevector is replaced by an integral over v and the summation over the frequencies is replaced by an integral over the imaginary frequencies $\omega = \mathrm{i}\xi$. This approach has the advantage to replace the oscillating exponentials with smooth real functions that make the integral easy to integrate numerically. Nevertheless, by doing such a deformation contour, one is losing the spectral information contained in the expression (98). What we are going to show in the following is that the main contribution to the force in the near field is coming from the coupled polaritons of both interfaces. Therefore, we will see that there is a complete analogy in the interpretation of the

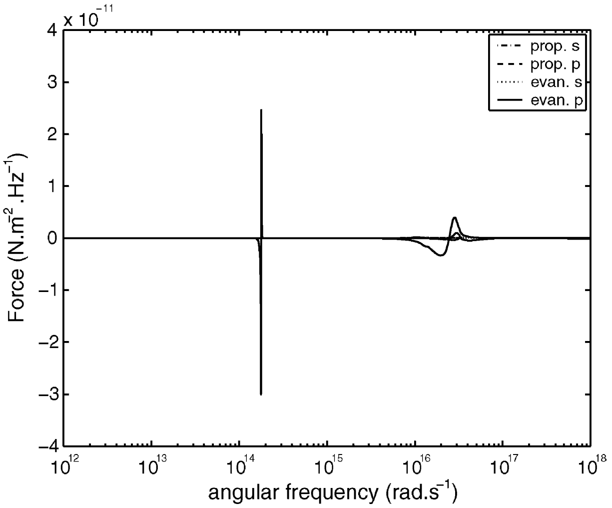

Fig. 23. Contributions of s- and p-polarized, propagating and evanescent modes to the force spectrum (as given by (98) after integration over the wavevector u). Distance $d = 10$ nm. Material: SiC, dielectric function with two resonances. The angular frequencies of the corresponding surface resonances are $1.78 \times 10^{14}\,\mathrm{s}^{-1}$ in the IR and $2.45 \times 10^{16}\,\mathrm{s}^{-1}$ in the UV [46]. From [120].

momentum transfer with the interpretation of the energy transfer in terms of interaction of surface-polaritons.

Let us study the force spectrum in the case of two real materials. In the case of SiC (Fig. 23), the force is dominated by the UV and IR contributions. Actually, due to the presence of the ω^3 in the expression (98), the UV contribution is much more important than the IR one.

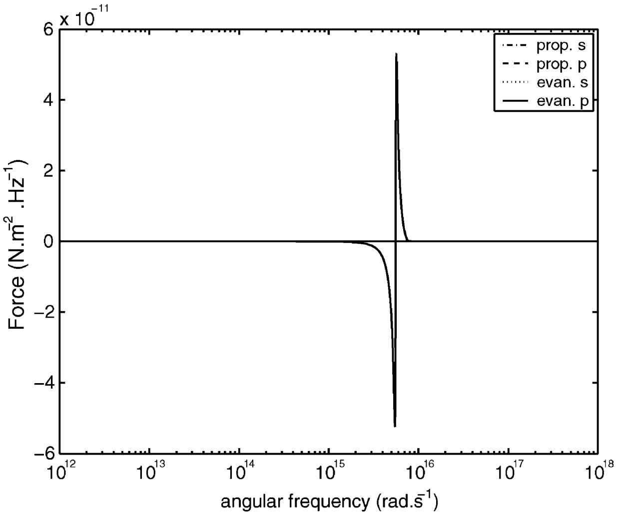

Fig. 24. Contributions of s- and p-polarized, propagating and evanescent modes to the force spectrum ((98) integrated on the wavevector u). Distance $d = 10$ nm. Material: aluminum, described by tabulated optical data [46]. From [120].

Fig. 24 represents the force spectrum between two aluminum half-spaces. It is seen that all the contributions are coming from frequencies very close to plasmon-polariton resonances. From expression (98), it is easy to separate the polarization contributions, the propagative contribution $(0 \leq u \leq 1)$ and the evanescent one $(u > 1)$. We see in Figs. 23 and 24 that the peaks exist only in p-polarization and for evanescent waves. This fact is an additional argument in favor of an interpretation of the force being caused by the interaction between polaritons which are not propagating and only appear in p-polarization. An interpretation of the phenomenon is the following. At frequencies close to the system resonances, i.e. close to the surface waves frequencies, the density of electromagnetic states increases. Thus, the amount of momentum carried in the gap increases too.[1] This interpretation is only valid at distances of the order of the wavelength of the surface wave. At larger distances, the force is dominated by the propagative contribution as first pointed out by Casimir. We note also that the contribution to the force at such small distances has a different sign whether the frequency is lower or higher than the resonant frequency. However, the total Casimir force between dielectrics is always positive and smaller than the one for perfect conductors.

8.3. Binding and antibinding resonances

The role of SPP can be further analysed by studying the variation of the integrand of the force $F(u, \omega)$ in the plane (u, ω). Close to the resonant surface-wave frequency ω_{SW}, the contributions to the force come from evanescent waves. We therefore limit our study to the case $u > 1$ and close to $\omega \sim \omega_{\mathrm{SW}}$. In Fig. 25a, we plot the integrand $F(u, \omega)$ for two aluminum half-spaces separated by a distance $d = 10$ nm. Two branches mainly contribute, the higher frequency branch yielding a repulsive contribution whereas the lower one gives an attractive contribution. These two branches actually follow the two-interface system dispersion relation given by

$$1 - r_{\mathrm{p}}^2 \, \mathrm{e}^{-2(\omega/c)vd} = 0. \tag{100}$$

The influence of the dispersion relation on the force is illustrated in Fig. 25b. In this figure, the quantity $1/|1 - r_{\mathrm{p}}^2 \, \mathrm{e}^{-2(\omega/c)vd}|^2$ is plotted in the (u, ω) plane. Upon comparison between Fig. 25a and b, it is clearly seen that the main contribution to the force can be attributed to the SPP. In addition, we observe in Fig. 25b a dark line which corresponds to minima of $1/|1 - r_{\mathrm{p}}^2 \, \mathrm{e}^{-2(\omega/c)vd}|^2$. The minima can be attributed to very large values of the reflection factor of a plane interface r_{p}. Thus, the dark line is the dispersion relation of a single SPP on a flat interface.

In Fig. 26, the integrand is plotted for two aluminum half-spaces separated by a distance $d = 100$ nm: the two branches tend to merge with the flat interface dispersion relation. One can thus propose the following interpretation: when the surfaces approach each other, the overlapping of the two SPP leads to two coupled modes and to a splitting of the polaritons frequencies [127,128]. The frequency splitting can be found from the solutions of (100) which are implicitly defined by

$$r_{\mathrm{p}}(u, \omega) = \pm \, \mathrm{e}^{\omega vd/c}.$$

The signs correspond to either symmetric or antisymmetric mode functions (for the magnetic field), as sketched in the inset of Fig. 26. The symmetric (antisymmetric) branch corresponds to a lower (higher)

---

[1] As for energy transfer case, momentum is carried by evanescent waves if and only if an upward and a downward wave are present.

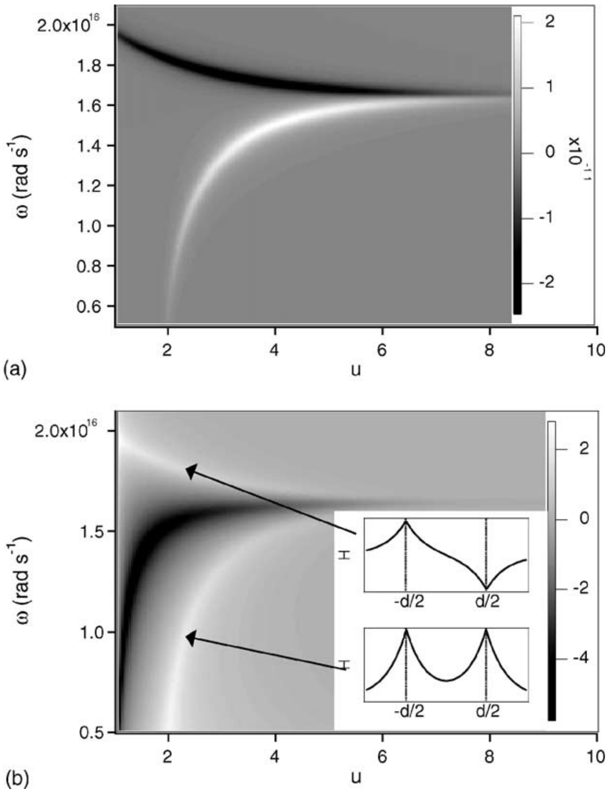

Fig. 25. (a) Wavevector resolved spectrum of the Casimir force (98) in the (u, ω) plane between two aluminum half-spaces separated by a distance of 10 nm. The frequency of the flat asymptote corresponds to the peaks of the force spectrum (Fig. 24): light (dark) areas: attractive (repulsive) force; (b) resonant denominator $|1/1 - r_{\mathrm{p}}^2 \, \mathrm{e}^{-2(\omega/c)vd}|^2$ in the (u, ω) plane, the gray scale giving the logarithm to base 10. The dispersion relation of the coupled surface resonance corresponds to light areas; dark area: dispersion for a single interface (20). The dielectric function is extracted from tabulated data [46]. The inset sketches the magnetic field of the coupled surface resonances (antisymmetric and symmetric combinations). From [120].

resonance frequency, respectively, similar to molecular orbitals and tunneling doublets. These branches contribute with opposite signs to the Casimir force, due to the following identity:

$$\frac{2r_{\mathrm{p}}^2(\omega, u)\, \mathrm{e}^{-2\omega vd/c}}{1 - r_{\mathrm{p}}^2(\omega, u)\, \mathrm{e}^{-2\omega vd/c}} = \frac{r_{\mathrm{p}}(\omega, u)\, \mathrm{e}^{-\omega vd/c}}{1 - r_{\mathrm{p}}(\omega, u)\, \mathrm{e}^{-\omega vd/c}} - \frac{r_{\mathrm{p}}(\omega, u)\, \mathrm{e}^{-\omega vd/c}}{1 + r_{\mathrm{p}}(\omega, u)\, \mathrm{e}^{-\omega vd/c}}, \tag{101}$$

where the first (second) term is peaked at the symmetric (antisymmetric) cavity mode. The symmetry of the resonance mode function hence determines the attractive or repulsive character of its contribution to the Casimir force.

8.4. Analytical formulation of the short-distance limit

Using a simple Lorentz–Drude model for the dielectric function,

$$\varepsilon(\omega) = 1 + \frac{2(\Omega^2 - \omega_0^2)}{\Omega^2 - \mathrm{i}\gamma\omega - \omega^2}, \tag{102}$$

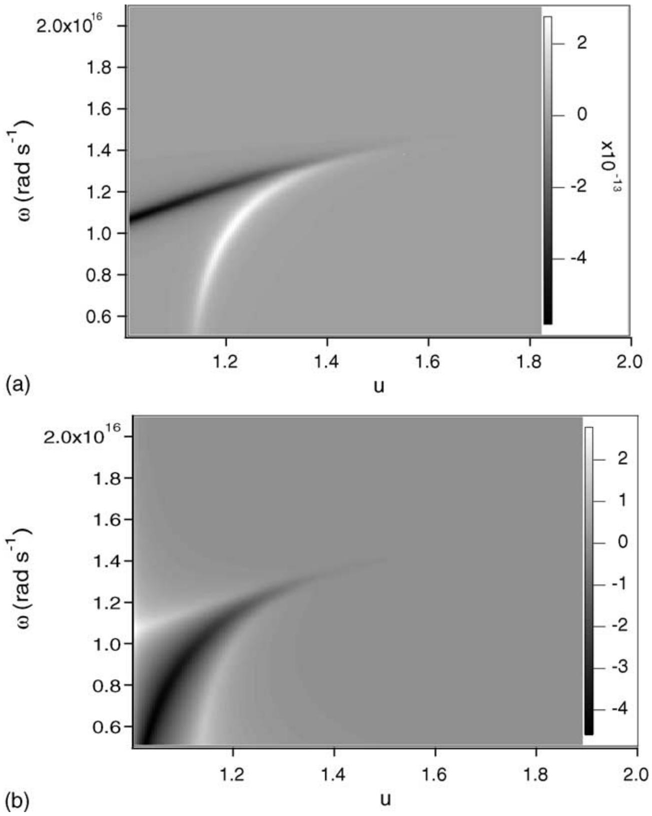

Fig. 26. Same as Fig. 25 but for $d = 100$ nm. From [120].

we can derive a simple analytic form of the force in the near-field limit that accounts for the modification of the local density of states due to the surface waves and that takes into account absorption effects. This model describes either dielectric or metals depending on the value of ω_0. The corresponding plasma frequency is $\sqrt{2(\Omega^2 - \omega_0^2)}$. With this convention, the large u asymptote of the SPP dispersion (20) occurs at $\omega \approx \Omega$. As the distance d reduces to a quantity small compared to the wavelength, the evanescent contribution to the force comes from higher and higher parallel wavevector. When $u \gg 1$, the reflection coefficient in p-polarization can be approximated by

$$u \gg 1: \quad r_{\mathrm{p}}(\omega, u) \approx \frac{\Omega^2 - \omega_0^2}{\Omega^2 - \mathrm{i}\gamma\omega - \omega^2}. \tag{103}$$

It is seen that the reflection factor has a complex pole. From (100), we thus get the following dispersion relation for the (anti)symmetric surface-plasmon resonances, neglecting for the moment the damping coefficient γ:

$$\omega_\pm^2 \approx \Omega^2 \mp \mathrm{e}^{-\omega_\pm ud/c}(\Omega^2 - \omega_0^2), \tag{104}$$

where we have used $v \approx u$ for $u \gg 1$. For large u, we solve by iteration and find that $\omega_\pm \lessgtr \Omega$. As announced above, the symmetric mode thus occurs at a lower resonance frequency.

To derive an analytical estimate for the Casimir force, we retain in (98) only the contribution of p-polarized, evanescent waves. The final result [120] contains two contributions:

$$F = \frac{\hbar \Omega}{4\pi d^3}\left(\alpha(z) - \frac{\gamma \,\mathrm{Li}_3(z^2)}{4\pi \Omega}\right), \tag{105}$$

where

$$\alpha(z) = \frac{1}{4}\sum_{n=1}^{\infty} z^{2n} \frac{(4n-3)!!}{n^3(4n-2)!!} \tag{106}$$

and

$$\mathrm{Li}_3(z^2) = \sum_{n=1}^{\infty} \frac{z^{2n}}{n^3}. \tag{107}$$

When $z \to 1$, we get the following asymptotics:

$$\alpha(z) \approx 0.1388 - 0.32(1-z) + 0.4(1-z)^2, \tag{108}$$

$$\mathrm{Li}_3(z^2) \approx \zeta(3) - \frac{\pi^2}{3}(1-z) + \left[3 - \frac{\pi^2}{6} - 2\ln\left[2(1-z)\right]\right](1-z)^2 \tag{109}$$

with $\zeta(3) \approx 1.202$. For a metal, the parameter z takes the value 1 so that we have $\alpha(1) \approx 0.1388$ and $\mathrm{Li}_3 \approx 1.202$. We compare (105) in Fig. 27 to the full integral (98) for the case of aluminum: the asymptotic estimation turns out to be quite accurate for distances $d \leq 0.1\lambda_{\mathrm{SPP}}$, where λ_{SPP} is the wavelength of the SPP with the largest frequency. In the case of aluminum, the first order correction in γ/Ω is 2.5% of the zeroth order value of the force. The plot also shows that for numerical integration, the tabulated data [46] and the Lorentz–Drude model (102) with parameters fitted around the surface resonance give very close results over a large range of distances. This is another indication that the short range Casimir force is dominated by a narrow frequency range.

8.5. *Friction forces*

The Casimir force that has been analysed in the previous section is not the only one that occurs when two bodies are approached one to each other. A particle moving in a vacuum experiences a friction force proportional to its velocity as first discussed by Einstein [102,129–132]. Again, the friction force arises from the fluctuations of the electromagnetic field. A major difference between friction forces and Casimir force is that the leading contributions come from the low frequencies for friction. By contrast, high frequencies contribution gives the largest contribution to vacuum energy and therefore gives the leading contribution to the Casimir force. The friction force has been studied recently for a particle in close proximity to an interface. This force has been used to develop a near field imagery technique called shear-force microscopy [133–135]. The exact origin of these forces is still unclear. Recently, experiments on shear force [136,137] have been conducted in ultra-high vacuum in order to eliminate forces due to a water monolayer for instance. Different models have been developed to explain the origin of the friction force between two parallel surfaces [40,138–141] in the framework of fluctuational electrodynamic fields. The case of a particle moving parallel to a surface has been considered in [142–144]. The friction force for particles moving perpendicular to the surface has also been considered experimentally [145] and

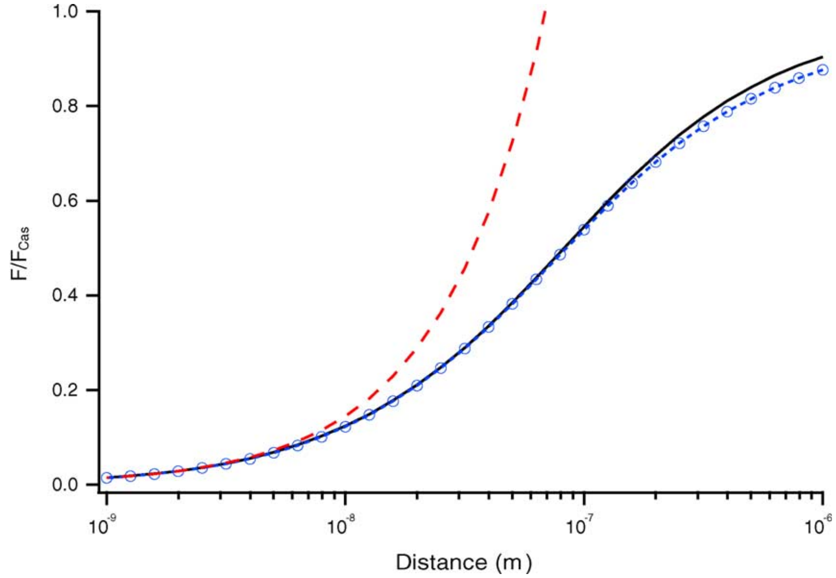

Fig. 27. Comparison of different expressions for the Casimir force between aluminum surfaces. We plot the ratio $F(d)/F_{\mathrm{Cas}}(d)$, where $F_{\mathrm{Cas}}(d) = \hbar c\pi^2/(240d^4)$ is the Casimir force for perfect mirrors. Solid line: numerical integration of (98), using tabulated data [46]. Short-dashed line with circles: same, with a model dielectric function of Drude form (102) with $\omega_0 = 0$, $\Omega = 1.66 \times 10^{16}$ s^{-1}, and $\gamma/\Omega = 0.036$. These parameters have been derived by fitting the value of the reflectivity. Long-dashed line: short-distance asymptotics (105) with the same values for ω_0, Ω and γ. From [120].

theoretically [146]. Volokitin and Persson [147,148] have shown that the friction force is much larger for the perpendicular case. The problem is still open because the discrepancy between theory and experiments is very large. Recently, it has been proposed [149] that the friction observed in the experiment by Stipe et al. could be due to the dielectric located below the gold film. Volokitin and Persson [147] have suggested that adsorbates might produce a very large enhancement of the friction forces. Clearly, more experiments are needed to clarify this issue.

9. Concluding remarks

Many years after the discovery of surface polaritons, new discoveries and effects are still being reported. A major reason is the development of near-field techniques that allows us to probe the properties of surfaces with a nanometric resolution and motivates further work. Although thermal excitation of surface waves had been studied in the past, their major role in many phenomena has been realized only recently. It has been shown that heat transfer is dramatically enhanced in the near field due to the resonant contribution of surface waves. It has been shown that the electromagnetic field emitted by a thermal source may be partially temporally coherent and partially spatially coherent in the near field. It has also been shown that the far-field emission properties of surfaces can be engineered by exciting and coupling efficiently surface waves. Partially spatially coherent thermal sources have been realized. Applications to emitting light devices are under study. The role of surface excitations in the Casimir force has been clarified and the agreement between experiments and models is now satisfactory. The situation for friction forces is far less clear. There are still large discrepancies between published data and models.

Acknowledgements

The authors are very grateful to Carsten Henkel and Lukas Novotny for many fruitful discussions.

Appendix A. Green's tensor

A.1. Green's tensor in a vacuum

The Green's tensor in a vacuum is defined by the relation:

$$\mathbf{E}(\mathbf{r}) = \mu_0\omega^2 \overleftrightarrow{\mathbf{G}}(\mathbf{r},\mathbf{r}')\mathbf{p}. \tag{A.1}$$

Its explicit form expression is given by:

$$\overleftrightarrow{\mathbf{G}}(\mathbf{r},\mathbf{r}',\omega) = \frac{k\,\mathrm{e}^{\mathrm{i}kR}}{4\pi}\left[\left(\frac{1}{kR}+\frac{\mathrm{i}}{(kR)^2}-\frac{1}{(kR)^3}\right)\overleftrightarrow{\mathbf{I}} + (\mathbf{u}_r\mathbf{u}_r)\left(\frac{3}{(kR)^3}-\frac{3\mathrm{i}}{(kR)^2}-\frac{1}{kR}\right)\right], \tag{A.2}$$

where $R = |\mathbf{r}-\mathbf{r}'|$, $\overleftrightarrow{\mathbf{I}}$ is the identity tensor and $\mathbf{u}_r\mathbf{u}_r$ is a tensor in dyadic notation such that $(\mathbf{u}_r\mathbf{u}_r)\mathbf{A} = \mathbf{u}_r(\mathbf{u}_r \cdot \mathbf{A})$.

A.2. Green's tensor above an interface

For the plane interface system, it is convenient to use the representation due to Sipe [45] that consists of a decomposition over elementary plane waves. We use again the dyadic notation for the tensors. For instance, the s-component of the electric field is given by $\hat{s}\hat{s}\mathbf{E} = \hat{s}(\hat{s}\cdot\mathbf{E})$. In the case of a Green tensor relating currents in the lower half-space ($\mathbf{r}'$ in medium 2) to a field in the upper half-space ($\mathbf{r}$ in medium 1), one has:

$$\overleftrightarrow{\mathbf{G}}^{EE}(\mathbf{r},\mathbf{r}',\omega) = \frac{\mathrm{i}}{2}\int\frac{\mathrm{d}^2\mathbf{K}}{4\pi^2}\,\frac{1}{\gamma_2}\left[\hat{s}t^{\mathrm{s}}_{21}\hat{s} + \hat{p}_1^+ t^{\mathrm{p}}_{21}\hat{p}_2^+\right]\mathrm{e}^{\mathrm{i}\mathbf{K}\cdot(\mathbf{R}-\mathbf{R}')}\,\mathrm{e}^{\mathrm{i}\gamma_1 z-\mathrm{i}\gamma_2 z'} \tag{A.3}$$

and

$$\overleftrightarrow{\mathbf{G}}^{HE}(\mathbf{r},\mathbf{r}',\omega) = \frac{k_0 n_1}{2}\int\frac{\mathrm{d}^2\mathbf{K}}{4\pi^2}\,\frac{1}{\gamma_2}\left[\hat{p}_1^+ t^{\mathrm{s}}_{21}\hat{s} - \hat{s}t^{\mathrm{p}}_{21}\hat{p}_2^+\right]\mathrm{e}^{\mathrm{i}\mathbf{K}\cdot(\mathbf{R}-\mathbf{R}')}\,\mathrm{e}^{\mathrm{i}\gamma_1 z-\mathrm{i}\gamma_2 z'}. \tag{A.4}$$

In the expression $\hat{s} = \mathbf{K}\times\hat{\mathbf{z}}/|K|$ and $\hat{p}_i^{\pm} = -[\gamma_i\mathbf{K}/|K| \mp K\hat{\mathbf{z}}]/(n_i k_0)$. The transmission factors are defined by:

$$t^{\mathrm{p}}_{21} = \frac{2n_1 n_2\gamma_2}{\varepsilon_1\gamma_2+\varepsilon_2\gamma_1}, \qquad t^{\mathrm{s}}_{21} = \frac{2\gamma_2}{\gamma_1+\gamma_2}. \tag{A.5}$$

Note that the transmission factor for p-polarization has a pole that corresponds to the surface wave. Thus the Green's tensor contains all the information on surface waves.

In the case of two points lying above the interface in medium 1, the tensor can be cast in the form:

$$\overset{\leftrightarrow}{\mathbf{G}}^{EE}(\mathbf{r},\mathbf{r}',\omega) = \mathrm{i}\int \frac{\mathrm{d}^2\mathbf{K}}{4\pi^2}\left[\frac{\hat{s}r_{12}^{\mathrm{s}}\hat{s} + \hat{p}_1^{+}r_{12}^{\mathrm{p}}\hat{p}_1^{-}}{2\gamma_1}\mathrm{e}^{\mathrm{i}\gamma_1(z+z')} + \frac{\hat{s}\hat{s} + \hat{p}\hat{p}}{2\gamma_1}\mathrm{e}^{\mathrm{i}\gamma_1|z-z'|} + \frac{\mathrm{i}\delta(z-z')}{k_0^2\varepsilon_1}\hat{z}\hat{z}\right]\mathrm{e}^{\mathrm{i}\mathbf{K}\cdot(\mathbf{R}-\mathbf{R}')} \tag{A.6}$$

$$\overset{\leftrightarrow}{\mathbf{G}}^{HE}(\mathbf{r},\mathbf{r}',\omega) = \int \frac{\mathrm{d}^2\mathbf{K}}{4\pi^2}\left\{\frac{k_0 n_1}{2\gamma_1}\left[(\hat{p}_1^{+}r_{12}^{\mathrm{s}}\hat{s} - \hat{s}r_{12}^{\mathrm{p}}\hat{p}_1^{-})\mathrm{e}^{\mathrm{i}\gamma_1(z+z')} + (\hat{p}\hat{s} - \hat{s}\hat{p})\mathrm{e}^{\mathrm{i}\gamma_1|z-z'|}\right.\right.$$
$$\left.\left. + \frac{\mathrm{i}}{k_0^2\varepsilon_1}\delta(z-z')(k_y\hat{x}\hat{z} - k_x\hat{y}\hat{z})\right]\right\}\mathrm{e}^{\mathrm{i}\mathbf{K}\cdot(\mathbf{R}-\mathbf{R}')}, \tag{A.7}$$

where the reflection factors are:

$$r_{12}^{\mathrm{p}} = \frac{-\varepsilon_1\gamma_2 + \varepsilon_2\gamma_1}{\varepsilon_1\gamma_2 + \varepsilon_2\gamma_1}, \qquad r_{12}^{\mathrm{s}} = \frac{\gamma_1 - \gamma_2}{\gamma_1 + \gamma_2}. \tag{A.8}$$

and where we have defined $\hat{p} = [K\hat{\mathbf{z}} - \gamma_3\hat{\mathbf{z}}(z-z')/|z-z'|]/k_0 n_3$.

A.3. Green's tensor for a two-interface system

We now consider a two-layer system. The upper medium is denoted as 1 and lies above $z = d$. The lower medium ($z < 0$) is medium 2. Medium 3 is defined by $d > z > 0$. The Green's tensor relating the currents in medium 2 to the field in medium 1 with a film of medium 3 between media 1 and 2 are given by

$$\overset{\leftrightarrow}{\mathbf{G}}^{EE}(\mathbf{r},\mathbf{r}',\omega) = \frac{\mathrm{i}}{2}\int \frac{\mathrm{d}^2\mathbf{K}}{4\pi^2}\frac{1}{\gamma_2}(\hat{s}t_{12}^{\mathrm{s}}\hat{s} + \hat{p}_1^{+}t_{12}^{\mathrm{p}}\hat{p}_2^{+})\,\mathrm{e}^{\mathrm{i}[\mathbf{K}\cdot(\mathbf{R}-\mathbf{R}')]}\,\mathrm{e}^{\mathrm{i}[\gamma_1(z-d)-\gamma_2 z']} \tag{A.9}$$

and

$$\overset{\leftrightarrow}{\mathbf{G}}^{HE}(\mathbf{r},\mathbf{r}',\omega) = \frac{k_0 n_2}{2}\int \frac{\mathrm{d}^2\mathbf{K}}{4\pi^2}\frac{1}{\gamma_2}(\hat{p}_1^{+}t_{21}^{\mathrm{s}}\hat{s} - \hat{s}t_{21}^{\mathrm{p}}\hat{p}_2^{+})\,\mathrm{e}^{\mathrm{i}[\mathbf{K}\cdot(\mathbf{R}-\mathbf{R}')]}\,\mathrm{e}^{\mathrm{i}[\gamma_1(z-d)-\mathrm{i}\gamma_2 z']}, \tag{A.10}$$

where

$$t_{21}^{\mathrm{s,p}} = \frac{t_{31}^{\mathrm{s,p}}t_{23}^{\mathrm{s,p}}\,\mathrm{e}^{\mathrm{i}\gamma_3 d}}{1 - r_{31}^{\mathrm{s,p}}r_{32}^{\mathrm{s,p}}\,\mathrm{e}^{\mathrm{i}2\gamma_3 d}}. \tag{A.11}$$

Note that the two-interface Green's tensor is very similar to the single interface one, except that the single interface transmission coefficient has to be replaced by a generalised transmission coefficient taking into account the multiple reflections.

When $\mathbf{r}$ and $\mathbf{r}'$ are in the film (medium 3), the Green's tensor can be cast in the form:

$$\overset{\leftrightarrow}{\mathbf{G}}^{EE}(\mathbf{r},\mathbf{r}',\omega) = \int \frac{\mathrm{d}^2\mathbf{K}}{4\pi^2}\overset{\leftrightarrow}{\mathbf{g}}^{EE}(\mathbf{K},z,z')\exp[\mathrm{i}\mathbf{K}(\mathbf{R}-\mathbf{R}')], \tag{A.12}$$

where $\mathbf{g}^{\leftrightarrow EE}(\mathbf{K},z,z')$ is the sum of three contributions:

$$\overset{\leftrightarrow}{\mathbf{g}}^{EE}(\mathbf{K},z,z') = \frac{\mathrm{i}}{2\gamma_3}[\hat{s}\hat{s} + \hat{p}\hat{p}]\exp[\mathrm{i}\gamma_3|z-z'|] - \frac{1}{k_0^2\varepsilon_3}\delta(z-z')\hat{\mathbf{z}}\hat{\mathbf{z}} + \frac{\mathrm{i}}{2\gamma_3}[\hat{s}\rho_{32}^{\mathrm{s}}\hat{s} + \hat{p}_3^{+}\rho_{32}^{\mathrm{p}}\hat{p}_3^{-}] \times \exp[\mathrm{i}\gamma_3(z+z')] + \frac{\mathrm{i}}{2\gamma_3}[\hat{s}\rho_{31}^{\mathrm{s}}\hat{s} + \hat{p}_3^{-}\rho_{31}^{\mathrm{p}}\hat{p}_3^{+}]\exp[\mathrm{i}\gamma_3(d-z+d-z')], \tag{A.13}$$

where

$$\rho_{31}^{\mathrm{s,p}} = \frac{r_{31}^{\mathrm{s,p}}}{1 - r_{31}^{\mathrm{s,p}}r_{32}^{\mathrm{s,p}}\,\mathrm{e}^{\mathrm{i}2\gamma_3 d}}, \qquad \rho_{32}^{\mathrm{s,p}} = \frac{r_{32}^{\mathrm{s,p}}}{1 - r_{31}^{\mathrm{s,p}}r_{32}^{\mathrm{s,p}}\,\mathrm{e}^{\mathrm{i}2\gamma_3 d}}. \tag{A.14}$$

Appendix B. Fluctuation–dissipation theorem

In this section, we derive the appropriate spectral density for an absorption measurement and for a quantum-counter measurement. The operator needed to describe the absorption of a photon involves the normally ordered correlation function of the field operator $\langle E_k^{(-)}E_l^{(+)}\rangle$, where $E^{(+/-)}$ is defined using only the positive or negative frequencies of the spectrum. We quote from Agarwal [31] the cross-spectral density of the normally and antinormally ordered electric fields:

$$\mathcal{E}_{kl}^{(\mathrm{N})}(\mathbf{r},\mathbf{r}',\omega) = \eta(-\omega)\mu_0\hbar\omega^2\left[1 + \coth\left(\frac{\hbar\omega}{2k_{\mathrm{B}}T}\right)\right]\mathrm{Im}[G_{kl}^{EE}(\mathbf{r},\mathbf{r}',\omega)], \tag{B.1}$$

$$\mathcal{E}_{kl}^{(\mathrm{A})}(\mathbf{r},\mathbf{r}',\omega) = \eta(\omega)\mu_0\hbar\omega^2\left[1 + \coth\left(\frac{\hbar\omega}{2k_{\mathrm{B}}T}\right)\right]\mathrm{Im}[G_{kl}^{EE}(\mathbf{r},\mathbf{r}',\omega)], \tag{B.2}$$

where $\eta(\omega)$ is the Heaviside function. It is seen that the normally ordered cross-spectral density involves only negative frequencies whereas the antinormally ordered correlation involves only positive frequencies. They can be viewed as an analytic signal. Despite the apparent symmetry of the above equations, there is a critical difference as will be seen in the next section.

B.1. Absorption measurement

Let us now derive the time-correlation function for the electric field. From Agarwal [31], we have

$$\langle E_k(\mathbf{r},t+\tau)E_l(\mathbf{r}',t)\rangle = 2\,\mathrm{Re}[\langle E_k^{(-)}(\mathbf{r},t+\tau)E_l^{(+)}(\mathbf{r}',t)\rangle]. \tag{B.3}$$

Using the cross-spectral density (B.1), we get

$$\langle E_k(\mathbf{r},t+\tau)E_l(\mathbf{r}',t)\rangle = 2\,\mathrm{Re}\left[\int_{-\infty}^{0}\frac{\mathrm{d}\omega}{2\pi}\exp(-\mathrm{i}\omega\tau)\mu_0\hbar\omega^2\,\mathrm{Im}[G_{kl}^{E}]\left[1 + \coth\left(\frac{\hbar\omega}{2k_{\mathrm{B}}T}\right)\right]\right]. \tag{B.4}$$

We note that

$$\mathrm{Im}[G_{kl}^{E}(\mathbf{r},\mathbf{r}',-\omega)] = -\mathrm{Im}[G_{kl}^{E}(\mathbf{r},\mathbf{r}',\omega)] \tag{B.5}$$

and

$$\left[1+\coth\left(\frac{\hbar\omega}{2k_{\mathrm{B}}T}\right)\right] = -\frac{2}{\exp\left(\hbar|\omega|/k_{\mathrm{B}}T\right)-1} \tag{B.6}$$

so that the correlation function can be cast in the form:

$$\langle E_k(\mathbf{r},t+\tau)E_l(\mathbf{r}',t)\rangle = 2\,\mathrm{Re}\left[\int_0^\infty \frac{\mathrm{d}\omega}{2\pi}\exp\left(\mathrm{i}\omega\tau\right)2\mu_0\omega\,\mathrm{Im}[G_{kl}^{EE}]\Theta(\omega,T)\right]. \tag{B.7}$$

B.2. *Quantum-counter measurement*

We derive now the time-correlation starting from the antinormally ordered correlation function. This choice is appropriate for a quantum-counter experiment. The Casimir effect that depends on the total energy of the system pertains to this category. From Agarwal [31], we have

$$\langle E_k(\mathbf{r},t+\tau)E_l(\mathbf{r}',t)\rangle = 2\,\mathrm{Re}[\langle E_k^{(+)}(\mathbf{r},t+\tau)E_l^{(-)}(\mathbf{r}',t)\rangle]. \tag{B.8}$$

Using the cross-spectral density (B.1), we get

$$\langle E_k(\mathbf{r},t+\tau)E_l(\mathbf{r}',t)\rangle = 2\,\mathrm{Re}\left[\int_0^\infty \frac{\mathrm{d}\omega}{2\pi}\exp\left(-\mathrm{i}\omega\tau\right)\mu_0\hbar\omega^2\,\mathrm{Im}[G_{kl}^{EE}]\left[1+\coth\left(\frac{\hbar\omega}{2k_{\mathrm{B}}T}\right)\right]\right]. \tag{B.9}$$

We note that

$$\left[1+\coth\left(\frac{\hbar\omega}{2k_{\mathrm{B}}T}\right)\right] = 2+\frac{2}{\exp\left(\hbar\omega/k_{\mathrm{B}}T\right)-1}, \tag{B.10}$$

so that the correlation function can be cast in the form:

$$\langle E_k(\mathbf{r},t+\tau)E_l(\mathbf{r}',t)\rangle = 2\,\mathrm{Re}\left[\int_0^\infty \frac{\mathrm{d}\omega}{2\pi}\exp\left(-\mathrm{i}\omega\tau\right)2\mu_0\omega\,\mathrm{Im}[G_{kl}^{EE}][\hbar\omega+\Theta(\omega,T)]\right]. \tag{B.11}$$

We conclude by noting that both results have a similar structure and can be described by an effective spectrum defined for positive frequencies only. This analysis provides a justification for the heuristic argument often used to drop the vacuum energy fluctuation.

References

[1] R. Chance, A. Prock, R. Silbey, Adv. Chem. Phys. 37 (1978) 1.
[2] H. Failache, S. Saltiel, M. Fichet, D. Bloch, M. Ducloy, Appl. Phys. Lett. 60 (1992) 2484.
[3] R. Hillenbrand, T. Taubner, F. Keilmann, Nature 418 (2002) 159.
[4] T. Ebbesen, H. Lezec, H. Ghaemi, T. Thio, P. Wolff, Nature 391 (1998) 667.
[5] A. Krishnan, T. Thio, T. Kim, H. Lezec, T. Ebbesen, P. Wolff, J. Pendry, L. Martin-Moreno, F. Garcia-Vidal, Opt. Commun. 200 (2001) 1.
[6] J. Pendry, Phys. Rev. Lett. 85 (2000) 3966.
[7] A. Shchegrov, K. Joulain, R. Carminati, J.-J. Greffet, Phys. Rev. Lett. 85 (2000) 1548.
[8] R. Carminati, J.-J. Greffet, Phys. Rev. Lett. 82 (1999) 1660.
[9] C. Henkel, M. Wilkens, Europhys. Lett. 47 (1999) 414.
[10] J.-J. Greffet, R. Carminati, K. Joulain, J.-P. Mulet, S. Mainguy, Y. Chen, Nature 416 (2002) 61.
[11] C. Kittel, Introduction to Solid State Physics, 7th ed. Wiley, New York, 1996.

[12] N. Ashcroft, D. Mermin, Solid State Physics, International Edition, Saunders, Philadelphia, 1976.
[13] J. Ziman, Electrons and Phonons, Oxford University Press, Oxford, 1960.
[14] H. Raether, Surface Plasmons, Springer-Verlag, Berlin, 1988.
[15] V. Agranovitch, D. Mills, Surface Polaritons, North-Holland, Amsterdam, 1982.
[16] E. Economou, K. Ngai, Adv. Chem. Phys. 27 (1974) 265.
[17] E.A. Boardman, Electromagnetic Surface Modes, Wiley, New York, 1982.
[18] J. Le Gall, M. Olivier, J.-J. Greffet, Phys. Rev. B 55 (1997) 10105.
[19] P. Halevi, A. Boardman (Eds.), Electromagnetic Surface Modes, Wiley, New York, 1982.
[20] E. Arakawa, M. Williams, R. Ritchie, Phys. Rev. Lett. 31 (1973) 1127.
[21] K. Kliewer, R. Fuchs, Adv. Chem. Phys. 27 (1974) 355.
[22] A. Otto, Z. Phys. 241 (1971) 398.
[23] E. Kretschmann, Z. Phys. 216 (1971) 398.
[24] E.A. Vinogradov, G.N. Zhizhin, V.I. Yudson, in: V.M. Agranovich, D.L. Mills (Eds.), Surface Polaritons, North-Holland, Amsterdam, 1982, p. 145.
[25] W. Spitzer, D. Kleinman, D. Walsh, Phys. Rev. 113 (1959) 127.
[26] S. Rytov, Sov. Phys. JETP 6 (1958) 130.
[27] S. Rytov, Y. Kravtsov, V. Tatarskii, Principles of Statistical Radiophysics, vol. 3, Springer-Verlag, Berlin, 1989.
[28] P. Langevin, CR Acad. Sci., Paris 146 (1908) 530.
[29] L. Mandel, E. Wolf, Optical Coherence and Quantum Optics, Cambridge University Press, Cambridge, 1995.
[30] H.B. Callen, T.A. Welton, Phys. Rev. 83 (1951) 34.
[31] G. Agarwal, Phys. Rev. A 11 (1975) 230.
[32] C.-T. Tai, Dyadic Green's Functions in Electromagnetic Theory, 2nd ed. Oxford University Press, Oxford, 1996.
[33] G. Agarwal, Phys. Rev. A 11 (1975) 253.
[34] J. Jackson, Classical Electrodynamics, 2nd ed. Wiley, New York, 1975.
[35] C. Henkel, K. Joulain, R. Carminati, J.-J. Greffet, Opt. Commun. 186 (2000) 57.
[36] J. Tersoff, D. Hamann, Phys. Rev. B 31 (1985) 805.
[37] E. Economou, Green's Functions in Quantum Physics, Springer, Berlin, 1983.
[38] N.G.V. Kampen, B. Nijboer, K. Schram, Phys. Lett. A 26 (1968) 307.
[39] E. Gerlach, Phys. Rev. B 4 (1971) 393.
[40] J. Pendry, J. Phys.: Condens. Matter 9 (1997) 10301.
[41] F. Wijnands, J. Pendry, F.J. Garcia-Vidal, P.J. Roberts, L. Martin-Moreno, Opt. Quant. Electron. 29 (1997) 199.
[42] C. Chicanne, T. David, R. Quidant, J. Weeber, Y. Lacroute, E. Bourillot, A. Dereux, G. Colas des Francs, C. Girard, Phys. Rev. Lett. 88 (2002) 097402.
[43] G. Colas des Francs, C. Girard, J.-C. Weeber, C. Chicanne, T. David, A. Dereux, D. Peyrade, Phys. Rev. Lett. 86 (2001) 4950.
[44] K. Joulain, R. Carminati, J.-P. Mulet, J.-J. Greffet, Phys. Rev. B 68 (2003) 245405.
[45] J. Sipe, J. Opt. Soc. Am. B 4 (1987) 481.
[46] E. Palik, Handbook of Optical Constants of Solids, Academic Press, San Diego, 1991.
[47] W. Harrisson, Solid State Theory, Dover, New York, 1980.
[48] J. Goodman, Statistical Optics, Wiley, New York, 1985.
[49] T. Setälä, M. Kaivola, A. Friberg, Phys. Rev. Lett. 88 (2002) 123902.
[50] M. Nieto-Vesperinas, Scattering and Diffraction in Physical Optics, Wiley, New York, 1991.
[51] P. Hesketh, J.N. Zemel, B. Gebhart, Nature 324 (1986) 549.
[52] P. Hesketh, J.N. Zemel, B. Gebhart, Phys. Rev. B 37 (1988) 10795.
[53] P. Hesketh, J.N. Zemel, B. Gebhart, Phys. Rev. B 37 (1988) 10803.
[54] M. Kreiter, J. Auster, R. Sambles, S. Herminghaus, S. Mittler-Neher, W. Knoll, Opt. Commun. 168 (1999) 117.
[55] A. Heinzel, V. Boerner, A. Gombert, B. Bläsi, V. Wittwer, J. Luther, J. Mod. Opt. 47 (2000) 2399.
[56] F. Marquier, K. Joulain, J. Mulet, R. Carminati, Y. Chen, Phys. Rev. B 69 (2004) 155412.
[57] O.G. Kollyukh, A. Liptuga, V. Morozhenko, V. Pipa, Opt. Commun. 225 (2003) 349.
[58] P. Ben-Abdallah, J. Opt. Soc. Am. A 21 (2004) 1368.
[59] Z.M. Zhang, C.J. Fu, Q.Z. Zhu, Adv. Heat Transfer 37 (2003) 179.

[60] F. Ghmari, T. Ghbara, M. Laroche, R. Carminati, J.-J. Greffet, J. Appl. Phys. 96 (2004) 2656.
[61] P. Beckmann, A. Spizzichino, The Scattering of Electromagnetic Waves, Pergamon Press, Oxford, 1963.
[62] J.A. Desanto, G.S. Brown, Progress in Optics, vol. XIII, North-Holland, Amsterdam, 1986.
[63] J. Ogilvy, Theory of Wave Scattering from Random Rough Surfaces, Adam Hilger, Bristol, 1991.
[64] L. Tsang, J. Kong, Scattering of Electromagnetic Waves: Advanced Topics, Wiley, New York, 2001.
[65] A.G. Voronovich, Wave Scattering from Rough Surfaces, Springer-Verlag, Berlin, 1994.
[66] C. Baylard, J.-J. Greffet, A.A. Maradudin, J. Opt. Soc. Am. A 10 (1993) 2637.
[67] M. Auslander, S. Hava, Infrared Phys. Technol. 36 (1999) 414.
[68] M. Auslander, D. Levy, S. Hava, Appl. Opt. 37 (1998) 369.
[69] S. Hava, J. Ivri, M. Auslander, J. Appl. Phys. 85 (1999) 7893.
[70] M. Auslander, D. Levy, S. Hava, Appl. Opt. 37 (1998) 369.
[71] H. Sai, H. Yugami, Y. Akiyama, Y. Kanamori, K. Hane, J. Opt. Soc. Am. A 18 (2001) 1471.
[72] F. Marquier, K. Joulain, J. Mulet, R. Carminati, J.-J. Greffet, Opt. Commun. 237 (2004) 379.
[73] F. Kusunoki, J. Takahara, T. Kobayashi, Electron. Lett. 39 (2003) 23.
[74] M.U. Pralle, N. Moelders, M. McNeal, I. Puscasu, A.C. Greenwald, J.T. Daly, E.A. Johnson, T. George, D.S. Choi, I. ElKady, R. Biswas, Appl. Phys. Lett. 81 (2002) 4685.
[75] W.L. Barnes, Nat. Mater. 3 (2004) 588.
[76] K. Okamoto, I. Niki, A. Shvartser, Y. Narukawa, T. Mukai, A. Scherer, Nat. Mater. 3 (2004) 601.
[77] E. Cravalho, C. Tien, R. Caren, J. Heat Transfer 89 (1967) 351.
[78] R. Boehm, C. Tien, J. Heat Transfer 92 (1970) 405.
[79] D. Polder, D. van Hove, Phys. Rev. B 4 (1971) 3303.
[80] M.L. Levin, V. Polevai, Sov. Phys. JETP 52 (1980) 1054.
[81] J. Loomis, H. Maris, Phys. Rev. B 50 (1994) 18517.
[82] J. Pendry, J. Phys.: Condens. Matter 11 (1999) 6621.
[83] A. Volokitin, B. Persson, Phys. Rev. B 63 (2001) 205404.
[84] G. Chen, Microscale Thermophys. Eng. 1 (1997) 215.
[85] J. Mulet, K. Joulain, R. Carminati, J.-J. Greffet, Microscale Thermophys. Eng. 6 (2002) 209.
[86] J.L. Pan, Opt. Lett. 25 (2001) 369.
[87] J.L. Pan, Opt. Lett. 26 (2001) 482.
[88] A.A. Maradudin, Opt. Lett. 6 (2001) 479.
[89] J. Mulet, K. Joulain, R. Carminati, J.-J. Greffet, Opt. Lett. 26 (2001) 480.
[90] C.M. Heargraves, Phys. Rev. Lett. 30A (1969) 491.
[91] K. Dransfeld, J. Xu, J. Microsc. 152 (1988) 35.
[92] J.B. Xu, K. Lauger, R. Moller, K. Dransfeld, I.H. Wilson, J. Appl. Phys. 76 (1994) 7209.
[93] I. Dorofeyev, J. Phys. D: Appl. Phys. 31 (1998) 600.
[94] J. Mulet, K. Joulain, R. Carminati, J.-J. Greffet, Appl. Phys. Lett. 78 (2001) 2931.
[95] A. Narayanaswamy, G. Chen, Appl. Phys. Lett. 82 (2003) 3544.
[96] T.H. Forster, Ann. Phys. (Leipzig) 6 (1948) 55.
[97] C.F. Bohren, D. Huffman, Absorption and Scattering of Light by Small Particles, Wiley, New York, 1983.
[98] R. Carminati, J. Saenz, J. Greffet, M. Nieto-Vesperinas, Phys. Rev. A 62 (2000) 012712.
[99] H. Casimir, Proc. Konikl. Ned. Akad. Wetenschap. 51 (1948) 793.
[100] H. Casimir, D. Polder, Phys. Rev. 73 (1948) 360.
[101] V. Mostepanenko, N.N. Trunov, The Casimir Effect and its Applications, Oxford Science Publications, Oxford, 1997.
[102] P.W. Milonni, The Quantum Vacuum: An Introduction to Quantum Electrodynamics, Academic Press, San Diego, 1994
[103] G. Plunien, B. Muller, W. Greiner, Phys. Rep. 134 (1986) 87.
[104] M. Bordag, U. Mohideen, V.M. Mostepanenko, Phys. Rep. 53 (2001) 1.
[105] S. Lamoreaux, Am. J. Phys. 67 (1999) 850.
[106] K. Milton, hep-th/0406024.
[107] E. Lifshitz, Sov. Phys. JETP 2 (1956) 73.
[108] G. Agarwal, Phys. Rev. A 11 (1975) 243.
[109] S. Lamoreaux, Phys. Rev. Lett. 78 (1997) 5.

[110] U. Mohideen, A. Roy, Phys. Rev. Lett. 81 (1998) 4549.
[111] B.W. Harris, F. Chen, U. Mohideen, Phys. Rev. A 62 (2000) 052109.
[112] T. Ederth, Phys. Rev. A 62 (2000) 062104.
[113] G. Bressi, G. Carugno, R. Onofrio, G. Ruos, Phys. Rev. Lett. 88 (2002) 041804.
[114] R. Decca, D. Lopez, E. Fischbach, D. Krause, Phys. Rev. Lett. 91 (2003) 050402.
[115] H. Chan, V. Aksyuk, R. Kleinman, D. Bishop, F. Capasso, Phys. Rev. Lett. 87 (2001) 211801.
[116] H. Chan, V. Aksyuk, R. Kleinman, D. Bishop, F. Capasso, Science 291 (2001) 1941.
[117] A. Lambrecht, S. Reynaud, Eur. Phys. J. D 8 (2000) 309.
[118] C. Genet, A. Lambrecht, S. Reynaud, Phys. Rev. A 62 (2000) 012110.
[119] G. Klimchitskaya, V. Mostepanenko, Phys. Rev. A 63 (2001) 062108.
[120] C. Henkel, K. Joulain, J.-P. Mulet, J.-J. Greffet, Phys. Rev. A 69 (2004) 023808.
[121] J. Schwinger, L. DeRaad, K. Milton, Ann. Phys. 115 (1978) 1–23.
[122] P. Milonni, R. Cook, M. Goggin, Phys. Rev. A 38 (1988) 1621.
[123] V. Hushwater, Am. J. Phys. 65 (1997) 381.
[124] C. Genet, A. Lambrecht, S. Reynaud, Phys. Rev. A 67 (2003) 043811.
[125] O. Kenneth, I. Klich, A. Mann, M. Revzen, Phys. Rev. Lett. 89 (2002) 033001.
[126] E. Buks, M. Roukes, Nature 419 (2002) 119.
[127] D. Marcuse, Theory of Dielectric Optical Waveguides, 2nd ed. Academic Press, San Diego, 1991.
[128] D. Sarid, Phys. Rev. Lett. 47 (1981) 1927.
[129] A. Einstein, L. Hopf, Ann. Phys. (Leipzig) 33 (1910) 1105.
[130] A. Einstein, O. Stern, Ann. Phys. (Leipzig) 40 (1913) 551.
[131] P. Milonni, M. Shih, Am. J. Phys. 59 (1991) 684.
[132] V. Mkrtchian, V. Parsegian, R. Podgornik, W.M. Saslow, Phys. Rev. Lett. 91 (2004) 220801.
[133] E. Betzig, P. Finn, J. Weiner, Phys. Rev. B 62 (2000) 13174.
[134] R. Toledo-Crow, P. Yang, Y. Chen, M. Vaez-Iravani, Appl. Phys. Lett. 60 (1992) 2957.
[135] K. Karrai, R. Grober, Appl. Phys. Lett. 66 (1995) 1842.
[136] K. Karrai, I. Tiemann, Phys. Rev. B 62 (2000) 13174.
[137] B. Stipe, H. Mamin, T. Stowe, T. Kenny, D. Rugar, Phys. Rev. Lett. 87 (2001) 096801.
[138] E.V. Teodorovitch, Proc. R. Soc. London A 362 (1978) 71.
[139] L.S. Levitov, Europhys. Lett. 8 (1989) 499.
[140] G. Barton, Ann. Phys. NY 245 (1996) 361.
[141] A. Volokitin, B. Persson, J. Phys.: Condens. Matter 11 (1999) 345.
[142] W.L. Schaich, J. Harris, J. Phys. F: Met. Phys. 11 (1981) 65.
[143] M.S. Tomassone, A. Widom, Phys. Rev. B 56 (1997) 4938.
[144] A. Kyasov, G. Dedkov, Surf. Sci. 463 (2000) 11.
[145] I. Dorofeyev, H. Fuchs, G. Wenning, B. Gotsmann, Phys. Rev. Lett. 83 (1999) 848.
[146] I. Dorofeyev, H. Fuchs, B. Gotsmann, J. Jersch, Phys. Rev. B 64 (2001) 035403.
[147] A. Volokitin, B. Persson, Phys. Rev. Lett. 91 (2003) 106101.
[148] A. Volokitin, B. Persson, Phys. Rev. B 68 (2003) 155420.
[149] J. Zurita-Sanchez, J.-J. Greffet, L. Novotny, Phys. Rev. A 69 (2004) 022902.
[150] G. Domingues, S. Volz, K. Joulain, J.-J. Greffet, Phys. Rev. Lett. 94 (2005) 085901.

Monte Carlo transient phonon transport in silicon and germanium at nanoscales

D. Lacroix, K. Joulain et D. Lemonnier

Physical Review B, vol 72, pp064305 (2005)

PHYSICAL REVIEW B **72**, 064305 (2005)

Monte Carlo transient phonon transport in silicon and germanium at nanoscales

David Lacroix,* Karl Joulain,† and Denis Lemonnier‡
Laboratoire d'Études Thermiques, ENSMA, 1, Avenue Clément Ader 86960 Futuroscope Cedex, France

(Received 8 April 2005; revised manuscript received 6 July 2005; published 23 August 2005)

Heat transport at nanoscales in semiconductors is investigated with a statistical method. The Boltzmann transport equation (BTE), which characterizes phonon motion and interaction within the crystal lattice, has been simulated with a Monte Carlo technique. Our model takes into account media frequency properties through the dispersion curves for longitudinal and transverse acoustic branches. The BTE collisional term involving phonon scattering processes is simulated with the relaxation times approximation theory. A new distribution function accounting for the collisional processes has been developed in order to respect energy conservation during phonons scattering events. This nondeterministic approach provides satisfactory results in what concerns phonon transport in both ballistic and diffusion regimes. The simulation code has been tested with silicon and germanium thin films; temperature propagation within samples is presented and compared to analytical solutions (in the diffusion regime). The two-material bulk thermal conductivity is retrieved for temperature ranging between 100 K and 500 K. Heat transfer within a plane wall with a large thermal gradient (250 K to 500 K) is proposed in order to expose the model ability to simulate conductivity thermal dependence on heat exchange at nanoscales. Finally, size effects and validity of heat conduction law are investigated for several slab thicknesses.

DOI: 10.1103/PhysRevB.72.064305 PACS number(s): 63.20.−e, 05.10.Ln, 44.10.+i, 65.40.−b

I. INTRODUCTION

The development of nanotechnologies has led to an unprecedented size reduction of the electronic and mechanical devices. For example, transistors of a few nanometer size are now openly considered.[1] The heat that will be dissipated by joule effect in these semiconductor junctions will reach soon the levels of the heat dissipated in a light bulb. This high volumetric heat dissipation in electronic devices will have to be evacuated very efficiently in order to avoid possible failures of the systems. This task will not be achieved without a precise knowledge of the phenomena governing the heat transfer at nanoscale. Furthermore, new technologies based on a local heating are being developed in order to enlarge the computer hard disk capacity. The ultimate limit of storage is to write a byte at the atomic scale. This goal is already feasible with near-field microscope probes but at a too slow rate. A way to write bytes at the nanometer scale is the melting of a polymer by heating it on a very short time scale ($\leqslant 1$ ns) by an array of heated near-field probes.[2] In this example, the heat transfer has to be controlled not only at the nanometer scale but also at the nanosecond scale.

Through these two examples, one can anticipate that the foreseeing technological challenges in miniaturization will have to solve more and more problems of heat transfer at short time and space scale. However, the physics of heat transfer usually used (Fourier's law, radiative transfer equation) can no longer be applied when some characteristic length scales are reached.[3] In thermal radiation, for example, wave effects appear as the system characteristic lengths becomes lower than the typical wavelength ($\lambda \sim 10\ \mu$m at $T = 300$ K).[4,5] A substantial increase of the radiative heat transfer can even be reached at nanometric distances.[6] On its side, heat conduction is classically described by the Fourier law and the heat conduction equation ($\partial T/\partial t = \alpha \Delta T$) which is a diffusion equation. It is well known that this kind of equation can be interpreted as a random walk of particles.[7] In the case of heat conduction, we are actually dealing with energy carriers which are electrons in metals and phonons in crystalline materials. When these carriers undergo a large number of collisions, the use of the diffusion equation is valid whereas a more careful study is required when the number of interactions between carriers lowers.

A way to achieve this goal is to consider the evolution of a distribution function $f(\mathbf{r},\mathbf{p},t)$ which describes the number of particles in a certain elementary volume $d^3\mathbf{r}d^3\mathbf{p}$ around the point $(\mathbf{r},\mathbf{p})$ in the phase space. The evolution equation of f, called the Boltzmann transport equation (BTE), makes f vary in space and time under the influence of advection, external force, and collision.[8] Note that this approach is not relevant to treat the wave aspects of the problem such as interference or tunneling. The understanding and the modeling of the collision term is actually the key point in the resolution of the BTE. It can sometimes be fully expressed as in radiation transfer. Then the collision term is in that case the sum of an absorption term, an elastic scattering term, and an emission term proportional to an equilibrium distribution.[9] Many resolution techniques have been developed in radiation transfer such as the discrete ordinates method, the Monte Carlo method, or the ray-tracing method.[10] They can hardly be used when the collision processes are inelastic as it is the case for electrons and phonons.[11] For example, the phonons, which are eigenmodes of the harmonic oscillators constituting the crystal, can only interact through the anharmonic term of the potential leading to three or more phonon collisions. These interactions preserve neither the number of phonons nor their frequency in the collision process. Nevertheless, these three or four phonon interactions tend to restore thermal equilibrium, i.e., to help the phonons to follow an equilibrium distribution function which can be easily determined from thermodynamic equilibrium considerations. Thus, many of the studies approximate the collision term in the BTE by the so-called relaxation time approximation: the distribution function $f(\mathbf{r},\mathbf{p},t)$ relaxes to an equilibrium function $f^0(\mathbf{r},\mathbf{p})$ on a time scale $\tau(\mathbf{p})$. The BTE resulting from this approximation is nothing but the radiative transfer equation without scattering.[12] All the numerical tools developed in thermal radiation can therefore be used in this case. The key point in this model is to calculate a suitable $\tau(\mathbf{p})$ in order to characterize the collisions.

In the middle of the 20th century, a great theoretical effort has been made to determine the relaxation times of the phonons in a bulk material. At ambient temperature, it has been shown that the main contribution to the relaxation time finds its origin in the anharmonic phonon interaction. These anharmonic interactions can be triadic or quartic. Triadic interactions involve three phonons (for example, two phonons anihilate to give birth to a third one) whereas quartic interactions involve four phonons (two phonon anihilate to give birth to two others). Quartic interactions contribute often less to the phonon relaxation time, but sometimes have to be taken into account, especially in the case of high temperatures ($T > 1000$ K) as it has been shown by Ecsedy and Klemens.[13] At ambient and low temperature, semiconductor (such as Si and Ge, which are treated here) studies are usually limited to triadic interactions.[14] Nevertheless, taking them into account or not does not change the ways the BTE can be solved. Among these anharmonic processes, two different kinds can be identified. The so-called normal processes (N), which maintain the momentum in the collision, and the Umklapp processes (U), which do not preserve the momentum. The former do not affect the material thermal resistance, contrary to the latter. These Umklapp processes follow selection rules[15] and it is an amazing feat to calculate them.[16]

In the case of semiconductors such as silicon (Si), germanium (Ge),[17,18] and gallium arsenide (GaAs),[19,20] the relaxation times have allowed us to compute semianalytically thermal conductivities in good agreement with measurements. Resolution of the BTE have been achieved on these materials in bulk situations, thin film, or superlattice configuration.[12,21–23] At short time scale, these resolutions have been compared to classical solutions[24,25] and some modifications of the BTE have been proposed.[26] The resolutions based on the discrete ordinates method or on the finite volumes method converge very quickly numerically but have a major drawback: they are governed by a single relaxation time taking into account all the different processes of relaxation such as the anharmonic interactions between phonons, the interactions with impurities and dislocations, or the scattering on the material boundaries. The Matthiesen rule, which states that the inverse of the total relaxation term is the sum of the relaxation times due to every different phenomena, is usually used. In the context of the BTE in the relaxation time approximation, this means that all the different interaction or scattering phenomena tend to restore thermal equilibrium.

An alternative way to solve the BTE is the Monte Carlo method. This method is quite computer time greedy because it necessitates to following a large number of energy carriers, but it becomes competitive when the complexity of the problem increases, particularly for nontrivial geometries. This method is therefore useful in order to calculate the heat transfer in electronic devices of any shape. Moreover, in this method, different scattering phenomena (impurities scattering, boundary scattering, and inelastic scattering) can be treated separately. The resolution of the BTE by the Monte Carlo method has been performed for electrons[27–32] but has been little used in the case of phonons. Peterson[33] performed a Monte Carlo simulation for phonons in the Debye approximation with a single relaxation time. He presented results both in the transient regime and in equilibrium situation. Mazumder and Majumdar[34] followed Peterson's approach but included in their simulation the dispersion and the different acoustic polarization branches. They retrieved both the ballistic and the diffusion situation but did not show any result in the transient regime. Another limit of this last paper is that the N processes and the U processes are not treated separately although they do not contribute in the same way to the conductivity.

The starting point in our work is these two contributions. We follow individual phonons in a space divided into cells. The phonons, after a drift phase, are able to interact and to be scattered. The speed and the rate at which phonons scatter depends on the frequency. We ensure that energy is conserved after each scattering process. This procedure is different whether the phonons interact through an N process or a U process. This paper is therefore an improvement of existing phonon Monte Carlo methods and is validated on simple examples such as a semiconductor film heated at two different temperatures.

Section II recalls the basic hypothesis governing the BTE. Fundamental quantities such as the number of phonons, the energy, and the density of states are also defined. The phonon properties are also presented through their dispersion relations. Section III exposes the Monte Carlo method used in this paper. Boundary conditions, phonon drift, and scattering procedures are given in detail. Section IV presents transient results in the diffusion and ballistic regimes. Thermal conductivities of silicon and germanium between 100 K and 500 K are numerically estimated. The influence of conductivity thermal dependence on heat conduction within a slab is studied. Finally, size effects on phonon transport at very short scales are considered.

II. THEORY

A. Boltzmann transport equation

The Boltzmann transport equation (BTE) is used to model the phonon behavior in a crystal lattice. This equation is related to the variation of the distribution function $f(t,\mathbf{r},\mathbf{K})$ which depends on time t, location $\mathbf{r}$, and wave vector $\mathbf{K}$. $f(t,\mathbf{r},\mathbf{K})$ can also be defined as the mean particle number at time t in the $d^3\mathbf{r}$ volume around $\mathbf{r}$ with $\mathbf{K}$ wave vector and $d^3\mathbf{K}$ accuracy. In the absence of external force, the BTE expression is[35]

$$\frac{\partial f}{\partial t} + \nabla_{\mathbf{K}}\omega \cdot \nabla_{\mathbf{r}} f = \left.\frac{\partial f}{\partial t}\right|_{\text{collision}} \tag{1}$$

with the phonon group velocity $\mathbf{v}_g = \nabla_{\mathbf{K}}\omega$.

Integration of the distribution function over all the wave vectors of the first Brillouin zone and all the locations leads to the phonon number $N(t)$ at a given time in the crystal. The lhs term of Eq. (1) accounts for the phonon drift in the medium and the rhs term for the equilibrium restoration due to phonon collisions with themselves, impurities, and boundaries.

The collisional term modeling is the key point in the BTE resolution. In the case of photons, it appears as the sum of an absorption term, of an emission term, and of an elastic scattering term in which a scattering phase function relates a photon in the incoming and outgoing propagation directions during a scattering event.[9] However, in the case of phonons, there is no absorption, nor emission, but only scattering events. Scattering events at the borders can simply be treated during the drift phase, i.e., when a phonon reaches a border. Scattering with impurities can be treated similarly to the isotropic scattering of photons when addressing thermal radiation. Scattering of phonons due to the anharmonic terms of the potential are quite difficult to express. We know nevertheless that these terms are responsible for the thermal conductivity, i.e., tend to restore thermal equilibrium. Therefore, in this work we use the relaxation time approximation for three phonon scattering processes. The collision time used in this formalism comes from normal and Umklapp relaxation times which are further estimated.

B. Lattice modeling

As it has been exposed previously, the thermal behavior of the crystal can be considered from the phonon characteristics (location, velocity, and polarization) within the medium. They might be obtained through the BTE solution since the distribution function can be easily related to the energy and therefore to the temperature. Using an integrated distribution function, one can express the total vibrational energy of the crystal as[36]

$$E = \sum_p \sum_{\mathbf{K}} \left(\langle n_{\mathbf{K},p} \rangle + \frac{1}{2} \right) \hbar\omega, \tag{2}$$

where $\langle n_{\mathbf{K},p} \rangle$ is the local thermodynamic phonon population with polarization p and wave vector $\mathbf{K}$ described by the Bose-Einstein distribution function

$$\langle n_{\mathbf{K},p} \rangle = \frac{1}{\exp\left(\frac{\hbar\omega}{k_B T}\right) - 1}. \tag{3}$$

E is the material volumic energy. It is obtained by summation in Eq. (2) of each quantum $\hbar\omega$ over the two polarizations for transverse, longitudinal, and optical modes of phonon propagation. Assuming that the phonon wave vectors are sufficiently dense in the $\mathbf{K}$ space, the summation over $\mathbf{K}$ can be replaced by an integral. Moreover, using $D_p(\omega)$, the phonon density of state, we can achieve the integration in the frequency domain. This two modifications yield

$$E = \sum_p \int_\omega \left(\langle n_{\omega,p} \rangle + \frac{1}{2} \right) \hbar\omega D_p(\omega) g_p d\omega, \tag{4}$$

with $D_p(\omega)d\omega$ the number of vibrational modes in the frequency range $[\omega, \omega + d\omega]$ for polarization p and g_p the degeneracy of the considered branch. In the case of an isotropic three-dimensional crystal $(V = L^3)$ we have[36]

$$D_p(\omega)d\omega = \frac{d\mathbf{K}}{(2\pi/L)^3} = \frac{VK^2 dK}{2\pi^2}. \tag{5}$$

The 1/2 term in Eq. (2) is the constant zero point energy which does not participate to the energy transfer in the material, therefore it has been suppressed. Using the group velocity definition, Eq. (4) might be rewritten

$$E = V \sum_p \int_\omega \left[\frac{\hbar\omega}{\exp\left(\frac{\hbar\omega}{k_B T}\right) - 1} \right] \frac{K^2}{2\pi^2 v_g} g_p d\omega. \tag{6}$$

The numerical scheme we are going to present is mainly based upon energy considerations. The previous expression Eq. (6) will be also used to estimate the material temperature by means of a numerical inversion.

C. Dispersion curves

Only a few studies on that topic take into account dispersion. Indeed, frequency dependence makes calculations longer, accounting for velocity variation. However, realistic simulation of phonon propagation through the crystal must take into account interaction between the different branches. Here optical phonons are not considered because of their low group velocity: they do not contribute significantly to the heat transfer. These modes can actually contribute indirectly through the interaction with other modes such as the acoustic modes. By modifying their relaxation times, they can inflence the total thermal conductivity of the material. Nevertheless, in this work, we did not consider this phenomenon. Consequently only transverse and longitudinal branches of silicon and germanium are presented here (Fig. 1). We have made the common isotropic assumption for wave vectors and consider the [001] direction in $\mathbf{K}$ space. For silicon, we used data obtained from a quadratic fit,[31] whereas germanium experimental curves[37] have been fitted by cubic splines. Phonon group velocity has then been extracted from this data. Note that in silicon and germanium, two acoustic branches have been considered. The transverse branch is degenerated $(g_T = 2)$ whereas the longitudinal branch is non-degenerated $(g_L = 1)$.

III. MONTE CARLO METHOD

The Monte Carlo technique has been widely used in order to solve transport equations. In the heat transfer field, Monte Carlo solutions of radiative transfer equation are often considered as reference benchmarks. The method accuracy only lies on the number of samples used. Among others, the main advantages of this method are

- the simple treatment of transient problems,

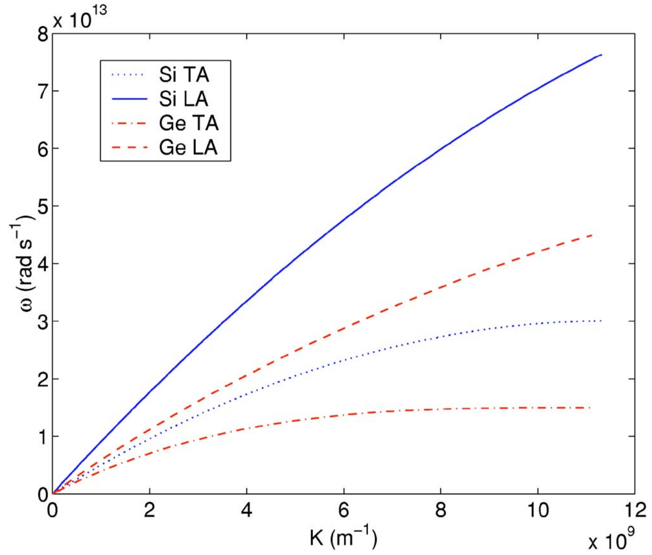

FIG. 1. (Color online) Phonon dispersion curves for silicon and germanium in the first Brillouin zone, $\mathbf{K}_{\max\ \mathrm{Si}}=1.1326\times10^{10}\ \mathrm{m}^{-1}$ and $\mathbf{K}_{\max\ \mathrm{Ge}}=1.1105\times10^{10}\ \mathrm{m}^{-1}$.

- the ability to consider complex geometries, and
- the possibility to follow independently each scattering process (for instance, phonon-phonon, phonon-impurity, and phonon-boundary processes).

The main drawback is computational time. However, this method remains a good choice between deterministic approaches such as the discrete ordinates method (DOM) or ”exact solutions” such as those provided by molecular dynamics which is limited to very small structures.

A. Simulation domain and boundary conditions

As it was said before, the geometry of the studied material does not matter. Here, a simple cubic cells stack (Fig. 2) is considered since it can be readily related to the plane wall geometry commonly used in thermal problems. Cylindrical cells or multidimensional stacks can also be considered in order to model nanowires or real semi-conductors.

Concerning boundary conditions, we assume that the lateral walls of the cells (in x and y directions) are specularly reflecting in most of the simulation cases. This means that walls are adiabatic and perfectly smooth. Note also that in that case, the dimension in the x and y directions should not change the result in the simulation. Indeed, when reflection is specular on the lateral cells boundaries, the momentum is preserved in the z direction. The heat flux and the temperature along z should thus not be affected. At both ends of the medium, temperature is assumed to be constant. Therefore, energy in the first and the last cells is calculated from equilibrium distribution functions. Incoming phonons in these cells are thermalized at each time step. Consequently theses cells act as blackbodies.

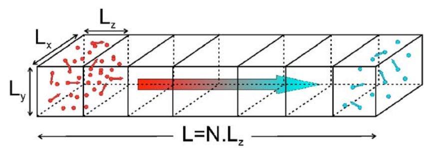

FIG. 2. (Color online) Studied model. Phonon location, energy, and velocity are randomly chosen in each cell according to dispersion curves and local temperature.

At this stage, an important point is the choice of the three discretizations: temporal, spatial, and spectral. Spatial discretization is directly related to the material geometry: usually cells length are about $L_z \sim 100$ nm for micrometric objects and can be smaller in the case of thin films or nanowires, for instance. The time step choice depends on two parameters: the cell size and the group velocity at a given frequency. In order to consider all scattering events and to avoid ballistic jump over several cells, we state that the time step must be lower than $\Delta t < L_z / V_g^{\max}$.

The spectral discretization is uniform; we used $N_b = 1000$ spectral bins in the range $[0, \omega_{\mathrm{LA}}^{\max}]$. We have checked that larger discretizations do not increase the result accuracy.

B. Initialization

The first step of the simulation procedure, once medium, geometry, and mesh have been chosen, is to initialize the state of phonons within each cell describing the material. Hence, the number of phonons present in each cell is required. It will be obtained considering the local temperature within the cell and using a modified expression of Eq. (6). In this equation, energy is given for all the quanta $\hbar\omega$ associated to a spectral bin. Therefore, it can be rewritten to give the total number of phonons in a cell as

$$N = V \sum_{p=\mathrm{TA,LA}} \sum_{b=1}^{N_b} \left[\frac{1}{\exp\left(\frac{\hbar \omega_{b,p}}{k_B T}\right) - 1} \right] \frac{K_{b,p}^2}{2\pi^2 v_{gb,p}} g_p \Delta\omega. \qquad (7)$$

The number of phonons obtained with Eq. (7) is usually very large, for instance in a 10 nm silicon cube at 300 K, N can be estimated around 5.45×10^5. In the case of nanoscale structures, direct simulations can be achieved if the temperature is relatively low. In the case of microscale samples or multidimensional cell stacking, a weighting factor shall be used to achieve Monte Carlo simulations. Hence, Peterson's[33] technique has been used. The actual number of phonons N is divided by a constant weight W in order to obtain the number of simulated phonons $N^\star$

$$N^\star = \frac{N}{W}. \qquad (8)$$

In our simulations W's value is set around $W \sim 10^4$ for micrometric structures, in order to preserve accuracy.

During the initialization process, a temperature step is prescribed in the medium. The first cell is raised to the hot temperature T_h, the last to the cold one T_c. All the phonons in the intermediate boxes are also at T_c. Associated theoretical energy in the whole structure is obtained from Eq. (6). This energy should match the calculated energy $E^\star$ within all the cells, written into the following form:

$$E^\star = \sum_{c=1}^{N_{\text{cell}}} \sum_{n=1}^{N^\star} W \times \hbar \omega_{n,c}. \tag{9}$$

As a consequence, during the initialization, phonons should be added by packs of W at a given frequency, sampled from a normalized number density function F. According to Mazumder and Majumdar's work,[34] this function is constructed doing the cumulative summation of the number of phonons in the ith spectral bin over the total number of phonons Eq. (7):

$$F_i(T) = \frac{\sum_{j=1}^{i} N_j(T)}{\sum_{j=1}^{N_b} N_j(T)}. \tag{10}$$

In this process, a random number R is drawn (all the random numbers discussed here check $0 \leqslant R \leqslant 1$) and the corresponding value F_i gives the frequency ω_i, knowing that the $F_{i-1} \leqslant R \leqslant F_i$ location is achieved with a bisection algorithm. The actual frequency of the phonon is randomly chosen in the spectral interval prescribing

$$\omega_i = \omega_{0,i} + (2R-1)\frac{\Delta\omega}{2}, \tag{11}$$

where $\omega_{0,i}$ is the central frequency of the ith interval.

Once the frequency is known, the polarization of the phonon has to be determined. It can belong to the TA or LA branch with respect to the Bose-Einstein distribution and the density of states. For a given frequency ω_i, the number of phonons on each branch are $N_{\text{LA}}(\omega_i) = \langle n_{\text{LA}}(\omega_i)\rangle D_{\text{LA}}(\omega_i)$ and $N_{\text{TA}}(\omega_i) = 2 \times \langle n_{\text{TA}}(\omega_i)\rangle D_{\text{TA}}(\omega_i)$, where the density of states are calculated with Eq. (5) in which the relation between ω and K are taken from the dispersion curves. The associated probability to find a LA phonon is expressed as

$$P_{\text{LA}}(\omega_i) = \frac{N_{\text{LA}}(\omega_i)}{N_{\text{LA}}(\omega_i) + N_{\text{TA}}(\omega_i)}. \tag{12}$$

A new random number R is drawn: if $R < P_{\text{LA}}(\omega_i)$, the phonon belongs to the LA branch, otherwise it is a transverse one.

The knowledge of the frequency and the polarization leads to the estimation of the phonon group velocity and the phonon wave vector merely using the dispersion curves and their derivatives. Assuming isotropy within the crystal, the direction $\mathbf{\Omega}$ is obtained from two random numbers R and R' randomly distributed between 0 and 1. Indeed, chosing a direction in 3D consists in chosing two angles (θ, ϕ) which are the spherical coordinates angles. Moreover, these angles have to be chosen so that the corresponding directions are uniformly distributed in the 4π full space solid angle. The elementary solid angle is $d\Omega = \sin\theta d\theta d\phi = -d(\cos\theta) d\phi$ so we see that $\cos\theta$ has to be uniformly distributed between -1 and 1 and ϕ beteween 0 and 2π. Hence $\mathbf{\Omega}$ is written as

$$\mathbf{\Omega} = \begin{cases} \sin\theta\cos\phi \\ \sin\theta\sin\phi \\ \cos\theta \end{cases} \tag{13}$$

where $\cos\theta = 2R - 1$ and $\phi = 2\pi R'$.

The last operation of the initialization procedure is to give a random position to the phonon within the cell. In the grid previously considered, location of the nth phonon in the cell c, whose lengths are L_x, L_y, and L_z, is

$$\mathbf{r}_{\text{n,c}} = \mathbf{r}_{\text{c}} + L_x R\mathbf{i} + L_y R'\mathbf{j} + L_z R''\mathbf{k} \tag{14}$$

where $\mathbf{r}_{\text{c}}$ is the coordinates of the cell and R, R', and R'' are three random numbers.

C. Drift

Once the initialization stage is achieved, phonons are allowed to drift inside the nanostructure. Considering the time step Δt and their velocities, each phonon position is updated: $\mathbf{r}_{\text{drift}} = \mathbf{r}_{\text{old}} + \mathbf{v}_{\text{g}}\Delta t$. In the case of shifting outside of the lateral boundaries (in $\mathbf{i}$ and $\mathbf{j}$ directions), the phonon is specularly reflected at the wall. In the case of diffuse reflection with a particular degree d ($0 \leqslant d \leqslant 1$, $d=0$ purely specular, $d=1$ purely diffuse) a random number R is drawn. When R is lower than d a new phonon propagation direction is calculated using Eq. (13).

When a phonon reaches the bottom ($z_{\min}$) or the top ($z_{\max}$) of a cell, it is allowed to carry on its way in the previous or next cell, respectively. As a result, it is going to modify the cell energy and by extension its local temperature. At the end of the drift phase, the actual energy $\widetilde{E^\star}$ is computed in all the cells using Eq. (9). Then, the actual temperature $\widetilde{T}$ is obtained with Eq. (6) doing a Newton-Raphson inversion.[38] Phonons drifting in the first and last boxes are thermalized to the cold or hot temperature in order to keep boundary cells acting as blackbody sources.

D. Scattering

In the Monte Carlo simulation, the scattering process has been treated independently from the drift. The phonon-phonon scattering aims at restoring local thermal equilibrium in the crystal since it changes phonon frequency. Collisions with impurities or crystal defects as well as boundary scattering do not change frequency but solely the direction $\mathbf{\Omega}$. These last phenomena are significant when low temperatures are reached and the phonon mean free path becomes large. In the present study we do not consider impurity and defect scattering for calculation. Besides, the bulk hypothesis is assumed, there is no boundary scattering. The phonons are specularly reflected at the side limits. Hence, only three-phonon interactions have been considered.

As already said before, there are two kinds of three-phonon processes: normal processes (N) which preserve momentum and Umklapp processes (U) which do not preserve momentum by a reciprocal lattice vector. These two mechanisms have consequences on the thermal conductivity of the crystal. When the temperature is sufficiently high ($T \gtrsim T_{\text{Debye}}$), U processes become significant and directly modify heat propagation due to the resistivity effect on energy transport. On the other hand, normal scattering also affects heat transfer since it modifies frequency distribution of the phonons. For phonons described by $(p,\omega,\mathbf{K})$ and $(p',\omega',\mathbf{K}')$ scattering to $(p'',\omega'',\mathbf{K}'')$, the following relations are checked

$$\text{energy:}\quad \hbar\omega + \hbar\omega' \leftrightarrow \hbar\omega'',$$

$$N \text{ processes:}\quad \mathbf{K}+\mathbf{K}' \leftrightarrow \mathbf{K}'',$$

$$U \text{ processes:}\quad \mathbf{K}+\mathbf{K}' \leftrightarrow \mathbf{K}''+\mathbf{G}, \tag{15}$$

where **G** is a lattice reciprocal vector. Scattering also involves polarization in the way that acoustic transverse and longitudinal phonons can interact. According to Srivastava,[39] for N and U processes different combinations are possible:

$$N \text{ and } U \text{ processes:}$$

$$\mathrm{T}+\mathrm{T} \rightleftharpoons \mathrm{L},\quad \mathrm{L}+\mathrm{T} \rightleftharpoons \mathrm{L}, \text{ and } \mathrm{T}+\mathrm{L} \rightleftharpoons \mathrm{L},$$

$$N \text{ processes only:}\quad \mathrm{T}+\mathrm{T} \rightleftharpoons \mathrm{T} \text{ and } \mathrm{L}+\mathrm{L} \rightleftharpoons \mathrm{L}. \tag{16}$$

For the N processes only, all the participating phonons must be collinear to achieve scattering. Usually these interactions are neglected.

Direct simulation of phonons scattering is an awkward challenge. With Monte Carlo simulations, it is possible to estimate phonon collisions with neighbors as in the gas kinetic theory calculating a three-particle interaction cross section. However, in the present study, the frequency discretization might not be sufficiently thin to assess every three-phonon processes. Thus the collisional process is treated in the relaxation time approximation. Several studies on that topic have been carried out since the early work of Klemens;[15] a detailed paper of Han and Klemens[14] recalled them.

Relaxation times τ have been proposed for several crystals. They depend on the scattering processes, the temperature, and the frequency. Holland's work on silicon[18] and the recent study of Singh for germanium[40] provide various τ values. The independence of the scattering processes is used to consider a global three-phonon inverse relaxation time accounting for N and U processes τ_{NU}. It has been obtained using the Mathiessen rule ($\tau_{NU}^{-1}=\tau_N^{-1}+\tau_U^{-1}$).

In order to be implemented in the Monte Carlo simulation, the scattering routine requires an associated collision probability P_{scat}. This one is derived saying that the probability for a phonon to be scattered between t and $t+dt$ is dt/τ. Thus,

$$P_{\mathrm{scat}} = 1 - \exp\left(\frac{-\Delta t}{\tau_{NU}}\right). \tag{17}$$

A random number R is drawn; if $R<P_{\mathrm{scat}}$, the phonon is scattered. As a result, new frequency, polarization, wave vector, group velocity, and direction have to be resampled with respect of energy and momentum conservation. Relaxation times are temperature and frequency dependent. For each simulated phonon considered τ_{NU} is calculated at every time step.

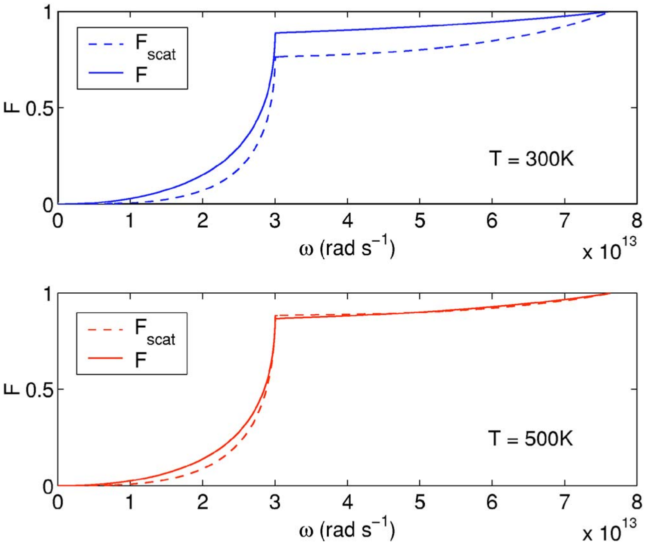

FIG. 3. (Color online) Normalized number density function in silicon with and without P_{scat} correction.

In previous studies on that topic,[33,34] the frequency sampling after collision was achieved from the normalized number density function F at the actual temperature $\widetilde{T}$ of the cell obtained at the end of the drift procedure. In this approach the actual energy after the scattering stage is usually different from the "target" one obtained with temperature $\widetilde{T}$. Hence a subsequent "creation/destruction" scheme is necessary to ensure energy conservation. In fact, in the preceding procedure at thermal equilibrium, the probability of destroying a phonon of frequency ω and polarization p is different from the probability of creating this phonon. This means that the Kirchhoff law (creation balances destruction) is not respected. In order to create phonons at the same rate they are destroyed at thermal equilibrium, the distribution function used to sample the frequencies of the phonons after scattering has to be modulated by the probability of scatterring. So we define a new distribution function

$$F_{\mathrm{scat}}(\widetilde{T}) = \frac{\sum_{j=1}^{i} N_j(\widetilde{T}) \times P_{\mathrm{scat}\ j}}{\sum_{j=1}^{N_b} N_j(\widetilde{T}) \times P_{\mathrm{scat}\ j}}. \tag{18}$$

Taking into account the scattering probability in the distribution function F_{scat} ensures that a destructed phonon on both transverse and longitudinal branches can be resampled with a not too weak energy as it can be seen in Fig. 3.

According to the described simulation procedure after the initialization step, phonons in cell c are described by $[T_c, F(T_c), N^{\star}(T_c), E^{\star}(T_c)]$. They are allowed to drift and the state of cell c before scattering is $[\widetilde{T}_c, F(T_c), N'^{\star}(\widetilde{T}_c), E'^{\star}(\widetilde{T}_c)]$. Then three-phonons collisions occur and change energy by frequency resetting of the colliding phonons (using the distribution function F_{scat}, leading to the final state $[\widetilde{T}_c,\ F_{\mathrm{scat}}(\widetilde{T}_c),\ N'^{\star}(\widetilde{T}_c),\ E''^{\star}(\widetilde{T}_c)]$). Hence energy can be expressed as

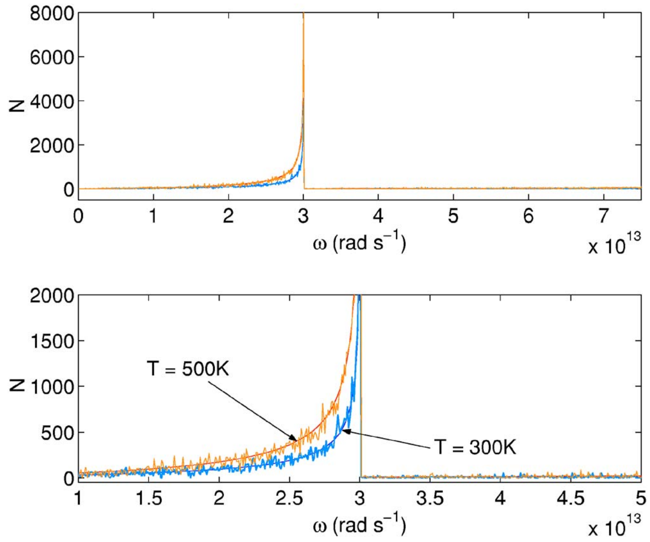

FIG. 4. (Color online) Frequency spectra at 300 K and 500 K for silicon.

$$E''^{\star} = \underbrace{\sum_{i=1}^{N'^{\star}_{\mathrm{scat}}} \hbar\tilde{\omega}i}_{\Rightarrow F_{\mathrm{scat}}(\tilde{T}_c)} + \underbrace{\sum_{i=1}^{N'^{\star}-N'^{\star}_{\mathrm{scat}}} \hbar\omega_i}_{\Rightarrow F(T_c)} \qquad (19)$$

Furthermore the number of colliding phonons can simply be expressed as $N'^{\star}_{\mathrm{scat}}(\tilde{T}_c)=P_{\mathrm{scat}}\times N'^{\star}(\tilde{T}_c)$. One then sees that, if we want to preserve energy at thermal equilibrium, the new normalized number density function F_{scat} must take into account this collisional probability. Energy conservation during Monte Carlo simulation might be noticed from frequency distribution (Fig. 4, which matches the theoretical distribution given by Eq. (7)].

Concerning momentum conservation, the task is harder to address since the Monte Carlo process considers phonons one by one. Consequently triadic N or U interactions cannot be rigorously treated. In a first approach, we propose the following procedure to take into account the fact that U processes contribute to the thermal resistance whereas the N processes do not. When the phonons scatter through a U process, their directions after scattering are randomly chosen as in the initialization procedure. Therefore, these phonons are randomly scattered and contribute to the diffusion of heat. On the contrary, it is assumed that scattering phonons experiencing an N process do not change their propagation direction $\mathbf{\Omega}$.

Statistically, for a given temperature and frequency, the phonons are destroyed by scattering at the same rate they appear. A phonon which scatters has a great chance to be replaced in the computation by a phonon of a near frequency. Therefore, by this treatment, the N processes "approximately" preserve momentum. Nevertheless, a more accurate treatment should be done in order to respect exactly the momentum in the N processes. For a plane-parallel geometry, it seems possible to guarantee the momentum conservation in a single direction.

In fact, the relaxation time estimation[14] states that there is a frequency limit ω_{limit} for the transverse acoustic branch. ω_{limit} actually corresponds to $\mathbf{K}=\mathbf{K}_{\mathrm{max}}/2$. Below this limit frequency, there are no U processes. On the other hand, for $\omega > \omega_{\mathrm{limit}}$, N processes are no longer considered and the propagation direction must be resampled in the case of a collision. In what concerns the longitudinal acoustic branch, there is no limit frequency. According to Holland[18] only N processes exist. However, applying this assumption implies that momentum has to be conserved for each scattering event involving a LA phonon. This leads to thermal conductivity values higher than the theoretical ones for temperatures between 100 K and 250 K. In order to ensure a more realistic momentum conservation we set that half of the colliding phonons keep their original $\mathbf{\Omega}$, and the others (U processes) are directionally resampled.

IV. RESULTS AND DISCUSSION

Different kinds of simulations have been performed so as to check the computational method. Tests in both diffusion and ballistic regimes are carried out for silicon and germanium. Moreover, if small thermal gradients are considered, one can estimate the thermal conductivity k from the heat flux through the structure. This has been realized for Si and Ge between 100 K and 500 K.

Knowing that the conductivity varies with temperature according to a power law in the case of Si and Ge for T greater than 100 K, it is obvious that a large thermal gradient applied to our media should not bring a purely linear solution. Hence simulations in this specific case have been done. We will see that our model correctly predicts the steady-state regime when compared to the steady-state analytical solution.

Eventually, we studied size effects on thermal behavior of nanostructures. It appears that the ballistic regime can be retrieved at room temperature when the sample size is close to the nanometer scale.

A. High-temperature transient calculations

Concerning high-temperature transient calculations, the simulated case is described by the following parameters:

- hot and cold temperatures: $T_h=310$ K and $T_c=290$ K,
- medium geometry: stack of 40 cellules ($L_x=L_y=5\times10^{-7}$ m,$L_z=5\times10^{-8}$ m),
- time step and spectral discretization: $\Delta t=5$ ps and $N_b=1000$ bins, and
- weighting factor: $W=3.5\times10^{4}$ for Si and $W=8\times10^{4}$ for Ge.

Both materials were tested. Germanium calculation results are presented here (Fig. 5). In order to assess the Monte Carlo solution, transient theoretical comparison exists in the case of the Fourier limit. Nevertheless, it requires that the thermal diffusivity α remains constant. In the chosen temperature range, according to the IOFFE database,[41] Ge thermal diffusivity is equal to $\alpha=0.36\times10^{-4}$ m^2 s^{-1}.

The considered test case has been described in Özişik's book[42] on the heat conduction equation. Within the described structure heat transfer is along the z axis and analytical so-

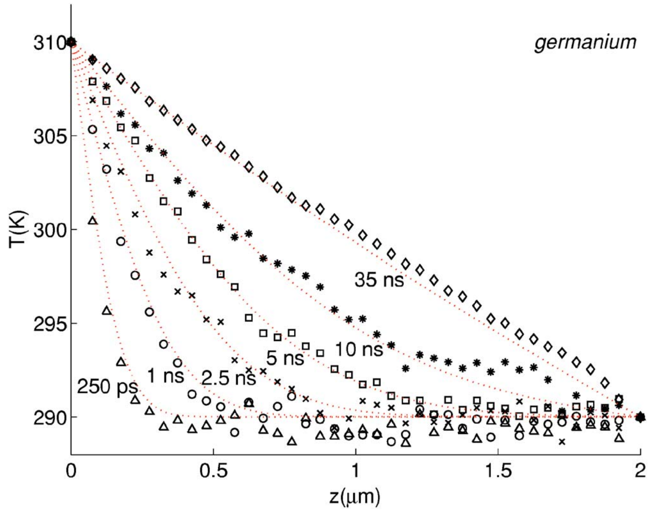

FIG. 5. Transient temperature in Fourier's regime for germanium and comparison with the analytical solution of heat conduction equation with a constant thermal diffusivity ($\alpha_{\mathrm{Ge}} = 0.36 \times 10^{-4}\ \mathrm{m}^2\,\mathrm{s}^{-1}$) (dotted curves).

lution for a one-dimensional medium could be obtained from an integral transform. Temperature distribution in the slab is given by an infinite sum that requires enough terms in the case of short time calculation. However, a simpler analytical solution might be obtained with Laplace's transform

$$\frac{T(z,t)-T(L,t)}{T(0,t)-T(L,t)} = \left[\operatorname{erfc}\left(\frac{z}{2\sqrt{\alpha t}}\right) - \operatorname{erfc}\left(\frac{2L-z}{2\sqrt{\alpha t}}\right) + \operatorname{erfc}\left(\frac{2L+z}{2\sqrt{\alpha t}}\right)\right], \tag{20}$$

with erfc the complementary error function. The theoretical solution is only valid for short time and its accuracy is better than 1% if the Fourier number ($\mathrm{Fo} = \alpha t / L^2$) checks $\mathrm{Fo} \leqslant 0.7$. In the case of a 2 μm germanium slab it leads to $t \leqslant 78$ ns, which is large enough to reach steady state.

The calculated values have been obtained from ten simulations being averaged (Fig. 5), the random number seed being reset for each computations. The Monte Carlo model's ability to predict correctly temperature from the first moments till steady state is clearly illustrated. The remaining noise can be reduced with lower values of W weighting factor. The diffusion regime is obtained after 30 ns. Similar results are obtained for silicon, however the simulated slab has to be larger ($L=4$ μm) because ballistic effects are observed near the cold limit. This point will be discussed later.

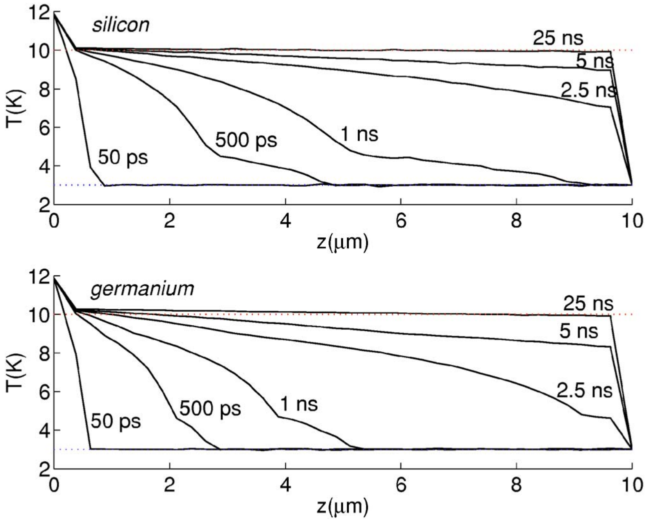

FIG. 6. (Color online) Transient temperature in the ballistic regime for silicon and germanium.

B. Low-temperature transient calculations

For low temperatures, heat transport inside the slab is different since phonon interactions change. In this case U collisions are negligible and the only resistive processes are assigned to impurities, defects, and boundary scattering. These phenomena have to be carefully assessed in the case of thermal conductivity estimation below 100 K. In fact, for very low temperatures the phonon mean free path grows and becomes larger than the structure length. Hence, phonons can travel from hot to cold extremities without colliding. This is the ballistic regime similar to the one observed with photons exchanged between two black plates at different temperatures.[43] In this peculiar case temperature in steady state is equal to the following constant value:

$$T_{\mathrm{ballistic}} = \left[\frac{T_h^4 + T_c^4}{2}\right]^{1/4} \tag{21}$$

The simulation case parameters are

- hot and cold temperatures: $T_h = 11.88$ K, $T_c = 3$ K, and $T_{\mathrm{ballistic}} = 10$ K;
- medium geometry: stack of 40 cellules ($L_x = L_y = 5 \times 10^{-7}$ m, $L_z = 2.5 \times 10^{-7}$ m);
- time step and spectral discretization: $\Delta t = 5$ ps and $N_b = 1000$ bins; and
- weighting factor: $W=20$ for Si and $W=30$ for Ge.

Results for silicon and germanium (Fig. 6) give the expected results for the ballistic limit. It can be noticed that the current representation exhibits an artificial link between black boundaries and the first medium cell due to the spatial discretization.

It can be seen that hot phonons do not fly straight toward the cold limit. More than 1 ns is necessary to heat the last cell in the case of silicon. This is in agreement with velocities prescribed by dispersion curves. Heat propagation in germanium is slower since phonon group speed is also lower. Note also that in both materials, the temperature seems to propagate at two different velocities. For example, the 500 ps and 1 ns temperature curves exhibit two components. The fastest one propagates at the longitudinal wave velocity whereas the slowest is traveling at the transverse wave velocity. Results at low temperatures obtained with our method have already been predicted by Joshi and Majumdar[24] in similar cases, who applied successfully the equation of phonon radiative transfer (EPRT) in the ballistic regime.

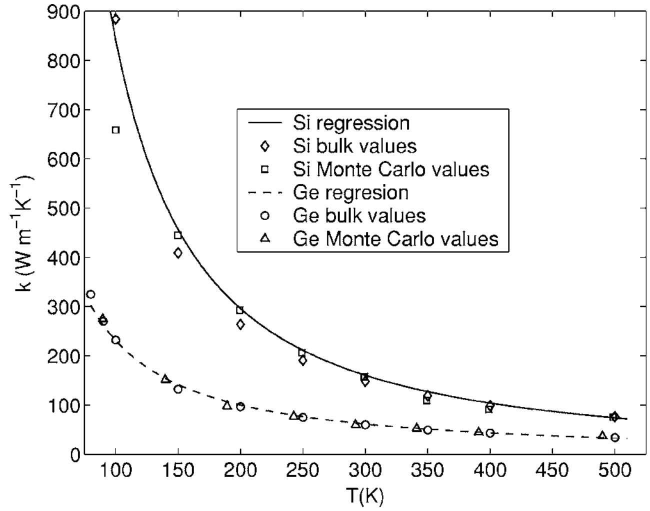

FIG. 7. Silicon and germanium thermal conductivities; comparison between bulk theoretical values and Monte Carlo calculated values.

C. Si and Ge thermal conductivities

There are several ways to perform the thermal conductivity calculation of a semiconductor. Among these techniques, Holland's method[18] based on phonons kinetic theory was largely employed. Molecular dynamic simulations can also be used to obtain k. In the present study thermal conductivity has been determined knowing the heat flux (phonon energy transport) through the medium for a given thermal gradient directly applying Fourier's law. As in Mazumder's work,[34] the temperature difference between hot and cold extremities is set to 20 K so as to determine average conductivities. The phonon heat flux is calculated along the z axis according to the following relation:

$$\phi = \sum_{n=1}^{N^\star} W\hbar\omega_n \mathbf{v}_{gn} \cdot \mathbf{k}. \tag{22}$$

Simulations have been carried out between 100 K and 500 K (Fig. 7) on 2 μm thick samples.

Comparison of the Monte Carlo calculated conductivities is achieved with bulk data. Solid and dashed curves are linear power law regression of theoretical data in the considered thermal range. These values are used in next analytical calculations. We have appraised for $200\ \mathrm{K} \leqslant T \leqslant 600\ \mathrm{K}$;

$$k_{\mathrm{Si}}(T) = \frac{\exp(12.570)}{T^{1.326}},$$

$$k_{\mathrm{Ge}}(T) = \frac{\exp(10.659)}{T^{1.150}}. \tag{23}$$

For germanium a very good agreement is obtained with bulk values in the whole temperature domain. The maximum relative error is under 8%. In this case, at 100 K, the phonon mean free path is lowered to the micrometer according to Dames.[44] Consequently the stucture size is large enough to assume the acoustic thick limit. Furthermore, this calculation benefits from recent relaxation time estimation, which has been fixed with a good accuracy.[40] The influence of these factors on calculated conductivity is usually strong. Silicon results are also close to the bulk ones until 150 K where the relative error is equal to 7%. For lower temperatures, discrepancy between theory and simulation increases. This gap can be assigned to size effects since the phonon mean free path grows when temperature is falling. Here, it becomes similar to the slab size. Yet, if we refer to Asheghi's[45] work on thin films, thermal conductivity, at temperatures below 100 K, significantly decreases in comparison with bulk property due to stronger reduction of phonon mean free path by boundaries. Actually, for pure 3 μm silicon film, thermal conductivity is close to 600 W m^{-1} K^{-1} at 100 K.[45] This value is comparable to the 658 W m^{-1} K^{-1} obtained for our 2 μm film by Monte Carlo simulation.

D. Effect of nonlinear conductivity

In this fourth part, transient simulations with samples heated under a large thermal step have been conducted. The purpose of such calculations was to underline the model capacity to correctly predict steady state when medium properties $[k(T)]$ vary with temperature. In the previous part thermal conductivities of both bulk materials have been estimated with a power law [Eq. (23)]. Hence, the analytic solution for temperature profile within a slab can be easily determined in steady state by the resolution of a first-order differential equation as

$$T(z)_{\text{Steady state}} = \left[\left(\frac{z}{L}\right)T_c^{(\gamma+1)} + \left(1 - \frac{z}{L}\right)T_h^{(\gamma+1)}\right]^{1/(\gamma+1)}, \tag{24}$$

where conductivity can be written as $\lambda(T) = C \times T^{\gamma}$.

In order to avoid boundary effects in the case of silicon, a 4 μm thick sample, with larger cells ($L_z = 1 \times 10^{-7}$ m), is used. The initial geometry is kept for the germanium slab. Temperatures are now $T_h = 500$ K and $T_c = 250$ K. The time step remains equal to 5 ps. In both cases (Fig. 8) Monte Carlo simulations give a very good estimation of the steady-state behavior. Results are averaged over five computations on the last 1000 time steps (i.e., after 45 ns of elapsed time). At the cold limit of the germanium sample a weak deviation exists between simulation and theory. The relative error on temperature remains smaller than 1.5%, in this area. This mismatch could be assigned to boundary effects, associating diffusive and ballistic regimes near the limits as we will detail in the last part. It could also be due to the accuracy of the bulk thermal conductivity fitting at low temperatures.

Besides, inversion of such curves can theoretically provide the variation of k on a given thermal range, as long as the medium is in the acoustic thick limit.

E. Size effect on heat diffusion

From the previous calculations, it is obvious that the phonon mean free path modification with the temperature acts as a major factor in heat conduction. So, if the structure size is adjusted in order to match the mean free path at any temperature, ballistic phenomena should be observed. In this

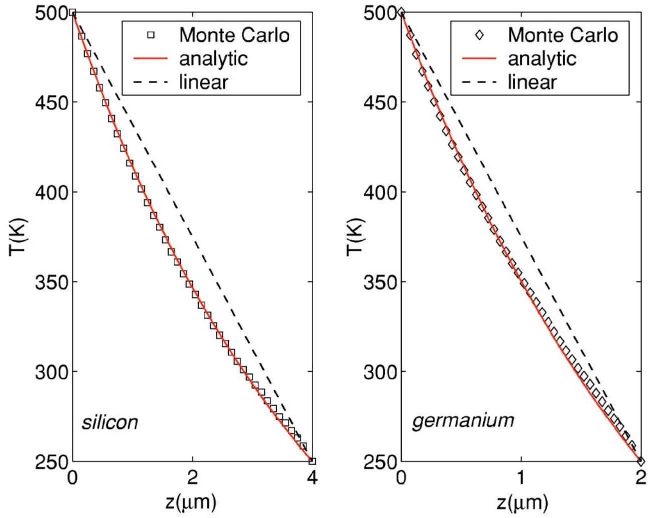

FIG. 8. (Color online) Steady-state temperature in Fourier's regime for silicon and germanium in the case of a large thermal gradient; comparison to the heat conduction equation analytical solution for temperature dependent conductivity.

study only silicon is used and the simulation parameters are

- hot and cold temperatures: $T_h=310$ K and $T_c=290$ K,
- number of cells: 40, and
- total length and time step $(L,\Delta t)$: (2 nm, 5×10^{-3} ps), (20 nm, 5×10^{-2} ps), (200 nm, 5×10^{-1} ps), (2 μm, 5 ps), and (4 μm, 5 ps).

Weighting parameters and lateral cell lengths are adjusted in order to keep approximately 18 000 phonons in each cell.

Temperature profiles when steady state is reached have been plotted for each sample versus adimensional length z/L. Comparison to diffusive and ballistic regime is displayed in Fig. 9. With the imposed boundary temperatures the ballistic limit is equal to $T_{\text{ballistic}}=300.5$ K.

In the case of structure length lower than 200 nm ballistic trend mixed to phonon diffuse transport is observed. The temperature profile gets closer to the ballistic limit for sample size around the nanometer scale. Nevertheless, this approximately represents ten atom layers and therefore might encounter the simulation limitation. On the contrary, in a silicon sample thicker than 4 μm, temperature reaches the Fourier's regime and can be similarly obtained with heat conduction equation at least cost.

V. CONCLUSIONS

An improved Monte Carlo scheme that allows transient heat transfer calculations at time and space nanoscales, on the basis of phonon transport, has been presented. This model accounts for phonon transitions between longitudinal and transverse acoustic branches and can be simply applied to several semiconductors if their dispersion relations are known. A particular attention has been paid to the energy and momentum conservation during collision process.

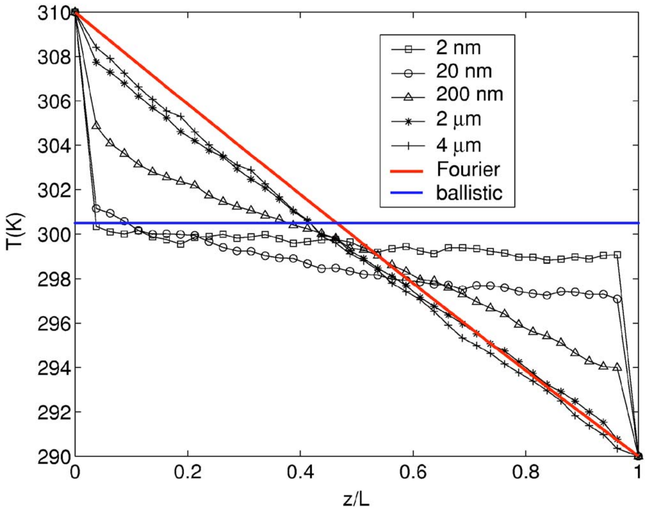

FIG. 9. (Color online) Steady-state temperature for silicon, influence of the slab thickness; comparison to the analytical solution in the diffusive and ballistic limits.

Numerical result forecasts have been successfully assessed in different heat transfer modes. In slab configuration, a good agreement was found for both extreme phonon motions which are the diffusive and ballistic ones. Bulk thermal conductivities of silicon and germanium have been numerically retrieved with a maximal error lower than 8%. Besides, our Monte Carlo model correctly predicts temperature profile in more peculiar situations, when strong thermal gradient or very small sizes are encountered.

Nevertheless some key points need to be refined. Among them the momentum conservation procedure might be improved, especially for one-dimensional applications. Also, a treatment of the optical phonons influence would improve our model. Indeed, according to the recent study of Narumanchi,[25] capacitive properties prediction need the optical phonons to be taken into account. This influence seems less critical for conductivity predictions in the studied temperature range.[13] Moreover, regarding the collision process, improvements might be expected. Using theoretical values of τ recalled by Han and Klemens,[14] direct calculation of phonon scattering relaxation time can be realized in each authorized spectral bin. Hence, a more realistic approach of three-phonon interactions should be achieved.

We are currently working on these improvements but also on other potential implementations of the method such as those related to the superlattices and the nanowires.

*Also at Laboratoire d'Énergétique et de Mécanique Théorique et Appliquée, Université Henri Poincaré, Nancy 1, 54506 Vandœuvre Cedex, France. Electronic address: David.Lacroix@lemta.uhp-nancy.fr

†Electronic address: karl.joulain@let.ensma.fr

‡Electronic address: denis.lemonnier@let.ensma.fr

[1] *International Technology Roadmap for Semiconductors*, URL http://public.itrs.net.

[2] P. Vettiger, G. Gross, M. Despont, U. Dreschler, U. Dürig, B. Gotsmann, W. Häberle, M. Lantz, H. Rothuizen, R. Stutz, and G. Binnig, IEEE Trans. Nanotechnol. **1**, 39 (2001).

[3] D. Cahill, W. Ford, K. Goodson, G. Mahan, A. Majumdar, H. Maris, R. Merlin, and S. Phillpot, J. Appl. Phys. **93**, 793 (2003).

[4] D. Polder and D. V. Hove, Phys. Rev. B **4**, 3303 (1971).

[5] J. J. Loomis and H. J. Maris, Phys. Rev. B **50**, 18517 (1994).

[6] J. Mulet, K. Joulain, R. Carminati, and J.-J. Greffet, Appl. Phys. Lett. **78**, 2931 (2001).

[7] A. Einstein, Ann. Phys. **17**, 549 (1905).

[8] J. Ziman, *Electrons and Phonons* (Oxford University Press, Oxford, 1960).

[9] S. Chandrasekhar, *Radiative Transfer* (Dover, New York, 1960).

[10] M. Modest, *Radiative Heat Transfer* (Academic Press, San Diego, 2003), 2nd ed.

[11] L. Landau and E. Lifshitz, *Physical kinetics: volume 10 (Course of theoretical physics)* (Pergamon Press, Oxford, 1981).

[12] A. Majumdar, J. Heat Transfer **115**, 7 (1993).

[13] D. Ecsedy and P. Klemens, Phys. Rev. B **15**, 5957 (1977).

[14] Y.-J. Han and P. G. Klemens, Phys. Rev. B **48**, 6033 (1993).

[15] P. Klemens, Proc. R. Soc. London, Ser. A **208**, 108 (1951).

[16] C. Herring, Phys. Rev. **95**, 954 (1954).

[17] J. Callaway, Phys. Rev. **113**, 1046 (1959).

[18] M. Holland, Phys. Rev. **132**, 2461 (1963).

[19] J. Waugh and G. Dolling, Phys. Rev. B **4**, 3303 (1971).

[20] C. Bhandari and G. Verma, Phys. Rev. **140**, A2101 (1965).

[21] G. Chen, J. Heat Transfer **119**, 220 (1997).

[22] K. Goodson, J. Heat Transfer **118**, 279 (1996).

[23] D. Lemonnier and M. Lallemand, Heat Technol. **18**, 63 (2000).

[24] A. Joshi and A. Majumdar, J. Appl. Phys. **74**, 31 (1993).

[25] S. Narumanchi, J. Heat Transfer **126**, 946 (2004).

[26] G. Chen, Phys. Rev. Lett. **86**, 2297 (2001).

[27] C. Jacobini and L. Reggiani, Rev. Mod. Phys. **55**, 645 (1983).

[28] M. V. Fischetti and S. E. Laux, Phys. Rev. B **38**, 9721 (1988).

[29] P. Lugli, P. Bordone, L. Reggiani, M. Rieger, P. Kocevar, and S. M. Goodnick, Phys. Rev. B **39**, 7852 (1989).

[30] M. V. Fischetti and S. E. Laux, Phys. Rev. B **48**, 2244 (1993).

[31] E. Pop, R. Dutton, and K. Goodson, J. Appl. Phys. **96**, 4998 (2004).

[32] E. Pop, R. Dutton, and K. Goodson, Appl. Phys. Lett. **86**, 082101 (2005).

[33] R. Peterson, J. Heat Transfer **116**, 815 (1994).

[34] S. Mazumder and A. Majumdar, J. Heat Transfer **123**, 749 (2001).

[35] N. Ashcroft and N. Mermin, *Solid State Physics* (Saunders College, Philiadelphia, 1976), international ed.

[36] C. Kittel, *Introduction to Solid State Physics* (John Wiley and Sons, Philadelphia, 2004).

[37] G. Nilson and G. Nelin, Phys. Rev. B **3**, 364 (1971).

[38] W. Press, B. Flannery, S. Teukolsky, and W. Vetterling, *Numerical Recipes, The Art of Scientific Computing* (Cambridge University Press, Cambridge, 1960).

[39] G. Srivastava, *The Physics of Phonons* (Adam Hilger, Bristol, UK, 1990).

[40] B. Singh, M. Roy, V. Menon, and K. Sood, J. Phys. Chem. Solids **64**, 2369 (2003).

[41] *Semiconductors on nsm*, URL http://www.ioffe.rssi.ru/SVA/NSM/Semicond/.

[42] M. N. Özişik, *Boundary Value Problems of Heat Conduction* (Dover Publications, New York, 1968).

[43] M. Heaslet and R. Warming, Int. J. Heat Mass Transfer **8**, 979 (1965).

[44] C. Dames and G. Chen, J. Appl. Phys. **89**, 682 (2003).

[45] M. Asheghi, K. Kurabayashi, R. Kasnavi, and K. Goodson, J. Appl. Phys. **91**, 5079 (2002).

Casimir force between designed materials : What is possible and what not

C. Henkel et K. Joulain

Europhysics Letters, vol 72, pp929–935 (2005)

EUROPHYSICS LETTERS 15 December 2005

Europhys. Lett., **72** (6), pp. 929–935 (2005)
DOI: `10.1209/epl/i2005-10344-3`

Casimir force between designed materials: What is possible and what not

C. Henkel[1] and K. Joulain[2]

[1] *Institut für Physik, Universität Potsdam - Germany*
[2] *Laboratoire d'Etudes Thermiques, Ecole Nationale Supérieure de Mécanique Aéronautique - Poitiers, France*

received 29 March 2005; accepted in final form 24 October 2005

PACS. `42.50.Pq` – Cavity quantum electrodynamics; micromasers.
PACS. `42.50.Lc` – Quantum fluctuations, quantum noise, and quantum jumps.
PACS. `78.67.-n` – Optical properties of low-dimensional, mesoscopic, and nanoscale materials and structures.

Abstract. – We establish strict upper limits for the Casimir interaction between multilayered structures of arbitrary dielectric or diamagnetic materials. We discuss the appearance of different power laws due to frequency-dependent material constants. Simple analytical expressions are in good agreement with numerical calculations based on Lifshitz theory. We discuss the improvements required for current (meta) materials to achieve a repulsive Casimir force.

Introduction. – The optical properties of materials that show both a dielectric and magnetic response, have recently attracted much attention (see [1] for a review). A number of striking phenomena like perfect lensing and a reversed Doppler effect have been predicted, and experimenters have begun to explore the large parameter space of structural units that can be assembled into artificial materials. Breakthroughs have been reported on the way towards designed susceptibitilies in the near-infrared and visible spectral range [2,3]. Quantum electrodynamics in meta materials has recently been explored with particular emphasis on left-handed or negative-index materials [4,5]. We discuss here to what extent the Casimir interaction between two meta material plates can be manipulated by engineering their magneto-dielectric response. Strict limits for the Casimir interaction are proven that apply to all causal and linear materials, including both bulk and multilayer structures. We illustrate these results by computations of the Casimir pressure, considering materials with frequency-dispersive response functions like those encountered in effective medium theories. We derive power law exponents and prefactors and find that a strongly modified Casimir interaction is possible in a range of distances around the resonance wavelength of the response functions. We give estimates for the required temperature range and structure size: it is not unreasonable to expect that improvements in fabrication and detection will allow for experimental observations.

One of the most striking changes to the Casimir interaction is a crossover to repulsion. This has been predicted previously for idealized magnetodielectric materials [6–8] and objects suspended in a liquid [9, 10]. In the latter case, repulsion has been observed experimentally with colloidal particles [11] and is also used in a recent proposal for measuring Casimir torques [12]. Casimir repulsion between mirrors separated by vacuum requires a strong magnetic response [7, 13] that hardly occurs in conventional ferromagnets [14, 15]. Indeed, to manipulate the Casimir force in the micrometer range and below, where it can be conveniently measured, the key challenge is to achieve a magnetic susceptibility at high frequencies, approaching the visible range. Now, there is a well-known argument due to Landau, Lifshitz, and Pitaevskii that $\mu(\omega) = 1$ in the visible [16]. This objection, however, only applies to materials whose magnetization is of atomic origin, where the magnetic susceptibility is $\chi_{\mathrm{m}} \sim (v/c)^2 \ll 1$. An array of split ring resonators with sub-wavelength size typically gives, on the contrary, $\chi_{\mathrm{m}} \sim (\omega/\vartheta)^2 f \sim 1$, where ϑ is the resonance frequency and f the filling factor [17, 18]. As we illustrate below, artificial materials that are structured on the sub-micron scale are promising candidates for a strongly modified Casimir interaction.

Lifshitz theory. – For two perfectly conducting plates held at zero temperature and separated by a distance d, Casimir derived a force per unit area given by $F_C = \pi^2 \hbar c/(240\, d^4)$ [19]. We use the convention that $F_C > 0$ corresponds to attraction. For linear media with complex, frequency-dependent material parameters, the force can be computed from Lifshitz theory [20]. This expression has been re-derived, for plates of arbitrary material and for multilayer mirrors, using different methods [21–31]. At finite temperature, it can be written in the form

$$F_L \;=\; 2k_B T \sum_{n=0}^{\infty}{}' \int\limits_{\xi_n/c}^{\infty} \frac{\mathrm{d}\kappa}{2\pi}\, \kappa^2 \sum_{\lambda} \left(\frac{\mathrm{e}^{2\kappa d}}{r_{\lambda 1} r_{\lambda 2}} - 1 \right)^{-1}, \tag{1}$$

where the sum is over the imaginary Matsubara frequencies $\omega_n = \mathrm{i}\xi_n \equiv 2\pi \mathrm{i} n k_B T/\hbar$ (the $n = 0$ term being multiplied by 1/2), and κ is related to the wave vector component perpendicular to the mirrors, $k_z = (\omega_n^2/c^2 - k_x^2 - k_y^2)^{1/2} \equiv \mathrm{i}\,\kappa$. The $r_{\lambda\alpha}$ (λ = TE, TM, α = 1, 2) are the reflection coefficients at mirror α for electromagnetic waves with polarization λ [22, 23]. For homogeneous, thick plates, they are given by

$$r_{\mathrm{TM}} \;=\; \frac{\varepsilon(\mathrm{i}\xi_n) c\kappa - \sqrt{\xi_n^2(\varepsilon(\mathrm{i}\xi_n)\mu(\mathrm{i}\xi_n) - 1) + \kappa^2 c^2}}{\varepsilon(\mathrm{i}\xi_n) c\kappa + \sqrt{\xi_n^2(\varepsilon(\mathrm{i}\xi_n)\mu(\mathrm{i}\xi_n) - 1) + \kappa^2 c^2}} \tag{2}$$

(exchange ε and μ for r_{TE}). The zeros of $D_\lambda \equiv \mathrm{e}^{2\kappa d}/(r_{\lambda 1} r_{\lambda 2}) - 1$ at real frequencies define the eigenmodes of the cavity formed by the two mirrors.

Strict limits. – To derive upper and lower limits for F_L, we use that the Kramers-Kronig relations [16] imply real and positive material functions at imaginary frequencies, $\varepsilon(\mathrm{i}\xi) \geq 1$, provided the material is passive (non-negative absorption $\operatorname{Im}\varepsilon(\omega) \geq 0$). As a consequence, the Fresnel formulas (2) imply $-1 \leq r_{\lambda\alpha} \leq 1$, and we find

$$-\frac{1}{\mathrm{e}^{2\kappa d} + 1} \leq \frac{1}{D_\lambda} \leq \frac{1}{\mathrm{e}^{2\kappa d} - 1} \tag{3}$$

with the stronger inequalities $0 \leq 1/D_\lambda \leq 1/(\mathrm{e}^{2\kappa d} - 1)$ holding for identical plates. In the latter case, the Casimir force is hence necessarily attractive. The inequalities (3) saturate for a perfectly conducting mirror facing a perfectly permeable one ($\varepsilon_1 = \infty$, $\mu_2 = \infty$, say), and for identical, perfectly reflecting mirrors, respectively. The resulting forces at zero temperature are [6, 20]

$$T = 0: \quad -\frac{7}{8} F_C \leq F_L \leq F_C. \tag{4}$$

In the high-temperature limit, we get similarly [32] $-\frac{3}{4} F_T \leq F_L \leq F_T \equiv \zeta(3) k_B T/(8\pi d^3)$ by keeping in eq. (1) only the $n = 0$ term in the sum.

Consider now a mirror made from layers of arbitrary passive materials. Reflection coefficients for such a system can be obtained recursively. For a layer "b" separating a medium "a" from a substrate "c", for example,

$$r_{abc} = \frac{r_{ab} + r_{bc}\,\mathrm{e}^{2\mathrm{i}k_b w}}{1 + r_{ab}r_{bc}\,\mathrm{e}^{2\mathrm{i}k_b w}}, \tag{5}$$

where r_{ab} (r_{bc}) describes the reflection from the interface ab (bc), respectively, and w is the layer thickness [33,34]. If the substrate c is a multilayer system itself, r_{bc} is the corresponding reflection coefficient. For the imaginary frequencies occurring in the Lifshitz expression (1), the wave vector in the layer is purely imaginary, $k_b = \mathrm{i}\,\kappa_b$, and single-interface coefficients are real (eq. (2)). From eq. (5), they remain real for multilayer mirrors. In addition, the mapping $r_{ab} \mapsto r_{abc}$ is a conformal one, and if $r_{bc}\,\mathrm{e}^{-2\kappa_b w}$ is real and $\in [-1,1]$, the interval $[-1,1]$ is mapped onto itself. For multilayer mirrors, we thus obtain again the inequalities $-1 \le r_\lambda \le 1$. This generalizes the limits of refs. [31,35] that are obtained only for layered dielectric mirrors, using transfer matrices.

Casimir interaction between metamaterials. – To illustrate these generally valid results, we focus on meta materials described by effective medium theory [1,17,18]. We adopt Lorentz-Drude formulas for ε and μ:

$$\varepsilon_\alpha(\mathrm{i}\,\xi) = 1 + \frac{\Omega_\alpha^2}{\omega_\alpha^2 + \xi^2}, \qquad \mu_\alpha(\mathrm{i}\,\xi) = 1 + \frac{\Theta_\alpha^2}{\vartheta_\alpha^2 + \xi^2}. \tag{6}$$

Regarding the permeability, we have taken the limit of weak absorption and computed $\mu(\mathrm{i}\,\xi)$ in terms of $\mathrm{Im}\,\mu(\omega)$ using the Kramers-Kronig relations. This is necessary to ensure high-frequency transparency of the medium. We denote in the following by Ω a typical resonance or plasma frequency occurring in eqs. (6). The corresponding wavelength, $\Lambda = 2\pi c/\Omega$, provides a convenient distance scale. Note that a (magnetic) resonance wavelength as short as $\sim 3\,\mu$m has already been achieved with material nanofabrication [3]. The key advantage of meta materials is that their electric and magnetic "plasma frequencies" Ω_α and Θ_α are fairly large as well: a value of $\Theta_\alpha \approx \vartheta_\alpha\sqrt{f} \le (c/a)\sqrt{f}$ is typical for a split-ring resonator array with period a and filling factor f [17]. This property is also necessary, of course, to achieve a left-handed medium ($\varepsilon_\alpha(\omega)$, $\mu_\alpha(\omega) < 0$ for some real frequencies). The magnetic plasma frequencies occurring in conventional ferromagnets are much smaller [14], and the impact on the Casimir interaction is weak, as reported recently [13].

In the plots shown below, the Casimir pressure is normalized to $\hbar\Omega/d^3$ (see after eq. (7)). In order of magnitude, this corresponds to $10^4\,\mathrm{pN\,mm^{-2}}/(\Lambda/\mu\mathrm{m})^4$ at a distance $d = \Lambda/2$. This can be measured with sensitive torsion balances [36,37] or cantilevers [38,39]. We plot in fig. 1 the result of a numerical integration of eq. (1), the curves corresponding to different material pairings. One sees that in all cases, the force satisfies the limits (4) that exclude the shaded areas. We observe that materials with negative index of refraction around Ω show a strongly reduced attraction (fig. 1(b)). This can be attributed to the reduced mirror reflectivity due to impedance matching. Casimir repulsion is achieved for some distances between mirrors made from different materials (fig. 1(c, d)). At short distance, *i.e.* $d \ll \Lambda/2\pi$, even these pairings show attraction with a power law $1/d^3$. Coating one mirror with a magnetic layer (fig. 1(c)), there is a sign change around the layer thickness w: for $\Lambda/2\pi \ll d \ll w$, the layer behaves like a thick plate, and its material parameters lead to repulsion. The layer can be ignored for $w \ll d$, and one recovers the attraction between the (identical) substrates. This is consistent with asymptotic analysis based on the reflection coefficient (5), as we outline below. Detailed

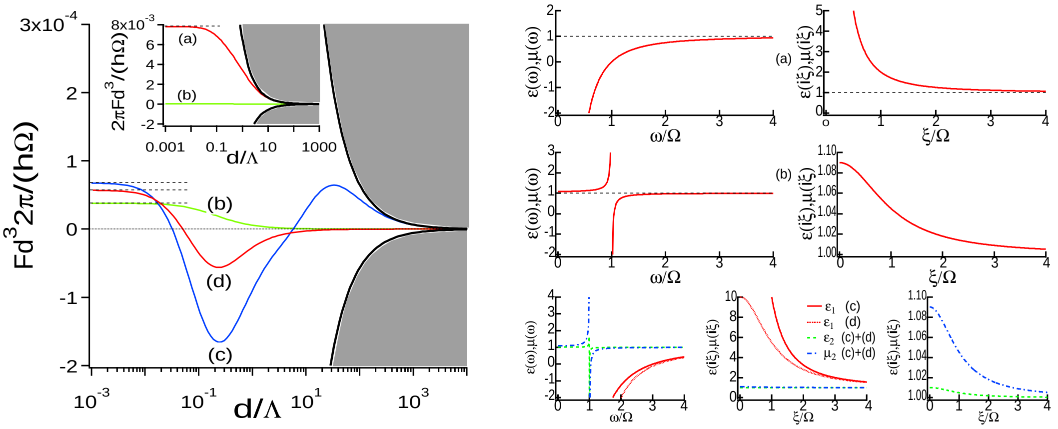

Fig. 1 – Casimir force between planar mirrors of different dispersive materials at zero temperature. Left: plot of the force per unit area, normalized to $\hbar\Omega/d^3$ *vs.* the plate separation scaled to $\Lambda \equiv 2\pi c/\Omega$. Here, Ω is a typical plasma or resonance frequency. Shaded areas: excluded by the inequalities (4). Dashed lines: short-distance asymptotics c_3/d^3 with coefficient (7), providing another upper limit for homogeneous mirrors. Right: material response functions along the real and imaginary frequency axis. Plots labeled (a) (inset): two identical non-magnetic Drude metals (in eq. (6), $\Omega_\alpha \equiv \Omega$, $\omega_\alpha = 0$, $\mu_\alpha(\xi) \equiv 1$, $\alpha = 1, 2$). Label (b): two identical left-handed meta materials with overlapping dielectric and magnetic resonances ($\Omega_\alpha \equiv 0.3\,\Omega$, $\omega_\alpha = \Omega$, $\Theta_\alpha = 0.3\,\Omega$, $\vartheta_\alpha = \Omega$). Label (c): two identical non-magnetic Drude metals one of which is coated with a left-handed meta material (Drude metals with $\Omega_1 = 3\,\Omega$, $\omega_1 = 0$, $\mu_1(\xi) \equiv 1$; left-handed coating with thickness $w = 10 \times 2\pi c/\Omega$ and material parameters (dominantly magnetic response) $\Omega_2 \equiv 0.1\,\Omega$, $\omega_2 = \Omega$, $\Theta_2 = 0.3\,\Omega$, $\vartheta_2 = \Omega$). Label (d): two meta materials, one purely dielectric, the other mainly magnetic ($\Omega_1 = 3\,\Omega$, $\omega_1 = \Omega$, $\mu_1(\xi) \equiv 1$, $\Omega_2 = 0.1\,\Omega$, $\omega_2 = \Omega$, $\Theta_2 = 0.3\,\Omega$, $\vartheta_2 = \Omega$).

calculations show that a large resonance frequency is not sufficient to achieve repulsion, the oscillator strength of the resonances (proportional to Ω_1 and Θ_2) must be large enough so that $\hbar\Omega_1, \hbar\Theta_2 \gg \max(k_B T, \hbar c/d)$. As the temperature is raised, the distance range where repulsion is observed disappears, see fig. 2. One then finds a $1/d^3$ power law at large distance as well.

The different regimes of fig. 1 can be understood from an asymptotic analysis of eq. (1). At short distance ($d \ll \Lambda/2\pi$), the integral is dominated by a region in the (κ, ξ)-plane where the Fresnel coefficients (2) take the nonretarded forms $r_{\rm TM} \to R(\varepsilon) \equiv (\varepsilon - 1)/(\varepsilon + 1) > 0$ assuming that $\varepsilon > 1$ and similarly $r_{\rm TE} \to R(\mu) > 0$ unless $\mu = 1$. Proceeding like Lifshitz [20,40] yields to leading order a power law $F_L = c_3/d^3$ with a *positive* Hamaker constant given by

$$c_3 = \frac{k_B T}{4\pi} \sum_{n=0}^{\infty}{}' \{ \mathrm{Li}_3[R(\varepsilon_1(\xi_n)) R(\varepsilon_2(\xi_n))] + \mathrm{Li}_3[R(\mu_1(\xi_n)) R(\mu_2(\xi_n))] \} , \tag{7}$$

where $\mathrm{Li}_n(z) \equiv \sum_{k=1}^{\infty} z^k/k^n$. It must be noted that for the special case of homogeneous plates, this asymptotic expression actually provides another, much stricter, upper limit to the Casimir force, since $r_{\mathrm{TM}\alpha} \le R(\varepsilon_\alpha)$, $r_{\mathrm{TE}\alpha} \le R(\mu_\alpha)$ and $\mathrm{Li}_3(z)$ is a monotonous function (see fig. 1). In order of magnitude, $c_3 \sim \hbar\Omega$ at low temperatures ($k_B T \ll \hbar\Omega$). Compared to ideal mirrors, dispersive plates thus show a much weaker Casimir interaction that is in general attractive (fig. 1 and ref. [35]). At larger distances, $\Lambda/2\pi \ll d \ll \Lambda_T \equiv \hbar c/k_B T$, the Casimir force follows a $1/d^4$ power law, and repulsion is found provided one of the materials is dominantly magnetic. Here, the non-dispersive results of ref. [7] are recovered. Finally, for

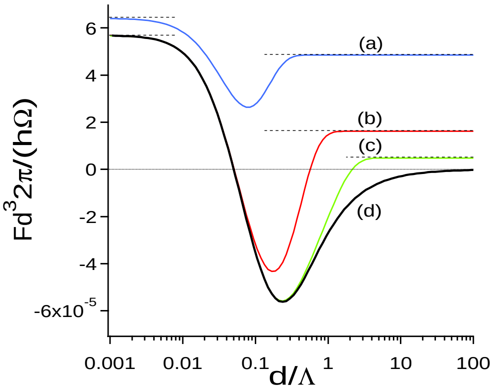

Fig. 2 – Casimir force between two different meta materials as the temperature is raised. The material parameters are identical to line (d) of fig. 1. The temperature takes the values $k_BT =$ (a) 0.3, (b) 0.1, (c) 0.03, (d) $0\,\hbar\Omega$. Same scaling as in fig. 1. Dashed lines correspond to the short- and long-distance asymptotics discussed in the text.

$d \gg \Lambda_T$, the leading order force is the term $n = 0$ in the sum (1), again an attractive $1/d^3$ law, with a coefficient given by an expression similar to (7), but involving the static material constants, see [7].

The impact of temperature is illustrated in fig. 2: at high temperature, $k_BT \gg \hbar\Omega$, the second Matsubara frequency ξ_1 falls already into the mirrors' transparency zone, and the $1/d^3$ power law is valid at all distances. As $T \to 0$, the intermediate repulsive zone appears in the range $\Lambda/2\pi \ll d \ll \Lambda_T/2\pi$. A good agreement with the analytical $1/d^3$ asymptotics is found outside this zone, as shown by the dashed lines. For the resonance wavelength $\Lambda = 3\,\mu$m mentioned above, cooling to a temperature $T \approx 0.1\,\hbar\Omega/k_B \sim 50\,$K is required to "open up" the repulsive window. This temperature increases, of course, with materials whose response extends to higher frequencies.

Finally, we would like to illustrate the kind of peculiar asymptotics that becomes possible with carefully matched material parameters. This follows ref. [21] that computes the Van der Waals force on a water film coated on both sides by lipid membranes, finding a weak dependence on the ultraviolet frequency range because both materials have a similar electron density. Consider thus a liquid-filled gap with a similar electron density as medium 2 so that $\varepsilon_0 = \varepsilon_2$, and a permeability $\mu_0 = \mu_1 \equiv 1$ matched to medium 1. For simplicity, we assume that these equalities hold at all frequencies. In this case, we can show that the force is repulsive at all distances, even at finite temperature. Indeed, both contributions in eq. (7) vanish, and the leading order term for high temperatures also vanishes. The high-temperature limit is given by the $n = 1$ term in (1). This gives a distance dependence proportional to $\exp[-4\pi d/\Lambda_T]$ similar to what has been observed in some experiments with colloids (mentioned in [41]). As the temperature is lowered, this exponential regime still applies for $d \gg \Lambda_T$. If $k_BT \ll \hbar\Omega$, the $1/d^4$ regime of ref. [7] exists at intermediate distances $\Lambda/2\pi \ll d \ll \Lambda_T/2\pi$. The short-distance regime sets in for $d \ll \Lambda$, and an analysis similar to the one leading to eq. (7) gives $(T = 0)$

$$F_L = \frac{\hbar}{\pi} \sum_{n=1}^{\infty} (2nd)^{2n-3} \int_0^{\infty} \frac{\mathrm{d}\xi}{2\pi} \Gamma(3-2n, 2n\xi\, d/c) \left(-\frac{\varepsilon_1 - \varepsilon_0}{\varepsilon_1 + \varepsilon_0} \frac{(\mu_2 - \mu_1)\xi^2}{4c^2} \right)^n \tag{8}$$

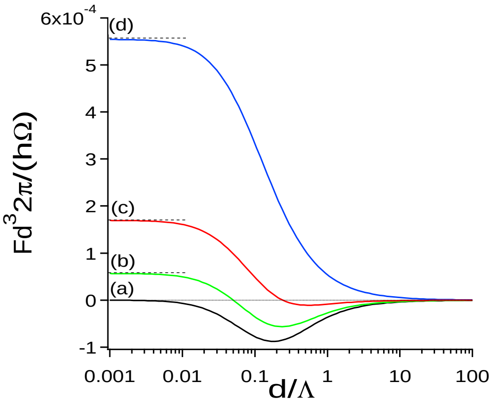

Fig. 3 – Casimir force between two different meta materials as the residual dielectric response of mirror 2 is changed. Same scaling as in fig. 1, $T = 0$. Dashed lines: short-distance asymptotics (7). The dielectric response for mirror 2 is of Lorentz-Drude form with fixed cutoff frequency and variable oscillator strength. Material functions as in fig. 1(d), except $\varepsilon_2(0) = 1$ (a), 1.01 (b), 1.03 (c), 1.1 (d).

with $\Gamma(k, z) \equiv \int_z^\infty \mathrm{d}t\, t^{k-1} \mathrm{e}^{-t}$. At short distance, the sum is dominated by the first term, so that to leading order, we get a repulsive power law $F_L = -c_1/d$ (fig. 3(a)). In order of magnitude, $c_1 \sim \hbar\Omega^3/c^2$ and therefore again $-F_L \ll F_C$, with a crossover occurring around $\Lambda/2\pi$ (see fig. 3(a)). Due to our assumption of a perfect matching $\varepsilon_2 = \varepsilon_0$, this kind of behaviour seems quite remote from experimental reality. As shown in fig. 3(b-d), a slight mismatch between the dielectric functions of liquid and plate leads back to an attractive force, first at short distances, then suppressing the repulsive window altogether.

Conclusion. – We have generalized strict upper and lower limits for the Casimir force. We have shown that a strongly modified Casimir force can occur between dispersive and absorbing mirrors with a sufficiently large magnetic susceptibility, extending results restricted to non-dispersive materials [7]. The most promising way to achieve this repulsion seems the use of meta materials engineered at scales between the nanometer and the micron because they provide a fairly large magnetic oscillator strength. Our results are intrinsically limited to distances $d \gg a$ by our use of effective medium theory. Sufficiently small structures and sufficiently low temperatures then ensure that in the range $a \ll d \ll \Lambda_T/2\pi$, the Casimir interaction can be strongly altered: even if repulsion cannot be achieved in a first step, we expect a significant reduction of the Casimir attraction at distances of a few microns (fig. 1).

* * *

Our thanks for comments and discussion goes to J.-J. Greffet, J.-P. Mulet, M. Wilkens, M. Tomaš, C. Genet, A. Lambrecht, S. Reynaud, and L. Pitaevskii. We thank anonymous referees for constructive criticism. We acknowledge financial support from the bilateral French-German programme "Procope" under project numbers 03199RH and D/0205739.

REFERENCES

[1] Ramakrishna S. A., *Rep. Prog. Phys.*, **68** (2005) 449.

[2] Yen T. J. *et al.*, *Science*, **303** (2004) 1494.

[3] Linden S., Enkrich C., Wegener M., Zhou J., Koschny T. and Soukoulis C. M., *Science*, **306** (2004) 1351; Grigorenko A. N., Geim A. K., Gleeson H. F., Zhang Y., Firsov A. A., Khrushchev I. Y. and Petrovic J., *Nature*, **438** (2005) 335.

[4] Klimov V. V., *Opt. Commun.*, **211** (2002) 183.

[5] Kästel J. and Fleischhauer M., *Phys. Rev. A*, **71** (2005) 011804.

[6] Boyer T. H., *Phys. Rev. A*, **9** (1974) 2078.

[7] Kenneth O., Klich I., Mann A. and Revzen M., *Phys. Rev. Lett.*, **89** (2002) 033001.

[8] Boyer T. H., *Am. J. Phys.*, **71** (2003) 990.

[9] Hartmann U., *Phys. Rev. B*, **43** (1991) 2404.

[10] Israelachvili J. N., *Intermolecular and Surface Forces*, 2nd edition (Academic Press, San Diego) 2000.

[11] Lee S.-W. and Sigmund W. M., *J. Colloid Interface Sci.*, **243** (2001) 365.

[12] Munday J. N., Iannuzzi D., Barash Y. and Capasso F., *Phys. Rev. A*, **71** (2005) 042102.

[13] Tomaš M. S., *Phys. Lett. A*, **342** (2005) 381.

[14] Camley R. E., Jensen M. R. F., Feiven S. A. and Parker T. J., *J. Appl. Phys.*, **83** (1998) 6280.

[15] Iannuzzi D. and Capasso F., *Phys. Rev. Lett.*, **91** (2003) 029101; Kenneth O., Klich I., Mann A. and Revzen M., *Phys. Rev. Lett.*, **91** (2003) 029102.

[16] Landau L. D., Lifshitz E. M. and Pitaevskii L. P., *Electrodynamics of Continuous Media*, 2nd edition (Pergamon, Oxford) 1984.

[17] Pendry J. B., Holden A. J., Robbins D. J. and Stewart W. J., *IEEE Trans. Microwave Theory Tech.*, **47** (1999) 2075.

[18] Smith D. R., Rye P., Vier D. C., Starr A. F., Mock J. J. and Perram T., *IEICE Trans. Electron.*, **E87-C** (2004) 359.

[19] Casimir H. B. G., *Proc. K. Ned. Akad. Wet.*, **51** (1948) 793.

[20] Lifshitz E. M., *Sov. Phys. JETP*, **2** (1956) 73 (*Z. Eksp. Teor. Fiz. USSR*, **29** (1955) 94).

[21] Parsegian V. A. and Ninham B. W., *Nature*, **224** (1969) 1197.

[22] Ninham B. W. and Parsegian V. A., *J. Chem. Phys.*, **53** (1970) 3398.

[23] Richmond P. and Ninham B. W., *J. Phys. C*, **4** (1971) 1988.

[24] Schram K., *Phys. Lett. A*, **43** (1973) 282.

[25] Schwinger J., DeRaad L. L. jr. and Milton K. A., *Ann. Phys. (N.Y.)*, **115** (1978) 1.

[26] Kupiszewska D., *Phys. Rev. A*, **46** (1992) 2286.

[27] Zhou F. and Spruch L., *Phys. Rev. A*, **52** (1995) 297.

[28] Klimchitskaya G. L., Mohideen U. and Mostepanenko V. M., *Phys. Rev. A*, **61** (2000) 062107.

[29] Esquivel-Sirvent R., Villarreal C. and Cocoletzi G. H., *Phys. Rev. A*, **64** (2001) 052108.

[30] Tomaš M. S., *Phys. Rev. A*, **66** (2002) 052103.

[31] Genet C., Lambrecht A. and Reynaud S., *Phys. Rev. A*, **67** (2003) 043811.

[32] Santos F. C., Tenório A. and Tort A. C., *Phys. Rev. D*, **60** (1999) 105022.

[33] Born M. and Wolf E., *Principles of Optics*, 6th edition (Pergamon Press, Oxford) 1959.

[34] Yeh P., *Optical Waves in Layered Media* (John Wiley & Sons, New York) 1988.

[35] Lambrecht A., Jaekel M.-T. and Reynaud S., *Phys. Lett. A*, **225** (1997) 188.

[36] Lamoreaux S. K., *Phys. Rev. Lett.*, **78** (1997) 5; **81** (1998) 5475 (E).

[37] Chan H. B., Aksyuk V. A., Kleiman R. N., Bishop D. J. and Capasso F., *Science*, **291** (2001) 1941.

[38] Mohideen U. and Roy A., *Phys. Rev. Lett.*, **81** (1998) 4549.

[39] Bressi G., Carugno G., Onofrio R. and Ruoso G., *Phys. Rev. Lett.*, **88** (2002) 041804.

[40] Henkel C., Joulain K., Mulet J.-P. and Greffet J.-J., *Phys. Rev. A*, **69** (2004) 023808.

[41] Ackler H. D., French R. H. and Chiang Y.-M., *J. Colloid Interface Sci.*, **179** (1996) 460.

Electromagnetic field correlations near a surface with a nonlocal optical response

C. Henkel et K. Joulain

À paraître dans Applied Physics B

Appl. Phys. B – special issue 'Nano optics' – manuscript No.
(will be inserted by the editor)

Electromagnetic field correlations near a surface with a nonlocal optical response

Carsten Henkel[1]***, Karl Joulain**[2]

[1] Institut für Physik, Universität Potsdam, Germany,
[2] Laboratoire d'Etudes Thermiques, Ecole Nationale Supérieure de Mécanique Aéronautique, Poitiers, France

31 December 2005

Abstract The coherence length of the thermal electromagnetic field near a planar surface has a minimum value related to the nonlocal dielectric response of the material. We perform two model calculations of the electric energy density and the field's degree of spatial coherence. Above a polar crystal, the lattice constant gives the minimum coherence length. It also gives the upper limit to the near field energy density, cutting off its $1/z^3$ divergence. Near an electron plasma described by the semiclassical Lindhard dielectric function, the corresponding length scale is fixed by plasma screening to the Thomas-Fermi length. The electron mean free path, however, sets a larger scale where significant deviations from the local description are visible.

PACS: 42.25.Kb Coherence – 07.79.Fc Near-field scanning optical microscopes – 44.40.+a Thermal radiation – 78.20.-e Optical properties of bulk materials and thin films

1 Introduction

Thermal electromagnetic radiation in vacuum, as described by the celebrated blackdody spectrum discovered by Max Planck [1], is usually taken as a typical example of incoherent radiation. This is not quite true, however: if the radiation is detected at a given frequency, it is spatially coherent on a scale set by the wavelength [2, 3]. When one approaches a macroscopic object, the radiation spectrum and its coherence is profoundly changed, depending on the properties of the object. For example, if the object supports resonant modes like surface plasmon polaritons, the field is coherent across the propagation length of these modes [4]. The opposite case is possible as well: the coherence length becomes comparable to the observation distance, much smaller than the wavelength, close to an absorbing object with a local

---

* email: `Carsten.Henkel@physik.uni-potsdam.de`

dielectric function [5]. It has been suggested already by Rytov and colleagues that this behaviour is an artefact because at some small scale, nonlocal effects must come into play [2]. This is what we discuss in this paper in a semi-quantitative way. We use two models for nonlocal dielectric functions and identify the scale for the field's coherence length using explicit asymptotic formulas. A nonlocal dielectric response is of primary importance for semiconductor quantum wells, see for example Ref.[6], but the issue of spatial coherence has not been analyzed in this context, to our knowledge.

We focus on the spatial coherence of the electromagnetic field at nanometer distance in the vacuum (medium 1) above a solid material (medium 2). We chose a planar geometry which is sufficiently simple to allow for an essentially analytical description, thus avoiding the need for extensive numerics. On the other hand, many effects have been discussed in this setting: the fluorescence rate of molecules near metals and thin films [7], scanning near-field microscopy of sub-wavelength objects deposited on a substrate [8], the momentum exchange between a tip and a sample (related to the Casimir force, see, e.g., [9]) and the energy exchange between a tip and a sample [10–13].

2 Basic notation

2.1 Field correlations

The spatial coherence of the electric field is determined by the two-point expectation value [14]

$$\langle E_i(\mathbf{r}_1, t_1) E_j(\mathbf{r}_2, t_2) \rangle = \int \frac{\mathrm{d}\omega}{2\pi} \mathcal{E}_{ij}(\mathbf{r}_1, \mathbf{r}_2; \omega) \mathrm{e}^{\mathrm{i}\omega(t_1 - t_2)}, \tag{1}$$

where the average is taken in a stationary statistical ensemble (thermal equilibrium in the simplest case). We focus in the following on the cross-correlation spectrum $\mathcal{E}_{ij}(\mathbf{r}_1, \mathbf{r}_2; \omega)$ and a frequency in the infrared to visible range. Far from any sources and in global equilibrium, the corresponding wavelength $\lambda = 2\pi c/\omega$ sets the scale for the field's spatial coherence length: the cross-correlations tend to zero if the distance $|\mathbf{r}_1 - \mathbf{r}_2|$ exceeds λ. In the vicinity of a source, the coherence length ℓ_{coh} significantly differs from λ, as Henkel and co-workers have shown previously [5], and it changes with the observation point.

The spectrally resolved electric energy density is given by the trace

$$u_E(\mathbf{r}; \omega) = \frac{\varepsilon_0}{2} \sum_i \mathcal{E}_{ii}(\mathbf{r}, \mathbf{r}; \omega), \tag{2}$$

and its value in thermal equilibrium allows to define an electric, local density of states, as discussed in more detail by Joulain and co-workers [15]. The normalized tensor

$$c_{ij}(\mathbf{r}_1, \mathbf{r}_2; \omega) = \frac{\frac{1}{2}\varepsilon_0 \mathcal{E}_{ij}(\mathbf{r}_1, \mathbf{r}_2; \omega)}{\sqrt{u_E(\mathbf{r}_1; \omega) u_E(\mathbf{r}_2; \omega)}}, \tag{3}$$

to be considered below, allows to introduce a spatial degree of coherence. In the following, we call a “coherence function” both, $\mathcal{E}_{ij}(\mathbf{r}_1, \mathbf{r}_2; \omega)$ and Eq.(3). Definitions for a degree of polarization based on this 3×3 matrix (with $\mathbf{r}_1 = \mathbf{r}_2$) have been put forward as well, see [16,17]. For the sake of simplicity, we suppress the frequency arguments in the following.

2.2 Planar surface with local response

In a previous paper, Henkel and co-workers have shown that in the vacuum above a planar dielectric surface at temperature T, described by a local permittivity ε_2, the spatial coherence function is of the form [5] (see also [18,19])

$$\mathcal{E}_{ij}(\mathbf{r}_1, \mathbf{r}_2) = \frac{\Theta(\omega, T)}{2\pi\varepsilon_0\omega\,\tilde{r}^5}\mathrm{Im}\frac{\varepsilon_2 - 1}{\varepsilon_2 + 1}\begin{pmatrix} \tilde{r}^2 - 3\rho^2 & 0 & 3\rho(z_1 + z_2) \\ 0 & \tilde{r}^2 & 0 \\ -3\rho(z_1 + z_2) & 0 & 3(z_1 + z_2)^2 - \tilde{r}^2 \end{pmatrix} \quad (4)$$

where $\Theta(\omega, T) = \hbar\omega/(e^{\hbar\omega/kT} - 1)$. We assume that the field is observed in vacuum (relative permittivity $\varepsilon_1 = 1$). The surface is given by $z = 0$. We have chosen the x-axis such that $\mathbf{r}_1 - \mathbf{r}_2$ lies in the xz-plane and $\rho = x_1 - x_2$. The quantity $\tilde{r}^2 = \rho^2 + (z_1 + z_2)^2$ is the (squared) distance between $\mathbf{r}_1$ and the image point of $\mathbf{r}_2$ across the interface.

Eq.(4) applies to leading order when both distances z_1, z_2 are much smaller than the wavelength λ; for other regimes and higher order corrections, see Ref.[5] and, at $\rho = 0$, Ref.[20]. In the following, we focus on the correlation function at a constant height $z = z_1 = z_2$ and discuss its dependence on the lateral separation ρ; note that ρ can be positive or negative. The normalized coherence function (4) is qualitatively similar to a Lorentzian: the yy-component, for example, follows a law $\sim [4z^2 + \rho^2]^{-3/2}$. The spatial coherence length is thus equal to z, and decreases without apparent limitation as the surface is approached. The electric energy density derived from (4) diverges like $1/z^3$:

$$u_E(z) = [\Theta(\omega, T)/(8\pi\, z^3)]\mathrm{Im}[(\varepsilon_2 - 1)/(\varepsilon_2 + 1)]. \quad (5)$$

Both points have been noted by Rytov and co-workers [2], who have also argued that this unphysical result is due to the assumption of a local dielectric response down to the smallest scales. A cutoff would occur naturally in a non-local treatment or taking into account the atomistic structure of the material. This is what we show here in detail, using two different model calculations. Doing this, we also provide a basis for the phenomenological cutoff introduced recently by Kittel and co-workers [13] in the context of heat transfer from a hot, sharp tip into a cold, planar substrate.

2.3 Overview

We will use two models to calculate the coherence function. In both, we focus, as mentioned before, on the fields near a planar surface and compute the field correlations in the vacuum above it, at sub-wavelength distances.

The first model is based on the fluctuation electrodynamics introduced by Rytov and co-workers [2] where the sources of the field are described by fluctuating polarization currents below the surface. This approach relies on the fluctuation-dissipation theorem that links the spectrum of the polarization current to the dielectric function of the material below the surface. We argue that the currents are spatially correlated on a scale equal to or larger than the material's microscopic lattice constant. We then show that the radiation generated outside the surface shows a minimum coherence length given by this scale; this cuts off the divergences appearing in a local description of the material, as noted in Refs.[2, 13]. This model can be applied to polar ionic crystals in the frequency domain where the dielectric response is dominated by phonon-polariton resonances. It can also cover a non-equilibrium situation where the surface is heated to a different temperature or shows weak temperature gradients [21, 22].

The second model describes the dielectric response of an electron plasma and applies to the plasmon-polariton resonances occurring in metals. We use here directly the fluctuation-dissipation theorem for the electric field [23, 24], restricting ourselves to a field-matter system in "global equilibrium". The coherence function is determined by reflection coefficients from the surface for which we take the Lindhard form, taking into account the non-local response of the electron plasma. It is shown that the field's coherence length is limited by the Thomas-Fermi screening length, but significant deviations from the local description occur already on the (typically larger) scale of the electron mean free path.

3 Polar crystal

3.1 Current correlations

We assume here that the fluctuating currents that generate the radiation field, are correlated below a certain distance l. Above this distance, the medium response can be considered as local. A lower limit for l is certainly the lattice period a: at scales smaller than a, the concept of a continuous material characterized by a dielectric constant does not make sense any more.

In this situation, the cross correlation spectrum of the fluctuating currents, as given by the fluctuation-dissipation theorem, is no longer delta-correlated in space. We choose here to smoothen the spatial delta fonction into a gaussian. The fluctuation-dissipation theorem for the currents thus takes the form

$$\langle j_k^*(\mathbf{r}_1, \omega) j_l(\mathbf{r}_2, \omega') \rangle = 2\omega\varepsilon_0 \mathrm{Im}[\varepsilon(\bar{\mathbf{r}})] \frac{e^{-(\mathbf{r}_1 - \mathbf{r}_2)^2/l^2}}{\pi^{3/2} l^3} \Theta(\omega, T) \delta_{kl} \delta(\omega - \omega'), \quad (6)$$

where $\bar{\mathbf{r}} = \frac{1}{2}(\mathbf{r}_1 + \mathbf{r}_2)$. The gaussian form for the spatial smoothing is chosen for convenience; another functional dependence will lead to qualitatively similar results.

3.2 Transmitted field

We then write the cross correlation spectrum for the electric field in terms of Green functions and the currents. We use the convention

$$E_i(\mathbf{r},\omega) = \mathrm{i}\mu_0\omega \int d^3\mathbf{r}' \sum_k G_{ik}(\mathbf{r},\mathbf{r}';\omega) j_k(\mathbf{r}',\omega). \tag{7}$$

To proceed further in the calculation, the Green function is written as a Weyl plane wave expansion ([25] and appendix). In the present case, the Green function relates the current on one side of an interface to the electric field on the other side of the interface. It depends on the Fresnel transmission coefficients through this interface.

Using (6) and integrating over the half-space filled with the dielectric, one obtains

$$\mathcal{E}_{ij}(\mathbf{r}_1,\mathbf{r}_2) = 2\mu_0\Theta(\omega,T)\omega \int_0^{2\pi} \frac{\mathrm{d}\theta}{2\pi} \int_0^{\infty} \frac{K\,\mathrm{Re}(\gamma_2)\mathrm{d}K}{2\pi\,|\gamma_2|^2} \tag{8}$$
$$\times e^{-iK\rho\cos\theta} e^{-2\mathrm{Im}(\gamma_1)z} e^{-K^2l^2/4} e^{-\mathrm{Re}(\gamma_2)^2l^2/4} g^*_{ik}(\mathbf{K}) g_{jk}(\mathbf{K})$$

In the preceding equation, the wavenumber in the medium $i = 1, 2$ is $\mathbf{k}_i = (\mathbf{K}, \gamma_i)$ where $\mathbf{K} = K\cos\theta\,\mathbf{e}_x + K\sin\theta\,\mathbf{e}_y$ and $\gamma_i^2 = \epsilon_i(\omega/c)^2 - k^2$. The tensor $g_{ij}(\mathbf{K})$ is related to the Green tensor and defined in the Appendix.

The cross-spectral correlation function depends on four characteristic lengths: the wavelength λ, the distance to the interface z, the locality distance l and the separation ρ between the field points. The latter is the variable considered in our problem. At the wavelengths we work with, we always have $l \ll \lambda$. When z is larger than λ (in the far field), the factor $e^{-2\mathrm{Im}(\gamma_1)z}$ actually limits the integration over K to $0 \le K \le \omega/c$, i.e., to propagating waves. The cross-spectral correlation function, in this regime, drops to 0 when ρ exceeds $\lambda/2$, as in the blackbody radiation field. In the intermediate regime $l \ll z \ll \lambda$, the integral is dominated by the range $\omega/c \ll K \ll 1/l$, where the exponentials containing l are close to unity. Hence, the results of Ref.[5] are recovered. Finally, when $z \ll l$, $e^{-2\mathrm{Im}(\gamma_1)z}$ and $e^{-\mathrm{Re}(\gamma_2)^2l^2/4}$ both approach unity in the relevant range $|\sqrt{\varepsilon_2}|\omega/c \ll K < 1/l$. This is the regime we discuss in more detail in the following.

We note in passing that we use our calculation is based on the solution to the transmission problem valid for a local medium. Actually, this solution applies when the wave vector K is smaller than $1/l$ when the medium can be described as homogeneous. But from (8) one sees that whatever the values of z, there is anyway a cut-off in the integration over K at approximately $1/l$. Therefore, one might consider that the local expression of the Fresnel coefficients remains valid. We believe that our model, even if it not rigorously accurate, is useful in view of the insight one gains from the analytic result.

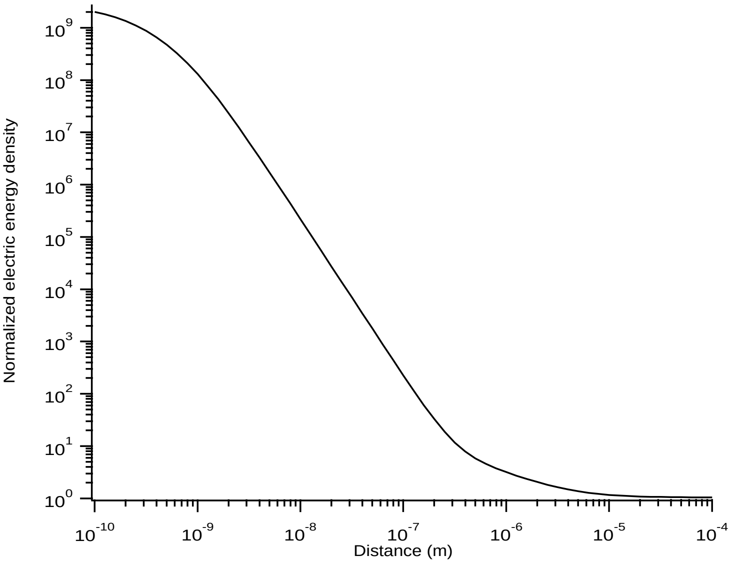

Fig. 1 Normalized electric energy density above a surface of silicon carbide vs. the distance z to the surface. The electric energy density is normalized to the electric energy density in the far field. The locality scale is taken as $l = 1\text{nm}$. The SiC permittivity is described by an oscillator model in the visible-infrared part of the spectrum [27].

3.3 Asymptotics and discussion

Using the limit of $g_{ij}(\mathrm{K})$ for large K, we obtain from (8) the following asymptotic expression for the cross spectral correlation tensor

$$\mathcal{E}_{ij}(\mathbf{r}_1, \mathbf{r}_2) \approx \frac{8\Theta(\omega,T)\mathrm{Im}(\varepsilon_2)}{\varepsilon_0 \pi \omega |\varepsilon_2 + 1|^2 l^3} \tag{9}$$
$$\times \begin{pmatrix} \frac{\sqrt{\pi}}{2}[M_{3/2} - \frac{3}{4}\frac{\rho^2}{l^2}M_{5/2}] & 0 & -2\frac{\rho}{l}e^{-\rho^2/l^2} \\ 0 & \frac{\sqrt{\pi}}{2}[M_{3/2} + \frac{3}{4}\frac{\rho^2}{l^2}M_{5/2}] & 0 \\ 2\frac{\rho}{l}e^{-\rho^2/l^2} & 0 & \sqrt{\pi}M_{3/2} \end{pmatrix},$$

where $M_{3/2} = M(\frac{3}{2}, 1, -\frac{\rho^2}{l^2})$ and $M_{5/2} = M(\frac{5}{2}, 3, -\frac{\rho^2}{l^2})$, and $M(a, b, z)$ is the confluent hypergeometric function [26]. When $\rho \ll l$, $M_{3/2}$ and $M_{5/2}$ both approach unity. Putting $\rho = 0$ in the cross-spectral correlation tensor and taking the trace, we get the electric energy density versus z:

$$z \ll l: \qquad u_E(z) = \frac{2\Theta(\omega,T)}{\pi^{1/2}\omega\, l^3}\mathrm{Im}\frac{\varepsilon_2 - 1}{\varepsilon_2 + 1}. \tag{10}$$

It appears (see Fig.1) that it saturates at short z to a quantity that only depends on l as $1/l^3$: the non-locality scale l thus sets the ultimate length below which the field properties are “frozen” to their value for $z \approx l$.

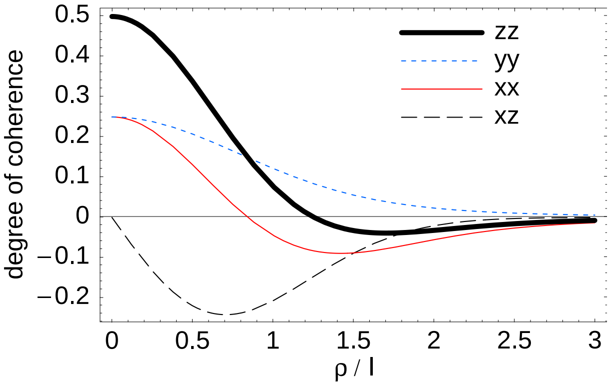

Fig. 2 Normalized spatial coherence function vs. lateral separation ρ in units of the nonlocality scale l. The nonzero components in Eq.(9) are plotted and normalized to the trace of the coherence tensor.

When $\rho \gg l$, all the components of the correlation tensors drop to zero, see Fig.2. This decrease is exponentially fast for the xz and zx components. For the other components, the asymptotic behaviour for large ρ simply scales like $1/\rho^3$ and does not depend on l anymore. This follows from the large argument asymptotics $M_{3/2} \approx \frac{-1}{2\sqrt{\pi}} \frac{l^3}{\rho^3}$ and $M_{5/2} \approx \frac{2}{\sqrt{\pi}} \frac{l^5}{\rho^5}$. Note that in this case, we recover an algebraic decay similar to the local medium case given in Eq.(4).

To summarize this section, we have shown that when we take into account the non-local nature of matter by introducing a locality length l for the sources of the field, the correlation length is about l when the distance to the interface $z < l$. In this regime, the energy density saturates to a value given by the electrostatic energy density expression taken in $z = l$.

4 Nonlocal plasma

We consider in this section another simple situation where the field correlation function can be calculated fairly easily. Restricting ourselves to a field in thermal equilibrium between field and surface, we use directly the fluctuation-dissipation theorem for the field. The relevant information is thus encoded in the electric Green tensor (i.e., the field's response function). The Green tensor contains a part due to the reflection from the surface that is actually dominating in the sub-wavelength distance regime we are interested in. We first review the corresponding reflection coefficients for an electron plasma, taking into account the finite response time of the electrons and their scattering. These two effects make the plasma behave like a nonlocal medium and give rise to the so-called anomalous skin effect. We then discuss the large-wavevector asymptotics of the reflection coefficients and the corresponding limits on the spatial coherence function. It turns out that the scattering mean free path is one key quantity that limits the coherence length at short observation distances.

4.1 Reflection coefficients

We focus here on the electronic contribution to the dielectric function and describe the background ions, interband absorption etc. by a local permittivity ε_b to avoid unnecessary complications. As is well known [28], the dielectric function of a bulk plasma is actually a tensor with two distinct spatial Fourier coefficients, a “longitudinal” $\varepsilon_l(q)$ and a “transverse” $\varepsilon_t(q)$ where q is the modulus of the wavevector. (As before, we suppress the frequency dependence for simplicity.) The fields outside the metal surface are characterized by the reflection coefficients $r_{s,p}(K)$ that depend only on the magnitude $K = |\mathbf{K}|$ of the incident wavevector projected onto the interface. Out of the two polarizations s and p, we need in the following only $r_p(K)$ in the (non-retarded) regime $K \gg \omega/c$. This coefficient is given, e.g., in the review paper by Ford and Weber [29]:

$$r_p(K) = \frac{1/Z_p(K) - 1}{1/Z_p(K) + 1} \tag{11}$$

We use here a dimensionless surface impedance $Z_p(K)$ that reads in the non-retarded limit

$$Z_p(K) = 4K \int\limits_0^\infty \frac{\mathrm{d}k_z}{2\pi} \frac{1}{q^2 \varepsilon_l(q)}, \qquad q^2 = K^2 + k_z^2, \tag{12}$$

it involves the longitudinal dielectric function only for which we take the Lindhard formula [29,30]

$$\varepsilon_l(q) = \varepsilon_b + \frac{3\Omega^2}{\omega + \mathrm{i}\nu} \frac{u^2 f_l(u)}{\omega + \mathrm{i}\nu f_l(u)} \tag{13}$$

$$u = \frac{\omega + \mathrm{i}\nu}{q v_F} \equiv \frac{1}{q\ell} \tag{14}$$

$$f_l(u) = 1 - \frac{u}{2} \log\left(\frac{u+1}{u-1}\right). \tag{15}$$

The plasma frequency is given by $\Omega^2 = ne^2/(m\varepsilon_0)$ with $n, -e, m$ the electron density, charge, and mass, respectively.

From the nonlocal permittivity (13–15), two characteristic length scales can be read off: the mean free path $l_{\mathrm{mfp}} = v_F/\nu$ and v_F/ω, the maximum distance over which an electron at the Fermi energy can move ballistically during one period of the applied electric field. In the following, we use the complex length $\ell = v_F/(\omega + \mathrm{i}\nu)$ defined in (14) to simplify the notation.

The Fermi wavelength does not explicitly appear in Eqs.(13–15) because the semiclassical version of the Lindhard dielectric function we take here is based on a semiclassical description of the electron gas (classical particles with Fermi statistics). This description is valid as long as q is much smaller than the Fermi wave vector $k_F = mv_F/\hbar$. Our model thus applies reasonably well to a “clean metal” where the mean free path is much longer than the Fermi wavelength, and to distances above $1/k_F$ (typically a few Å). Ref.[29] gives a more general dielectric function that covers the regime $q \geq k_F$ as well.

4.2 Coherence function

The fluctuation-dissipation theorem for the electric field, combined with the Green tensor describing the reflection from a planar surface, gives the following integral representation for the field's coherence function:

$$\mathcal{E}_{ij}(\mathbf{r}_1, \mathbf{r}_2) = \mu_0 \omega \Theta(\omega, T) \int\limits_0^\infty \frac{K \mathrm{d}K}{2\pi} \sum_{\mu = \mathrm{s,p}} \mathcal{C}_{ij}^{(\mu)}(K\rho) \, \mathrm{Re} \, \frac{r_\mu(K) \, \mathrm{e}^{2\mathrm{i}\gamma_1 z}}{\gamma_1} \tag{16}$$

with $\gamma_1 = (\omega^2/c^2 - K^2)^{1/2}$ ($\mathrm{Im}\,\gamma_1 \geq 0$). For more details, see for example [31, 32]. We have omitted the free-space part of the Green tensor that gives the same result as for the blackbody field. This part actually becomes negligible compared to the surface part given here if we focus on the sub-wavelength regime, $z_1 = z_2 = z \ll \lambda$: the integration domain $\omega/c \leq K < \infty$ (which is absent in the free-space field) then makes the dominant contribution to the integral.

The tensors $\mathcal{C}_{ij}^{(\mu)}(K\rho)$ in (18) depend on the lateral (signed) distance $\rho = x_1 - x_2$, as introduced after Eq.(4). In p-polarization, it is given by

$$\mathcal{C}^{(\mathrm{p})}(K\rho) = \frac{K^2 c^2}{2\omega^2} \begin{pmatrix} J_0 - J_2 & 0 & 2J_1 \\ 0 & J_0 + J_2 & 0 \\ -2J_1 & 0 & 2J_0 \end{pmatrix}, \tag{17}$$

involving the Bessel functions $J_n = J_n(K\rho)$, $n = 0, 1, 2$. A similar expression applies in s-polarization. We can focus, for short distances, on the range $\omega/c \ll K$, expand the reflection coefficients and find that $|r_s| \ll |r_p|$; hence, the s-polarization is neglected in the following. This also justifies our taking the non-retarded limit of the reflection coefficient (11). To the same accuracy, we approximate $\gamma_1 \approx i|K|$. Finally, the correlation tensor becomes

$$\mathcal{E}_{ij}(\mathbf{r}_1, \mathbf{r}_2) = \mu_0 \omega \Theta(\omega, T) \int\limits_0^\infty \frac{\mathrm{d}K}{2\pi} \mathrm{e}^{-2Kz} \sum_{\mu = \mathrm{s,p}} \mathcal{C}_{ij}^{(\mu)}(K\rho) \, \mathrm{Im} \, r_\mu(K). \tag{18}$$

We anticipate from the integral representation (18) that the wave-vector dependence of $\mathrm{Im}\, r_p(K)$ determines the spatial coherence length: if K_c is the scale on which $\mathrm{Im}\, r_p(K) \to 0$, we expect that the divergence of the energy density is smoothed out for $z \ll 1/K_c$ and that the lateral coherence length remains finite: $\ell_{\mathrm{coh}} \sim 1/K_c$ for $z \leq 1/K_c$.

4.3 Local medium

Let us illustrate first how the Lindhard reflection coefficient reduces to its local form (the Fresnel formula). If the q-dependence of $\varepsilon_l(q)$ can be neglected, writing $\varepsilon_l(q) \to \varepsilon_{\mathrm{loc}}$, the surface impedance (12) integrates to $Z_p \to 1/\varepsilon_{\mathrm{loc}}$. Eq.(11) then recovers the reflection coefficient for electrostatic images, $r_p \to (\varepsilon_{\mathrm{loc}} - 1)/(\varepsilon_{\mathrm{loc}} + 1)$ which is the large K limit of the Fresnel formula for TM polarization. The integration of the Bessel functions and exponentials over K in Eq.(18) can be carried out, and we get Eq.(4) with its unphysical $1/z^3$ divergence.

The same divergence would be obtained here from the background permittivity ε_b that we assume local. To focus on the nonlocal contribution from the electron plasma, we consider the regime where ε_b is real so that the leading-order, local contribution analogous to Eq.(4) vanishes.

4.4 Nonlocal reflection coefficient

To get a qualitative insight into the impact of nonlocality, we perform an asymptotic analysis of the dielectric function (13–15):

$$\varepsilon_l(q) \approx \begin{cases} \varepsilon_b - \dfrac{\Omega^2}{\omega(\omega + \mathrm{i}\nu)} \left[1 + (q\ell)^2 \left(\dfrac{3}{5} + \dfrac{\mathrm{i}\nu}{3\omega} \right) \right], & |q\ell| \ll 1 \\ \varepsilon_b \left(1 + \dfrac{1}{q^2 \Lambda^2} \right) + \dfrac{\mathrm{i}C}{q^3}, & |q\ell| \gg 1 \end{cases} \tag{19}$$

where $\Lambda = \sqrt{\varepsilon_b v_F^2 / (3\Omega^2)}$ is the Thomas-Fermi length that provides another length scale, and we use the notation $C = 3\pi\omega\Omega^2/v_F^3$. We recall that ℓ is the complex characteristic length defined in (14). Note that for small q, we recover the usual, local Drude expression for an electron plasma

$$\varepsilon_{\mathrm{loc}} = \varepsilon_b - \frac{\Omega^2}{\omega(\omega + \mathrm{i}\nu)}. \tag{20}$$

At large q, one gets the dielectric function for Thomas-Fermi screening [28] with a screening length on the order of v_F/Ω plus an imaginary correction.

From the integral (12) for the surface impedance, we find that the typical wavenumber is of the order of $q \geq K$. Hence the two limits quoted above translate into the following asymptotics of the reflection coefficient, after performing the integrations,

$$\operatorname{Im} r_p(K) \approx \begin{cases} \operatorname{Im} \dfrac{\varepsilon_{loc} - 1}{\varepsilon_{loc} + 1}, & |K\ell| \ll 1, \\ \dfrac{4}{3\varepsilon_b^2} \dfrac{C K \Lambda^4 g(K\Lambda)}{\left| 1 + K/(\varepsilon_b \sqrt{K^2 + 1/\Lambda^2}) \right|^2}, & |K\ell| \gg 1. \end{cases} \tag{21}$$

The dimensionless function $g(K\Lambda)$ is the integral

$$g(K\Lambda) = \int_0^\infty \frac{\mathrm{d}t}{\sqrt{(K\Lambda)^2 + t^2}\,[(K\Lambda)^2 + 1 + t^2]^2}. \tag{22}$$

This can be evaluated in closed, but barely instructive form involving a hypergeometric function; its limiting behaviour is

$$\begin{aligned} g(K\Lambda) &\approx \ln(1/K\Lambda) + \ln 2 - \tfrac{1}{2} && \text{for } K\Lambda \ll 1, \\ g(K\Lambda) &= \tfrac{2}{3}(K\Lambda)^{-4} && \text{for } K\Lambda \gg 1. \end{aligned} \tag{23}$$

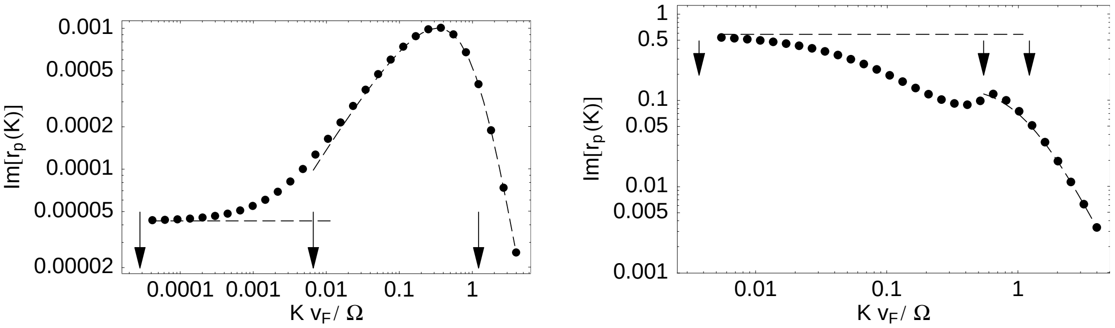

Fig. 3 Reflection coefficient $\operatorname{Im} r_{\rm p}(K)$ vs. the normalized wave vector $K v_F/\Omega$. Dashed lines: asymptotical formulas (21). Solid line with symbols: numerical calculation. The arrows mark, from left to right, the characteristic scales ω/c, $1/|\ell|$ and $1/\Lambda$. Chosen parameters: $\Omega/\nu = 192$, $c/v_F = 148$, ($v_F/\Omega = 0.84\,$Å), taken from the Drude description of aluminium [28]. We take $\varepsilon_b = 2$ to model the contribution of bound electrons. Left panel: $\omega = 0.8\,\nu$ or $\lambda = 19\,\mu{\rm m}$. Right panel: $\omega = 0.55\,\Omega$ ($\lambda = 140\,{\rm nm}$), near the large-K asymptote of the surface plasmon resonance in the local approximation (given by $\varepsilon_{\rm loc} + 1 = 0$).

The first line applies to the intermediate case $1/|\ell| \ll K \ll 1/\Lambda$, the second one to the regime $K \gg 1/\Lambda, 1/|\ell|$. In both cases, Eq.(21) implies that $|\operatorname{Im} r_p(K)| \ll 1$.

The reflection coefficient is plotted in Fig.3 where the asymptotic expressions (21) are represented as dashed lines. We find good agreement outside the crossover range $K|\ell| \sim 1$. In the frequency range of the anomalous skin effect, $\omega \sim \nu$ (left panel, $\lambda = 19\,\mu{\rm m}$ in the infrared), the nonlocal plasma shows an increased $\operatorname{Im} r_{\rm p}(K)$, with a cutoff occurring beyond $K_c \sim 1/\Lambda$ [see Eq.(23)]. This effect is well known [29] and is related to the enhanced spontaneous emission rate for a nonlocal metallic surface that was recently pointed out [33]. The reflection loss remains small in absolute numbers because of the large conductivity of the material. The opposite behaviour is found near the (local, non-retarded) surface plasmon resonance (right panel, $\lambda = 140\,{\rm nm}$ in the far UV): $\operatorname{Im} r_{\rm p}(K)$ decreases from its local value, with a weakly resonant feature emerging around $K \sim 1/|\ell|$.

From these plots, we observe that the characteristic wave vector scale K_c strongly depends on the frequency range. An upper limit is set by $1/\Lambda$, involving the Thomas-Fermi screening length, but significant changes already occur on the scale $1/|\ell|$. The characteristic distance below which non-local effects become manifest, is thus given by the largest of $|\ell|$ and Λ. This is typically $|\ell|$, since in order of magnitude, $|\ell|/\Lambda \sim \Omega/|\omega + {\rm i}\nu|$ which is much larger than unity for good conductors up to the visible domain. At frequencies smaller (larger) than the damping rate ν, the mean free path $l_{\rm mfp}$ (the "ballistic amplitude" v_F/ω): sets the scale for nonlocal effects, respectively.

We note that for typical metals, the Thomas-Fermi scale Λ does not differ much from the Fermi wavelength $1/k_F$. The asymptotics derived above within the semiclassical Lindhard model (13) is therefore only qualitatively valid at short distances (large wavevectors).

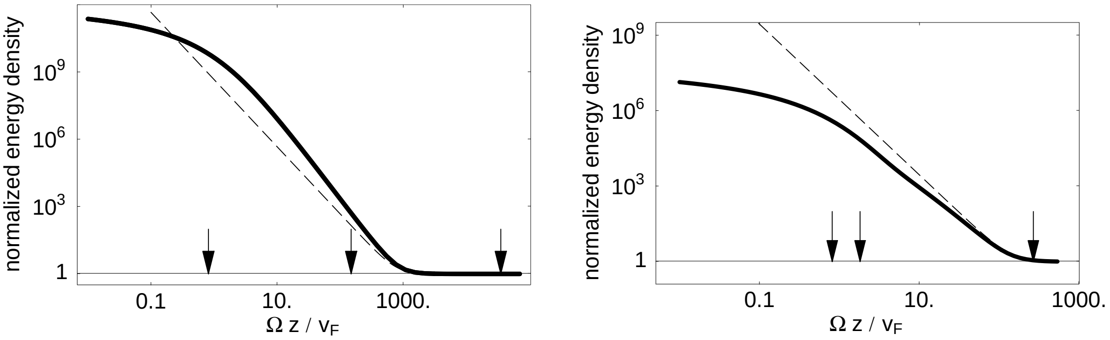

Fig. 4 Electric energy density, normalized to its far-field value, vs. normalized distance $\Omega z/v_F$. Dashed line: local dielectric. Solid line: numerical calculation (left: $\omega = 0.8\,\nu$; right: $\omega = 0.55\,\Omega$; other parameters as in Fig.3). The arrows mark, from left to right, the characteristic distances Λ, $|\ell|$, and $\lambda = 2\pi c/\omega$.

4.5 Energy density and lateral coherence

The numerical calculation of the correlation function Eq.(18) can be done efficiently using a numerical interpolation of $\operatorname{Im} r_p(K)$ that we continue for large and small K using the asymptotics derived above.

We plot in Fig.4 the electric energy density as a function of distance, for the same two frequencies as in Fig.3. Deviations from the local approximation (dashed line) occur at distances smaller than $|\ell|$: enhancement at low frequencies ($\omega \sim \nu$, left panel), suppression near the surface plasmon resonance (right panel), which is consistent with the trends seen in Fig.3. A saturation at small distances is also visible, although it occurs for fairly small values of $\Omega z/v_F$ (where the semi-classical Lindhard function is in practice no longer valid). We note also that for $z \geq \lambda$, the plots are only qualitative since the calculation does not take into account retardation.

Finally, we illustrate the finiteness of the coherence length as the distance of observation enters the nonlocal regime. We plot in Fig.5 the zz-component of the normalized coherence tensor (3), as a function of the lateral separation ρ/z. In the local regime, one would get a universal curve independent of the distance. This is no longer true near a nonlocal metal: when Thomas-Fermi screening sets in ($z \leq \Lambda$), the form of the coherence function changes and its width (the coherence length) becomes much larger than z.

5 Concluding remarks

We have discussed in this paper the impact of a nonlocal dielectric response on the spatial coherence of thermal electromagnetic near fields above a planar surface. Using two different models to describe the nonlocal response, we have shown that when the sources of the field have a finite correlation length, this length sets the minimum scale for the coherence length of the field as well. This behaviour is

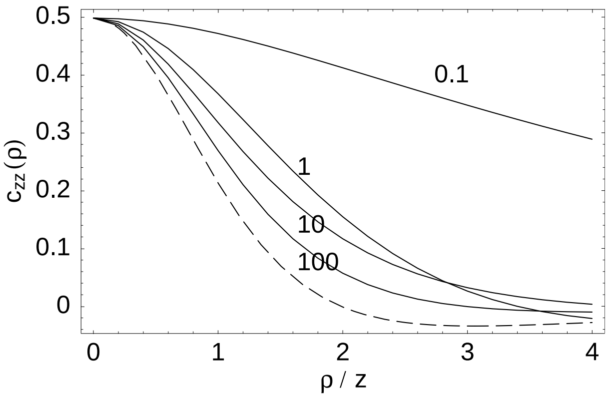

Fig. 5 Normalized degree of spatial coherence for z-polarized fields, probed at a lateral separation ρ. The numbers on the curves (solid lines) give the normalized distance $\Omega z/v_F = 100, 10, 1, 0.1$, with the normalized Thomas-Fermi screening length being $\Omega\Lambda/v_F = (\varepsilon_b/3)^{1/2} \approx 0.8$. Dashed line: result for a local dielectric in the near-field limit $z \ll \lambda$, taken from Eq.(4). The chosen parameters are those of Fig.3, right panel.

qualitatively similar to what we found previously when investigating the contribution of thermally excited surface plasmons where coherence length and plasmon propagation length coincide [5]. We have thus provided semi-quantitative evidence for the impact of nonlocality that has been conjectured already by Rytov's group [2].

The calculation for an electron plasma model highlights, on the one hand, the crucial role played by Thomas-Fermi screening, that sets the minimum coherence length. On the other hand, significant deviations from the local description already occur at scales below the electron mean free path (Fig.3 and Fig.4), although these are not accompanied by an increase in spatial coherence.

Our calculations can be improved taking into account quantum effects in the Lindhard dielectric function [29], which will lead to quantitative changes at short distance. Indeed, for typical metals, the Thomas-Fermi screening length v_F/Ω and the Fermi wavelength $1/k_F$ are fairly close [28]. A comparison to other models of nonlocal dielectric functions would be interesting as well. On the experimental side, it would be interesting to compare the recent data on heat transfer between a scanning tip and a surface [13] with a microscopic calculation along the lines used here. We also mention that in the context of the Casimir force, nonlocal surface impedances have been studied. The nonlocal correction is particularly relevant at finite temperature and large distances and leads to a behaviour of the Casimir force that is qualitatively similar, even without absorption, to the local, lossy Drude model, see for example Refs.[34, 35]. Finally, it remains to study the impact of another property of real metals, the smooth rather than abrupt transition of the electron density profile at the surface: this can be described by effective surface displacements that depend on both polarization and wave vector, thus adding to the nonlocal effects considered here [36].

We thank Rémi Carminati and Jean-Jacques Greffet for discussion and Illarion Dorofeyev and Francesco Intravaia for helpful comments. C.H. acknowledges support from the European Commission (network FASTNet and projects ACQP and QUELE).

A Appendix

Les us consider the Green tensor relating an electric current in a medium 2 ($z' < 0$) to the electric field in medium 1 ($z > 0$) that we take as vacuum ($\varepsilon_1 = 1$). This tensor can be written as an expansion in plane waves (Weyl expansion)

$$G_{ij}(\mathbf{r}, \mathbf{r}') = \frac{\mathrm{i}}{2} \int \frac{\mathrm{d}^2\mathbf{K}}{(2\pi)^2\, \gamma_2} g_{ij}(\mathbf{K}) e^{i\mathbf{K}\cdot(\mathbf{R}-\mathbf{R}')} e^{i\gamma_1 z} e^{-i\gamma_2 z'}, \tag{24}$$

where $\mathbf{K}$ is the wave vector component parallel to the interface. The γ_i are the z-components of the wave vector: $\gamma_i^2 = \epsilon_i(\omega/c)^2 - K^2$. In the notation of Ref.[5],

$$g_{ij}(\mathbf{K}) = \sum_{\mu=s,p} e^{(t)}_{\mu,i} e^{(2)}_{\mu,j} t^{21}_{\mu} \tag{25}$$

The polarization vectors for the s and p polarization are

$$\mathbf{e}^{(t)}_{\mathrm{s}} = \mathbf{e}^{(2)}_{\mathrm{s}} = \hat{\mathbf{K}} \times \hat{\mathbf{e}}_z \tag{26}$$

$$\mathbf{e}^{(t)}_{\mathrm{p}} = \frac{K\hat{\mathbf{z}} - \gamma\hat{\mathbf{K}}}{\omega/c} \tag{27}$$

$$\mathbf{e}^{(2)}_{\mathrm{p}} = \frac{K\hat{\mathbf{z}} - \gamma_2\hat{\mathbf{K}}}{\sqrt{\varepsilon_2}\,\omega/c} \tag{28}$$

where $\hat{\mathbf{K}}$ is the unit vector parallel to $\mathbf{K}$. The t^{21}_{μ} are the Fresnel transmission coefficients between media 2 and 1:

$$t^{21}_{\mathrm{s}} = \frac{2\gamma_2}{\gamma_1 + \gamma_2}, \qquad t^{21}_{\mathrm{p}} = \frac{2\gamma_2\sqrt{\varepsilon_2}}{\varepsilon_2\gamma_1 + \gamma_2}. \tag{29}$$

References

1. M. Planck: Verh. Dt. phys. Ges. (Berlin) **2**, 237 (1900)
2. S. M. Rytov, Y. A. Kravtsov, V. I. Tatarskii: *Elements of Random Fields*, Vol. 3 of *Principles of Statistical Radiophysics*. Berlin: Springer 1989
3. F. Gori, D. Ambrosini, V. Bagini: Opt. Commun. **107**, 331 (1994)
4. R. Carminati, J.-J. Greffet: Phys. Rev. Lett. **82**, 1660 (1999)
5. C. Henkel, K. Joulain, R. Carminati, J.-J. Greffet: Opt. Commun. **186**, 57 (2000) [physics/0008028]
6. O. D. Stefano, S. Savasta, R. Girlanda: Phys. Rev. A **60**, 1614 (1999)
7. R. R. Chance, A. Prock, R. Silbey: in *Advances in Chemical Physics XXXVII*, edited by I. Prigogine, S. A. Rice. New York: Wiley & Sons 1978, pp. 1–65
8. R. C. Dunn: Chem. Rev. **99**, 2891 (1999)
9. F. Chen, U. Mohideen, G. L. Klimchitskaya, V. M. Mostepanenko: Phys. Rev. Lett. **88**, 101801 (2002)

10. J.-B. Xu, K. Lauger, R. Moller, K. Dransfeld, I. H. Wilson: J. Appl. Phys. **76**, 7209 (1994)
11. J. B. Pendry: J. Phys. Cond. Matt. **11**, 6621 (1999)
12. J.-P. Mulet, K. Joulain, R. Carminati, J.-J. Greffet: Appl. Phys. Lett. **78**, 2931 (2001)
13. A. Kittel, W. Müller-Hirsch, J. Parisi, S.-A. Biehs, D. Reddig, M. Holthaus: Phys. Rev. Lett. **95**, 224301 (2005)
14. L. Mandel, E. Wolf: *Optical coherence and quantum optics*. Cambridge: Cambridge University Press 1995
15. K. Joulain, R. Carminati, J.-P. Mulet, J.-J. Greffet: Phys. Rev. B **68**, 245405 (2003) [physics/0307018]
16. T. Setälä, M. Kaivola, A. T. Friberg: Phys. Rev. Lett. **88**, 123902 (2002)
17. J. Ellis, A. Dogariu, S. Ponomarenko, E. Wolf: Opt. Lett. **29**, 1536 (2004)
18. C. Girard, C. Joachim, S. Gauthier: Rep. Prog. Phys. **63**, 893 (2000)
19. C. Henkel: *Coherence theory of atomic de Broglie waves and electromagnetic near fields*. Potsdam: Universitätsverlag 2004, online at http://opus.kobv.de/ubp/volltexte/2005/135/
20. S. Scheel, L. Knöll, D.-G. Welsch: acta phys. slov. **49**, 585 (1999) [quant-ph/9905007], proceedings of the 6th Central European Workshop on Quantum Optics, Chudobin, Czech Republic, April 30 - May 3, 1999
21. D. Polder, M. V. Hove: Phys. Rev. B **4**, 3303 (1971)
22. C. H. Henry, R. F. Kazarinov: Rev. Mod. Phys. **68**, 801 (1996)
23. H. B. Callen, T. A. Welton: Phys. Rev. **83**, 34 (1951)
24. W. Eckhardt: Opt. Commun. **41**, 305 (1982)
25. J. M. Wylie, J. E. Sipe: Phys. Rev. A **30**, 1185 (1984)
26. *Handbook of Mathematical Functions*, ninth ed., edited by M. Abramowitz, I. A. Stegun. New York: Dover Publications, Inc. 1972
27. *Handbook of optical constants of solids*, edited by E. Palik. San Diego: Academic 1985
28. N. W. Ashcroft, N. D. Mermin: *Solid State Physics*. Philadelphia: Saunders 1976
29. G. W. Ford, W. H. Weber: Phys. Rep. **113**, 195 (1984)
30. K. L. Kliewer, R. Fuchs: Phys. Rev. **172**, 607 (1968)
31. G. S. Agarwal: Phys. Rev. A **11**, 230 (1975)
32. I. Dorofeyev, H. Fuchs, J. Jersch: Phys. Rev. E **65**, 026610 (2002)
33. I. A. Larkin, M. I. Stockman, M. Achermann, V. I. Klimov: Phys. Rev. B **69**, 121403(R) (2004)
34. V. B. Svetovoy, R. Esquivel: Phys. Rev. E **72**, 036113 (2005)
35. B. E. Sernelius: Phys. Rev. B **71**, 235114 (2005)
36. P. J. Feibelman: Progr. Surf. Sci. **12**, 287 (1982)

References

1. M. Planck: Verh. Dt. phys. Ges. (Berlin) **2**, 237 (1900)
2. S. M. Rytov, Y. A. Kravtsov, V. I. Tatarskii: *Elements of Random Fields*, Vol. 3 of *Principles of Statistical Radiophysics*. Berlin: Springer 1989
3. F. Gori, D. Ambrosini, V. Bagini: Opt. Commun. **107**, 331 (1994)
4. R. Carminati, J.-J. Greffet: Phys. Rev. Lett. **82**, 1660 (1999)
5. C. Henkel, K. Joulain, R. Carminati, J.-J. Greffet: Opt. Commun. **186**, 57 (2000)
6. O. D. Stefano, S. Savasta, R. Girlanda: Phys. Rev. A **60**, 1614 (1999)
7. R. R. Chance, A. Prock, R. Silbey: in *Advances in Chemical Physics XXXVII*, edited by I. Prigogine, S. A. Rice. New York: Wiley & Sons 1978, pp. 1–65

8. R. C. Dunn: Chem. Rev. **99**, 2891 (1999)
9. F. Chen, U. Mohideen, G. L. Klimchitskaya, V. M. Mostepanenko: Phys. Rev. Lett. **88**, 101801 (2002)
10. J.-B. Xu, K. Lauger, R. Moller, K. Dransfeld, I. H. Wilson: J. Appl. Phys. **76**, 7209 (1994)
11. J. B. Pendry: J. Phys. Cond. Matt. **11**, 6621 (1999)
12. J.-P. Mulet, K. Joulain, R. Carminati, J.-J. Greffet: Appl. Phys. Lett. **78**, 2931 (2001)
13. A. Kittel, W. Müller-Hirsch, J. Parisi, S.-A. Biehs, D. Reddig, M. Holthaus: Phys. Rev. Lett. **95**, 224301 (2005)
14. L. Mandel, E. Wolf: *Optical coherence and quantum optics*. Cambridge: Cambridge University Press 1995
15. K. Joulain, R. Carminati, J.-P. Mulet, J.-J. Greffet: Phys. Rev. B **68**, 245405 (2003)
16. T. Setälä, M. Kaivola, A. T. Friberg: Phys. Rev. Lett. **88**, 123902 (2002)
17. J. Ellis, A. Dogariu, S. Ponomarenko, E. Wolf: Opt. Lett. **29**, 1536 (2004)
18. C. Girard, C. Joachim, S. Gauthier: Rep. Prog. Phys. **63**, 893 (2000)
19. C. Henkel: *Coherence theory of atomic de Broglie waves and electromagnetic near fields*. Potsdam: Universitätsverlag 2004, online at http://opus.kobv.de/ubp/volltexte/2005/135/
20. S. Scheel, L. Knöll, D.-G. Welsch: acta phys. slov. **49**, 585 (1999) [quant-ph/9905007].
21. D. Polder, M. V. Hove: Phys. Rev. B **4**, 3303 (1971)
22. C. H. Henry, R. F. Kazarinov: Rev. Mod. Phys. **68**, 801 (1996)
23. H. B. Callen, T. A. Welton: Phys. Rev. **83**, 34 (1951)
24. W. Eckhardt: Opt. Commun. **41**, 305 (1982)
25. J. M. Wylie, J. E. Sipe: Phys. Rev. A **30**, 1185 (1984)
26. *Handbook of Mathematical Functions*, ninth ed., edited by M. Abramowitz, I. A. Stegun. New York: Dover Publications, Inc. 1972
27. *Handbook of optical constants of solids*, edited by E. Palik. San Diego: Academic 1985
28. N. W. Ashcroft, N. D. Mermin: *Solid State Physics*. Philadelphia: Saunders 1976
29. G. W. Ford, W. H. Weber: Phys. Rep. **113**, 195 (1984)
30. K. L. Kliewer, R. Fuchs: Phys. Rev. **172**, 607 (1968)
31. G. S. Agarwal: Phys. Rev. A **11**, 230 (1975)
32. I. Dorofeyev, H. Fuchs, J. Jersch: Phys. Rev. E **65**, 026610 (2002)
33. I. A. Larkin, M. I. Stockman, M. Achermann, V. I. Klimov: Phys. Rev. B **69**, 121403(R) (2004)
34. V. B. Svetovoy, R. Esquivel: Phys. Rev. E **72**, 036113 (2005)
35. B. E. Sernelius: Phys. Rev. B **71**, 235114 (2005)
36. P. J. Feibelman: Progr. Surf. Sci. **12**, 287 (1982)